Non-linear interactions between US waves and contact interface

Dorra Nouira

Ph.D. Thesis

Nonlinear interactions between US waves and contact interface

Jointly awarded at the
University of Rome 'La Sapienza'
Dottorato di ricerca in Meccanica Teorica ed Applicata XIX ciclo

and at the
'University of Bordeaux'
Ecole doctorale: Sciences pour l'ingénieur (SPI)
Spécialité: Mécanique

By
Dorra NOUIRA

PhD Committee :

President	Odile ABRAHAM	Research director (GeoEND, Nantes)
Co-director	Anissa MEZIANE	Professor (University of Bordeaux)
Co-director	Francesco MASSI	Associate Professor (University of Rome 'La Sapienza')
Reviewer	Ilker Murat KOC	Professor (ITU Turkey)
Reviewer	Bruno LOMBARD	Research director (LMA, Marseille)
Examiner	Laurent BAILLET	Professor (Université Grenoble)
Examiner	Adnan AKAY	Professor (Bilkent university, Ankara)

11/12/2020

Research laboratories:
Dipartimento di Meccanica ed Aeronautica (DIMA)
Institut de mécanique (I2M)

Acknowledgements

This thesis arises in the framework of a ‘cotutelle’ thesis between La Sapienza of Rome and l’Institut de Mécanique et d’Ingénierie de Bordeaux (I2M). Firstly, I would like to thank both institutions for supporting this research and making it possible. Then, I am grateful to my French and Italian supervisors: the Professors Anissa Meziane and Francesco Massi for their professional guidance during the development of this research work. It has been a great pleasure working with you. Thank you for your support both scientifically and morally.

I would like to also express my gratitude to the Professor Laurent Baillet for his valuable collaboration and contribution to the research work. Sincere thanks goes to professors Bruno Lombard and Murat Ilker Koc for accepting the responsibility of reviewing the thesis. I would like to finish by extending my greeting to all friends, colleagues, professors, people that I have had the opportunity and the pleasure to meet during the thesis. Among them, Marie-Marthe, Fiona, Amir, Federica, Manuel, Mailcol and Ilaria.

Concluding, a last but certainly not least thanks to my family Jalel, Lilila and Amine to whom this thesis is dedicated.

Table of contents

General introduction

The identification of interface features is one major topic in different research domains and with several industrial applications. As an example, tribology and structural health monitoring are often confronted to the identification of interface parameters for the analysis of either the contact or structural response.

More specifically, the early characterisation of material damage is a key element in controlling the durability and reliability of in-service components and materials. Conventional non-destructive testing (NDT) methods often offer interesting solutions in terms of damage characterisation. However, these methods fail to detect localised damage such as closed cracks or micro-cracks. The latter phenomenon occurs frequently in the industrial field by fatigue or corrosion, for example, and represent the precursor of the final failure. It is, therefore, very important to identify.

Damage is often preceded by local changes in the mechanical characteristics of the material, which increase its nonlinear properties. A closed crack could be seen as a zero-volume heterogeneity. In the following, the term ‘contact interface’ will be then used to refer to both interfaces between solids in contact and localized defects inside the bulk of the solids.

In the recent decades, wave propagation has been proposed as a powerful tool for investigating the nonlinearities introduced into a system by material damaging or contact interfaces. In fact, during the propagation of acoustic waves, their spectrum is enriched with new frequencies. This is due to the nonlinear wave-crack interaction, which is commonly manifested by the generation of harmonics, i.e. multiple frequency components of the incident frequency. In order to detect and characterize defects (contact interfaces), it is therefore opportune to develop methods that exploit these particular wave-interface interactions. From recent works, nonlinear methods seem to have the potential to detect and characterize localized defects. The challenge is to set up a method sensitive to this type of interactions (detecting and characterizing them) while being independent on other nonlinearities of the system (material, electronic amplification etc.). For this purpose, a detailed understanding and modelling of the physical mechanisms, involved in the wave-interface interaction, is required to analyse the nonlinear signature and identify the governing contact parameters. The determination of these parameters could be then be used in non-destructive methods for the interface characterization.

In this context, this PhD work focuses on the analysis of the wave-interface interaction, while accounting for different phenomena, both in compression and in traction. The main objective is to understand the mechanisms responsible for the nonlinearity generated by the interface-wave interaction for characterization purposes. The proposed approach is based on a combination of numerical and experimental analyses. Indeed, given that the interface phenomena involved in the nonlinear contact response are extremely complex, the numerical analysis allows a better understanding of these types of interactions as a function of the involved physical parameters. This is achieved by using adapted numerical models to investigate the effect of each parameter at once. On the other hand, the experimental analysis allows retrieving specific information for the model and validating the numerical results on a real case. The practical objective of the thesis is to develop the tools and propose the outlines of a methodology allowing the identification of the parameters governing the interface-wave interaction, potentially useful for interface characterization.

The first Chapter opens with a brief presentation of the different types of nonlinearities encountered during wave propagation with a particular interest to contact nonlinearity, which is a general term used to describe the contact phenomena occurring at the interface during dynamic or acoustic excitation. In order to analyse the mechanisms involved in the contact nonlinearity, numerical modelling is required. The first section presents then the recent literature on the different modelling approaches of the interface-wave interaction. The analysis of existing methods enables to identify the requirements for the characteristics of a suitable numerical tool. In the second section of the chapter, the nonlinear NDT methods applied to the interface characterization are presented. The study will help to decide on the methods to be used in the following.

The second Chapter presents the overall approach and the tools used to carry out the analyses developed in this PhD work, concerning the characterization of contact interfaces in mechanical systems. First, the methodological approach of the research work, done during the thesis, is presented. Then, the numerical tools developed and used to carry out the numerical nonlinear contact analyses are described. Finally, the experimental tools, used to retrieve interface parameters and validate the numerical model are presented. All the different tools have been assembled in this work for investigating the main features of a contact interface, both in traction and compression.

Once the numerical models have been set up and numerically validated, they allow obtaining the acoustic response due to the interaction of acoustic waves with an interface, and thus allow investigating the influence of the various parameters on the generated nonlinearity. A contact

law describing adhesion in traction (elasticity coupled with damage) and non-penetration conditions in compression has been, first, introduced. The objective of the third Chapter is then the investigation of the interaction between longitudinal waves and a contact interface that follows this contact law, through the evolution of fundamental and second harmonics. A parametric analysis has been carried out and resulted in a promising approach for characterization.

However, because real surfaces are rough and not perfectly flat, this approach is not suitable for modelling the weak nonlinear response of tightly closed interfaces. In this context, the aim of the fourth Chapter is to present a numerical and experimental analysis to provide a basic insight into the nonlinear vibrational response of a contact interface, as a basis for evaluating and modelling the nonlinear contact through stress-dependent stiffness in compression.

So far, the effects of introducing contact stiffness in compression or traction have been studied separately in different contexts. The fifth Chapter presents an overall approach for modelling the nonlinear scattering induced by a contact interface by combining the two latter laws, with the aim of capturing both the weak nonlinear response of a rough interface and the strong nonlinear response of a “clapping” interface. This association of nonlinear behaviours is missing from the literature and the study of its effects on the wave-interface interaction would make it possible to complete the previous studies in the nonlinear contact framework.

Chapter 1: Overview of mechanical models of rough contact

1.1 Introduction

It is inevitable that all components and structures demonstrate a process of deteriorating of their properties and performances with time. Apart from ageing, the main reason for this is initiation and evolution of damage, under in-service loading and/or environmental conditions. Although in practice it is possible to foresee ageing or continuous deterioration, severe and/or unexpected structural damage could have fatal consequences. Thus, early damage detection and characterization is of a prime importance for safety management of structural assets. An objective of non-destructive testing (NDT) is to detect these defects and characterize them in order to decide on their degree of risk to the structure. This process of characterizing and understanding the contribution of the defect to the dynamic response of the system is crucial for many applications. These include robotic applications [1], grippers [2], micro-bearings [3], adhesive surfaces [4] and wherever dry contact occurs between solids [5]. In the case of structural diagnostic, health monitoring and quality control of components and joints, these are based on the measurement and interpretation of wave interaction with joint interfaces or component defects [6].

Among the various NDT methods, ultrasound allow an inspection of the whole volume of the structure, with relatively easy and non-restrictive processing in terms of safety and regulations. During their propagation in nonlinear media, the behavior of us or vibration waves can be altered. In fact, this propagation can lead to potential distortions in the signal, pseudo periodic or even chaotic behaviour. These nonlinear behaviours observed in different solids may be the result of a variety of mechanisms occurring at different scales. These mechanisms can be classified into three categories: geometric nonlinearities, material nonlinearities and contact nonlinearities.

Geometric nonlinearities are often associated with large deformations. Therefore, they are not considered in the context of linear vibro-acoustic, which is based on the assumption of small deformations.

The **nonlinearities within the material** correspond to a nonlinear stress-strain relationship. There are two main categories of material nonlinearities: classical and non-classical

nonlinearities. The classic volume nonlinearity is related to the microscopic effects distributed in the volume of the material. This type of nonlinearity can be considered in the mechanics equations by introducing the elastic constants of higher orders. The non-classical volume nonlinearities can be related for example to the hysteretic behaviour of the material or slow dynamics [7]. The effects induced by these nonlinearities depend on the propagation distance (nonlinearities within the volume).

Contact nonlinearities are considered non-classical, but they are localised. One example is intermittent 'clapping', which is similar to a shock between two constituents of a system.

Herein, localised nonlinear contact problems are the focus of this work, in the context of vibro-acoustics. This problem is related to the nonlinear interaction between one (or more) acoustic waves(s) and an interface (e.g. closed cracks). The nonlinearities generated by the wave-interface interaction are related to contact dynamics between the opposite faces of the interface, when excited with a sufficiently large vibro-acoustic excitation. For a normal incidence, the dynamic of contact is mainly translated by the 'clapping' mechanism, caused by alternating opening and closing of the interface. Indeed, when a sufficiently large incident wave reaches an imperfect contact interface at normal incidence, the compression part is transmitted while the part in traction opens the interface and is reflected. The transmitted signal loses symmetry with respect to its mean value. This form of distortion gives rise to generation of even and odd harmonics. The principle of this mechanism is given in Figure 1.

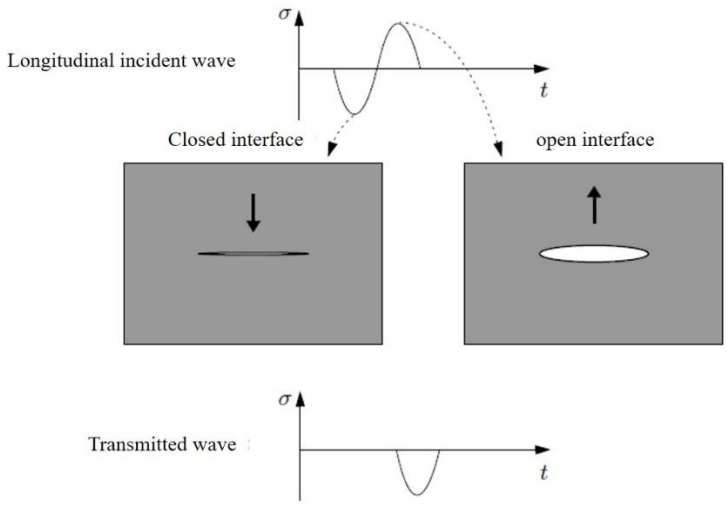

Figure 1 Nonlinear contact for an interface and a longitudinal wave under normal incidence: only compression waves are transmitted through the interface

However, in case of more realistic interface (e.g. crack) the surfaces in contact are not generally flat due to roughness and other factors. In addition, loss of contact does not occur instantly; the interface is damaged before being completely peeled off. This phenomena is described by the adhesion mechanism. Several different theoretical approaches have been proposed in the literature; however none of them have gained wide acceptance mainly because they separate these different nonlinear mechanisms. In this work, different nonlinear effects will be combined (roughness, clapping and adhesion) in order to enrich the physical understanding of nonlinear phenomena associated with interface-wave interactions.

Experimentally, several US dynamic and vibration methods have been developed for interface characterization. Conventional NDT methods consist of measuring the evolution of a parameter such as propagation velocity, attenuation or the transmission and reflection coefficients of the waves reflected by the interface, in order to determine the mechanical properties of the material, an interface or to detect the presence of a defect.

A defect will change the phase or amplitude of the measured signal and thus be detected. However, if the damaged area does not sufficiently interfere with sound propagation, as may be the case for a micro-crack distribution or closed crack, the linear NDT methods are no longer effective. However, a closed crack is as damaging as an open one to the structure. To overcome this limit, nonlinear acoustic methods can be used. In contrast to linear methods, which rely on amplitudes or phase effects, the nonlinear methods are based on changes in the frequency content of the vibro-acoustic wave during its propagation (see Figure 2). Changing the frequency of the signal, or even appearance of new frequencies in the spectrum, are the result of the interaction between a high amplitude wave and heterogeneities, such as plastic deformation zone, a crack or a contact interface with a nonlinear mechanical behaviour.

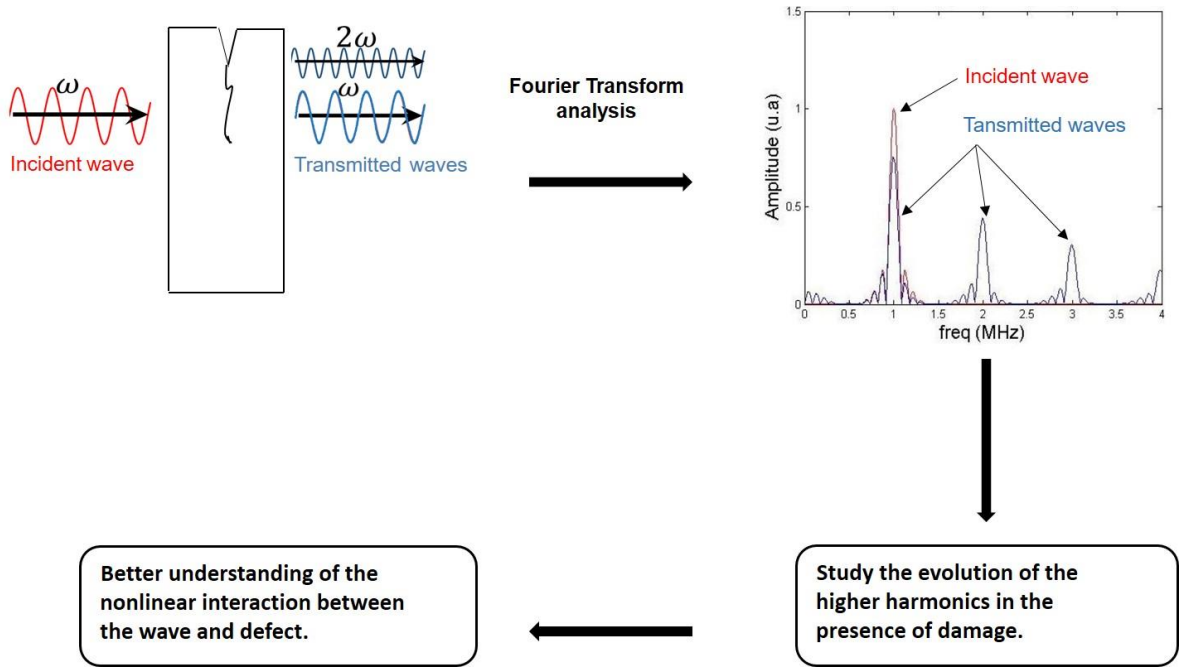

Figure 2 Illustration of the fundamental approach for nonlinear NDT methods. The focus here is on generation of higher harmonics.

Despite the different nonlinear mechanisms, whether in volume or contact, generate similar nonlinear effects; there is a general agreement that these nonlinear effects are relatively small in an undamaged material and remarkably strong in the presence of defect. This is the main attraction of NDT methods using nonlinear acoustics for defect detection. The main condition for collecting a nonlinear response is to generate significant excitations. Various methods can be used to do so: hammer impact, ultrasonic transducers, lasers, etc. Depending on the type of excitation used, most of these methods can be classified into three main categories:

- Excitation with a single acoustic wave: method of generating higher harmonics, sub-harmonics, nonlinear resonance.
- Vibro-acoustic excitation: method based on modal excitation combined with ultrasonic excitation leading to nonlinear modulations.
- Excitation with two acoustic waves. In the presence of a defect, a variant consists of modulating high-frequency and low-frequency waves.

The efficiency of these nonlinear methods has been demonstrated in numerous experiments. However, nonlinear phenomena associated with the interaction of damage with an us wave is not fully understood. This relates particularly to wave-interface interactions. A major problem is the variety of physical phenomena that can influence an interface behaviour. In fact, it is sometimes very difficult to separate the mechanisms involved in the generation of nonlinear

effects. It is clear then that modelling and numerical simulations, where various mechanisms can be easily switched on and off, are required for an in-depth analysis of these interactions. Therefore, the first part of this chapter covers various modelling aspects related to nonlinear wave-interface interactions. It is important to note that this section does not intend to review all the models that have been proposed. Only models used or related to our study will be included in the review.

The nonlinear interaction between a wave and interface generates several nonlinear effects. Hence, several NDT methods have been developed based on these effects in order to monitor damage in solids. The second part of the chapter reviews existing nonlinear methods for interface characterization.

1.2 Modeling of contact interfaces

One of the objectives of the NDT is to detect and characterise cracks as early as possible. A crack can be viewed as a finite size contact interface whose mechanical behaviour is nonlinear and complex. In this regard, nonlinear contact is responsible for several acoustic phenomena, such as the generation of higher and lower harmonics, hysteresis effects and amplitude modulation if two waves meet at the interface. Contact phenomena are complex, and interface behaviour is, in general, nonlinear.

In this section, different approaches to modelling the nonlinear interaction between a propagating wave and contact interface are presented. These approaches can be classified in two categories: the first one models the interface as a volume with nonlinear properties. Subsequently, it allows defining the relationship between the contact pressure and strain. The second one is based on the modelling of the interface by a contact law. Thus, it provides a relation between the contact pressure and the relative displacement at the interface.

1.2.1. Bilinear models

The bi-linear model is one of the best-known nonlinear interface models. It is based on bi-linear stiffness [8] (see Figure 3), also known as stiffness asymmetry, which consists in modelling the interface as a zone where the stress-strain relationship is asymmetrical. The relative behavioural law is a piecewise continuous function as follows

$$\sigma = E\varepsilon\left(1 - H(\varepsilon - \varepsilon_0)\frac{\Delta E}{E}\right) \quad 1.1$$

where H is the Heaviside function, ε_0 is the initial static strain and $\Delta E = (E - (\frac{d\sigma}{d\varepsilon})_{\varepsilon>0})$ is the loss of stiffness.

This model is constructed based on the lateral motion of the interface, in the presence of tension and compression, leading to an interface opening/closing. When the interface is open, the global stiffness is reduced; when the interface is closed, the stiffness is not affected [9] [10]. For one-dimensional case, this model treats the interface as a spring with a nonlinear stiffness coefficient consisting of two different stiffness values.

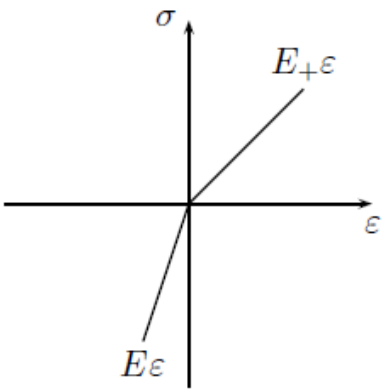

Figure 3 Evolution of the stress as a function of the strain according to the bi-modular model.

The bi-linear model is able to reproduce higher harmonics, but it still has several limitations. The first one concerns the absence of odd harmonics, as opposed to experimental observations [11] [12]. The second is the abrupt change in rigidity during the transition between the open and closed configurations of the interface. The homogeneity of the model is another important constraint [8].

According to other authors, due to the presence of roughness, the interface behaviour becomes more complex; hence, the shift from one stiffness value to another is not enough to represent it properly. Indeed, the actual contact area of an interface depends on the progressive deformation of the asperities under the applied load. Consequently, different models based on

contact laws, have been developed in order to account for the latter phenomena and will be presented in the next paragraph.

1.2.2. Contact laws

An alternative approach to model the nonlinear interaction between a propagating wave and a contact interface is to use contact laws. The dynamic behaviour of the interface during acoustic or vibration excitation may result in alternation of opening and closing of both sides of the interface.

1.2.2.1. Contact unilateral

An incident wave generates a compressive stress σ_i, which in turn creates a normal stress σ at the interface. To simplify, it is assumed that no load is applied to the solid. The unilateral contact (or Signorini's law) is the written:

$$\begin{cases} [u] \geq 0 \\ \sigma(t) \leq 0 \\ [u]\sigma(t) = 0 \end{cases} \qquad 1.2$$

where [u] is the relative displacement at the interface.
The first line of this system ensures the non-penetration of the solid through the rigid interface. When $[u] > 0$, the interface is open. The second equation indicates that only compressive stress can exist at the interface. When opening occurs, the contact pressure σ is null. Finally, the third line is called the complementarity equation. It ensures that the interface is either open or closed.
The first analytical model explaining the generation of higher harmonics in the case of a closed crack using a unilateral contact law was reported by Richardson in 1979 [13]. The model studies the nonlinear interaction between a plane longitudinal wave in normal incidence and a flat contact interface separating two semi-infinite elastic media. The two sides of the interface are held in contact by an applied pre-stress. The unilateral contact law describes the alternation of opening and closing of the interface during acoustic excitation while ensuring the non-interpenetration during contact phases. The evolution of the second harmonic amplitude was studied as a function of a non-dimensional load factor and showed a passage through an optimal

value. These results were experimentally validated in the case of a contact interface between two blocks of aluminium [14].

1.2.2.2. Rough interface models in compression

One of the main methods used to model a contact interface is to use a spring and a viscous damper in parallel. Contact stiffness can be obtained from analytical contact models, for instance, the Herzian contact model for spherical contacts [15]. In the case of rough surfaces in contact, the Greenwood and Williamson [16] statistical model and its successive reformulations [6] [17] [18] [19] have been used to obtain overall mean stiffness. Experimental values have been extracted using indirect methods [20] or system identification methods [21]. Recently, Jin et. al. [22] used a quasi-static model developed within the GW framework, in which all the microscopic geometric features of contact interfaces are extracted directly from high-resolution scanning electron microscopy (SEM) images of real fatigue cracks.

However, the development of increasingly sophisticated numerical models with contact interfaces means that more reliable and fine contact parameters need to be defined. Contact stiffness has been proved to be sensitive to contact conditions such as contact pressure [23] [24] [25], third body rheology [26] and the true area of contact [27].

In more detail, the force is supported by surface asperities. As the force increases, more asperities come into contact, while each asperity undergoes flattening deformation. In [28], three contact states can be identified: total sliding, partial slip and contact loss. In the case of partial slip, roughness has been described by Aleshin [28] using the Method of Memory Diagrams (MMD), a model developed to describe partial slip for rough surfaces in contact. The MMD model was then extended to take into account the other two regimes of total sliding and contact loss [29] [30]. The contact interface has a further nonlinear behaviour due to asymmetry between traction [31] [32] and compression configurations. During compression, the change in the contact interface configuration, as a function of contact pressure, also results in nonlinearity in the interface response.

When these nonlinearities are activated by the interaction between propagating waves and the contact interface, higher-order harmonics are then generated [33]. While these effects have been well studied in the ultrasonic field [34], they also represent a new area of investigation from a vibrational point of view [17]. In particular, the generation and features of second harmonics [35] deserve to be further analysed and exploited.

1.2.2.3. Rough interface modelling with a traction-free condition

The nonlinear stiffness laws presented in section 1.2.2.2, aim to represent the nonlinear compliance introduced by rough surfaces asperities during compression, which has been experimentally observed and reported in literature [36]. However, these laws do not describe the zero-stress condition corresponding to a loss of contact and is, thus, limited to cases where the interface remains in contact during wave propagation. By contrast, the unilateral contact, introduced in section 1.2.2.1, describes a traction-free condition during contact loss. However, it considers an infinitely rigid contact in compression, limiting the validity to perfectly smooth interfaces. These two laws are complementary and have been combined in [37] where the nonlinear stiffness has been described by quadratic springs:

$$\begin{cases} \sigma(t) = -\sigma_0 + K_0[u] - K_1[u]^2 \leq 0, & [u] \leq [u]_c \quad \text{during contact} \\ \sigma(t) = 0, & [u] \geq [u]_c \quad \text{during loss of contact} \end{cases} \qquad 1.3$$

where the contact pressure σ is characterized by a spring law as long as it remains negative. When the contact pressure reaches zero, which is attained for a critical interface gap opening $[u]_c$, the contact is lost and the stress subsequently remains equal to zero while the relative displacement $[u]$ increases. This contact law ensures that both strong nonlinear response induced by clapping and the nonlinear response due to rough surface contact are considered.
The results show that the linear response is hardly modified by the presence of nonlinear springs, contrary to the second harmonic, whose amplitude is increasing with the nonlinear spring constant and decreasing with the frequency. The second harmonic response shows a peak of amplitude for low compression stress (see Figure 4).

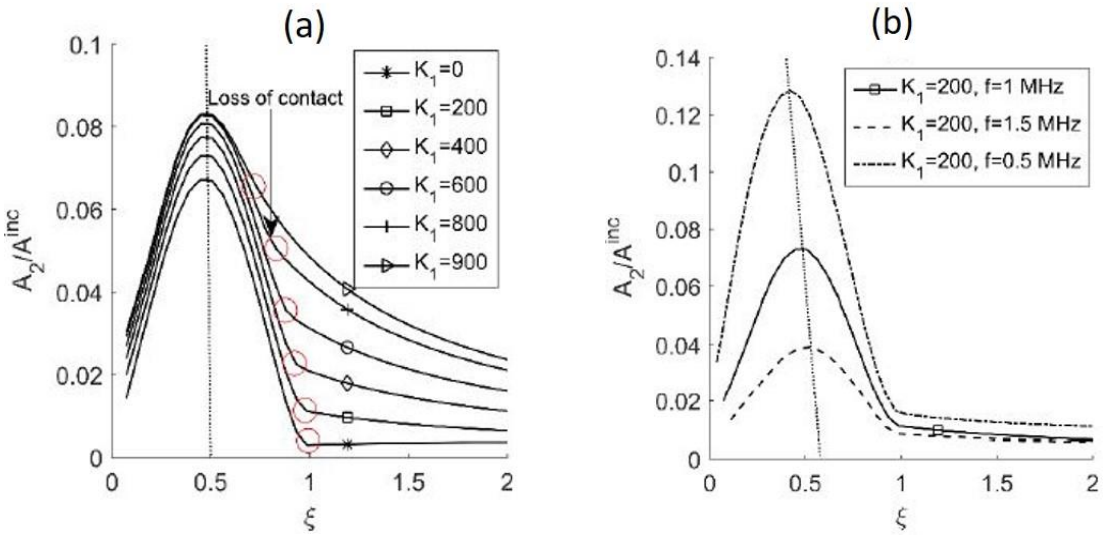

Figure 4 Evolution of (a) the second harmonic as a function of the non-dimensional load ξ, through a variation of the pre-stress σ_0 for a nonlinear spring model with loss of contact. The nonlinear stiffness K_1 is varied from 0 to 900 MPa/µm^2. The loss of contact is marked by the red circles in (a). (b) Second harmonic as a function of the non-dimensional load ξ, for different incident frequency and a fixed value of $K_1 = 200$ MPa/µm^2. The incident wave amplitude is defined to generate a constant incident stress of $\sigma_i^{max} = 1\ MPa$. *[37]*

1.2.2.4. Models involving adhesion

In addition to interface roughness, the nonlinear contact between a wave and an interface concerns imperfect interfaces that allow de-cohesion. It is therefore the object of a growing interest with regard to the possibilities offered for the detection of closed cracks and adhesion imperfections during a structural bonding. Lemaitre [38] has given a formulation of interface damage based on a visco-plastic analysis restricted to a surface. Needleman [39] has proposed a de-cohesion model without friction, based on atomistic considerations. An exponential representation is used for the interface potential. A few years later, Tvergaard [40] introduced a non-dimensional damage parameter to include a non-reversible evolution of de-cohesion. The same author added the coupling with frictional behaviour, which is active only when adhesion is totally broken. This induces a non-smooth evolution of the contact forces, which turn back to zero before friction starts.

Some works have been done considering an interphase model with the presence of a third body [41]. Although a third body approach would be attractive for the sake of simplicity of the concept, numerical simulations are difficult for two reasons. The first one is that the parameters and the real geometry of the third body are very hard to determine. The second one is that the numerical treatment (mesh..) is difficult because the interphase domain is one hundred to one

thousand smaller than the other considered domains. On the contrary, asymptotic methods and theoretical studies on the equivalent behaviour of the third body when the thickness decreases to zero are very constructive. One of the widely used models is the RCCM (Raous, Cangémi, Cocu and Monerie) contact law [42]. It is based on a mathematical and thermodynamic formulation of an interface law including unilateral contact, friction and adhesion and derives from the principle of virtual powers and thermodynamic laws.

The constitutive parameters of the model are the following

- C_N and C_T (N/m) are the initial stiffnesses of the interface
- w (J/m^2) is the limit of decohesion energy
- μ is the friction coefficient
- b (N.s/m) is the viscosity of the adhesion evolution

Adhesion is characterized, in this model, by the internal variable β, introduced first by Frémond [43] [44], which denotes the intensity of adhesion. It takes its values between 0 (no adhesion) and 1 (perfect adhesion). The use of a damageable stiffness of the interface, depending on β, ensures a good continuity between the two contact conditions (initial adhesion and final frictional sliding) during the competition between friction and adhesion.

Initially, when the adhesion is complete (β=1), the interface is elastic as long as the energy threshold w is not reached. After that, damage of the interface occurs and consequently, on the one hand the adhesion intensity β and the apparent stiffness $\beta^2 C_N$ and $\beta^2 C_T$ decrease, and on the other hand, friction begins to develop. When the adhesion vanishes totally ($\beta = 0$), we get the classical Signorini problem with Coulomb friction.

Figure 5 gives the normal and tangential behaviours of the interface during loading and unloading [42]. It should be noted that the Signorini conditions are strictly imposed when compression occurs. Regularisations such as penalisation or compliance are not used.

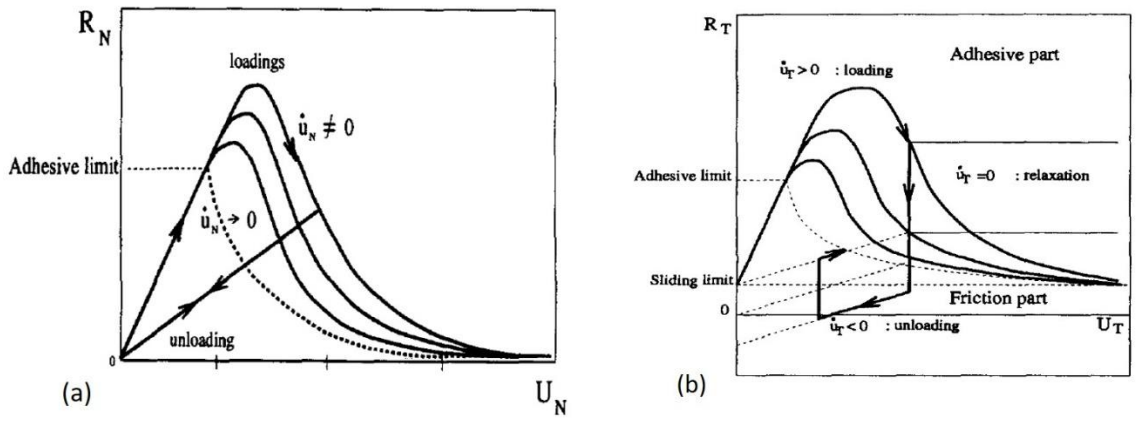

Figure 5 RCCM contact law. (a) Normal behaviour ($u_T = 0$) *[42]***. (b) Tangential behaviour (R_N is constant)** *[42]***.**

The initial conditions are supposed to be complete adhesion ($\beta = 1$) and zero displacement ($U_T = U_N = 0$). Considering first the normal behaviour in Figure 5 (a), under compressive action, the non-penetration condition is strictly verified ($U_N = 0$).

Under traction ($U_N \geq 0$), an adhesive resistance ($R_N = C_N U_N \beta^2$) is active (elasticity with damage). Three phases can be observed. During the first one, the adhesion intensity β is equal to 1 and the interface behaves like a spring with stiffness C_N. The intensity of adhesion starts to decrease when the displacement is sufficiently large such that the stress becomes larger than the elastic limit. The viscosity introduces, in addition to a dependence on strain velocity, a shift in the decay of the stress in relation to the damage and thus a normal maximum stress exceeding the elastic limit (see Figure 5 (a), ref [42]). When adhesion is totally broken, the classical Signorini problem is obtained.

Considering now the shear behaviour Figure 5 (b), note first that the friction acts only if a normal compression is applied; if a normal traction is applied ($U_N > 0$), the sliding limit ($\mu|R_N - \beta^2 C_N U_N|$) is zero and the tangential behaviour is elastic with damage ($R_T = \beta^2 C_T U_T$). Under compression, the sliding limit is ($\mu|R_N|$ because $u_N = 0$). As long as the norm of the tangential force $\|R_T\|$ is smaller than the sliding limit, sliding does not occur. When the sliding limit is reached, an elastic tangential displacement occurs. The adhesion begins to decrease when the adhesive limit is reached and evolution of β is decreased. When adhesion is lost (β goes to zero), the usual Coulomb friction conditions are obtained.

These different mechanisms, involved in the interface-wave interaction, are generally studied separately. There is little literature of models studying different nonlinear phenomena at the same time particularly roughness due to imperfect surfaces, clapping and adhesion. One of the

objectives of this thesis is to investigate these phenomena independently and then combine them for assessing their impact on the interface behaviour. The nonlinear interaction between wave(s) and contact interface is manifested by the enrichment of the spectrum with additional frequency components called harmonics, which is particularly interesting for interface characterization. In the next section, different nonlinear methods applied for interface characterization are reviewed.

1.3 NDT methods for interface characterization

Various nonlinear processes have been studied in the context of nonlinear characterization: nonlinear resonances, harmonic generation, non-linear wave-modulation spectroscopy, sub-harmonics… It is often observed that the measurements of nonlinear parameters from these nonlinear processes are more sensitive to the presence of an interface than linear elastic parameters (measured through linear vibro-acoustic methods), especially at early damage states [45]. Driven by industrial needs to improve the detectability of defects, nonlinear characterization methods have been the subject of a considerable number of research work. These methods can be grouped together under the abbreviation NEWS (Nonlinear Elastic Wave Spectroscopy) [46]. They differ by the nonlinear phenomenon exploited.

1.3.1. NL resonance spectroscopy

One of the non-linear phenomena caused by the presence of microscopic heterogeneities and defects distributed in volume of the material is the variation of the resonant frequency when increasing the excitation amplitude [47]. This phenomenon is directly related to the presence of heterogeneities, thus it can be used to quantify the damage level. This method is referred to as nonlinear resonance ultrasound spectroscopy NRUS [46] [48].

The method consists of evaluating one or more frequency peak shifts while increasing the amplitude. In fact, a sample is subjected to progressive damage induced by excitation around its resonance frequencies. The amplitude is increased gradually and the new resonance frequency is evaluated at each iteration. The resonance frequency shift indicates the presence of damage. Van Den Abeele and al. applied this technique to artificial slate slabs [48], which were progressively damaged by successive impacts in the centre of the slab. The shift in

resonance frequency is obtained when the excitation increases and is higher in the case of damaged sample. Figure 6 gives an example of an experimental result.

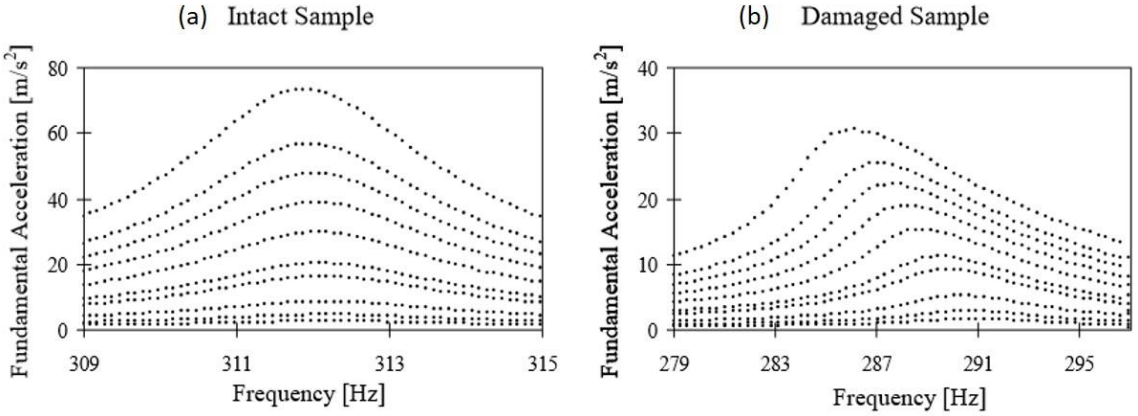

Figure 6 Amplitude-dependant resonance curves for (a) an intact sample and (b) damaged sample *[48]*

The frequency shift is characterized by a slope that accounts for the nonlinear parameter in this method. In fact, the slope increases with the damage. Therefore, the method quantifies the overall damage of the material; and has been applied to concrete [49], bone [50] and composite materials [51]. However, this method requires numerous measurements.

1.3.2. Generation of higher harmonics

The phenomenon of higher harmonic generation is one of the oldest phenomena in nonlinear acoustics. The first experimental demonstration of this phenomenon in solids was reported in 1963 by Breazeale and Thompson [52] and by Gedroits and Krasilnikov [53]. In these two studies, the generation of harmonics is the result of classical nonlinearity. In 1965, Hikata, Chick and Elbaum [54] showed that the phenomenon of higher harmonics generation increases considerably in the presence of defects. This work studies the detection of dislocation defects in metallic materials. Yermilin and al. [55] reported the first studies of harmonic generation in the case of fatigue cracks in 1973 and by Buck and al. [56] in 1976. These initially consider an artificial crack made by two aluminium blocks in contact. In a second step, the test was carried out on aluminium specimen AL2024 with a real fatigue crack. In both cases, the nonlinear interaction between a longitudinal wave at normal incidence and the pre-stressed contact interface was investigated. The results of this interaction show that the amplitude of the generated second harmonic presents a maximum as a function of the applied compression,

which was confirmed by Richardson's analytical model [13] published in 1979. A similar result was obtained by Taehyung Nam and al [57] using a longitudinal wave with oblique incidence on an interface of contact between two aluminium blocks. The reflected wave is analysed according to the normal stress applied. For the two angles (22.5° and 45°), the amplitude of the second harmonic goes through a maximum but with different amplitudes. The optimal of second harmonic amplitude as a function of the applied compression is characteristic of the nonlinear contact. Further details will be discussed in the chapter 3.

Another possibility to detect the damage is to study the evolution of the nonlinear parameter $\beta^* = \frac{A_2}{A_1^2}$ as a function of the applied load. Although this definition of the nonlinear parameter comes from the classical nonlinear acoustics theory, it is also used to assess nonlinearity caused by an interface. Buck and al. [56] show that this parameter reaches a maximum value when the applied compression is zero, and decreases exponentially as the applied compression increases. Biwa and al. obtained similar results again on aluminium blocks [58]. However, the evolution of the second harmonic shows a slight hysteresis effect depending on the applied load [58]. Lee and Jhang studied the evolution of the nonlinear parameter along a fatigue crack in an aluminium specimen [59]. A constant pressure is maintained on the transducers by a pneumatically controlled system to ensure a stable and repeatable measurement. For constant compression applied to the specimen, the nonlinear parameter β^*decreases progressively as it approaches the crack tip, and becomes constant once the point of the crack has been surpassed. Due to the stress concentration at the end of the crack, the nonlinear mechanisms are less activated, which limits the nonlinearity of the interface. For a given position, the parameter β^* decreases exponentially as the applied load increases. Another example of fatigue crack detection in a thin high resistance aluminium specimen using the nonlinear parameter β^* has been reported by Morris and al [60].

Several experimental works have studied the evolution of the nonlinear parameter β^* as a function of the number of fatigue cycles in different materials, such as aluminium alloys [61], nickel-based super alloys [62], carbon steel [63], titanium alloys and stainless steel [64]. The overall results show that the nonlinear parameter β^* is sensitive to the onset of fatigue damage. For example, Frouin and al [65] show that β^* starts to increase from 40% of the fatigue life. Classical techniques do not indicate the onset of a defect until 80 or 90% of the fatigue life [66].

Second harmonic measurement is also used to monitor ageing damage in materials such as aluminium alloys [56], titanium alloys [67], ferritic steels [68] and stainless steels [69]. The

results of all experiments show a sensitivity of the nonlinear parameter β^* as a function of the treatments during thermal ageing. For example, Yost and Cantrell [70] showed an increase of about 10% of β^* during the heat treatment of Al-2024.

The method of higher harmonic generation is also used to detect adhesion defects between an adhesive and a substrate, also known as 'kissing bonds' [71]. Since, bonding is an increasingly common means of assembly in aeronautics, the detection of adhesion defects (de-cohesion, contamination of various particles during assembly) represents a very important part of the process.

Also related to the evaluation of a joint, Ohara and al. studied the quality of diffusion welding between two steel bars [72]. A correlation between the temperature of welding, the strength of the joint and the amplitude of the second harmonic is obtained. A low welding temperature is synonymous with a low resistance, which results in a higher level of second harmonic.

From an experimental point of view, electronic system, or the coupling between the transducer and the test piece can introduce higher harmonics. The effect of electronic nonlinearity should be eliminated if possible to reveal the nonlinearity created by the interface. Blanloeuil [66] offers post-processing to extract the amplitude of the third harmonic independently of the nonlinearity of the measuring system, in the case of an incident shear wave. The principle consists in measuring the amplitude of the third harmonic generated by the electronic system for different incident amplitudes, the deducting it from the amplitude of the third harmonic generated by the interface using a correction coefficient. As the second harmonic is generally very low and difficult to measure precisely, Kim and al use the signal inversion method [73] (pulse inversion technique) to extract the second harmonic. This method is based upon the understanding that the phase-inversion of an impulse signal (180° phase shift) will lead to the phase inversion of the response obtained after propagation in linear medium, in contrast to a nonlinear medium due to the generation of harmonics. The principle is as follows: two waves in phase opposition are sent separately into the solid and the responses obtained are summed. Because of the 180° phase shift, the sum of the signals is destructive to the fundamental. On the other hand, the phase shift between two signals takes on a value of 360° for the second harmonic and their sum is therefore constructive. The amplitude of the second harmonic is doubled. Jhang proposes another way to evaluate the parameter β^* with more accuracy [74]. The signal processing employed involves a third-order autocorrelation coefficient, which has the property of suppressing the Gaussian noise contained in the signal and to bring out the multiple frequency components of each other. The measurement of the second harmonic is

more precise and the same applies to β^*. Regarding the coupling between the transducer and the sample, Makoto Fukuda and al. [75] suggest using an adhesive tape between the transducer and the sample surface to remove the second harmonic generated by the coupling.

The different techniques presented allow filter/estimate the parasitic nonlinearity generated by the experimental measurement chain and in particular the electronic system. As a result, the higher harmonic generation method is potentially interesting for the detection of closed cracks or interfaces in general, as it offers a simple analysis of the wave-interface interaction, and it is simpler to implement compared to other methods.

1.3.3. NL spectroscopy by wave modulation

In a non-linear material, whether in the classical sense or not, the principle of overlapping of linear acoustics is no longer valid and two waves may interact [76]. Nonlinear Wave Modulation Spectroscopy (NWMS) is based on this idea.

Two acoustic waves are generated simultaneously in the solid to be tested, the first is often of high frequency f_1 (probe wave) while the other has a lower frequency f_2 (pump wave).

In a healthy material, these two waves do not interact and the transmitted wave consists only of these two components. On the contrary, in a damaged material, the low frequency wave modulates the high frequency wave. The spectrum of the transmitted or reflected wave has the frequency components sum $f_{1+2} = f_1 + f_2$ and difference $f_{1-2} = f_1 - f_2$ [77].

These combinations in the spectrum of the measured signal indicate the presence of a defect. An advantage of this method is that it requires only one measurement to indicate the presence of damage, whether volumetric or localised. Furthermore, these frequency combinations are not generated by the electronic system if the excitations are independent.

To understand the operating principle, we consider a solid containing a crack, and where both waves are sent simultaneously. If the amplitude of the pumping wave is high, the crack will close during the compression phases and open during the traction phases. When the crack opens, the probe wave is less transmitted and its amplitude decreases. So there is a modulation of the high frequency wave by the low frequency wave. The principle is given in Figure 7. This description is simplified but allows us to understand the principle of the method in the case of a crack. In reality, the intrinsic non-linearity of a material, whether classical or not, also generates wave modulation.

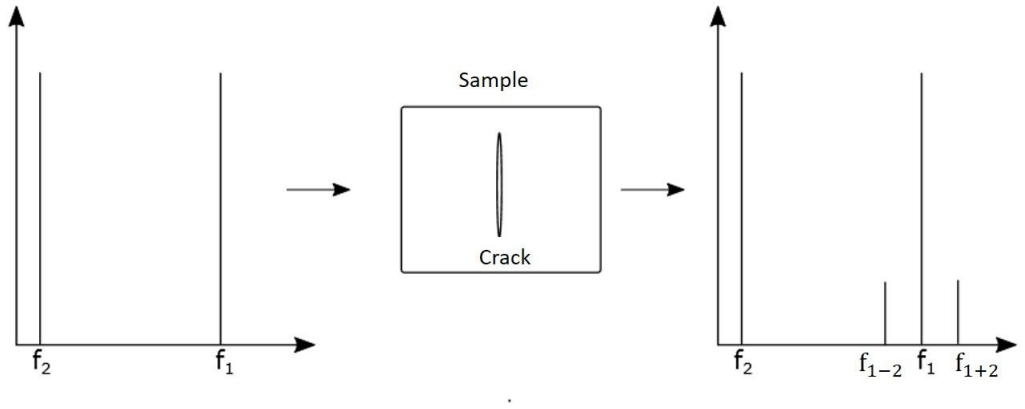

Figure 7 Nonlinear frequency modulation method. In the presence of defects, the high-frequency wave is modulated by the low-frequency wave. At the output, the spectrum contains additional frequency components: $f_{1-2} = f_1 - f_2$ and $f_{1+2} = f_1 + f_2$

Van Den Abeele and al. have applied this method to samples of Plexiglas [48]. Healthy materials show only the two initial components in the spectrum of the transmitted wave, whereas the sum and difference components appear in the case of a cracked sample. The amplitude of the frequency components f_{1+2} and f_{1-2} increases linearly with the excitation amplitude of the pump wave [48]. Applied to an engine connecting rod, the method is effective and reveals the presence of a crack [48]. Similarly, non-linear modulation has been used to monitor fatigue tests and crack propagation on steel [78] or aluminium [79] specimens under bending stress. Zaitsev et al. applied the method to a glass cylinder in which a crack was generated by thermal shock [80]. There are also applications to biological materials such as bone [81]. It is shown that the level of the components f_{1+2} and f_{1-2} allows the level of damage to be monitored. The work of Kim and al. has the particularity of using surface waves [79]. During the fatigue test, the measurements are carried out by applying a static flexural load to the bar. It is shown that the amplitude of the sum and difference components reaches a maximum when the load varies. In the case of a crack, the non-linear modulation therefore depends on the stress applied. Finally, it should be noted that in some of the studies mentioned above, low-frequency excitation is carried out using a hammer or a vibrating pot [78] ; this is known as vibro-acoustic methods. The non-linear modulation technique has been combined with an air coupling method [67]. Applied in transmission to a cracked polystyrene plate, it allows easy A-scan or B-scan examinations to be performed and the location of the crack to be determined [82]. Goursolle and al. associated the modulation method with temporal reversal techniques [86]. Reverse propagation by Finite Element calculation of f_{1+2} and f_{1-2} allows

the defect to be imaged. Used in pre-processing, time reversal allows the incident waves to be focused on the damaged area. Finally, the measurement of the modulation rate and the propagation speed of the low-frequency wave allowed Vila et al. to trace the non-linear parameter of a material [83]. The method is carried out in contact and is based on a special calibration protocol. Applied to a glass sample, the value and sign of β are in agreement with the values in the literature.

Another method of non-linear wave modulation is the non-collinear wave mixing method. This method was initially introduced to evaluate the classical non-linearity of materials, but can be easily extended to the non-linear characterization of a contact interface.

Figure 8 shows a schematic diagram of the principle of the method.

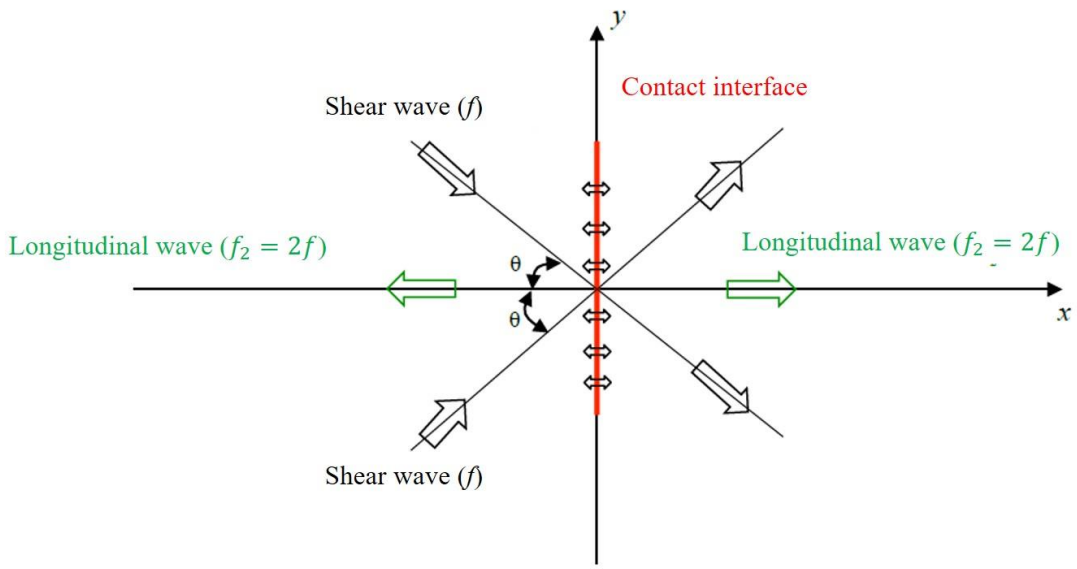

Figure 8 Principle of the non-collinear wave mixing method. Two shear waves are generated with the same angle of incidence θ in order to interact with the imperfect interface. A longitudinal wave of frequency $f_2 = 2f$ is then generated.

Two shear waves are generated simultaneously in the material. If the wave interaction contains a non-linearity (e.g. damaged material), a wave is generated, and its frequency is twice that of the incident waves. Compared to conventional collinear wave mixing techniques, the non-collinear wave mixing method has the advantage of modal, frequency, spatial and directional separation. Croxford et al [84] used the non-collinear wave mixing method on an aluminium alloy (Al2014-T4) part with a fatigue crack. The results show sensitivity to both plasticity and fatigue damage. Zhang et al [85] obtained similar results for plasticity in an inconel piece (IN 718). P. Blanloeuil et al [66] propose a numerical modelling by EF of the non-collinear wave

mixing applied to a closed crack. The results are promising for characterisation of this type of defect.

1.3.4. Sub-harmonics

The last decade has been marked by a growing interest in the use of subharmonics for the characterization of closed cracks. Subharmonics are generated by the nonlinear contact when the excitation amplitude becomes very large [86]. The selectivity of sub-harmonics for closed cracks is high since they are generated only by a contact interface, unlike higher harmonics or sum and difference components from modulation, which are also generated by the non-linearity of the volume of the material [86]. In addition, the electronic measuring system does not generate sub-harmonics. However, it is important to ensure that there is no clapping between the transducer and the solid under test.

The generation of sub-harmonics has been experimentally observed in several works [86]. Ohara and al. measured the evolution of subharmonics on a cracked beam with three-point flexion [72]. Flexion allows the state of compression applied to the crack to be varied. It is shown that the amplitude of the subharmonics increases with the flexural loading.

Studies have shown that sub-harmonics have a high spatial resolution in imagery [87]. On this basis, Ohara et al. have developed a subharmonic phased array for crack evaluation (SPACE) imaging method. The SPACE method was applied in the case of closed cracks [72] . The principle of this method is to excite the defect with high excitation in order to activate the nonlinear contact and generate the subharmonic component. This is recorded in addition to the fundamental component using a multi-element probe. The image produced from the fundamental component by a method such as the SAFT (Synthetic Aperture Focusing Technique) indicates open areas, while imaging from the sub-harmonic component allows closed areas to be located. The effect of an external traction load is studied [72]. As the load increases, the crack opens and the image area is reduced. As the crack passes through the specimen from one side to the other, its length is estimated at various points based on a scan of the specimen depth. Recently, some authors have proposed other imaging techniques based mainly on the acquisition of subharmonics by multi-elements probes.

In this research work, two of these methods will be used, namely higher harmonic generation for its simplicity and NRUS method for its efficiency and the fact that it can be applied to any type of geometry. This approach can be seen as a coupled nonlinear-resonance/harmonic generation method, allowing extracting the vibrational/acoustical responses of the system, at

the excitation frequency. These methods along with numerical modelling will provide access to nonlinear parameters that have not been reported in the literature yet and exhibit a strong dependence on damage. Indeed, numerical modelling will provide, in this context a better understanding of the interface-wave interaction and hence allow exploiting these observed nonlinear effects in view of characterising the different contact parameters.
In this context, our objective is to carry out the necessary numerical and experimental study in order to develop a methodology for identification of contact law parameter.

1.4 Positioning of the thesis work

The objective of this work is to investigate the wave/contact interface interactions in order to characterise contact interfaces. As shown in this chapter, many studies showed that nonlinear acoustics is efficient to detect defects, including contact, and it is promising for interface characterisation as it carries information on the non-linear behaviour of the interface. This investigation requires relying on efficient numerical and experimental tools in order to provide a deep analysis of these interactions.
The first decisive element is the choice of the contact interface law. Various models of non-classical nonlinearities were discussed. In general, the nonlinear mechanisms behind the discussed models can be classified, according to the material length scale, into microscopic, mesoscopic and macroscopic.
The first section of this Chapter reviews different modelling approaches for the interface-wave interaction. The presented models can be classified into two categories:

i. the first one includes models that are based on equivalent stress/strain relation (generally bilinear). They are simple to implement, but their disadvantage lies in the experimental determination of the interface stiffness and in the fact that they does not include some of the observed effects.
ii. the second one concerns the modelling of nonlinear contact via contact laws involving several physical mechanisms such as ‘clapping’, adhesion and compliance introduced by roughness. In the present work, this second approach has been chosen with the objective of set a numerical tool for analysing non-linear interaction between waves and interfaces, including adhesion in traction and non-linear compression behaviour due to asperities.

Then, different nonlinear methods have been presented in the following of the Chapter, which have shown to be efficient to detect cracks. Several experimental methods have been developed and some are presented in section 2. For interface detection, the nonlinear response of a contact was exploited, including the generation of new frequency components. The most basic approach is to generate higher harmonics. In order to overcome experimental limitations such as the low amplitude of harmonics, electronic nonlinearity or nonlinear effects common to several types of defects, other methods have been successively developed such as the NRUS method. These latter methods will be combined in the present work, each based on a different nonlinear effect, in order to understand the nonlinear contact mechanisms.

Moreover, because the investigation of non-linear interactions involve many parameters, even if there are few nonlinear effects, most of the time, the analysis of compression and traction nonlinearities have been separated into the literature. Concerning compression, a monotonic decrease of the second harmonic amplitude is generally observed when considering high compression of the interface. This behaviour is representative of rough surface contacts, and it is generally described by a power law function for higher pressures (more than 0.14 MPa). For lower pressures (lower than 0.14 MPa), to our knowledge, no particular models are found in literature to describe the interface stiffness. Herein, a 'novel' numerical model to describe the compliance introduced by rough surfaces over the whole pressure range should be proposed. Furthermore, experimental investigations also indicate that for low levels of compression and high incident wave amplitude, a stronger second harmonic response is observed, presenting a peak of amplitude when the applied pressure is varied. This behaviour is mainly attributed to clapping, e.g. intermittent loss of contact at the interface. This phenomenon is coupled with other mechanisms occurring when the interface is open, i.e. mainly adhesion phenomena. In terms of modelling, intermittent contact coupled with adhesion corresponds to a non-linear relation between the stress and the relative displacement between the two faces, which requires a further numerical approach. For this reason, RCCM contact law, accounting for clapping and adhesion, has been chosen in this work in numerical simulations to model the nonlinear response of the interface in traction. However, this approach is appropriate for the cases where the incident stress is larger than the compression stress at the interface and therefore not suitable for modelling response of tightly closed rough surface contact.

Accounting for all these considerations, in this thesis, we present a novel approach for modelling the nonlinear scattering induced by a contact interface. This was achievable by combining a nonlinear stiffness in compression and an RCCM contact law in traction, with the

aim of capturing both the weak nonlinear response of a rough interface and the strong nonlinear response due to adhesion and clapping phenomena, in view of an overall interface characterisation. From a numerical point of view, a flexible numerical tool that allows the introduction of several contact laws has been developed (Chapter 2). This numerical tool will first introduce the RCCM contact law, and an analysis of its nonlinear signature is then considered. Then a parametric study is carried out in order to identify the parameters governing the interface behaviour in traction. This aspect is interesting and revealed connections between interface response and interface properties that can be used in interface characterization (Chapter 3). Next, the developed nonlinear contact law in compression is introduced into the numerical model. Numerical results are compared first with experimental measurements in order to validate the model in compression (Chapter 4). Finally, both laws in compression and traction are implemented via the numerical tool. A contact law taking into account roughness, adhesion and clapping is then derived. This novel approach will enable to better understand the nonlinear interface-wave interaction for characterization purposes (Chapter 5). This overall approach, at the basis of this thesis, is summarized in Figure 9. First, the RCCM contact law will be used to describe the adhesion phenomenon in traction in chapter 3. Then, a nonlinear stiffness-pressure law representing the nonlinear compliance introduced by rough surface asperities during compression will be defined in details in chapter 4. Finally, this two latter models are combined in chapter 5, which constitutes a novel approach for modelling the nonlinear scattering induced by a contact interface.

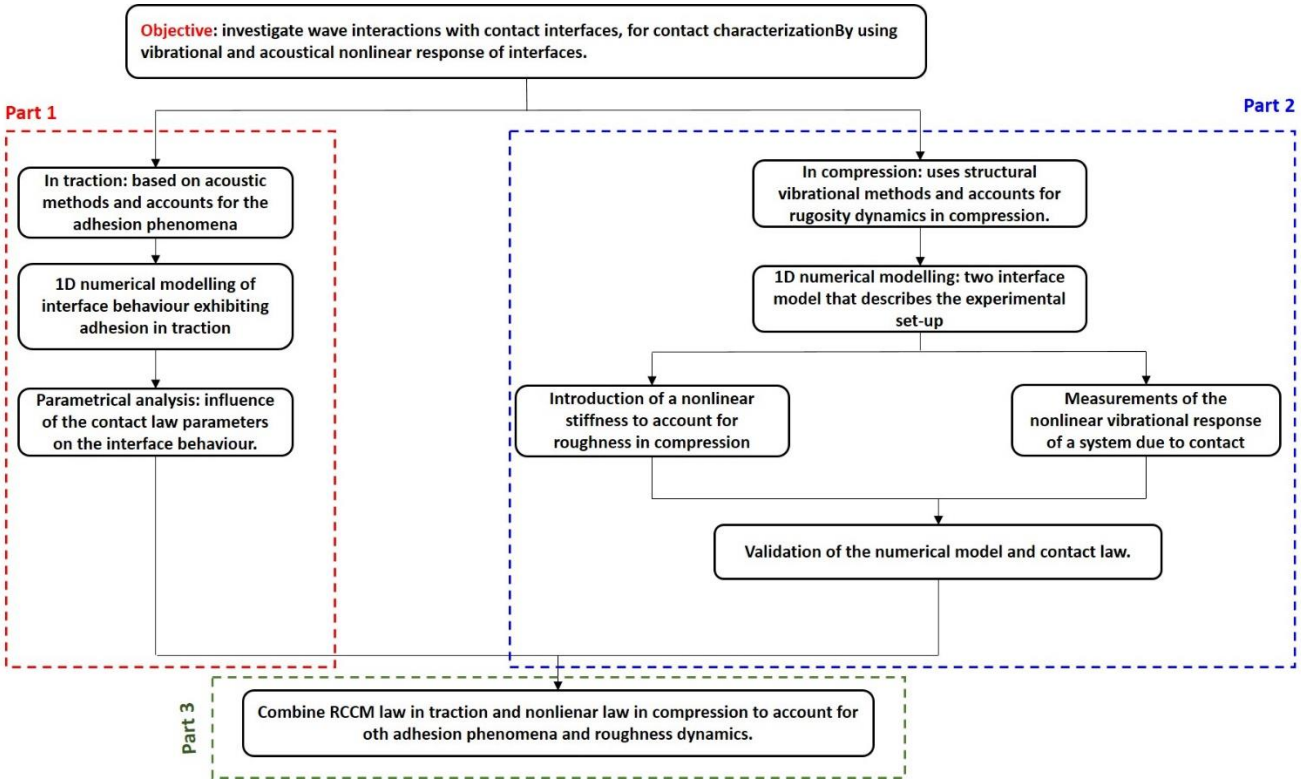

Figure 9 Thesis approach

Chapter 2: Materials and methods

This Chapter presents the overall approach and the tools used to carry out the analyses developed in this PhD work, concerning the characterization of contact interfaces in mechanical systems. First, the methodological approach of the research work done during the thesis is presented. Then, the numerical tools developed and used to carry out the numerical nonlinear contact analyses are described. The different numerical models (equations, geometry, boundary conditions, contact laws, etc.), developed for investigating the interaction between a wave and contact interfaces, are detailed. Finally, the experimental tools, used to validate and define the numerical contact law in compression, are presented. The used experimental setup ('Tribobrake') is detailed, together with the experimental protocol for the determination of the contact stiffness and the system dynamic response. All the different tools have been assembled in this work for investigating the main features of a contact interface, both in traction and compression.

2.1 Description of the methodology

The guiding thread of all the research work carried out during the thesis is the modelling of the interfaces, for the understanding of the physical phenomena involved in their nonlinear dynamic behaviour. The objective is to characterize a contact interface, which may present roughness and adhesion, by exploiting its nonlinear acoustic or vibrational response. Understanding the link between the interface nonlinear dynamic response and its physical features is a necessary step for developing non-destructive detection tools for the interface characterization.

Overall, the contact interface exhibits two different behaviours in traction and compression. The most basic model is the unilateral contact: no traction and infinite rigidity in compression. In this thesis, adhesion is considered in traction by using the RCCM law. While in compression, the nonlinear stiffness due to the surface roughness is considered. Our approach is to introduce both traction and compression features in an overall model, and analyse them from a dynamic point of view.

To this end, a complementary experimental and numerical analysis is proposed. As far as the numerical approach is concerned, two unidimensional models have been set-up. The first one

is a model with a single interface in contact with a rigid wall. It allows studying different contact laws namely the RCCM contact law, unilateral contact (traction) / NL stiffness (compression) and RCCM (traction)/NL stiffness (compression). The second model has been enriched with the possibility of introducing several interfaces in order to describe the experimental test bench. Regarding the experimental approach, an available experimental test bench (Tribobrake), allowing the measurement of the vibrational response of a system with contact interfaces, has been exploited for defining a part of the numerical model (the nonlinear stiffness in compression). In addition, the experimental measurements have been used to validate the nonlinear stiffness modelling by comparing the nonlinear dynamic response of the numerical and experimental system.

First, the traction and compression components of the contact law have been investigated separately. Then, both contacts laws in compression and traction were assembled together for providing the overall nonlinear modelling of the interface.

2.2 Experimental tools

2.2.1 Experimental set-up

The setup, used to identify and then validate the numerical nonlinear (NL) stiffness in compression, is illustrated in Figure 10.

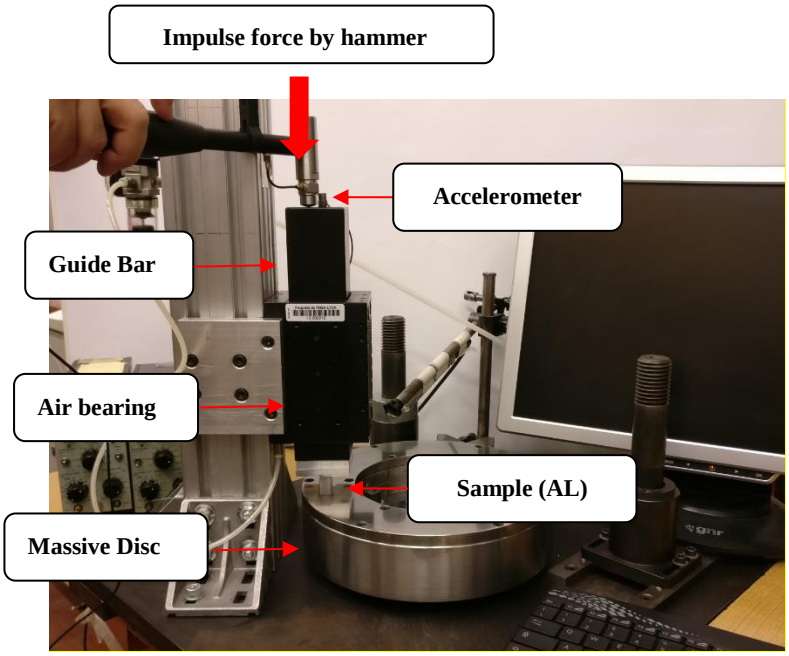

Figure 10 Experimental set-up

The system was designed to estimate the contact stiffness between two rough interfaces of different material samples, within a range of average contact pressure up to 1MPa, in both sticking and sliding conditions [26]. The system consists of a sample in contact with a massive steel disc and loaded by dead weights on a guide bar. The guide is maintained by an air bearing, to enable it to oscillate without introducing further stiffness and friction along the vertical direction.

The tested samples consist of aluminium (Al) and PMMA. The material properties and surface roughness parameters are presented in Table 1.

	Individual sample parameters			***Interface parameter***	
	Length (m)	***Contacting surface (m^2)***	***Young modulus (GPa)***	***Density (kgm^{-3})***	***Roughness (µm)Ra***
Aluminium	**0.015**	**1.15 x 10-4**	**71**	**2710**	**1**
PMMA	**0.015**	**1.15 x 10-4**	**5**	**1190**	**1**

Table 1 . Material and roughness parameters of the tested aluminium and PMMA sample.

An impulsive-type force is applied by an instrumented impact hammer (Brüel & Kjær type 8202) on the top of the guide bar, along the vertical direction, while the dynamic response of the system is recorded by an accelerometer placed as well on top of the guide bar. (see Figure 11)

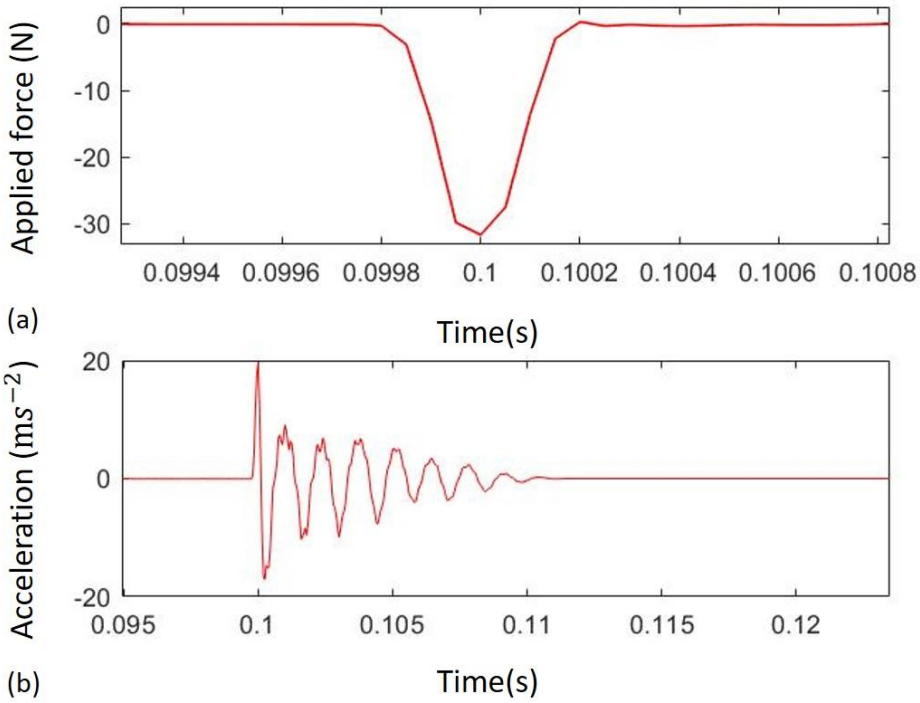

Figure 11 (a) Impulsive force signal over time; (b) Acceleration signal over time, obtained on the 'Tribobrake'. Test performed with impulsive contact force of 32 N. Sample (AL)

All the tests presented in this section are performed on the system with the overall weight of the guide bar on top of the sample, generating a static equilibrium pressure $p_0 = 0.14$ MPa. The force and acceleration signals are recorded using the acquisition system (SIRIUS – DEWESOFT), based on DualCoreADC® technology with dual 24-bit delta-sigma ADC (analogue to digital converter). An anti-aliasing filter on each analogue channel achieves a 160 dB dynamic range in time and frequency domains with 200 kHz sampling rate per channel. The data are then post-processed by Matlab.

Note that in the analysed configuration, the interface opening is not reached (impulse in compression).

2.2.2 Interface stiffness preliminary characterization

The contact stiffness of the tested samples was previously determined by experimental measurements, as reported in [26]. The proposed methodology for the estimation of normal stiffness is based on the dynamic contribution of the interface into the dynamic response of the mechanical system. A combined numerical and experimental approach is proposed for an indirect identification of the contact stiffness parameter. From an experimental point of view,

the setup (Tribobrake) has been designed and used to perform dynamic tests. Afterwards, a 3D finite element model, updated and representative of the experimental set-up, has been used to compare the numerical and experimental results, for estimating the normal contact stiffness between the considered contact surfaces.

Thus, the comparison between the results from the numerical model and the frequency response function obtained from experiments allows retrieving the value of the normal contact stiffness. In fact, a parametrical numerical modal analysis, as a function of the contact stiffness, is performed in order to meet the natural frequency of the investigated mode with the one measured experimentally. The numerical value of the contact stiffness that allows for a matching between experimental and numerical natural frequencies is retained as the estimated value of the interface stiffness.

From preliminary dynamic tests at different contact pressures, the contact stiffness has been estimated between 0.14 MPa and 1 MPa.

Table 2 shows the results for contact stiffness as a function of the average contact pressure for the (AL)-(AL) and (AL)-PMMA interface , with surface roughness of Ra = 1 μm.

The data highlight how the contact stiffness increases with the rise in the average contact pressure. The contact stiffness values range from 1.15 $x10^{12}$ Pa/m to 2.46 $x10^{12}$ Pa/m for the AL-AL interface and from $3x10^{11}$ to $6x10^{11}$ for a AL-PMMA interface, when the contact pressure increases from 0.14 MPa to 1 MPa.

Contact pressure [MPa]	***0.14***	***0.35***	***0.57***	***1***
Kc [Pa/m] for (AL) sample	**$1.15x10^{12}$**	**$1.75x10^{12}$**	**$1.63x10^{12}$**	**$2.46x10^{12}$**
Kc [Pa/m] for (PMMA) sample	**$3x10^{11}$**	**$4.6x10^{11}$**	**$4.95x10^{11}$**	**$6x10^{11}$**

Table 2 Normal contact stiffness as a function of the average contact pressure in sticking condition *[26]* **.**

These experimental results will be, here, exploited for defining the nonlinear trend of the numerical contact stiffness within the tested range of contact pressures. Indeed, in the following (chapter 4 and 5), these measurements of stiffness will be used to define a NL stiffness-pressure function that describes the interface behaviour in compression. The NL contact law will, also, be used to validate the numerical model in compression. It is, therefore, necessary to

numerically model the experimental setup. In the next section, the numerical tools used for the contact characterization are presented.

2.3 Numerical implementation tools

The different numerical frameworks and implementation of the equations are here detailed. First, the geometry and boundary conditions of the used models are presented: the first one for modelling the experimental setup; the second one for analysing the response of the developed contact law on a simple framework. Then, the equations and their numerical implementation are detailed, together with the different implemented contact laws.

2.3.1 1D modelling of the experimental system

A one-dimensional numerical model of the experimental set-up is implemented (Figure 12). It consists of the guide bar Ω_1 and the tested aluminium sample Ω_2, modelled by unidimensional deformable bodies.

Figure 12 Diagram (a) and numerical model; (b) of the set-up.

Two contacting interfaces are considered: the first at x=x_{C1} between the guide bar Ω_1 and the tested sample Ω_2, and the second at x=x_{C2} between the tested sample and the frame, considered as infinitely rigid in the model (tribometer disc). The model parameters are provided in Table 3.

.

Note that, in reality, the cross-sections of the guide bar Ω_1 and aluminium sample Ω_2 are different. Numerically, an equivalent 1D-model with the same cross-section S2 is considered, corresponding to the contact surface S2, by modifying the corresponding Young Modulus.

	Length L (m)	Mass m (Kg)	Young's Modulus E (GPa)	Density (kgm^{-3})	Contacting surface S_2 (m^2)
Guide bar (Ω_1)	0.229	1.61	71	2710	1.15 x10-4
Sample (Ω_2)	0.015	0.00467	71	2710	1.15 x10-4

Table 3. Geometry and material parameters of Ω_1 and Ω_2 in the numerical model.

2.3.2 Simplified model

This model is a simplification of the two-interface model (see Figure 12), where the system is reduced to a half-space model in contact with a rigid contact interface. The reflection of a normal incident plane wave at a contact interface is considered, as shown in Figure 13. The numerical model is defined for an homogeneous, isotropic elastic half-space, defined as Ω, and assumed to be initially in contact with a rigid wall at $x = 0$. Γ_c denotes the parts of the boundary where the solid and the wall are in contact. Here, a transparent boundary $\partial\Omega_t$ is defined in order to model an infinite medium. It is assumed that an initial static compressive stress $\sigma_0 = -p_0$ prevails. A source, placed at $x = -L$, generates an incident stress, in Ω, denoted σ_i. The maximal value of $|\sigma_i(t)|$ is noted σ_i^{max}.

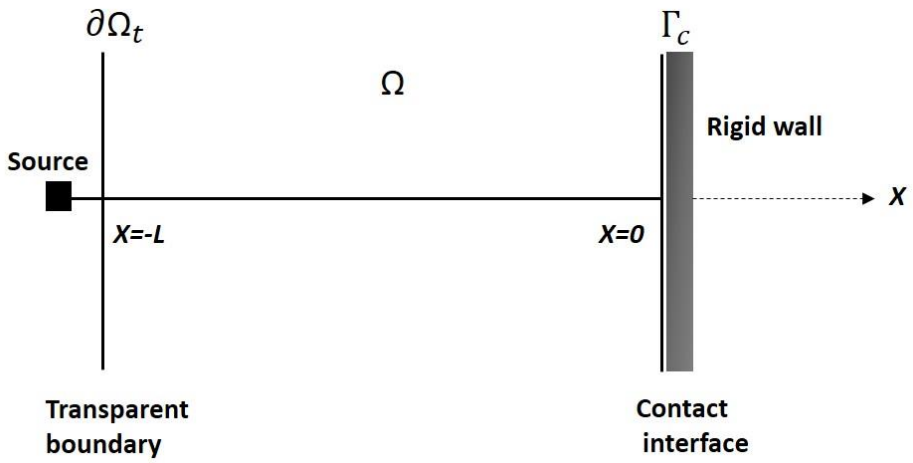

Figure 13 1D Configuration of the propagation of a plane wave through a contact interface located at $x = 0$.

By simplifying the model to a single interface, the focus turns to the effects of the analysed contact law and its parameters, without adding further complications related to the system geometry. The equations used for this model are the same obtained for the two-interface model, described in the following. However, additional assumptions must be included. Indeed, as the displacement of the rigid wall is zero, the relative displacement at the interface becomes the one of the solid. In addition, viscosity is not taken into account and the gravity acceleration is zero, since the system is horizontal.

In the following, the equations and numerical discretisation will be applied on the two-interface system (see Figure 12). During the implementation, when needed, these equations will be adjusted to the single interface configuration (see Figure 13) by using the conditions described above.

2.3.3 Equations

Recalling the equations will be developed for the two-interface model (see Figure 12). The elastic displacement $u = u(x,t)$ is defined relative to a static pressure p_0, the incident stress σ_i is given by the Hooke equation as follows

$$\sigma_i = E\frac{\partial u}{\partial x} - p_0, \tag{2.1}$$

where E is the Young's modulus of the material.

In the absence of elastic wave, the system is assumed free at one side (opposite to the contact side) and, for the model of the set-up, subject only to its own weight. In a first static step, the equilibrium position of the system can be calculated.

For the longitudinal waves, propagating along the x-direction (longitudinal) in both the guide bar and the aluminium sample, the equation of motion is the following:

$$\frac{\partial^2 u}{\partial \mathrm{t}^2} - c^2\frac{\partial^2 \mathrm{u}}{\partial \mathrm{x}^2} + h\frac{\partial \mathrm{u}}{\partial \mathrm{t}} = g \tag{2.2}$$

where u (x,t) is the displacement in the x-direction at time t, from the non-deformed configuration, c is the wave celerity, g is the gravity acceleration, h is the viscosity factor and t denotes the time.

The material nonlinearity is not considered, and consequently the only source of nonlinearity is generated at the interface. The general solution for the pad domain $x < x_{c1}$ is the sum of an incident wave and a reflected one; whereas on the sample domain ($x > x_{c1}$), the acoustic field consists only of the transmitted wave as follows:

$$\begin{cases} u(x,t) = f(x-ct) + g(x+ct)\,, & x < x_{c1}, t > 0 \\ u(x,t) = h(x-ct)\,, & x > x_{c1}, t > 0 \end{cases} \quad 2.3$$

where the function f ,describing the incident wave, is assumed to be given, while the functions g and h are to be determined in accordance with the boundary conditions at $x = 0$.
In view of equations (2.1) and (2.3), the pressure on both sides of the interface is given by

$$\begin{cases} \sigma(0^-,t) = E\left(f'(-ct) + g'(ct)\right) - \sigma_0 \\ \sigma(0^+,t) = E\,h'(-ct) - \sigma_0 \end{cases} \quad 2.4$$

It is recalled that the pressure across the interface is required to be continuous (by contrast to the displacement):

$$\sigma = \sigma(0^-,t) = \sigma(0^-,t) \quad 2.5$$

This interface pressure, as a function of the relative displacement, is defined by a contact law and allows describing the interface response. The relative displacement $[u]$ is calculated based on the expressions of the displacements on both sides of the contact interface

$$[u] = u(0^+,t) - u(0^-,t) \quad 2.6$$

The displacements at the top ($u(0^-,t)$) and bottom ($u(0^+,t)$) sides of the interface (Figure 12 (b)) are the following

$$\begin{cases} u(0^-,t) = f(-ct) + g(ct) \\ u(0^+,t) = h(-ct) \end{cases} \quad 2.7$$

Regardless of the choice of the contact law, the relative displacement satisfies the following differential equation:

$$[\dot{u}] = 2cf'(-ct) - \frac{2c}{E}(\sigma(t) + p_0) \quad 2.8$$

The solutions for the reflected and transmitted waves can be expressed as follows:

$$\begin{cases} g(x+ct) = -\frac{1}{2}[u(t+\frac{x}{c})] \\ h(x-ct) = f(x-ct) + \frac{1}{2}[u(t-\frac{x}{c})] \end{cases} \quad 2.9$$

For nonlinear contact laws, equation (2.8) is a nonlinear differential equation that, in general, can only be solved numerically. However, an analytical solution can be derived for the case where a linear spring law prevails in contact and contact loss, as discussed in chapter 5.
Overall, three different contact laws will be discussed in the next chapters:

- RCCM contact law to account for the adhesion phenomena in traction
- Traction-free + Nonlinear stiffness in compression to describe the compliance introduced by rough surface asperities during compression.
- RCCM (in traction) + Nonlinear stiffness in compression to account for both phenomena.

RCCM contact law behaviour

Equations (2.10) and (2.11) describe the unilateral contact with adhesion:

If the interface is closed

$$\begin{cases} [\mathrm{u}] = 0 \\ \sigma(t) < 0 \end{cases} \quad 2.10$$

If the interface is open

$$\begin{cases} [\mathrm{u}] > 0 \\ \sigma = C_N[\mathrm{u}]\beta^2 - p_0 \end{cases} \quad 2.11$$

Equation (2.12) gives the evolution of the adhesion intensity β

$$\frac{\partial \beta}{\partial t} = \frac{1}{b}(w - \beta(C_N {u_N}^2))^- \quad if\ \beta \in [0,1[\quad 2.12$$

Where w is the decohesion energy and $(q)^-$ denotes the negative part of the quantity q.

The problem of the RCCM law between a longitudinal wave and an interface is formulated. The initial conditions assume that the interface is initially closed and the contact conditions are given by equations (2.10) and (2.11). This contact law continuously relates the contact pressure σ with the relative displacement [u], as shown in Figure 14.

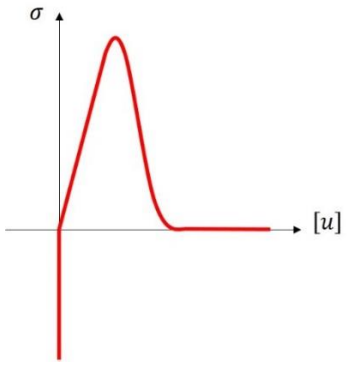

Figure 14 Graphical representation of the RCCM contact law

Traction-free + NL stiffness (in compression)

The unilateral contact law is characterized by a negative stress (compression only) and a closed interface, whereas loss of contact is characterized by a free boundary (zero pressure) and a positive gap opening, as shown in Figure 15 (a). Unilateral contact allows for intermittent clapping of the interface and is appropriate for cases where the incident stress is sufficient to overcome the static pressure p_0. However, the interface remains closed for lower incident stress, for which the incident wave propagates linearly.

Alternatively, a contact law, corresponding to nonlinear stiffness across the interface, can be defined by equation (2.13):

$$\sigma = \sigma_{NL}([\mathrm{u}]) - p_0 \qquad 2.13$$

where σ_{NL} is a nonlinear function of the relative displacement [u].

This nonlinear stiffness law continuously relates the stress at the interface with the relative displacement. However, the contact law does not account for intermittent clapping of the interface as shown in Figure 15 (b). Hence, this contact law is most appropriate for those cases where the stress generated by the incident wave is not sufficient to overcome the static pressure p_0, which would entail a loss of contact. These two laws are complementary and hence can be combined in order to account for the nonlinear interface stiffness in compression and

intermittent contact phenomena (see Figure 15 (c)). The nonlinear contact law is, then, defined as follows

If the interface is closed

$$\begin{cases} \sigma = \sigma_{NL}([\mathrm{u}]) - p_0 \\ \sigma(t) < 0 \end{cases} \qquad 2.14$$

If the interface is open

$$\begin{cases} [\mathrm{u}] > 0 \\ \sigma = 0 \end{cases} \qquad 2.15$$

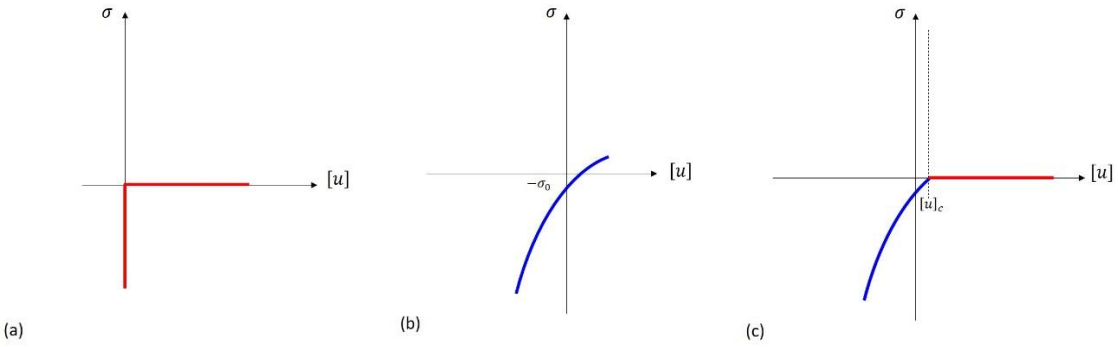

Figure 15 Graphical representation of the interface contact law. Graphical representation for (a) Unilateral contact; (b) nonlinear contact law and (c) combination of nonlinear stiffness with contact loss, where contact is lost when the contact pressure σ reaches zero and the relative displacement reaches a critical value $[u]_c$, considering that the reference ([u]=0) is the static state obtained when applying static pressure p_0.

RCCM (traction) + NL stiffness (compression)

On one hand, the RCCM contact law, shown in Figure 16 (a), takes into account the adhesion phenomena in traction, but considers an infinitely rigid contact in compression, limiting the validity of the model. On the other hand, the nonlinear stiffness law defined in equation (2.14), and shown in Figure 16 (b), represents the nonlinear compliance of the interface during compression, which has been experimentally observed and reported in the literature [36] [19] [37]. Therefore, in order to account for both these phenomena, the two laws have been here combined by using a nonlinear contact law in compression and the RCCM contact law in traction, as shown in Figure 16 (c). The equations describing the law are the following:

If the interface is closed

$$\begin{cases} \sigma = \sigma_{NL}([\mathrm{u}]) \\ \sigma(t) < 0 \end{cases} \qquad 2.16$$

If the interface is open

$$\begin{cases} [\mathrm{u}] > 0 \\ \sigma = C_N[\mathrm{u}]\beta^2 - p_0) \end{cases} \qquad 2.17$$

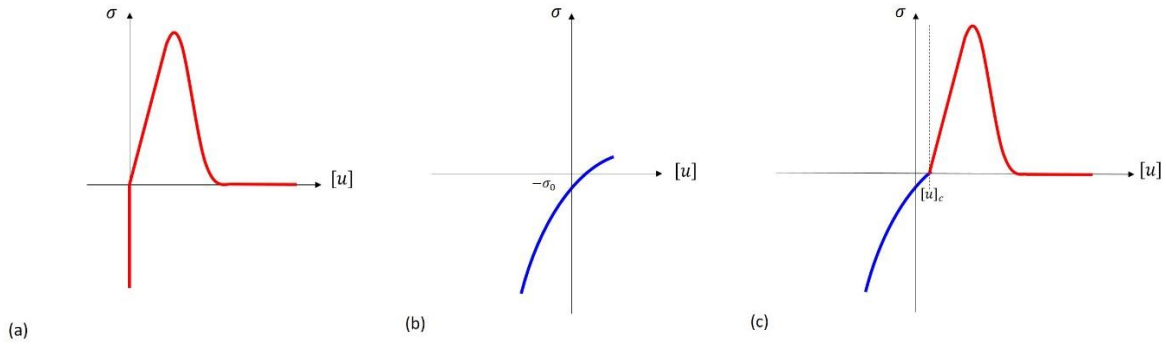

Figure 16 Graphical representation of the interface contact law. Graphical representation for (a)RCCM contact law; (b) nonlinear contact law and (c) combination of nonlinear stiffness with adhesion in traction, where contact is lost when the contact pressure σ reaches zero and the relative displacement reaches a critical value $[u]_c$.

Within the different Chapters, the choice of the contact law will be based on the objective of each specific study. In the following, the numerical implementation of these contact laws on the numerical model, equivalent to the 'Tribobrake', is presented.

2.3.4 Numerical implementation

The unidimensional wave equation (2.2) has been discretized using a second-order centred finite difference (FD) scheme, explicit in time, as shown in equation (2.18). This explicit numerical scheme has already been used and validated on Richardson's analytical solution for unilateral contact [13] and on other nonlinear contact laws [37].

$$\frac{u_k^{m+1} - 2u_k^m + u_k^{m-1}}{\delta t^2} - c^2 \frac{u_{k+1}^m - 2u_k^m + u_{k-1}^m}{\delta x^2} + h\frac{u_k^{m+1} - u_k^m}{\delta t} = g\,, \qquad 2.18$$
$$\forall k \epsilon [2, n_1 - 1] \cup [n_1 + 2, n_1 + n_2 - 1]$$

where the subscript k indicates the node number and m indicates the time step number, with δx and δt corresponding respectively to the space and time discretisation steps. n_1 and n_2 are respectively the total number of nodes contained in solids Ω_1 and Ω_2.
This second-order general scheme is conditionally stable under the classic Courant-Friedrichs-Lewy (CFL) condition:

$$\frac{c\delta t}{\delta x} < 1 \qquad 2.19$$

Equation (2.18) can be re-written to obtain the displacement at the next time step *m+1* for each internal node as follows:

$$u_k^{m+1} = u_k^m \left(\frac{2(1-\alpha_1)+\alpha_2}{1+\alpha_2}\right) + \frac{\alpha_1}{1+\alpha_2}(u_{k+1}^m + u_{k-1}^m) + \frac{1}{1+\alpha_2}(gdt^2 - u_k^{m-1}) \qquad 2.20$$

$$\forall k \epsilon [2, n_1 - 1] \cup [n_1 + 2, n_1 + n_2 - 1]$$

where $\alpha_1 = \frac{c^2 \delta t^2}{\delta x^2}$ and $\alpha_2 = h.dt$

The dynamic stress, generated at the left of the interface by the incident waves, is expressed with an off-centred backward 2nd order FD scheme

$$\sigma^- = E\,\frac{3u_{n_1}^m - 4u_{n_1-1}^m + u_{n_1-2}^m}{2\,\delta x} - p_0 \qquad 2.21$$

Whereas, the stress at the right side of the interface is evaluated from an off-centred forward 2nd order FD scheme

$$\sigma^+ = -E\,\frac{3u_{n_1+1}^m - 4u_{n_1+2}^m + u_{n_1+3}^m}{2\,\delta x} - p_0 \qquad 2.22$$

The relationship between the contact pressure and relative displacement is defined by the contact law. In this work, three different contact laws are considered.

RCCM contact law behaviour

If the interface is closed, we have:

$$\begin{cases} u_{n_1-1}^{m+1} = u_{n_1-1}^{m}\left(\dfrac{2(1-\alpha_1)+\alpha_2}{1+\alpha_2}\right) + \dfrac{\alpha_1}{1+\alpha_2}\left(u_{n_1-2}^{m}\right) + \dfrac{1}{1+\alpha_2}\left(gdt^2 - u_{n_1-1}^{m-1}\right) \\ u_{n_1}^{m} = 0 \\ u_{n+2}^{m+1} = u_{n_1+2}^{m}\left(\dfrac{2(1-\alpha_1)+\alpha_2}{1+\alpha_2}\right) + \dfrac{\alpha_1}{1+\alpha_2}\left(u_{n_1+3}^{m}\right) + \dfrac{1}{1+\alpha_2}\left(gdt^2 - u_{n_1+2}^{m-1}\right) \\ u_{n_1+1}^{m+1} = 0 \end{cases} \quad 2.23$$

During contact, the stress generated at the interface is expressed as follows

$$\begin{cases} \sigma^- = E\dfrac{-4u_{n_1-1}^{m} + u_{n_1-2}^{m}}{2\,\delta x} - p_0 \\ \sigma^+ = E\dfrac{4u_{n_1+2}^{m} - u_{n_1+3}^{m}}{2\,\delta x} - p_0 \end{cases} \quad 2.24$$

Contact is lost when the stress at the interface reaches $\sigma - C_N[u]\beta^2 + p_0 = 0$. Once reached, the interface is opened and the stress at the interface is positive. Using the previous boundary condition (

2.23) and equation (2.20), we obtain the following relations for the displacement at the interface at time *m+1* when the interface is opened:

$$\begin{cases} u_{n_1-1}^{m+1} = u_{n_1-1}^{m}\left(\dfrac{2(1-\alpha_1)+\alpha_2}{1+\alpha_2} + \dfrac{4E\alpha_1}{2\delta x\gamma(1+\alpha_2)}\right) + u_{n_1-2}^{m}\left(\dfrac{\alpha_1}{1+\alpha_2} - \dfrac{E\alpha_1}{2\delta x\gamma(1+\alpha_2)}\right) + \dfrac{1}{1+\alpha_2}\left(gdt^2 - u_{n_1-1}^{m-1}\right) - \dfrac{\alpha_1}{1+\alpha_2}\dfrac{C_N\beta^2}{\gamma}u_{n+1}^{m} \\ u_{n_1}^{m+1} = \dfrac{2E}{dx\gamma}u_{n_1-1}^{m+1} - \dfrac{E}{2dx\gamma}u_{n_1-2}^{m+1} - \dfrac{C_N\beta^2}{\gamma}u_{n_1+1}^{m+1} \\ u_{n_1+2}^{m+1} = u_{n_1+2}^{m}\left(\dfrac{2(1-\alpha_1)+\alpha_2}{1+\alpha_2} + \dfrac{4E\alpha_1}{2\delta x\gamma(1+\alpha_2)}\right) + u_{n_1+3}^{m}\left(\dfrac{\alpha_1}{1+\alpha_2} - \dfrac{E\alpha_1}{2\delta x\gamma(1+\alpha_2)}\right) + \dfrac{1}{1+\alpha_2}\left(gdt^2 - u_{n_1-1}^{m-1}\right) - \dfrac{\alpha_1}{1+\alpha_2}\dfrac{C_N\beta^2}{\gamma}u_{n}^{m} \\ u_{n_1+1}^{m+1} = \dfrac{2E}{dx\gamma}u_{n_1+2}^{m+1} - \dfrac{E}{2dx\gamma}u_{n_1+3}^{m+1} - \dfrac{C_N\beta^2}{\gamma}u_{n_1}^{m+1} \end{cases} \quad 2.25$$

where $\gamma = \dfrac{3E}{2dx} - C_N\beta^2$.

In this case, the stress at the interface is expressed by

$$\sigma = C_N[u]^m\beta^2 - p_0 \qquad 2.26$$

Traction-free + NL stiffness (in compression)

If the interface is closed, the dynamic stress generated by the incident wave is expressed with an off-centred 2nd order FD scheme:

$$\begin{aligned}\sigma^- &= -p_0 + \sigma_{NL}([u]^{m+1}) \\ &= -p_0 + E\frac{3u_{n_1}^{m+1} - 4u_{n_1-1}^{m+1} + u_{n_1-2}^{m+1}}{2\,\delta x}\end{aligned} \qquad 2.27$$

$$\begin{aligned}\sigma^+ &= -p_0 + \sigma_{NL}([u]^{m+1}) \\ &= -p_0 - E\frac{3u_{n_1+1}^{m} - 4u_{n_1+2}^{m} + u_{n_1+3}^{m}}{2\,\delta x}\end{aligned} \qquad 2.28$$

where σ_{NL} is a nonlinear function of the relative displacement.

Using equations (2.27) and (2.28), we obtain the following relations for the displacement at the interface at time *m+1*:

$$\begin{cases} u_{n_1}^{m+1} = \dfrac{4u_{n_1-1}^{m+1} - u_{n_1-2}^{m+1}}{3} + \dfrac{2\delta x}{3E}\left(\sigma_{NL}([u]^{m+1})\right) \\ u_{n_1+1}^{m+1} = \dfrac{4u_{n_1+2}^{m+1} - u_{n_1+3}^{m+1}}{3} - \dfrac{2\delta x}{3E}\left(\sigma_{NL}([u]^{m+1})\right) \end{cases} \qquad 2.29$$

Hence,

$$[u]^{m+1} = \frac{4u_{n_1+2}^{m+1} - u_{n_1+3}^{m+1} - 4u_{n_1-1}^{m+1} + u_{n_1-2}^{m+1}}{3} - \frac{4\delta x}{3E}\left(\sigma_{NL}([u]^{m+1})\right) \qquad 2.30$$

Which is the equation for the unknown relative displacement $[u]^{m+1}$ (recalling that the terms $u_{n_1+2}^{m+1}$, $u_{n_1+3}^{m+1}$, $u_{n_1-1}^{m+1}$ and $u_{n_1-2}^{m+1}$ can be obtained by computing, first, the result of the propagation equation).

In order to determine $[u]^{m+1}$, a nonlinear equation of the form $F([u]^{m+1}) = 0$ can be expressed and solved iteratively by Newton's method. F has the following expression:

$$F(u^{m+1}) = [u]^{m+1} - \frac{4u_{n_1+2}^{m+1} - u_{n_1+3}^{m+1} - 4u_{n_1-1}^{m+1} + u_{n_1-2}^{m+1}}{3} + \frac{4\delta x}{3E}(\sigma_{NL}([u]^{m+1})) \quad 2.31$$

If the interface is open, during loss of contact, we have $\sigma^- = \sigma^+ = 0$. Using equations (2.22) and (2.8), we obtain the values for the displacement on both sides of the interface:

$$\begin{cases} u_{n_1}^{m+1} = p_0 \dfrac{2\,\delta x}{3E} + \dfrac{4u_{n_1-1}^{m+1} - u_{n_1-2}^{m+1}}{3} \\ u_{n_1+1}^{m+1} = -p_0 \dfrac{2\,\delta x}{3E} + \dfrac{4u_{n_1+2}^{m+1} - u_{n_1+3}^{m+1}}{3} \end{cases} \quad 2.32$$

which completes the solution.

RCCM (traction) + NL stiffness (compression)

If the interface is closed, the dynamic stress generated by the acoustic wave is expressed by (2.27) and (2.28). The relative displacement is related to the contact pressure according to a nonlinear contact law denoted σ_{NL}. The displacements at the contact are as follows:

$$\begin{cases} u_{n_1}^{m+1} = \dfrac{4u_{n_1-1}^{m+1} - u_{n_1-2}^{m+1}}{3} + \dfrac{2\delta x}{3E}\left(\sigma_{NL}([u]^{m+1})\right) \\ u_{n_1+1}^{m+1} = \dfrac{4u_{n_1+2}^{m+1} - u_{n_1+3}^{m+1}}{3} - \dfrac{2\delta x}{3E}\left(\sigma_{NL}([u]^{m+1})\right) \end{cases} \quad 2.33$$

Hence,

$$[u]^{m+1} = \frac{4u_{n_1+2}^{m+1} - u_{n_1+3}^{m+1} - 4u_{n_1-1}^{m+1} + u_{n_1-2}^{m+1}}{3} - \frac{4\delta x}{3E}(\sigma_{NL}([u]^{m+1})) \quad 2.34$$

As stated above (Traction-free + NL stiffness (in compression) when interface is closed), to determine $[u]^{m+1}$, a nonlinear equation of the form $F([u]^{m+1}) = 0$ should be expressed and solved with Newton's method. F has the following expression:

$$F(u^{m+1}) = [u]^{m+1} - \frac{4u_{n_1+2}^{m+1} - u_{n_1+3}^{m+1} - 4u_{n_1-1}^{m+1} + u_{n_1-2}^{m+1}}{3} + \frac{4\delta x}{3E}(\sigma_{NL}([u]^{m+1})) \quad 2.35$$

When the contact is lost, the contact pressure is expressed by

$$\sigma = C_N[u]\beta^2 - p_0 \qquad 2.36$$

and the displacement at contact nodes $n_1 - 1$, n_1, $n_1 + 1$ and $n_1 + 2$ are the following:

$$\begin{cases} u_{n_1-1}^{m+1} = u_{n_1-1}^{m}\left(\frac{2(1-\alpha_1)+\alpha_2}{1+\alpha_2} + \frac{4E\alpha_1}{2\delta x\gamma(1+\alpha_2)}\right) + u_{n_1-2}^{m}\left(\frac{\alpha_1}{1+\alpha_2} - \frac{E\alpha_1}{2\delta x\gamma(1+\alpha_2)}\right) + \frac{1}{1+\alpha_2}\left(gdt^2 - u_{n_1-1}^{m-1}\right) - \frac{\alpha_1}{1+\alpha_2}\frac{C_N\beta^2}{\gamma}u_{n_1+1}^{m} \\ u_{n_1}^{m+1} = \frac{2E}{dx\gamma}u_{n_1-1}^{m+1} - \frac{E}{2dx\gamma}u_{n_1-2}^{m+1} - \frac{C_N\beta^2}{\gamma}u_{n_1+1}^{m+1} \\ u_{n_1+2}^{m+1} = u_{n_1+2}^{m}\left(\frac{2(1-\alpha_1)+\alpha_2}{1+\alpha_2} + \frac{4E\alpha_1}{2\delta x\gamma(1+\alpha_2)}\right) + u_{n_1+3}^{m}\left(\frac{\alpha_1}{1+\alpha_2} - \frac{E\alpha_1}{2\delta x\gamma(1+\alpha_2)}\right) + \frac{1}{1+\alpha_2}\left(gdt^2 - u_{n_1-1}^{m-1}\right) - \frac{\alpha_1}{1+\alpha_2}\frac{C_N\beta^2}{\gamma}u_{n_1}^{m} \\ u_{n_1+1}^{m+1} = \frac{2E}{dx\gamma}u_{n_1+2}^{m+1} - \frac{E}{2dx\gamma}u_{n_1+3}^{m+1} - \frac{C_N\beta^2}{\gamma}u_{n_1}^{m+1} \end{cases} \qquad 2.37$$

where $\gamma = \frac{3E}{2dx} - C_N\beta^2$.

2.3.5 Algorithm

Despite using different models and studying different contact laws, a general algorithm for describing the contact can be developed. In fact, the previous equation (2.20) can be expressed in a matrix form, such that the solution is advanced in time through a simple matrix-vector product

$$U^{m+1} = A\,U^{m} - U^{m-1} \qquad 2.38$$

where A is a tri-diagonal matrix and U is the vector containing the displacements at each time step. The boundary conditions must be used to express the missing relations in the system (2.40) for *k=1*, n_1, $n_1 + 1$ and $n_1 + n_2$.

The excitation $f(t)$ is imposed at the top of the guide bar (*x=-L*). Therefore, $u_{1(t)} = f(t)\ \forall t$ such that

$$u_1^{m+1} = f((m+1)\delta t) \qquad 2.39$$

This is implemented as a source term in the linear system through a vector B, where $B_1 = f((m+1)\delta t)$ and the other terms of B are zeros, leading to the linear system

$$U^{m+1} = A\,U^{m} - U^{m-1} + B \qquad 2.40$$

The contact nodes have different expressions depending on whether the interface is subjected to compression or traction. Therefore, the matrix $A = A_1$ will refer to the compression and $A = A_2$ will be used in traction. The choice between the matrixes A_1 and A_2 is made, at each time step, in accordance with the contact conditions.

The algorithm representing the numerical implementation on a single interface is shown in Figure 17. This algorithm is reapplied as many times as the number of interfaces. The numerical scheme is implemented using Matlab. Initially, the interface is closed. However, this algorithm is also valid for an interface initially open. The initial conditions will be then modified to take into account the initial relative displacement $[u]_0$.

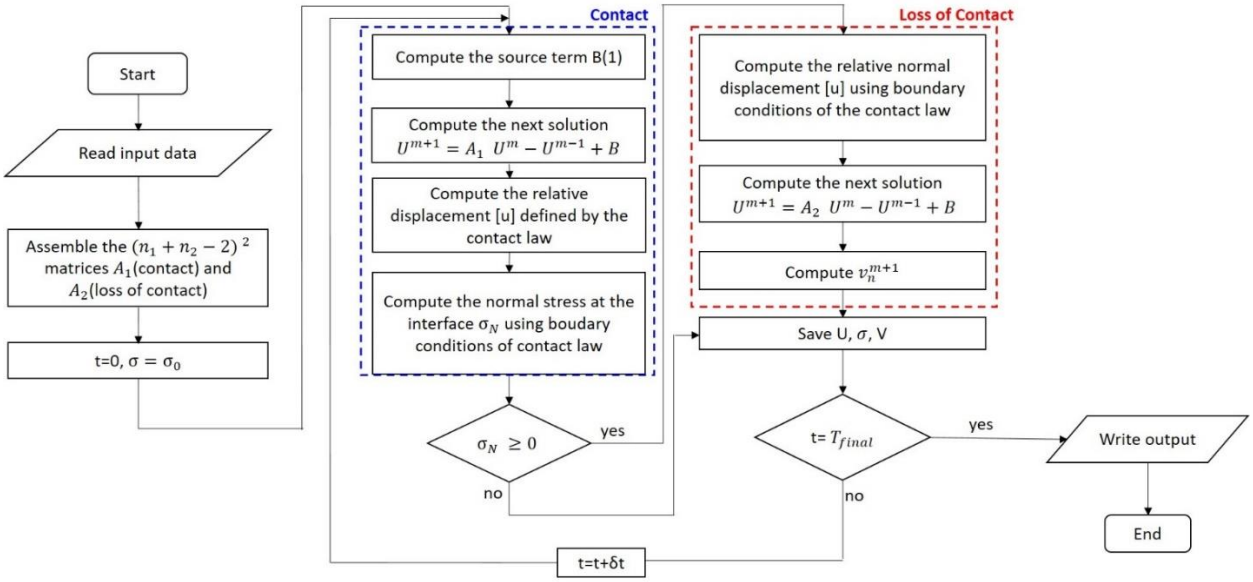

Figure 17 Numerical procedure to solve the contact problem. U and V are respectively the displacement and the velocity vectors.

In order to validate this algorithm, convergence will be verified for the different numerical schemes. The convergence study will be based on the value of the amplitude of the second harmonic. In fact, for a monochromatic incident wave, the second harmonic has the most important amplitude; therefore, it has a particular interest in the analysis of the response of contact interfaces. The procedure to obtain the second harmonic amplitude is the following:

- The incident wave σ_i is a 15 cycles sinusoidal signal modulated by a smooth rectangular window.

- The reflected wave is then windowed, transformed to the frequency domain, and

filtered to retain the second harmonic amplitude.

- The filtered signals are, then, normalized by the incident wave amplitude A_{inc} in order to highlight the nonlinear contribution originated by the contact interface.
- The result is then multiplied by 100 to express it as a percentage.
- Finally, the second harmonic efficiency is calculated as a function of a normalized load denoted ξ.

ξ is a parameter indicating whether the interface is in compression or traction. Its expression depends on the contact law in compression. In the most basic case, where the law is described by an infinite rigidity in compression, ξ is expressed as the ratio between the static pressure p_0 and the absolute value of the maximum of the incident stress σ_i^{max}:

$$\xi = \frac{p_0}{\sigma_i^{max}} \tag{2.41}$$

The solution, given by the smallest resolution, serves as a reference to validate the numerical solution. The error vector is calculated by subtracting the actual second harmonic efficiency$\frac{A_2}{A_{inc}}$, for a given mesh step, from the second harmonic efficiency for the smallest mesh step $\frac{A_2}{A_{inc}}\Big|_{ref}$. The difference between the two is then divided by $\frac{A_2}{A_{inc}}]_{ref}$ as follows

$$vect_{error}(\xi) = \frac{\frac{A_2}{A_{inc}}(\xi) - \frac{A_2}{A_{inc}}(\xi)\Big|_{ref}}{\frac{A_2}{A_{inc}}(\xi)\Big|_{ref}} \tag{2.42}$$

Hence, the value of the percent error is given by taking the norm of $vect_{error}$ and dividing it by Nb_ξ denoting the dimension of vector ξ:

$$Error = \frac{||vect_{error}(\xi)||_2}{Nb_\xi} \tag{2.43}$$

2.4 Concluding remarks

All the tools listed above are the bases for the works developed in this PhD thesis, as shown in Figure 18.

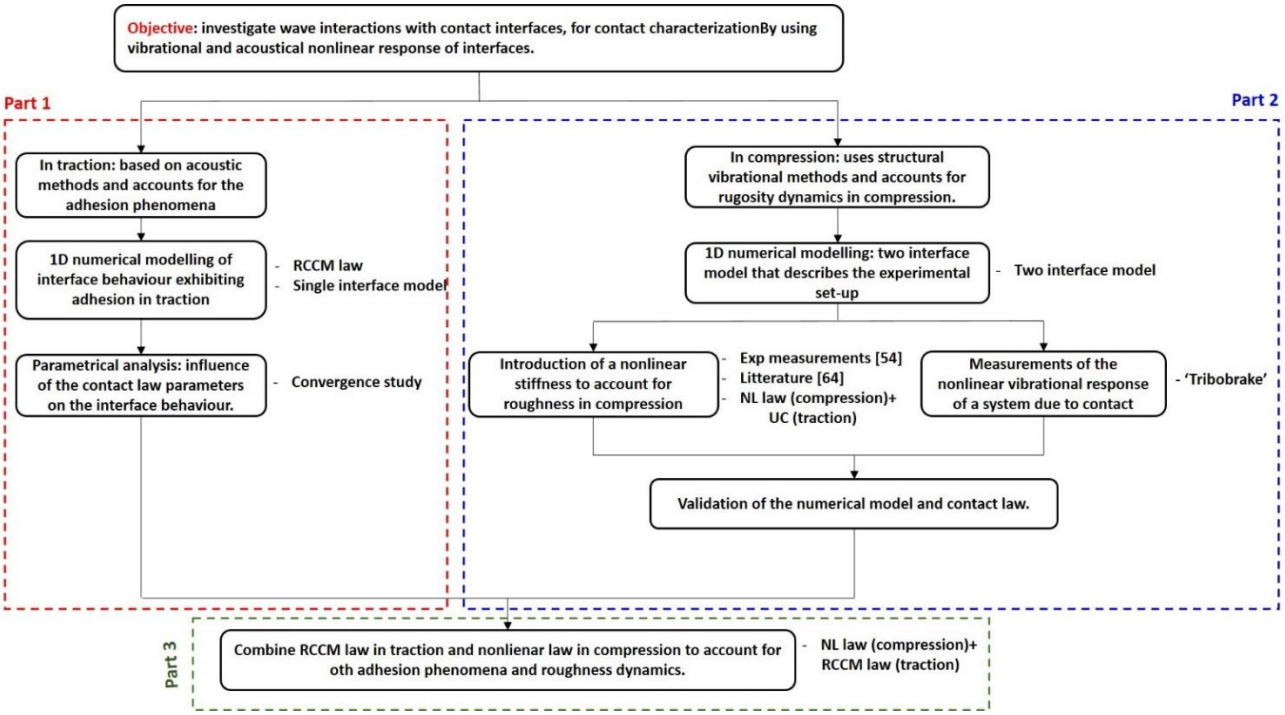

Figure 18 General outline of the thesis with the necessary tools for each stage.

Indeed, the experimental tools will allow defining, on one hand, a nonlinear contact law in compression accounting for the compliance due to surface roughness and the interface itself. On the other hand, the nonlinear response recovered during the experimental measurements will allow validating the proposed numerical model and the implemented nonlinear stiffness in compression. As for the numerical tools, they provide a basis for the different numerical simulations. While an investigation of the contact law in traction is performed as a function of the different parameters, the nonlinear contact stiffness in compression has been introduced, validated experimentally and assembled with the law in traction. The numerical code, presented here, allowed then for several parametrical analyses to verify the sensitivity of the dynamic nonlinear response to the different contact parameters.

Once validated, theses numerical tools will eventually allow to carry out further parametrical analyses to investigate features without having to damage the interface itself. This will be

illustrated in the next chapter, which proposes a detailed analysis on the interface behaviour in traction, while taking into account adhesion by the RCCM law. The aim is to understand its nonlinear signature and identify the governing parameters, which is a key factor for surface characterization.

Chapter 3: Nonlinear analysis of the RCCM contact law with adhesion

The numerical models have been set up in the previous chapter (Chapter 2) to address the interaction between an acoustic wave and a contact interface. Numerically validated, the models allow obtaining the acoustic response due to the interaction of acoustic waves with an interface, and thus will allow investigating the influence of the various parameters on the generated nonlinearity. Where appropriate, the obtained results will be compared with results from the literature. The model used in this chapter is the one presented in section 2.4 of chapter 2 (Figure 13), involving a semi-infinite space in nonlinear contact with a rigid wall. At the contact interface, the RCCM law [42] is imposed. Note that only normal behaviour is required in our configuration (normal incidence longitudinal plane wave and plane interface). This law describes adhesion in traction (elasticity coupled with damage) and non-penetration conditions in compression. The objective of this chapter is the investigation of the interaction between longitudinal waves and a contact interface that follows this contact law, through the evolution of fundamental and second harmonics. This study is based on previous analyses concerning the unilateral contact law [32] [13]. To our knowledge, RCCM law has never been studied in a context of nonlinear ultrasonic acoustics.

The study is divided into three main sub-sections:

- Validation of the numerical scheme for the studied model, by verifying convergence through grid size and time step;
- Analysis of the impact of the contact mechanism on the reflected wave and identification of the parameters that govern the nonlinear signature of the contact law;
- Study of the influence of the parameters involved in the contact mechanism on the second harmonic evolution.

First, the convergence of the numerical scheme is demonstrated. Then, an example for a longitudinal sinusoidal wave is presented and investigated. Finally, a parametrical study is conducted in order to identify the parameters governing the studied contact law and their impact on the nonlinear signature. The parameters in question are the parameter of RCCM contact law (contact stiffness, viscosity and decohesion energy) and the frequency of incident wave. It is noted that since the frequency is considered, one should verify the convergence for all the studied frequency values.

3.1 Validation of the numerical model

In order to focus on the interface behaviour, the model containing a semi-infinite medium in contact with a rigid wall is considered, as shown in Figure 19. A normal incidence longitudinal plane wave is generated at *x=-L*. It propagates in Ω and interacts with the contact interface at *x=0*, where the RCCM law is imposed. Note that a static pressure $p_0 \geq 0$ is imposed in Ω and consequently at the interface too. For more details, the reader can refer to paragraph 2.4 of chapter 2. Note that the interface remains undamaged throughout this section.

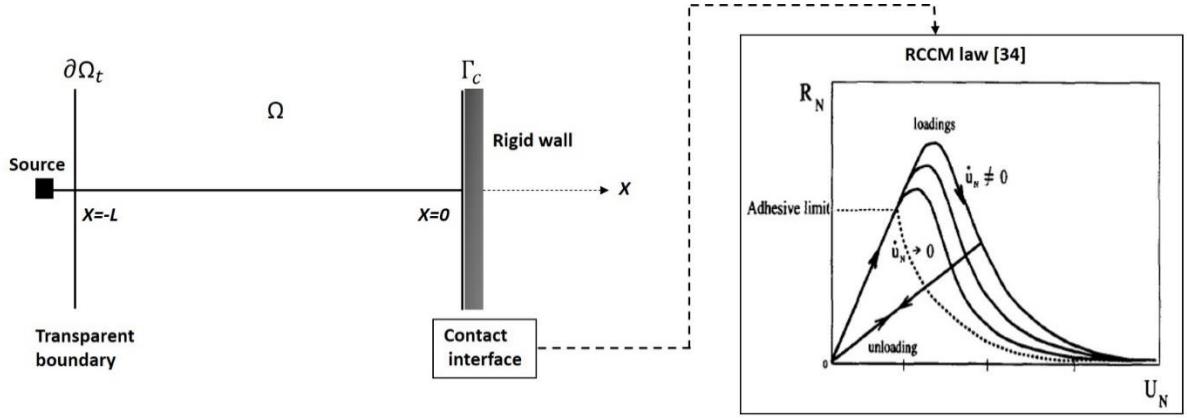

Figure 19 1D Configuration of the propagation of a plane wave through a contact interface located at $x = 0$ [42].

Depending on the magnitude of the incident wave, the interaction with the rigid wall can drive to an alternation of opening and closing of the interface, and thus shift from a perfect adhesion to a complete peel-off of the interface. Based on the mechanical conditions applied at the interface (i.e. parameter of the law vs magnitude of the incident wave and static pressure), the compressive wave can eventually cause opening and leading to damage the interface. This behaviour is described by the RCCM contact law, introduced at $x = 0$. It is recalled that the RCCM contact law accounts for a damageable adhesion in traction and non-penetration condition in compression (which can be considered as infinite stiffness in compression). The law is governed by the following parameters: the initial stiffness of the interface C_N, the decohesion energy w (J/m^2) and the viscosity b (N.s/m). The material used here is PMMA. The mechanical properties as well as the law parameters are presented in Table 4.

Law parameters			Mechanical parameters		
Normal stiffness C_N (Pa/m)	**Viscosity b (Pa.s)**	**Decohesion energy w (J/m^2)**	**Young Modulus E (GPa)**	**Poisson's ratio υ**	**Density ρ (kg/m^3)**
2.10^{13}	10^{-8}	0,1	5	0,4	1190

Table 4: Simulation parameters

The stiffness value is chosen different from zero so that the behaviour of the RCCM contact law can be distinguished from the unilateral case. About the viscosity, a very small value is chosen in order to minimize its impact on results, at this stage. This will be investigated further. For the value of the decohesion energy, it is calculated based on the Owens and Wendt expression for estimating the surface free energy [88]. For more details about the RCCM contact law, please refer to paragraph 1.3.2 of chapter 1.

The source, placed at $x = -L$, generates a longitudinal wave propagating in Ω. The incident wave $\sigma_i(t)$ is a 15 cycles sinusoidal signal modulated by a smooth rectangular window as shown in Figure 20. The maximal value of $|\sigma_i(t)|$ is noted σ_i^{max}.

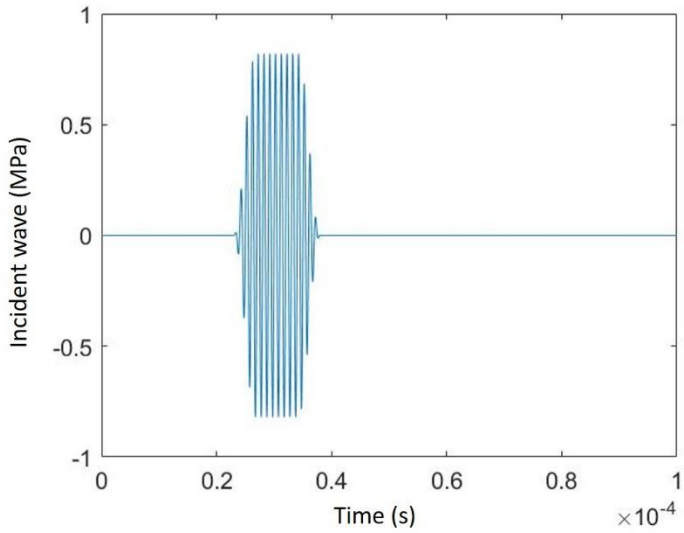

Figure 20 : Incident wave (case $\sigma_i^{max} = 0.82\ MPa$): stress generated in Ω over time measured at $x = -L$. Note that the magnitude of the incident contact stress is double the amplitude of incident wave σ_i. Frequency $f = 10^6\ Hz$. 15 cycles have been applied.

Nonlinear acoustic contact between a longitudinal wave and a contact interface generates both even and odd higher harmonics [13]. For a monochromatic incident wave, the second harmonic has the most important amplitude; therefore, it has a particular interest in the analysis of the response of contact interfaces. Hence, the convergence analysis is here based on the value of

the amplitude of the second harmonic. The procedure to obtain the second harmonic efficiency is the following:

i. We consider a sinusoidal incident wave $\sigma_i(t)$, as shown in Figure 20.

ii. The reflected wave (velocity) is then measured at x = -0.03 m, windowed, transformed to the frequency domain, and filtered to retain the second harmonic amplitude.

iii. The filtered signals are normalized by the incident wave amplitude A_{inc} (maximal value of velocity) in order to highlight the nonlinear contribution originated by the contact interface.

Figure 21 (a) illustrates the displacement solution at $x = -0.03m$, showing the incident and reflected waves. The linear increase of the displacement corresponds to the compression phase of the system. The correspondent spectrum is shown in Figure 21 (b).

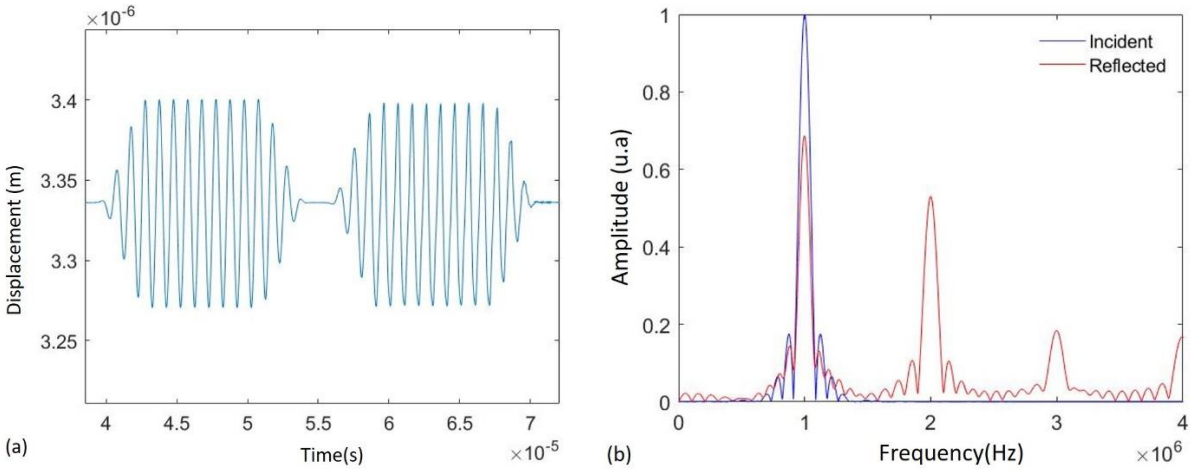

Figure 21(a) Time solution at x=-0.03 m and (b) the associated spectrum for the incident and reflected wave. The fundamental frequency f=1MHz, static pressure $p_0 = 0,4\ MPa$, contact stiffness $C_N = 2.10^{13}\ Pa/m$, undamaged interface, $\delta x = 2.10^{-5} m$ and $\delta t = 3.10^{-9}$.

The higher harmonics amplitudes are monitored and compared as a function of the dimensionless parameter ξ [37] [32], introduced in equation (2.38) of chapter 2:

$$\xi = \frac{p_0}{\sigma_i^{max}} \qquad 3.44$$

As for previous studies, when $\xi \geq 1$, the interface remains in compression and no motion occurs at the contact. Thus, the opening of the interface and hence its nonlinear adhesive behaviour will be activated and occur only for $\xi \in [0, 1]$.

The convergence, both in time and space, is here investigated for the different frequencies of interest and for an undamaged interface. To study the convergence of the model, it has been chosen to consider the convergence of second harmonic efficiency $\frac{A_2}{A_{inc}}(\xi)$, as stated in section 2.3.5 of chapter 2. To obtain its evolution, the incident wave amplitude, and hence the maximum incident stress σ_i^{max}, is varied while the static pressure $p_0 = 0.01\,MPa$ is maintained fixed. The solution given by the smallest resolution serves as a reference to verify the convergence. The error vector is calculated by subtracting the actual second harmonic efficiency $\frac{A_2}{A_{inc}}(\xi)$, for a given mesh step, from the second harmonic efficiency for the smallest mesh step $\frac{A_2}{A_{inc}}(\xi)]_{ref}$. The difference between the two is then divided by $\frac{A_2}{A_{inc}}]_{ref}$. The result is multiplied by 100 to express it as a percentage:

$$vect_{error}(\xi) = \frac{\frac{A_2}{A_{inc}}(\xi) - \frac{A_2}{A_{inc}}(\xi)]_{ref}}{\frac{A_2}{A_{inc}}(\xi)]_{ref}} \qquad 3.45$$

The value of percent error is given by taking the norm of $vect_{error}(\xi)$ and dividing it by Nb_ξ denoting the number of the dimensionless parameters $\xi \in]0; 1]$ considered to describe the evolution of $\frac{A_2}{A_{inc}}(\xi)$:

$$Error = \frac{||vect_{error}||_2}{Nb_\xi} \qquad 3.46$$

The study of convergence through grid space consists in varying the space discretization δx (11 values from 0.02mm to 0.2mm) while keeping the time step constant $\delta t = 2$ ns. The time step satisfies the CFL condition $c\,\frac{\delta t}{\delta x} < 1$ for the smallest δx, where c refers to the wave celerity. For all simulations, the post-processed signal is measured at the same position $x = -0.03\,m$. Likewise, the time convergence is evaluated by varying the time step δt, while the space step is fixed at the smallest space step value $\delta x = 0.02mm$. The Figure 22 gives the

evolutions of the second harmonic efficiency $\frac{A_2}{A_{inc}}$ as a function of the dimensionless parameter ξ, as well as the relative errors over time and space steps.

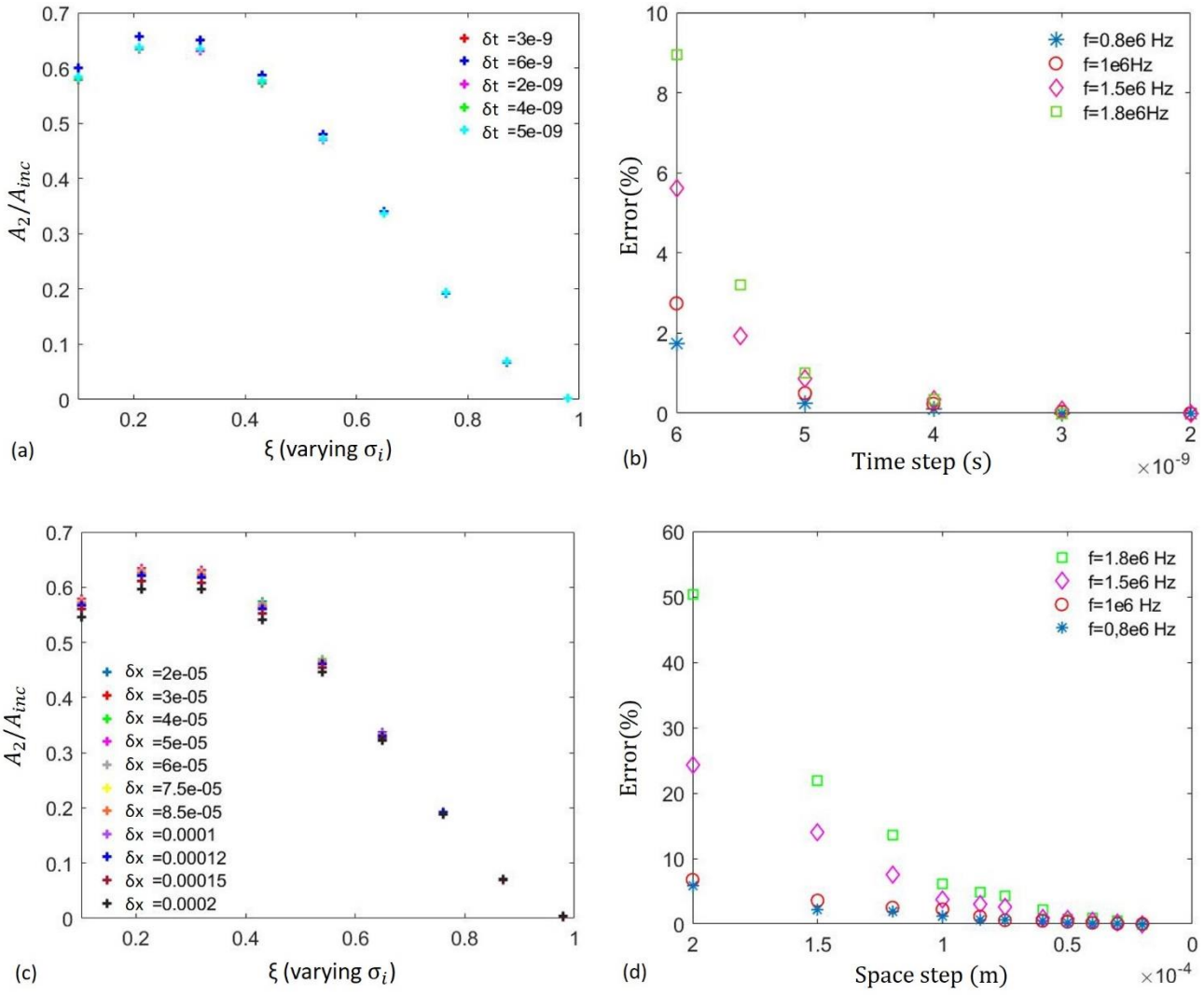

Figure 22 : (a) Second harmonic efficiency A_2/A_{inc} as a function of ξ for different time steps δt and $\delta x = 0.02mm$; (b) Error as a function of the time step; (c) Nonlinearity coefficient A_2/A_{inc} as a function of the dimensional parameter ξ for different space steps δx and δt=2ns and (d) Error as a function of the space step. Contact stiffness $C_N = 2.10^{13}\ Pa/m$.

Figure 22 (a) and (c) show the evolution of the second harmonic efficiency as a function of dimensionless parameter ξ for different values of δt and δx, respectively. It is noticed that the difference between the values of the second harmonic efficiency increases when increasing the incident wave amplitude (i.e. low ξ values).

Figure 22 (b) and (d) show a decrease in the percentage error when decreasing the mesh size, both in time and space. Thus, the numerical scheme converges for all the evaluated frequencies, both in time and space. However, one can notice that the space convergence is more difficult

to establish, compared to the time convergence. It is obtained for $\delta x < \frac{\lambda_{2f_0}}{30}$, where λ_{2f_0} is the wavelength of the second harmonic.

To conclude, the convergence has been verified for all the studied frequencies. In the following, the impact of the RCCM contact law on the nonlinear interface dynamic response is evaluated. The unilateral contact law will be considered as the reference case in our analysis.

3.2 Interface dynamic behaviour: comparison between RCCM contact law and unilateral law

This part aims at investigating the dynamical behaviour in traction of a contact interface exhibiting "damaging" adhesion during the interaction with a compressional wave. Three configurations are explored: opening without damaging the interface (1), opening with partial (2) and total (3) damaging of the interface. These configurations are obtained by varying the amplitude of the incident wave (see Figure 20). Note that the interface starts to be damaged from a stress equal to 1.41MPa ($\sigma_{lim} = \sqrt{C_N w}$, see Table 4 for parameters values).

The simulations consist in generating a compression plane wave at $x = -L$ (see Figure 21 (a)). The incident wave propagates forward along the positive *x*-direction; it interacts with the contact interface (activating or not nonlinear effects) and propagates backward along the negative *x*-direction. Then, this reflected wave, affected by the nonlinear interaction with the contact interface, can be analysed on the basis of the implemented contact law. In this part, the reflected wave, obtained with RCCM contact law, is compared to the one obtained with the classical unilateral contact. The RCCM contact law is governed by three parameters: the stiffness C_N, the decohesion energy w and the viscosity b. Compared to the unilateral contact case, the RCCM law affects the interface response in traction. Its impact depends heavily on the amplitude of the incident wave. Three cases corresponding to three different amplitudes of the incident wave are then evaluated. The first case, with an incident wave amplitude of 0.82 MPa, generates an elastic interface opening. The second one, with an incident wave amplitude of 1.6 MPa, generates an interface opening with partial damage. The last case, with an incident wave amplitude of 8.2 MPa, leads to the peel-off of the interface. For all cases, the incident wave is a sinusoidal compression wave with a frequency *f*=1 MHz as shown in Figure 20.

Recalling that the mechanical parameters, used in these simulations, are presented in Table 4.

First case: incident amplitude $\sigma_i^{max} = 0.82\ MPa$

The amplitude of the incident pressure is sufficient to open the interface but not to damage it, as shown in Figure 23 (a). In this case, the interface in traction behaves like a spring with a stiffness C_N and the nonlinearity is derived from the difference between the stiffness in traction and compression. Consequently, when the interface is open, the relative displacement is lower than the one obtained with the unilateral contact law (see Figure 23 (b)). Note that in case of traction at the interface, the contact stress is positive (see Figure 23 (c)).

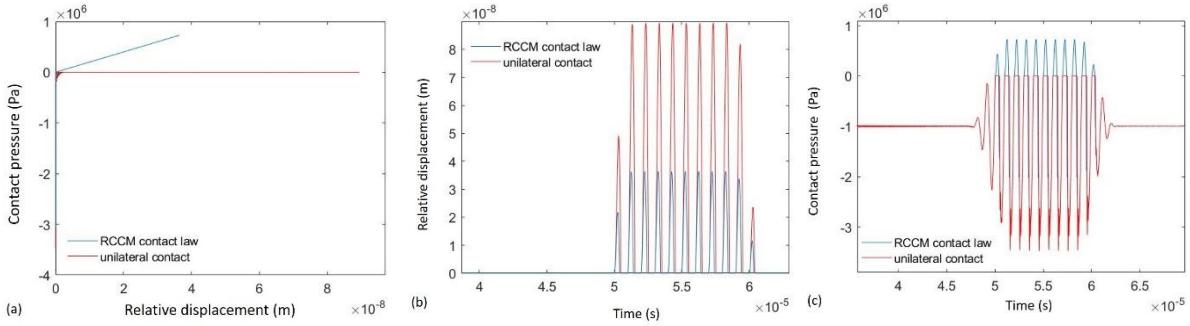

Figure 23 Comparison between the unilateral contact law and the RCCM law when β=1. The maximum incident pressure is $\sigma_i^{max} = 0.82\ MPa$. (a) Contact pressure as a function of the relative displacement at the interface; temporal evolution of (b) displacement and (c) the contact stress.

Figure 24 (a) illustrates the solution at $x = -0.03$m. The wave is generated once the equilibrium state is reached. Two waves are observed; the first one corresponds to the incident wave, while the second one refers to the reflected wave. The reflected wave, obtained with the unilateral contact law, shows the characteristic distortion of the UC (Unilateral Contact). In the case of the RCCM law, the stiffness in traction causes positive stress during opening, and thus a less drastic rectification of the normal contact stress and a smaller opening gap.

Figure 24 (b) gives the spectrum of the reflected wave for both laws. The spectra show that the second harmonic, generated with the RCCM contact law, is lower than the one obtained with the UC. Consequently, the RCCM contact law exhibits less nonlinearity compared to the unilateral contact. In fact, the nonlinearity, in this case, is only related to the contrast between the stiffness in traction and compression that can be considered here as infinite. Therefore, increasing the stiffness diminishes the contrast between the stiffness in traction and compression, leading to a dynamic behaviour that exhibits less nonlinearity.

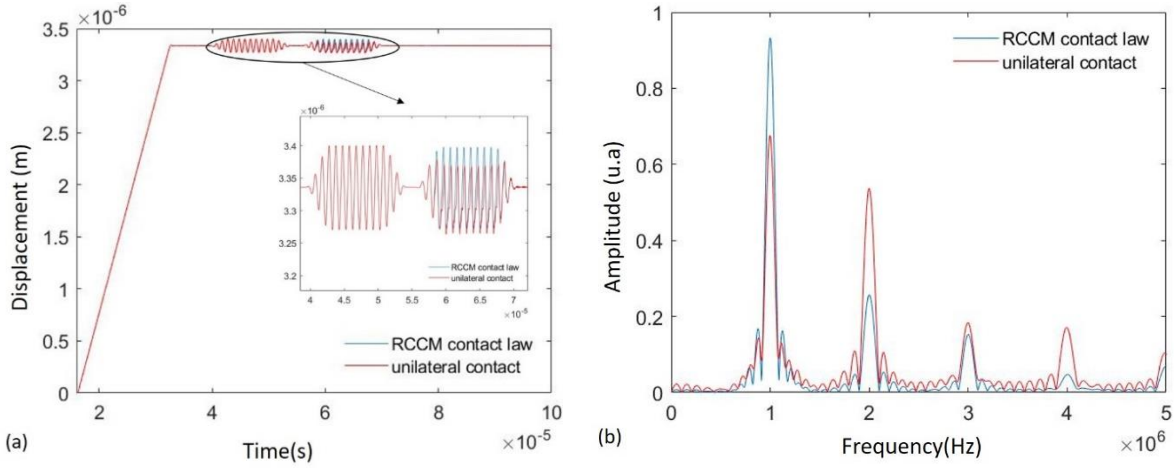

Figure 24 Comparison between the unilateral contact and the RCCM contact law with no damage (β=1). The maximum incident pressure is $\sigma_i^{max} = 0.82$ MPa. (a)Temporal evolution of displacement at x=-0.03m (b) Spectrum of reflected wave.

Second case: incident amplitude $\sigma_i^{max} = 1.6\ MPa$

This amplitude is sufficient to open and partially damage the interface ($\sigma_{lim} = \sqrt{C_N w}$=1.41 MPa). As mentioned before, each time the elastic limit is exceeded, the intensity of adhesion β decreases (see Figure 25 (a)) and so does the new elastic limit. The decrease of the elastic limit is due to a decrease of the stiffness when the interface is damaged (Figure 25 (b)).

At the end of the simulation, the intensity of adhesion is β_{end}=0.57. In this case, the nonlinear behaviour in traction is activated and the interface is damaged. Thus, during the interaction with the compression wave, the traction stiffness is changing (decreasing) along time due to the damage induced by the incident wave. This will affect the reflected wave and the second harmonic magnitude.

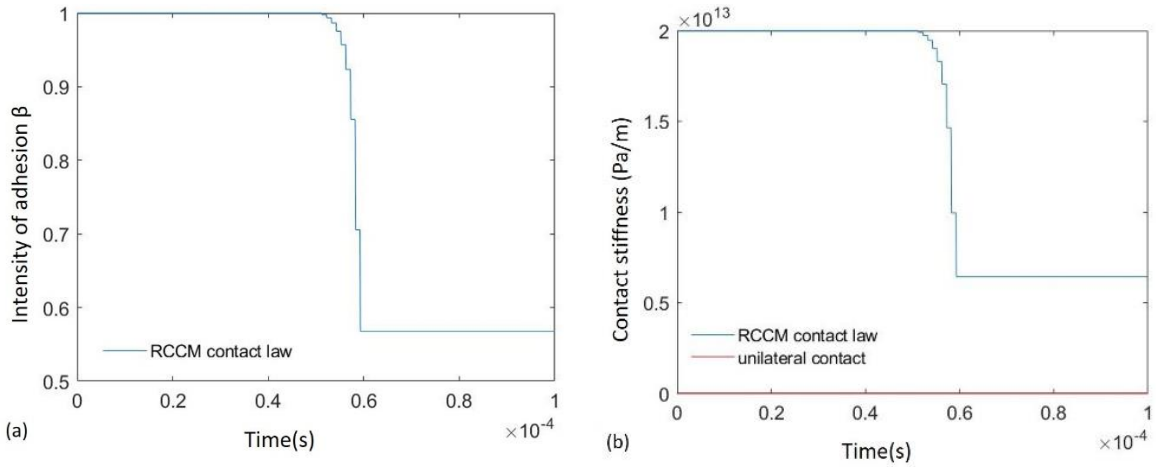

Figure 25 The maximum incident pressure is $\sigma_i^{max} = 1.6\ MPa$. (a) Intensity of adhesion β over time and (b) contact stiffness over time.

Figure 26 (a) shows the incident and reflected waves. The nonlinearity, due the contrast of stiffness in traction/compression is activated, similar to the first case, and it is further amplified due to the decrease of the contact stiffness over cycles. Consequently, the spectrum in Figure 26 (b) shows a greater value of the second harmonic compared to the first case, presented above. However, the obtained value of the second harmonic is still lower than the one generated by the unilateral contact.

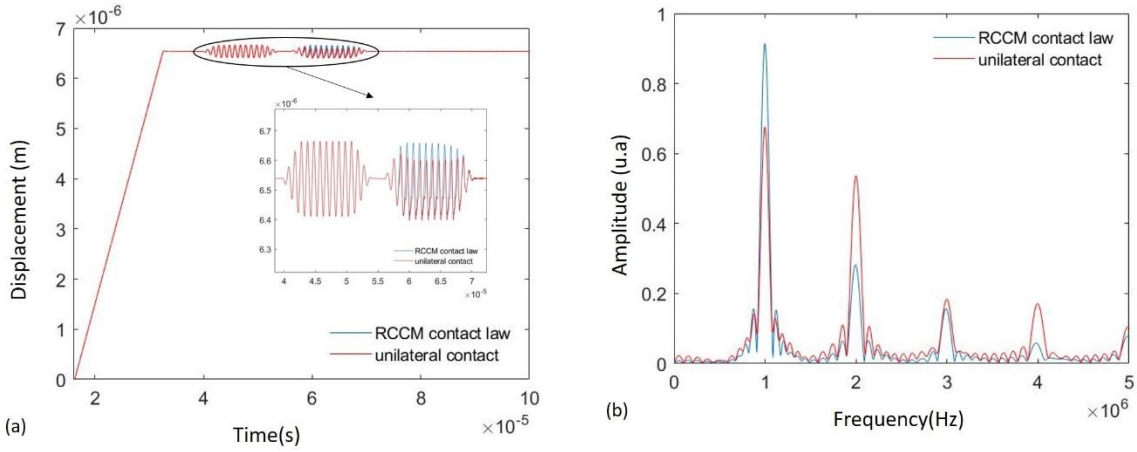

Figure 26 Comparison between the unilateral contact law and the RCCM law when β_{end} =0.57, at end of the simulation. The maximum incident pressure is $\sigma_i^{max} = 1.6\ MPa$. (a) Evolution of displacement at x=-0.03m over time and (b) Spectrum of the reflected wave.

The progressive evolution and damaging of the interface has an impact on the temporal evolutions. In fact, as shown in Figure 27, the normal contact pressure decreases (Figure 27 (a)) and the relative displacement at the interface increases (Figure 27 (b)) with the cycles. The different cycles are presented in the Figure 27 (c) highlighting the damaging of the interface through the dissipated energy and the diminishing of the stiffness in traction.

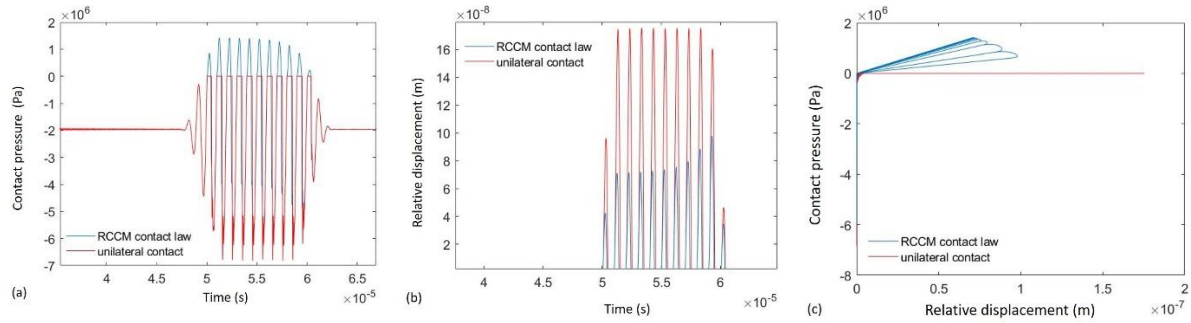

Figure 27 Comparison between the unilateral contact law and the RCCM law when β=0.57, at the end of the simulation. The maximum incident pressure is $\sigma_i^{max} = 1.6\ MPa$. (a) Evolution of contact pressure over time; (b) Evolution of the relative displacement over time and (c) Contact pressure as a function of the relative displacement at the interface.

Third case: incident stress amplitude $\sigma_i^{max} = 8.2\ MPa$

This amplitude damages completely the interface within two cycles. The intensity of adhesion β decreases over time until it reaches zero (Figure 28 (a)). Likewise, the contact stiffness decreases over cycles to zero as shown in Figure 28 (b).

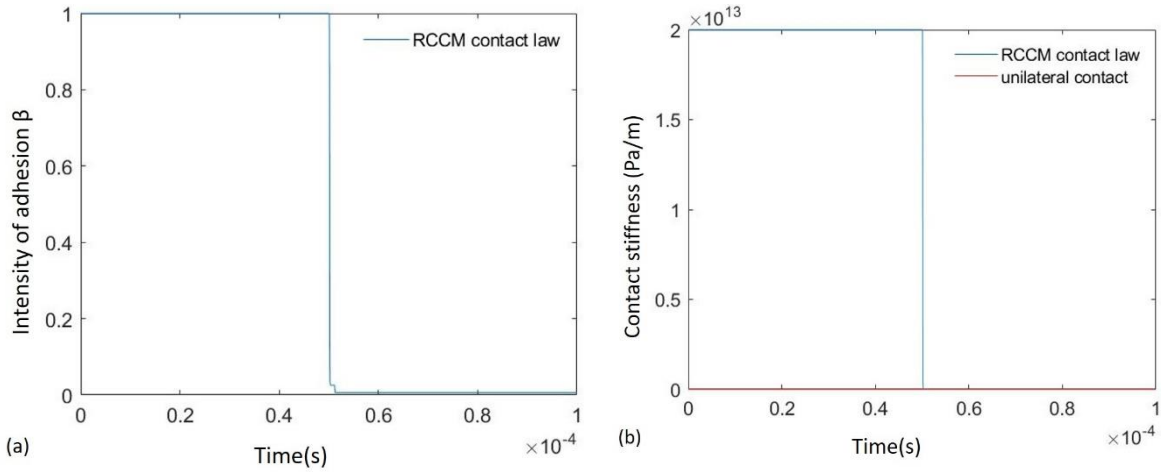

Figure 28 The maximum incident pressure is $\sigma_i^{max} = 8.2\ MPa$. (a) Intensity of adhesion β over time and (b) Contact stiffness over time.

The contrast between the contact stiffness in traction and compression becomes equivalent to the unilateral case at the end of the simulation. Thus, the reflected wave, obtained here with the RCCM contact law, is distorted in a way rather close to the one obtained with the unilateral contact law, as shown in Figure 29 (a). Consequently, the spectrum of the reflected wave is similar for the two laws (Figure 29 (b)).

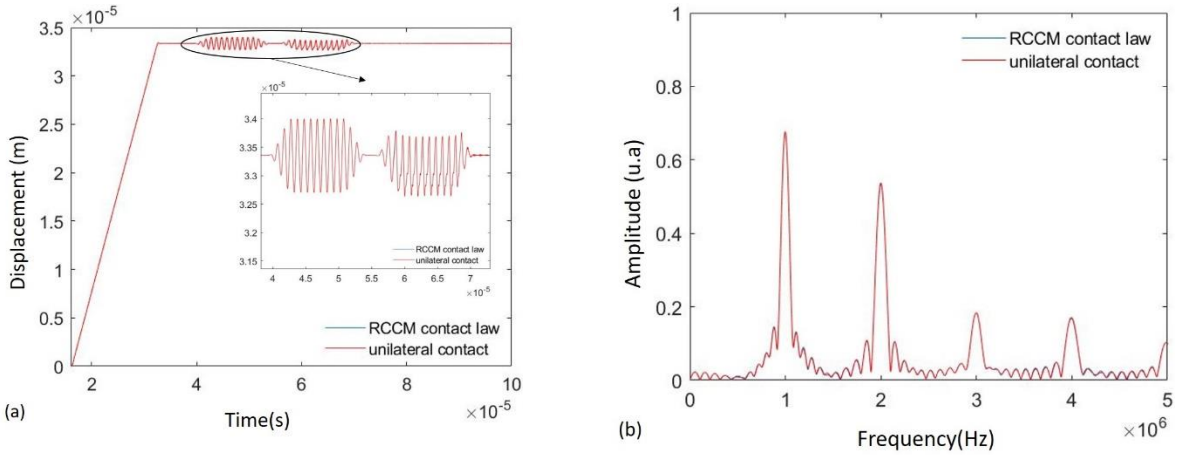

Figure 29 Comparison between the unilateral contact law and the RCCM law when β=0, at the end of the simulation. The maximum incident pressure is $\sigma_i^{max} = 8.2\ MPa$. (a) Evolution of displacement at $x = -0.03m$ over time and (b) Spectrum of the reflected wave.

Figure 30 (a) and (b) show that the evolutions of the contact pressure and relative displacement, obtained with the RCCM contact law, overlap here with the ones obtained with the unilateral contact. Similarly, the Figure 30(c) indicates that, within the second cycle, the RCCM contact law becomes equivalent to the unilateral contact law.

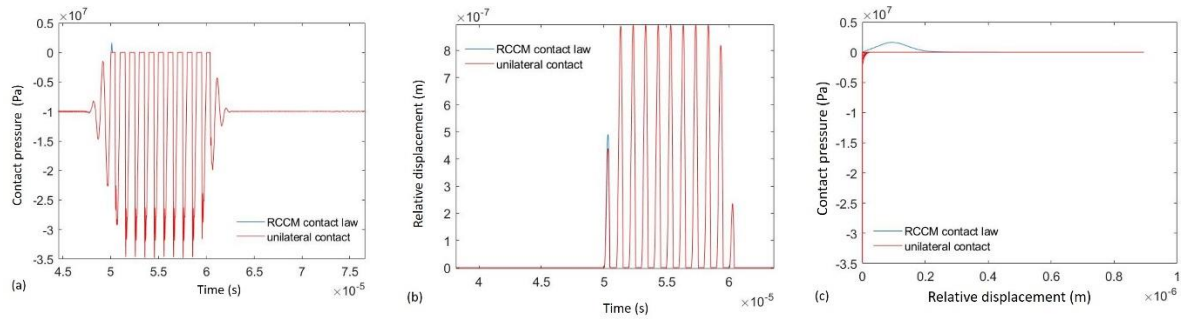

Figure 30 Comparison between the unilateral contact law and the RCCM law when β_{end}=0. The maximum incident pressure is $\sigma_i^{max} = 8.2\ MPa$. (a) Evolution of contact pressure over time; (b) Evolution of relative displacement over time and (c) Contact pressure as a function of the relative displacement.

To conclude, this first analysis shows how the reflected wave is largely affected by the damage of the interface, which behaves as a function of the response of the introduced RCCM to the imposed incident waves. Different parameters govern the interface behaviour and consequently the reflected wave distortion. Actually, the way the signal is distorted depends heavily on the initial contact stiffness and the damage occurred at the interface. First tests showed also a dependence to the frequency and viscosity. Consequently, the reflected wave contains the nonlinear signature of the interface, which is directly related to the different contact parameters. Then, the exploitation of its nonlinear response could allow obtaining information about the interface parameters and, thus, characterising the contact interface using inverse methods. Therefore, in the following, we propose to further analyse the influence of these parameters on the nonlinear interface response.

The first element to remember is that the way the interface is damaged will affect the distortion of the reflected wave. The second one is that the nonlinearity of the interface is directly related to the difference in stiffness between traction and compression. Consequently, the next part aims at better understanding the dynamic behaviour of the interface by studying the influence of the different parameters of the RCCM law on it. Moreover, because the introduction of the

stiffness (contact stiffness) into the numerical model induces a frequency dependence, the influence of the frequency will be preliminarily investigated in the next section.

3.3 Parametric analysis

In order to go further in the understanding of the nonlinear signature of the RCCM law, compared to the unilateral contact law, a parametric analysis is proposed. The goal is to identify the parameters that govern the interaction between a compression wave and a contact interface that behaves following the normal RCCM law, including adhesion. Based on that, a first part will be dedicated to evaluate the influence of the stiffness C_N and frequency f, while the interface remains undamaged. For this preliminary analysis, a high value of decohesion energy w is fixed to explore the influence of the contrast between traction/compression stiffness without damaging the interface. The second part will analyse the influence of decohesion energy w and viscosity b on the nonlinear signature of the contact law, in configurations where interface can be damaged. For all simulations, the results are analysed through the evolution of the second harmonic efficiency (A_2/ A_{inc}) and fundamental amplitude (A_1/ A_{inc}) as a function of the dimensionless parameter ξ (p_0/σ_i^{max}). These amplitudes (A_2/ A_{inc} and A_1/ A_{inc}) are obtained from the displacement of the reflected wave at x=-0.03m while varying σ_i^{max}, i.e. maximum incident wave amplitude and keeping p_0 constant.

For all simulations, the incident wave $\sigma_i(t)$ is a 15 cycles sinusoidal signal modulated by a smooth rectangular window, as shown in Figure 20.

3.3.1 Influence of the contact stiffness on the nonlinear signature of the RCCM law

In this part, all configurations of the simulations correspond to interfaces that are not damaged (β_{end}=1), in order to focus on the influence of the traction stiffness on dynamic behaviour of the interface, especially on its nonlinear signature. It is important to mention that this configuration corresponds to a bilinear law [8] (paragraph 1.3.1 of chapter 1) where the stiffness in compression is infinite.

Thus, the goal is to understand how the traction stiffness changes the nonlinear signature, by changing its value between the two limit cases: the unilateral contact case (nonlinear) and the bilateral case (linear) as shown in Figure 31.

Both of them are characterized by an infinitely rigid interface and a zero displacement $[u]$, in compression. In traction, the unilateral contact law induces a null contact stress, while the bilateral case is described by an infinitely rigid interface, i.e. a Dirichlet boundary condition at *x=0 ([u(x=0)] =0).*

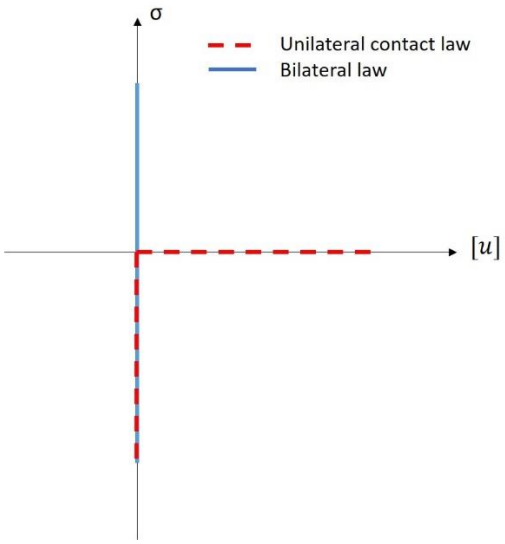

Figure 31 Stress function of the relative displacement for the unilateral contact and the bilateral laws.

The response of the interface is only driven by a linear spring in traction.

Figure 32 (a) shows the evolution of the contact stiffness as a function of the relative displacement for different contact stiffness. It indicates that the increase of the contact stiffness, from zero to $10^{15}\ Pa/m$, leads to a shift in the contact interface behaviour from a unilateral contact to a perfect contact (bilateral law). Consequently, while increasing the contact stiffness in traction, the contrast between the stiffness in compression and traction decreases and the transition from compression phase to traction induces less nonlinearity.

Then, in order to highlight the effect of the contact stiffness as a function of the incident wave amplitude, the simulations are repeated, at each stiffness value, for several incident wave values, leading to different opening conditions of the interface. The incident wave amplitude σ_i^{max}, and hence the incident stress σ_i, is varied , while the static pressure $p_0 = 0.082$ MPa remains fixed. The simulation parameters are presented in Table 5. A small viscosity value has been set, to minimize its impact on the results, at this stage. Moreover, as the interface remains here undamaged, this parameter does not play any role in the results.

Normal stiffness C_N (Pa/m)	**Viscosity b (Pa.s)**	**Decohesion energy w (J/m^2)**	**Frequency f (Hz)**
Varied	10^{-8}	1000	10^6

Table 5 simulation parameters for stiffness study

Figure 32 (b) shows the evolution of the second harmonic efficiency A_2/A_{inc} as a function of the dimensionless parameter ξ for different contact stiffness.

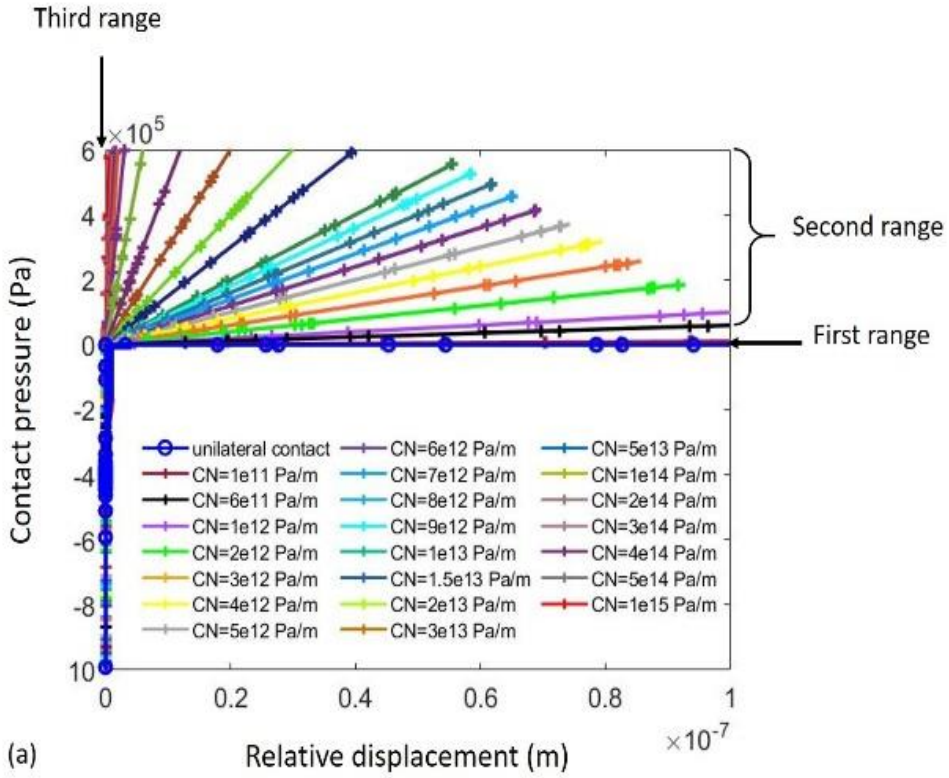

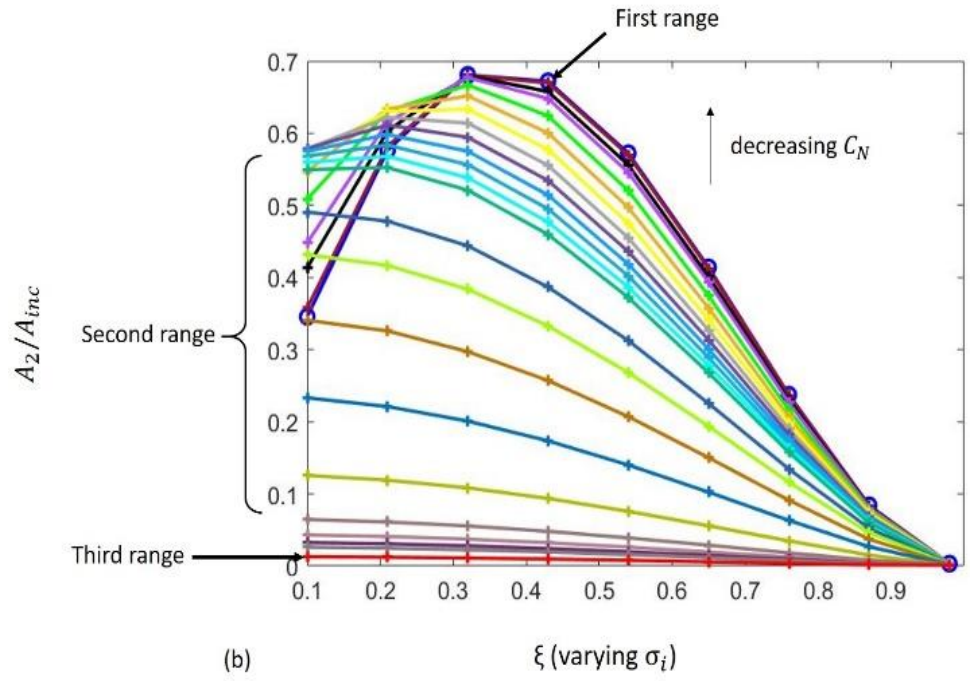

Figure 32 (a) Contact pressure as a function of the relative displacement . $\sigma_i^{max} = 0.82\ MPa$ for $\xi = \frac{p_0}{\sigma_i^{max}} = 0.1$ and *(b) Evolution of the ratio A_2/A_{inc} as a function of the dimensionless parameter ξ for different stiffness values $C_N \epsilon [0, 10^{15}] Pa/m$.* decohesion energy $w = 1000\ J/m^2$, viscosity $b = 10^{-8}\ N.s/m$. Note that the same colour code is used for both figures (a) and (b).

It is recalled that for values of $\xi > 1$, the incident stress is not sufficient to generate a loss of contact and hence no second harmonic is generated. By contrast, for values of $\xi < 1$, the incident stress is large enough to induce opening of the interface, which leads to a second harmonic generation. In the latter case, three different stiffness-dependent regions, as a function of ξ, can be identified. It is possible to separate stiffness value in three ranges that induce different evolutions of second harmonic efficiency as a function of ξ.

<u>First range: contact stiffness $C_N < 10^{11}\ Pa/m$</u>

The interface behaviour is quasi-similar to the unilateral contact. The nonlinearity exhibited by the interface is close to the unilateral case. Hence, the ratio A_2/A_{inc} is independent of the applied stiffness meaning that, within this range, the second harmonic efficiency is not sensitive to the traction stiffness variations C_N. As for the unilateral contact, a maximum of the second harmonic amplitude is obtained at about $\xi = 0.35$.

<u>Second range: contact stiffness $10^{11} < C_N < 10^{15}\ Pa/m$</u>

The nonlinear response is largely stiffness-dependent within these bounds. In fact, when increasing the stiffness within the range$]10^{11}, 10^{15}[$, the second harmonic efficiency A_2/A_{inc} drops. The interface behaviour shifts from the unilateral case to the bilateral spring case, leading to a lower value of second harmonic efficiency (lower nonlinearity). It is also noted that the maximum in the second harmonic, obtained at $\xi = 0.35$ for the unilateral contact in this case, shifts to the left when increasing the contact stiffness, until vanishing (a maximum in second harmonic amplitude does no longer exist for a value of stiffness around $5.10^{13}\ Pa/m$).

Third range: contact stiffness $C_N > 10^{15}\ Pa/m$

The contact with the rigid wall is quasi-equivalent to a perfect contact (bilateral). In fact, there is barely second harmonic generation and sensitivity to the stiffness is particularly small. Likewise, the ratio A_2/A_{inc} is quasi-independent of the applied stiffness.
Note also that for lower ξ values, the RCCM contact law may generate more nonlinearity compared to the UC with certain stiffness values as shown in Figure 33.

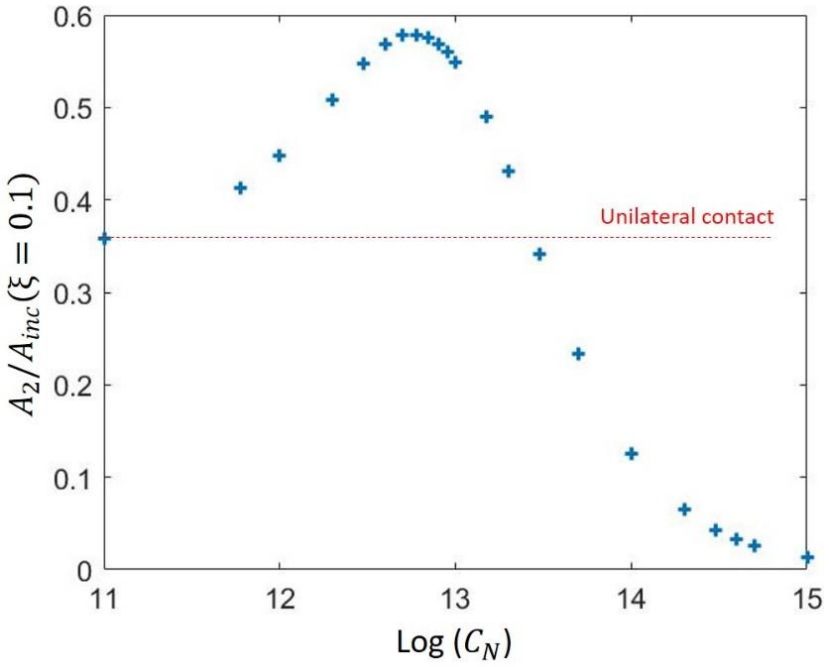

Figure 33 Evolution of the ratio A_2/A_{inc} as a function of the logarithm of the stiffness (the logarithm to the base 10). ξ=0.1. Without damaging the interface. $f = 10^6 Hz$.

Consequently, the stiffness, which is one of the parameters that differentiates the RCCM contact law from the unilateral contact law, has a major impact on the nonlinear signature of the contact interface.

This analysis has been preformed at a given frequency of the incident wave. Nevertheless, when introducing a stiffness in a dynamic system (including mass and stiffness distribution), a dependence on the frequency is expected. Then, contrary to the unilateral contact law, the frequency of incident wave can affect the nonlinear interaction between a propagating wave and an interface governed by the RCCM law. Consequently, in the next part, the impact of the frequency on the nonlinear signature of the RCCM contact law is investigated.

3.3.2 Influence of the frequency on the nonlinear signature of the RCCM contact law

The introduction of a stiffness in the numerical model induces a dependency to the frequency. Again, we consider the case where the interface behaviour remains undamaged (β=1). The response of the interface is driven by a linear spring in traction and an infinitely rigid interface in compression. Three different stiffness values in traction are evaluated, each referring to a specific range defined in the previous paragraph. $C_N = 10^{10}\ Pa/m$ and $C_N = 10^{15}\ Pa/m$, belong respectively to the first and last case, where the nonlinear signature of the RCCM contact law is not sensitive to the contact stiffness. $C_N = 2.10^{13}\ Pa/m$, belongs to the second range, where the nonlinear signature of the contact law is stiffness-dependant. The incident wave is the 15-cycle sinusoidal signal modulated by a smooth rectangular window (see Figure 20). The static pressure p_0 remains constant at $p_0 = 0.082\ MPa$, while the incident wave amplitude σ_i^{max} is varied. The mechanical parameters are those listed in Table 4. As for the frequency, its variation range is chosen to ensure convergence through grid size for all the tested frequencies. In the following, the amplitude of the first two harmonics is analysed as a function of the dimensionless parameter ξ defined in (3.44), while varying the frequency.

The interpretation of the different evolutions requires an in-depth analysis of the influence of the frequency on the nonlinear signature of the RCCM contact law. In fact, the impact of the frequency on nonlinear results is complex to understand. For example, Blanloeuil and. al. [37] showed that the introduction of a nonlinear stiffness in compression introduces a frequency dependence and leads to the redefinition of the dimensionless variable ξ. Moreover, because the effect of the introduced stiffness is strictly related to the effect of such stiffness into the dynamic response of the system and thus function of the frequency response of the system, we introduce here a parameter, called the normalized frequency $f_{normalized}$, taking into account both stiffness and frequency. This parameter was first introduced within the framework of

linear acoustics and derives from the reflexion coefficient formula for two mediums in contact with a stiffness. It is expressed as follows [36]:

$$f_{normalized} = \frac{\omega Z}{C_N} \qquad 3.4$$

Where Z is the acoustic impedance and ω is the angular frequency.

Figure 34 shows the evolution of the second harmonic efficiency A_2/A_{inc} as a function of the logarithm of the normalized frequency for two different incident wave amplitudes. Based on equation (3.4) at a fixed frequency and when the stiffness C_N reaches zero, the normalized frequency approaches positive infinity and so does its logarithm. In this case, the right side of the curve tends towards a unilateral contact behaviour as shown in Figure 34. However, when the stiffness tends towards infinity, the normalized frequency is equal to zero and its logarithm leans towards negative infinity. Hence, the left side of the curve approaches a perfect contact behaviour. In between these two domains lies the area where the nonlinear signature of the contact law varies with the normalized frequency. We retrieve then the three ranges of interest, where the nonlinear response sensitive to the stiffness variation in the intermediate range.

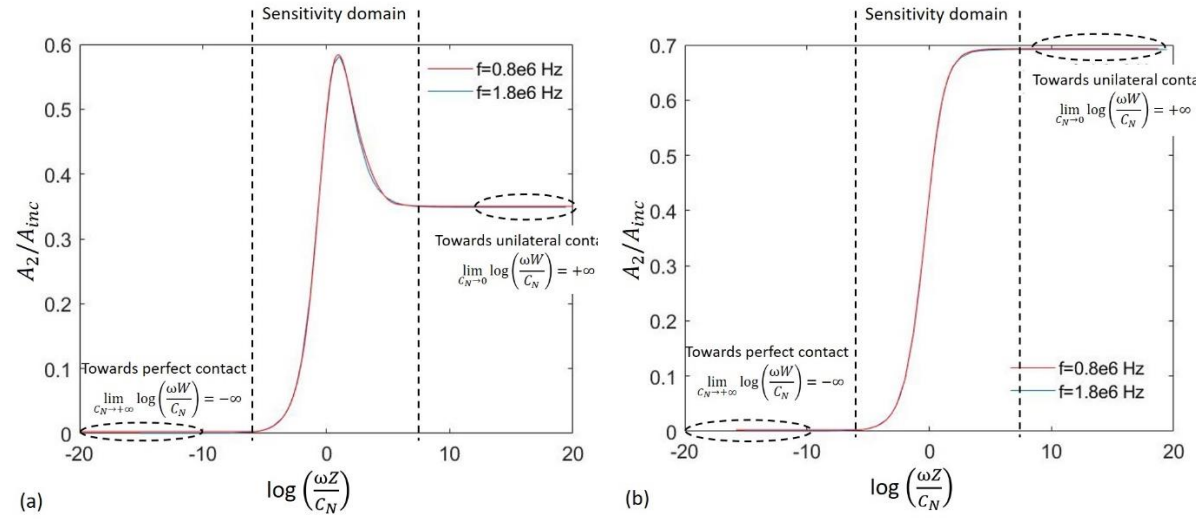

Figure 34 Evolution of the second harmonic efficiency A_2/A_{inc} as a function of the logarithm of the normalized frequency for frequencies $f = 1.8\ 10^6\ Hz$ and $f = 0.8\ 10^6\ Hz$, without damaging the interface. (a) ξ=0.1 (b) ξ=0.35

The maximum of the second harmonic efficiency A_2/A_{inc} occurs around the normalized stiffness equal to 1 (log(0)), showing then a maximum when the contact stiffness is close to the defined normalization value (see Figure 34 (a)). It is noted that the maximum of the ratio A_2/A_{inc} is not reached at exactly the same value (normalized frequency equal to 1). This could be attributed to the damping contribution introduced in the numerical model but not accounted

for by the normalized frequency. Indeed, the latter parameter takes into account only stiffness and densities. Besides, the normalized frequency accounts for the stiffness value in traction. However, the equivalent stiffness would be slightly different from the assumed value, as the stiffness in compression is infinite. In this context, the maximum of the second harmonic amplitude obtained for ξ=0.1 could be viewed as a 'resonance' phenomenon, obtained at a specific frequency. In the following, this specific frequency is called 'characteristic' frequency. Figure 35 shows the evolution of the ratio A_1/A_{inc} as a function of the logarithm of the normalized frequency for two different frequencies.

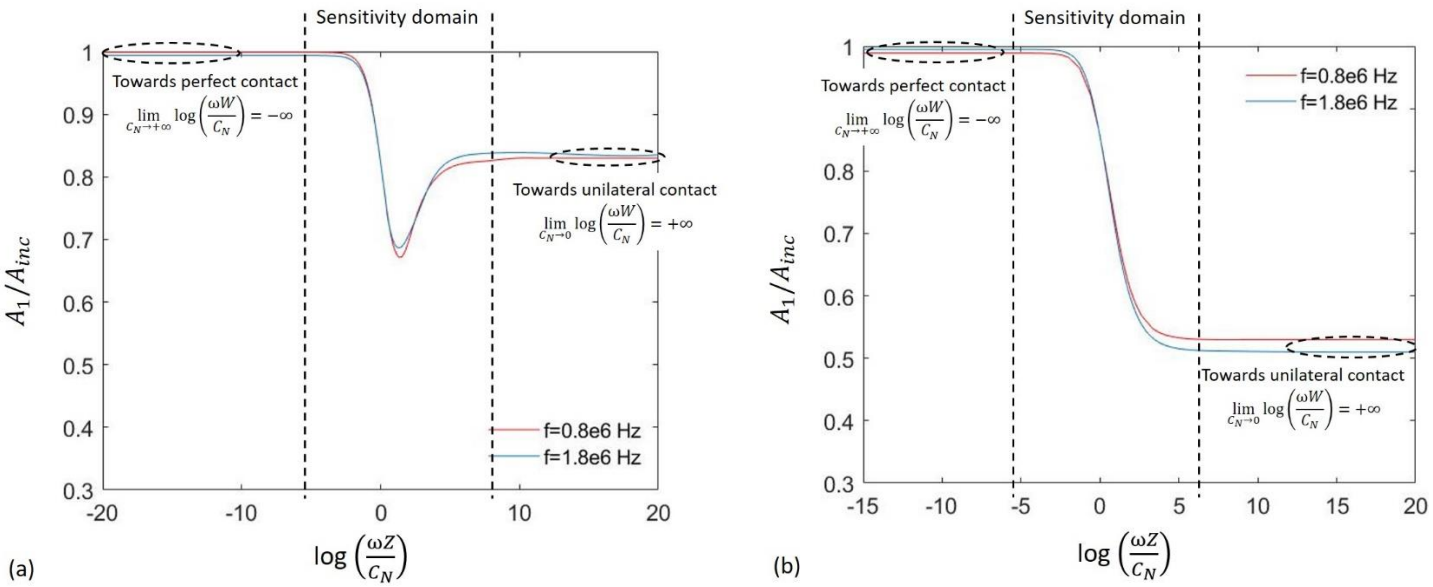

Figure 35 Evolution of the fundamental efficiency A_1/A_{inc} as a function of the logarithm normalized frequency for frequency $f = 1.8\ 10^6\ Hz$ and $f = 0.8\ 10^6\ Hz$, without damaging the interface. (a) ξ=0.1 (b) ξ=0.35.

Figure 35 (a) shows an anti-peak around zero (normalized frequency equal to 1). In fact, the energy of the fundamental has been transferred to the second harmonic.

This suggests that the influence of both parameters, frequency *f* and stiffness C_N, can be linked and studied through the normalized frequency $f_{normalized}$ (equation 3.4). Then, in the following, it is proposed to investigate the influence of those parameters on the second harmonic efficiency in the three different zones previously identified. For each range of sensitivity, the stiffness C_N is fixed and frequency f is varied. Each simulation (curve) will then corresponds to a value of normalized frequency, whose value compared to the characteristic frequency will determine the nonlinear efficiency and its evolution. The simulation parameters are listed in Table 6.

Normal stiffness C_N (Pa/m)	**Viscosity b (Pa.s)**	**Decohesion energy w (J/m^2)**	**Frequency f (Hz)**
From $\mathbf{10^{10}}$ to $\mathbf{10^{15}}$	10^{-8}	1000	10^6

Table 6 simulation parameters for frequency study

First case: contact stiffness $C_N = 10^{10}\ Pa/m$ belonging to the first range (close to UC)

Figure 36 shows the evolutions of the ratios A_2/A_{inc} and A_1/A_{inc} as a function of the dimensionless parameter ξ, for the different tested frequencies of the incident wave.

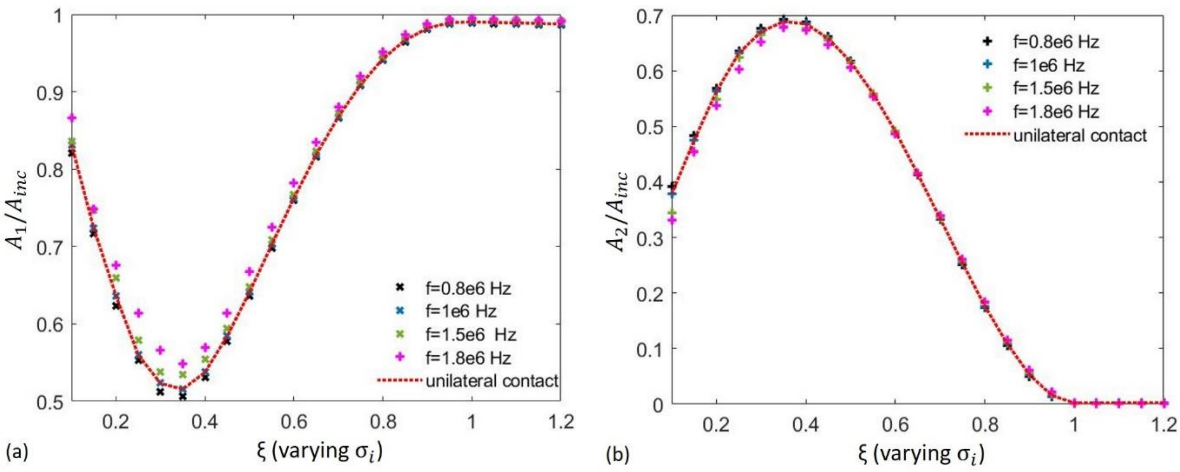

Figure 36(a) Evolution of the ratio A_1/A_{inc} and (b) of the ratio A_2/A_{inc} as a function of the dimensionless parameter $\xi = \frac{p_0}{\sigma_i^{max}}$. Frequency $f\epsilon[8\ 10^5, 1.8\ 10^6]\ Hz$. $C_N = 10^{10}\ Pa/m$. decohesion energy $w = 0.1\ J/m^2$, viscosity $b = 10^{-8}\ N.s/m$. $p_0 = 0.082\ MPa$.

Whatever the frequency is, the second harmonic efficiency A_2/A_{inc} goes through an optimal around $\xi_{opt} = 0.35$, similarly to unilateral contact behaviour. Thus, in this case, ξ_{opt} is quasi-independent from the imposed frequency between $[8\ 10^5, 1.8\ 10^6]$ Hz, for a contact stiffness $C_N = 10^{10}$ Pa/m. The ratio A_1/A_{inc} shows a local minimum at the same value of ξ. It is noted that the used model (see Figure 13) does not consider transmission; all the energy is reflected back to the interface. Thus, when ξ decreases between 0 and 0.35, the reflection becomes more and more nonlinear; A_2 increases and A_1decreases. The same happens when ξ decreases between 1 and 0.35. However, the magnitude of the second harmonic efficiency decreases with increasing frequency for all values of ξ, exhibiting a slight frequency-

dependence. In fact, the limit values determining the stiffness-dependence borders, defined earlier, vary with the frequency. For instance, $C_N = 10^{10}\ Pa/m$ belongs to the stiffness-independent domain for a frequency $f = 10^6 Hz$; the nonlinear signature is quasi-equivalent to the unilateral contact law. Figure 37 and Figure 38 show the evolution of the second harmonic efficiency A_2/A_{inc} as a function of the normalized frequency for different amplitudes of the incident wave. The normalized frequencies referring to the frequencies ($f = 0.8\ 10^6$ Hz and $f = 1.8\ 10^6$ Hz) are evaluated for a stiffness $C_N = 10^{10}$ Pa/m and positioned on the curves.

For $\xi = 0.1$ (see Figure 37), the two normalized frequencies lie on the right side of the characteristic frequency axis. On this part of the curve, the higher the frequency, the lower the second harmonic efficiency. Hence, an incident wave with a higher frequency value generates less nonlinearity for $\xi = 0.1$.

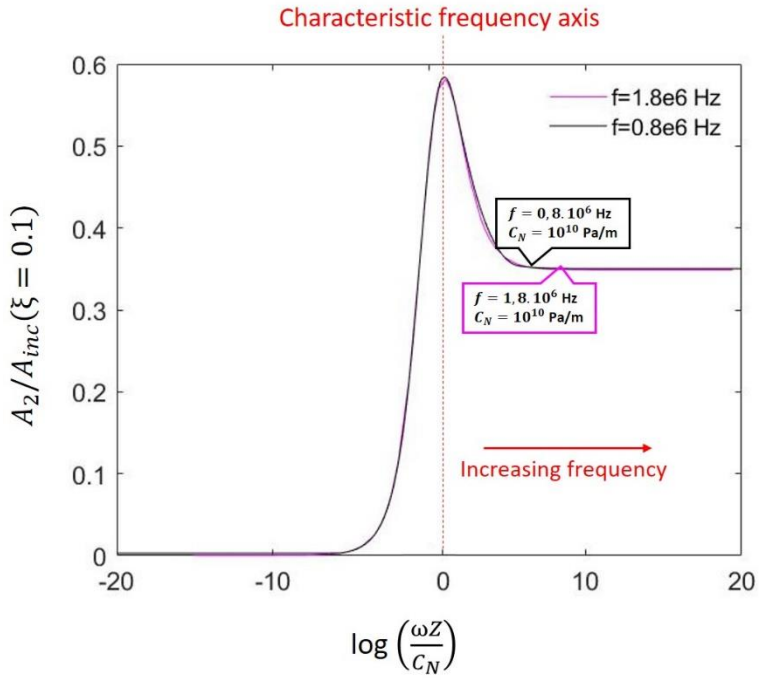

Figure 37 Evolution of the second harmonic efficiency A_2/A_{inc} as a function of the logarithm of the normalized frequency for the frequencies $f = 1.8\ 10^6\ Hz$ and $f = 0.8\ 10^6\ Hz$, without damaging the interface $\xi = 0.1$.

This reasoning remains valid for $\xi = 0.35$ and $\xi = 0.8$. Indeed, the normalized frequencies are located in a domain where an increase in frequency generates a (slight) decrease in second harmonic efficiency as shown in Figure 38.

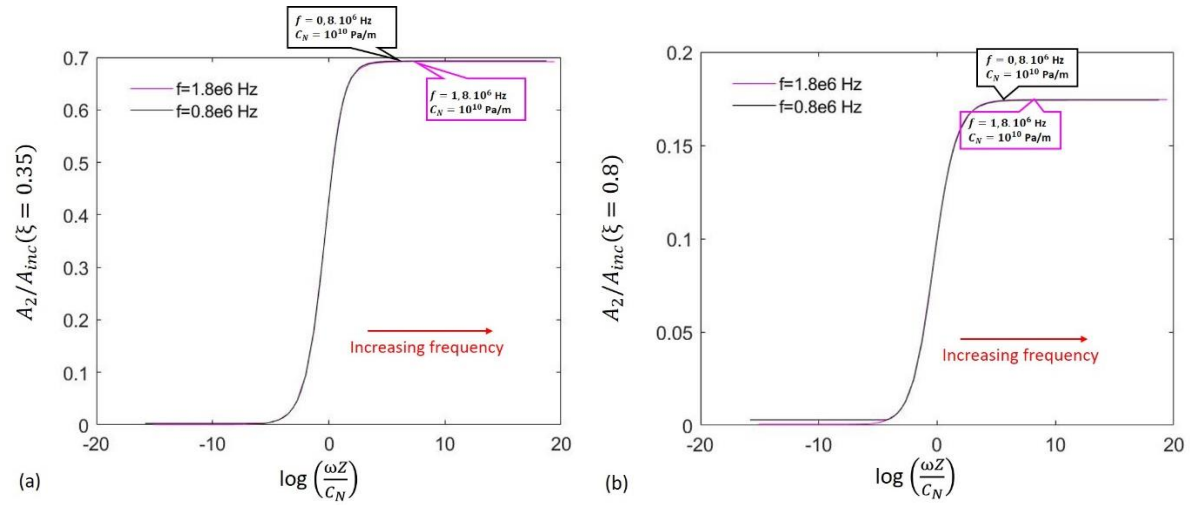

Figure 38 Evolution of the second harmonic efficiency A_2/A_{inc} as a function of the logarithm of the normalized frequency for the frequencies $f = 1.8\ 10^6\ Hz$ and $f = 0.8\ 10^6\ Hz$, without damaging the interface (a) $\xi = 0.35$ and (b) $\xi = 0.8$.

It is noted that the positions of the normalized frequencies are close to the asymptote of the unilateral contact behaviour, where the nonlinear signature does not vary significantly with the frequency. This explains the slight variation observed on the curve of the second harmonic efficiency A_2/A_{inc} as a function of the dimensionless parameter (see Figure 36 (b)). In order to observe a clear shift, one should decrease significantly the frequency.

Second case: contact stiffness $C_N = 2.10^{13}\ Pa/m$

Figure 39 shows the evolutions of the ratios A_2/A_{inc} and A_1/A_{inc} as a function of the dimensionless parameter ξ. It can be noted that, within this range, the evolution (form and amplitude) of both the ratios are clearly affected by changes in frequency.

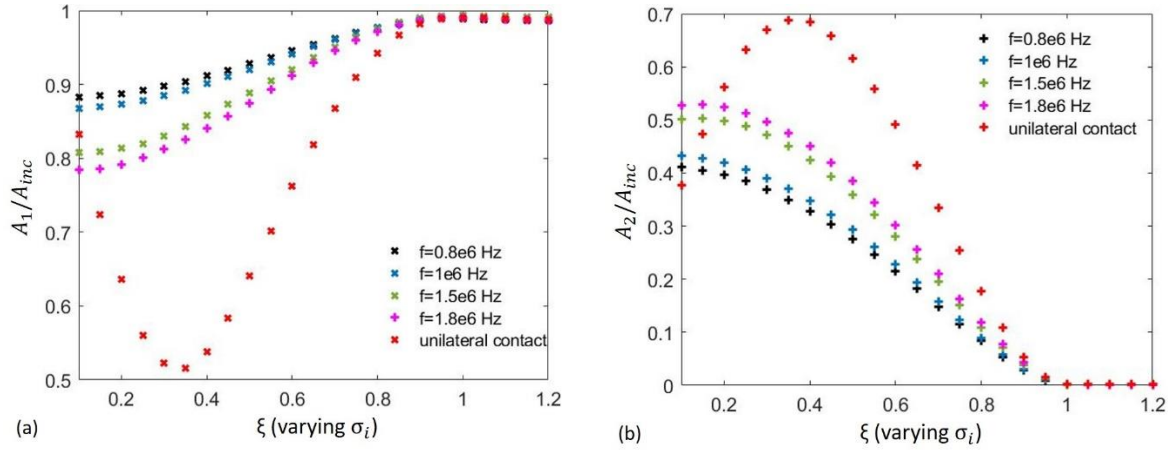

Figure 39 (a) Evolution of the ratio A_1/A_{inc} as a function of the dimensionless parameter ξ. (b) Evolution of the ratio A_2/A_{inc} as a function of the dimensionless parameter $\xi = \frac{p_0}{\sigma_i^{max}}$. Frequency $f\epsilon[8\,10^5, 1.5\,10^6]$ Hz. $C_N = 2.10^{13}$ Pa/m. Decohesion energy $w = 0.1\,J/m^2$, viscosity $b = 10^{-8}$ $N.s/m$. $p_0 = 0.082$ MPa

Contrary to the first case, for a stiffness within the range $[10^{11}, 10^{15}]$ Pa/m, the second harmonic generation increases with the frequency. In order to understand these evolutions, the second harmonic efficiency as a function of the logarithm of the normalized frequency is shown in Figure 40 and Figure 41.

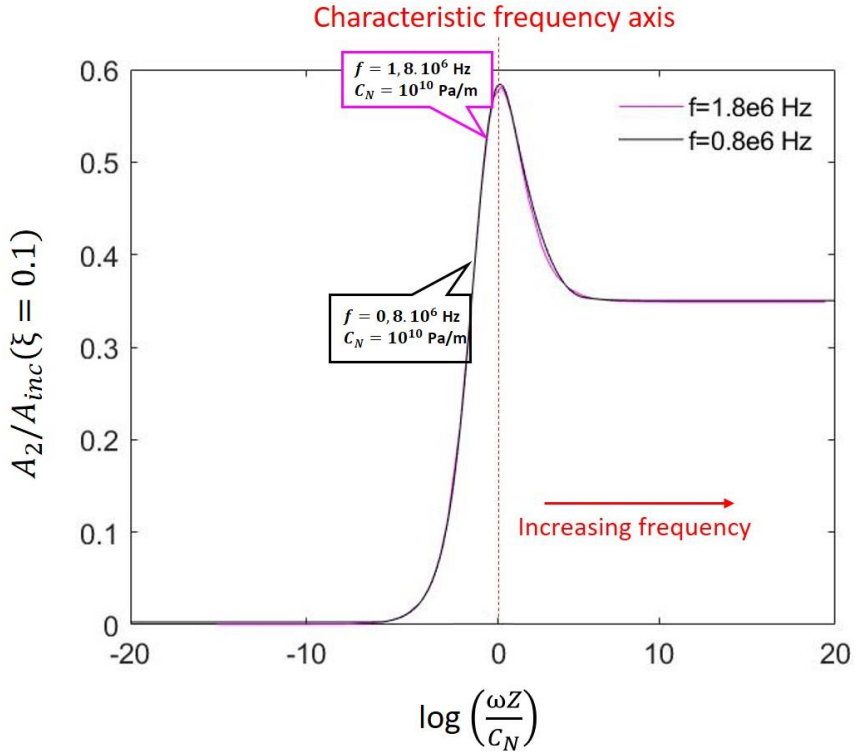

Figure 40 Evolution of the second harmonic efficiency A_2/A_{inc} as a function of the normalized frequency for frequencies $f = 1.8\,10^6$ Hz and $f = 0.8\,10^6$ Hz, without damaging the interface for $\xi = 0.1$

The normalized frequencies are positioned on the A_2/A_{inc} curves. Contrary to the previous case, the different normalized frequencies are on the left of the characteristic frequency axis. On this part of the curve, the second harmonic efficiency increases with the frequency. Hence, an incident wave with a higher frequency value generates more nonlinearity, which explains the increase of the second harmonic as a function of dimensionless parameter ξ when increasing the frequency in Figure 39, and thus the fact that for some case, the maximum of A_2/A_{inc} disappears.

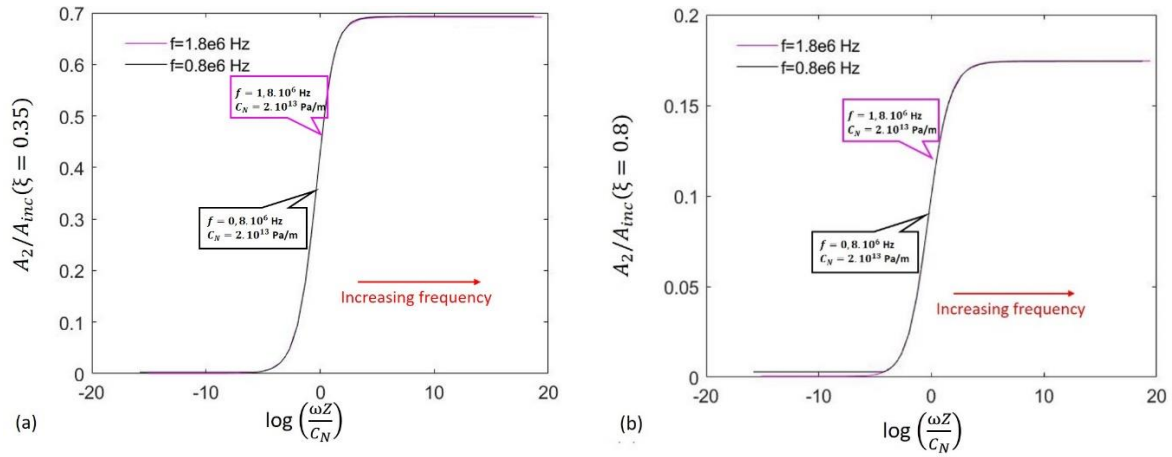

Figure 41 Evolution of the second harmonic efficiency A_2/A_{inc} as a function of the normalized frequency for frequencies $f = 1.8\ 10^6\ Hz$ and $f = 0.8\ 10^6\ Hz$, without damaging the interface. (a) $\xi = 0.3$ and (b) $\xi = 0.8$

Similarly to case $\xi = 0.1$, we note that the normalized frequencies for cases $\xi = 0.35$ and $\xi = 0.8$, lie on the section of the curve that increases with the frequency. Consequently, if the frequency is increased, the nonlinearity is increased. (See Figure 41)

Third case: contact stiffness $C_N = 10^{15}\ Pa/m$

Figure 42 shows the evolutions of the ratios A_2/A_{inc} and A_1/A_{inc} as a function of the dimensionless parameter ξ for the third range of stiffness.

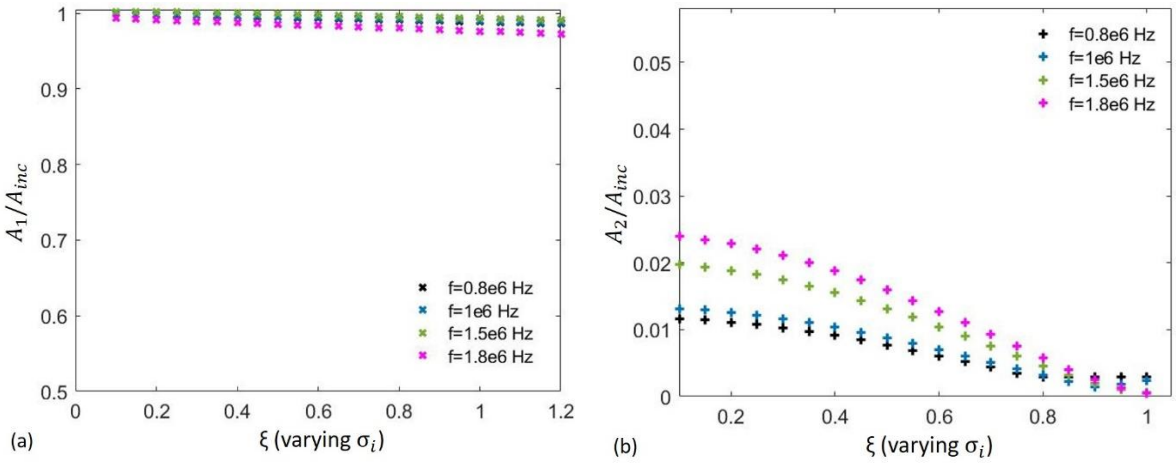

Figure 42 (a) Evolution of the ratio A_1/A_{inc} as a function of the dimensionless parameter ξ. (b)Evolution of the ratio A_2/A_{inc} as a function of the dimensionless parameter $\xi = \frac{p_0}{\sigma_i^{max}}$. frequency $f\epsilon[8\ 10^5, 1.8\ 10^6]$ Hz. $C_N = 10^{15}$ Pa/m.

In this case, the interface behaviour is a quasi-perfect contact due the high value of stiffness C_N and hence the second harmonic generation is very small (as there is no damage). However, the impact of the frequency on the nonlinear coefficient evolution is still observable. In fact, similarly to the previous case, increasing the frequency results in an increase in the second harmonic amplitude since the normalized frequencies are positioned on the left of the characteristic frequency axis (see Figure 43).

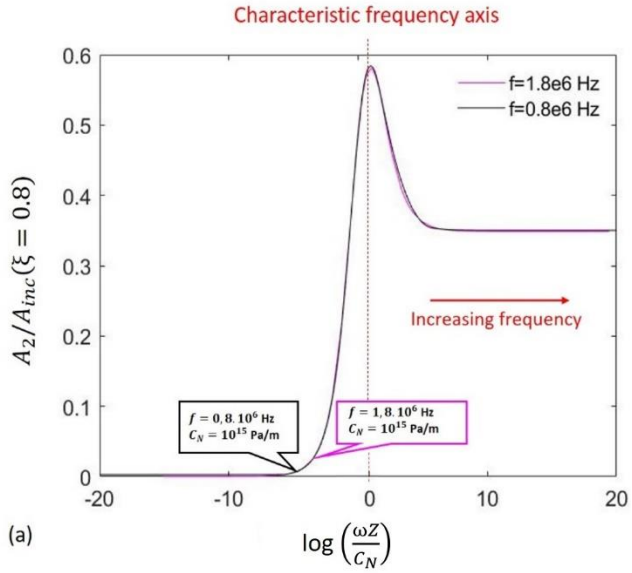

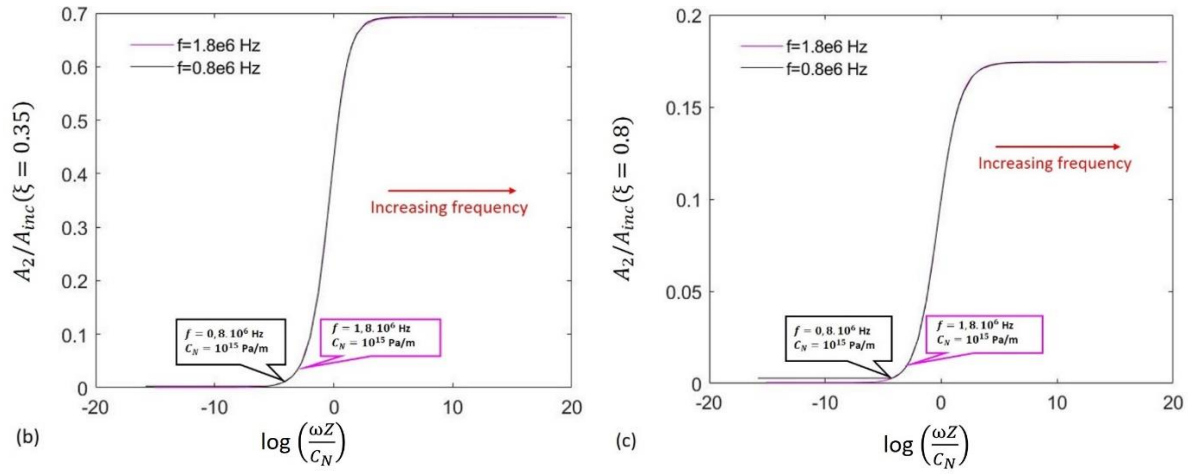

Figure 43 Evolution of the second harmonic efficiency A_2/A_{inc} as a function of the logarithm of the normalized frequency for frequencies $f = 1.8\ 10^6\ Hz$ and $f = 0.8\ 10^6\ Hz$, without damaging the interface. (a) $\xi = 0.1$; (b) $\xi = 0.35$ and (c) $\xi = 0.8$

Overall, for an undamaged interface behaviour, the nonlinear signature of the RCCM contact law is sensitive to the frequency of the incident wave, whose impact is strongly related to the value of the contact stiffness. Hence, the frequency of the incident wave can be adjusted so that the interface behaviour fits one of the three domains of sensitivity defined in this section. Thus, the value of the frequency will depend on the objectives of the study.

The latter analysis represents a major step towards a good understanding of the physical mechanisms involved in the interaction between vibro-acoustic waves and contact interfaces, which is the main objective of this thesis. In the next part, the nonlinear dynamic response of contact interfaces is further investigated through analysing the influence of the decohesion energy parameter on the nonlinear signature of the contact law.

3.3.3 Influence of the decohesion energy on the nonlinear signature of the RCCM contact law

In this paragraph, the parameters of the presented simulations may lead to interface damage (β_{end} <1 at the end of simulations).

The same three stiffness values as previously (paragraphs 3.3.1 and 3.3.2.) are considered in this section: $C_N = 10^{10}\ Pa/m$ and $C_N = 10^{15}\ Pa/m$, belong respectively to the first and last stiffness ranges, where the nonlinear signature of the RCCM contact law is not sensitive to the contact stiffness and $C_N = 2.10^{13}\ Pa/m$, belongs to the second range, where the nonlinear signature of the contact law is stiffness-dependant. It is important to recall that these sensitivity

domains are dependent on frequency and that this analysis could be done using normalized frequency (see equation 3.4). We chose not to present this study according to the normalized frequency but to keep the physical parameters explicitly.

The incident wave amplitude, and hence the dimensionless parameter ξ, is varied, while the static pressure p_0 is fixed. The simulation parameters are listed in Table 7.

Normal stiffness C_N (Pa/m)	**Viscosity b (Pa.s)**	**Decohesion energy w (J/m^2)**	**Frequency f (Hz)**
From $\mathbf{10^{10}}$ to $\mathbf{10^{15}}$	10^{-8}	from 10^{-3} to 1	10^{6}

Table 7 simulation parameters for decohesion energy study

First case: contact stiffness $C_N = 10^{10}\ Pa/m$, belonging to the first range

Figure 44 shows the evolution of the intensity of adhesion and contact stiffness as a function of ξ, for different decohesion energies w. Each dot in the graphic represents the ending value of the adhesion intensity and contact stiffness at the end of the corresponding simulation.

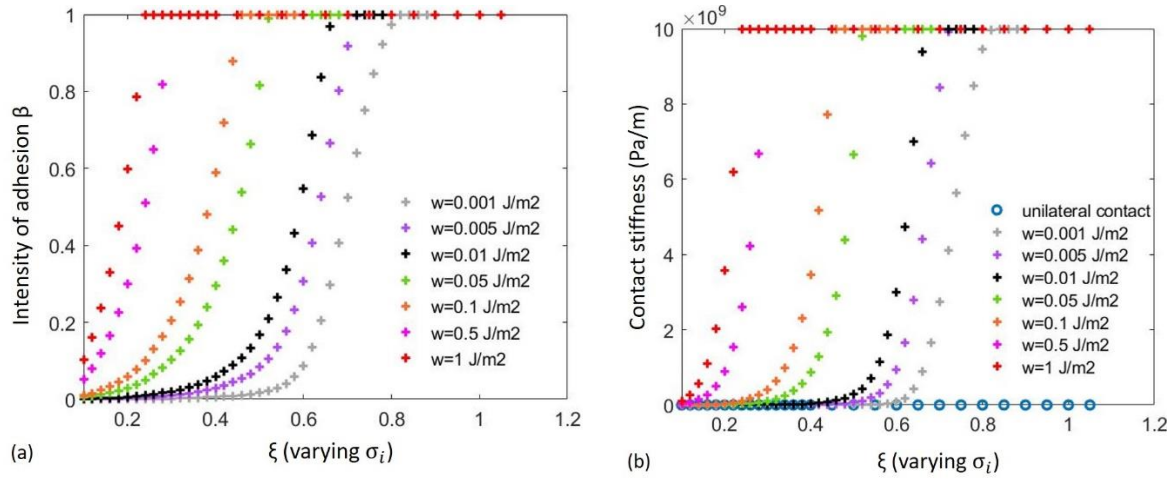

Figure 44 The maximum incident pressure is $max(\sigma_i^{max}) = 120\ MPa$ (corresponding to $\xi = 0.1$). (a) Intensity of adhesion as a function of the dimensionless parameter ξ and (b) Contact stiffness at the end of simulation as a function of the dimensionless parameter ξ. Contact *stiffness* $C_N = 10^{10} Pa/m$, decohesion energy $w\epsilon[10^{-3}, 1]\ J/m^2$ and viscosity $b = 10^{-8}\ N.s/m$.

As long as the incident wave amplitude is not enough to damage the interface, the adhesion is complete (β_{end}=1), the final contact stiffness is equal to the initial stiffness and the interface traction behaviour is elastic. Increasing the incident wave amplitude, the damage of the interface occurs gradually. Then, the intensity of adhesion β and the apparent stiffness $\beta^2 C_N$

decrease. When adhesion vanishes totally (β=0), we retrieve at the end the classical unilateral contact law ($C_N = 0$).

When increasing the decohesion energy w, the limit of elasticity $\sqrt{C_N w}$ increases. Thus, the incident energy, sufficient to damage the interface, increases too and the damage occurs for lower values of dimensionless parameter ξ, as shown in Figure 44 (a).

Figure 45 shows the evolutions of the ratios A_2/A_{inc} and A_1/A_{inc} as a function of the dimensionless parameter ξ.

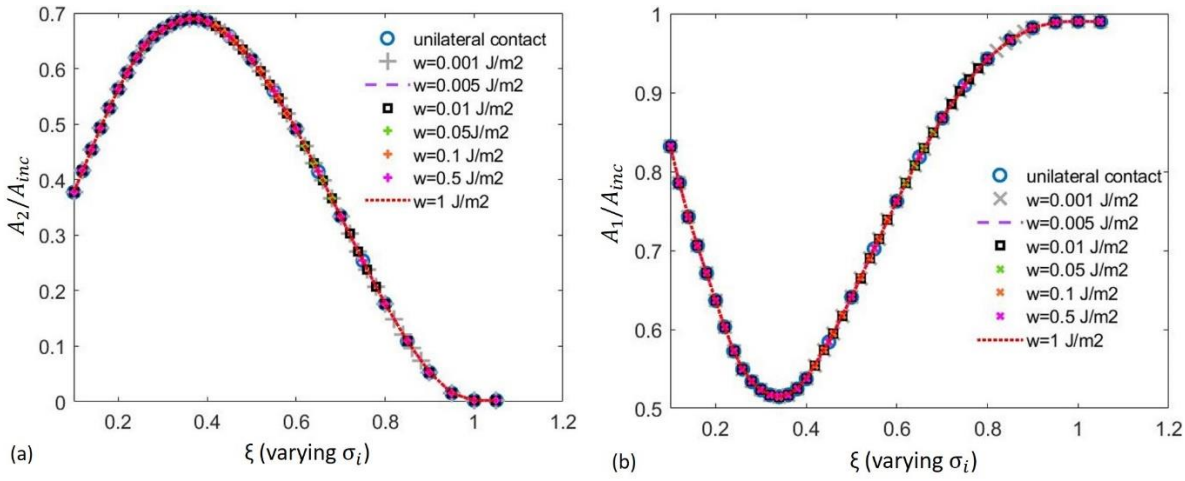

Figure 45 Evolution of (a) the ratio A_2/A_{inc} and (b) the ratio A_1/A_{inc} as a function of the dimensionless parameter $\xi = \frac{p_0}{\sigma_i^{max}}$. Decohesion energie $w\epsilon[10^{-3}, 1]$ J/m², $b = 10^{-8}$ Pa.s and $C_N = 10^{10}$ Pa/m.

The ratios A_2/A_{inc} and A_1/A_{inc} overlap with the unilateral contact ratios, for all decohesion energy values, even if the interface is not damaged. Thus, the nonlinear signature at the interface is quasi-independent of the decohesion energy for this range of stiffness. In fact, dynamically, the interface behaviour shifts from a quasi UC behaviour to a UC behaviour.

Second case: contact stiffness $C_N = 2.10^{13}\ Pa/m$, belonging to the second range of stiffness

Figure 46 shows the evolution of the intensity of adhesion and contact stiffness as a function of ξ, for different decohesion energies.

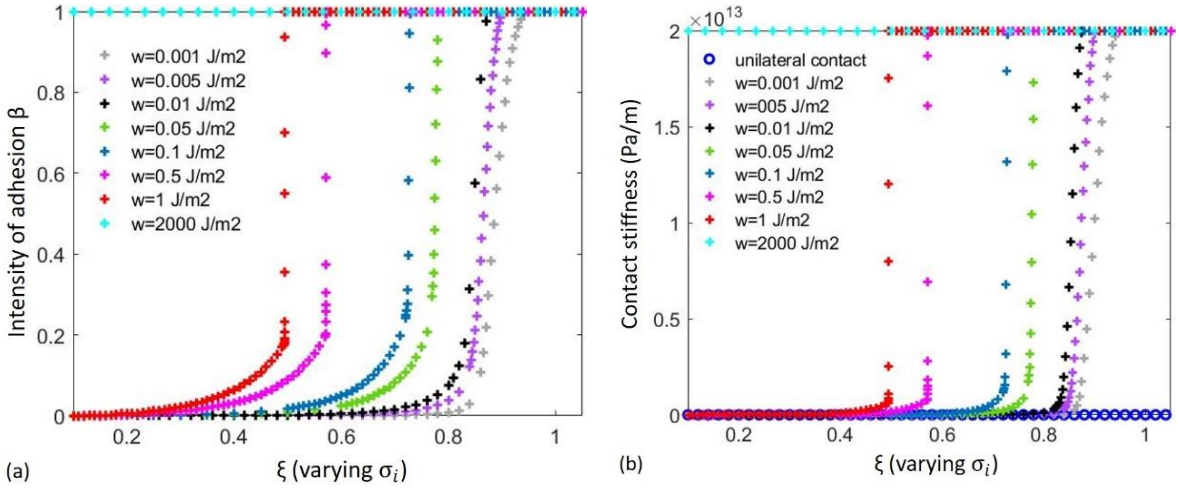

Figure 46 (a) Intensity of adhesion β as a function of the dimensionless parameter ξ and (b) Contact stiffness as a function of the dimensionless parameter ξ. *Contact stiffness* $C_N = 2.10^{13} Pa/m$, decohesion energy $w\epsilon[10^{-3}, 2000]\ J/m^2$ and viscosity $b = 10^{-8}\ N.s/m$.

Again, when increasing the decohesion energy, the damage at the interface occurs for lower ξ values, for higher incident wave magnitude. In fact, as mentioned in the previous paragraph, the increase of the decohesion energy leads to the increase in the elastic limit. Hence, the incident amplitude threshold, sufficient to damage the interface, increases and the damage of the interface occurs for a lower value of the dimensionless parameter ξ. Furthermore, it is noticed that the increase of the decohesion energy induces more sudden damage. The transition from an elastic behaviour to a completely damaged behaviour seems to be smoother in the case of $w = 10^{-3}\ J/m^2$ compared to the case of $w = 1\ J/m^2$, for example. In fact, the decohesion energy (which is the dissipated energy), is the area covered by the contact pressure as a function of the relative displacement as shown in Figure 47 (a). This area is increased by increasing the elastic limit. This increase in yield strength results in an increase in the deformation energy, which will be resituated to the system when the interface breaks. This phenomenon will cause the interface to open faster. (See Figure 47 (b))

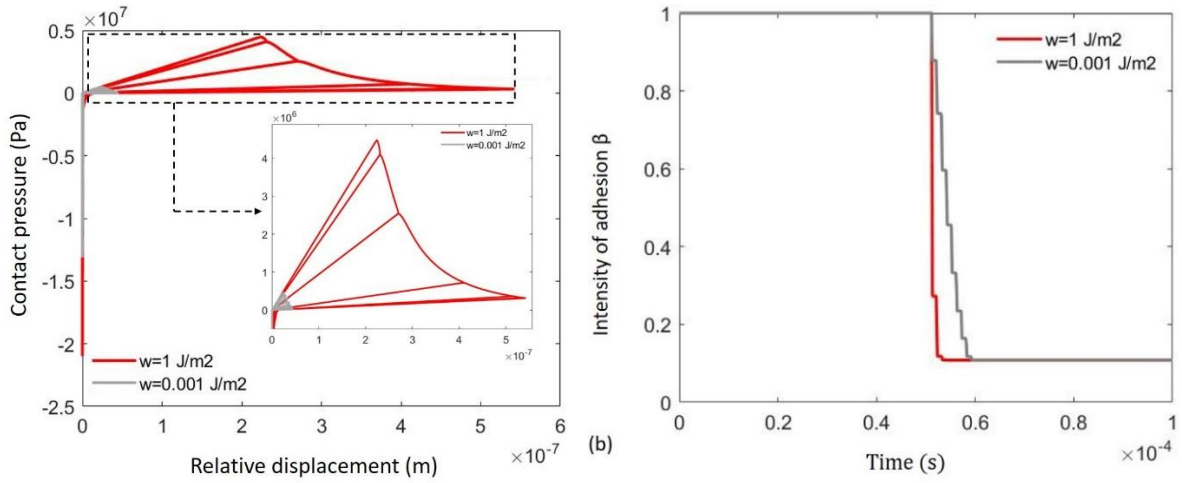

Figure 47 (a) Contact pressure as a function of the relative displacement and (b) Intensity of adhesion over time .Contact stiffness $C_N = 2.10^{13} Pa/m$, viscosity $b = 10^{-8}\ N.s/m$ and intensity of adhesion at the end of simulation $\beta end = 0.1$.

Furthermore, for the same value of intensity of adhesion, it is noticed that the duration of each contact loss is more important in the case of $w = 1\,J/m^2$ (see Figure 48). In fact, when the decohesion energy is increased, damage occurs for lower ξ values (i.e. higher incident wave amplitudes), where the interface is subjected to more traction than compression.

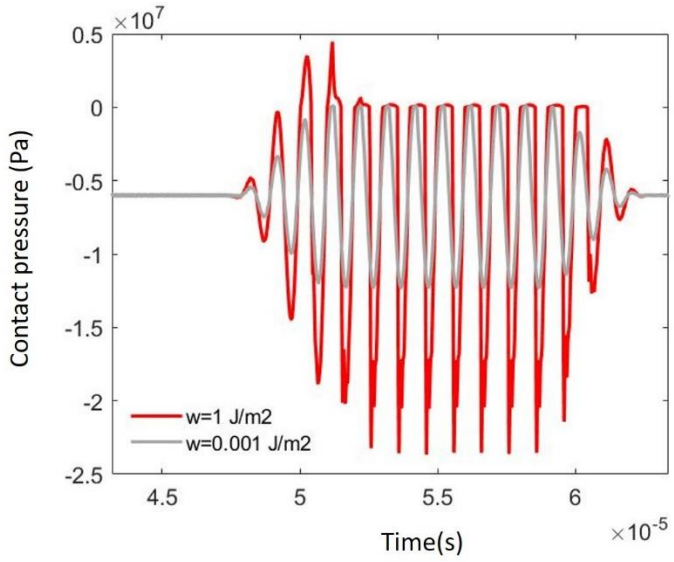

Figure 48 Contact pressure over time. Contact stiffness $C_N = 2.10^{13} Pa/m$, viscosity $b = 10^{-8}\ N.s/m$ and intensity of adhesion at the end of simulation $\beta_{end} = 0.1$.

Figure 49 shows the evolutions of the ratios A_2/A_{inc} and A_1/A_{inc} as a function of the dimensionless parameter ξ.

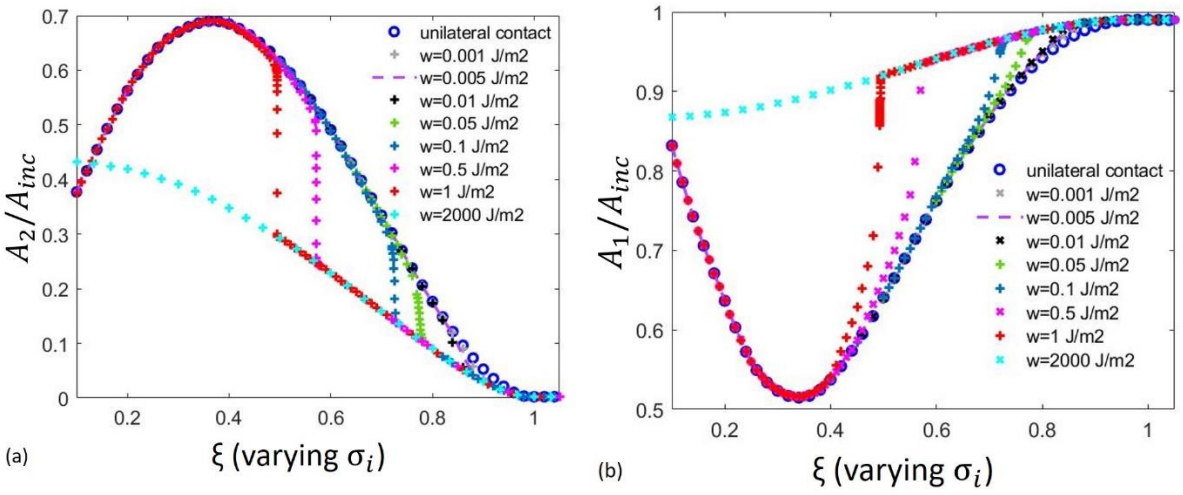

Figure 49 Evolution of (a) the ratio A_2/A_{inc} and (b) the ratio A_1/A_{inc} with the dimensionless parameter $\xi = \frac{p_0}{\sigma_i^{max}}$. decohesion energies $w\epsilon[10^{-3}, 1]\frac{J}{m^2}$, $b = 10^{-8}\ Pa.s$ and contact stiffness $C_N = 2.10^{13} Pa/m$.

While the limit of elasticity is not reached, the interface behaviour is elastic and the nonlinearity generated is only due to the contrast of stiffness in traction and compression. Consequently, the evolutions of A_2/A_{inc} and A_1/A_{inc} are identical to the ones obtained with an undamaged interface ($w = 1000\ J/m^2$). After that, damage of the interface occurs and consequently, the nonlinearity coefficient increases due to the damage. The nonlinear signature is then sensitive to the decohesion energy, on this zone. When the adhesion vanishes totally, the interface is completely damaged and the nonlinear signature is equivalent to the unilateral contact case. Note that the passage between the two different behaviours (UC and high w, i.e. no damage) is clearly visible on the nonlinear signature (A_2/A_{inc} and A_1/A_{inc}).

Third case: contact stiffness $C_N = 10^{15}\ Pa/m$

Figure 50 shows the evolution of the intensity of adhesion and contact stiffness as a function of ξ, for different decohesion energies.

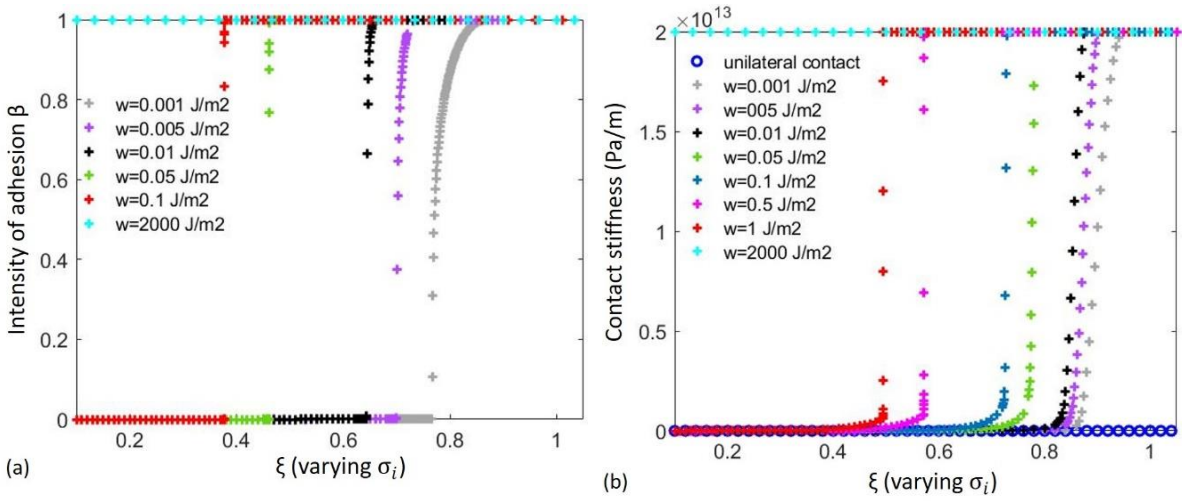

***Figure 50 The maximum incident pressure is $max(\sigma_i^{max}) = 25\ MPa$. (a) Intensity of adhesion β as a function of the dimensionless parameter ξ and (b) Contact stiffness as a function of the dimensionless parameter ξ. Contact stiffness $C_N = 10^{15} Pa/m$,* decohesion energy $w\epsilon[10^{-3}, 2000]\ J/m^2$ and viscosity $b = 10^{-8}\ N.s/m$.**

When increasing the decohesion, the interface is damaged for higher incident wave amplitudes (i.e. lower ξ). The damage occurred at the interface is even sharper since the interface behaviour goes from a perfect contact (bilateral case) to a completely damaged contact (unilateral case). Figure 51 shows the evolutions of the ratios A_2/A_{inc} and A_1/A_{inc}, as a function of the dimensionless parameter ξ.

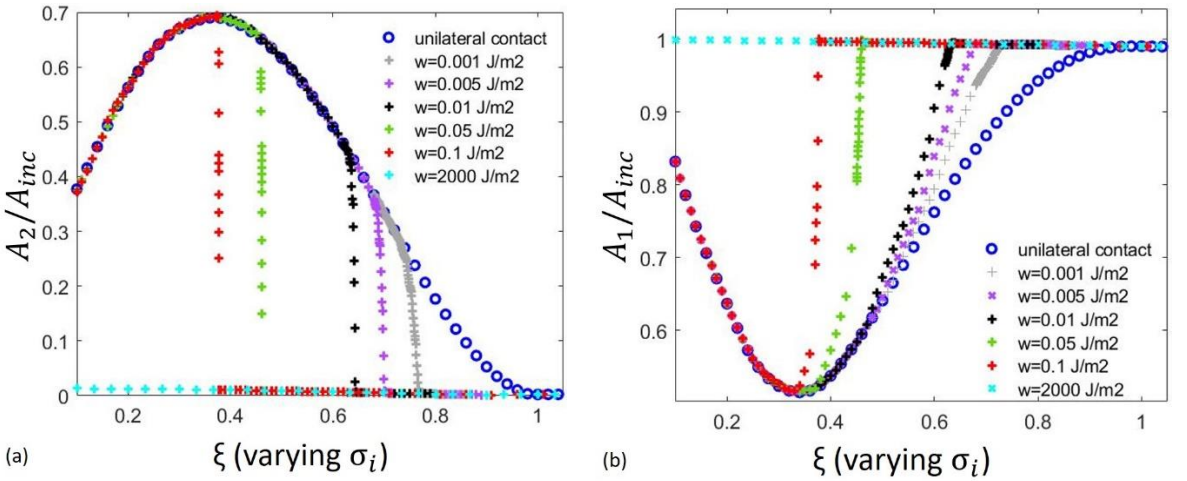

Figure 51 Evolution of (a) the ratio A_2/A_{inc} as a function of the dimensionless parameter $\xi = \frac{p_0}{\sigma_i^{max}}$ and (b) the ratio A_1/A_{inc} as a function of the dimensionless parameter ξ. decohesion energies $w\epsilon[10^{-3}, 1]\ J/m^2$, $b = 10^{-8}\ Pa.s$ and contact stiffness $C_N = 10^{15} Pa/m$.

Figure 51 shows radical transition from the undamaged case, which is quasi-linear to a completely peeled-off interface, with the highest nonlinearity level in this case. It is noted that not only the second harmonic but also the fundamental is sensitive to the decohesion energy

variation in this range of stiffness C_N. Then, the fundamental contains as well information of the different parameters of the interface.

Finally, another parameter that governs the damage process, according to the RCCM contact law, is the viscosity and it is investigated in the next section.

3.3.4 Influence of the viscosity on the nonlinear signature of the RCCM contact law

We evaluate, in this section, the influence of the viscosity on the RCCM contact law signature at the interface. As for the previous two paragraphs, the sensitivity to the viscosity is conducted for the same three values of the stiffness.

First case: contact stiffness $C_N = 10^{10}\ Pa/m$ belonging to the first range

Figure 52 shows the evolution of the intensity of adhesion and contact stiffness as a function of ξ, for different decohesion energies.

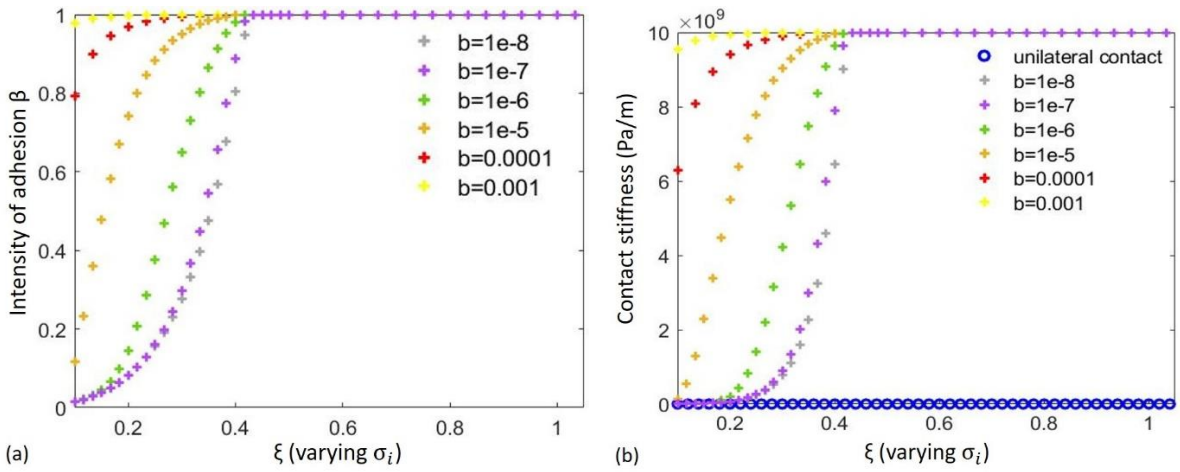

Figure 52 The maximum incident pressure is $max(\sigma_i^{max}) = 25\ MPa$. (a) Intensity of adhesion as a function of the dimensionless parameter ξ and (b) Contact stiffness as a function of the dimensionless parameter ξ. *Contact stiffness $C_N = 10^{10} Pa/m$,* decohesion energy $w = 0.1\ J/m^2$ and viscosity $b\epsilon[10^{-8}, 10^{-3}]\ N.s/m$.

The damage occurs for the same amplitude of the incident wave, when varying the viscosity of the interface. In fact, the limit of elasticity is only dependent on the decohesion energy and stiffness, here fixed. However, the viscosity affects the way the interface is damaged. Indeed, the damage velocity decreases when increasing the viscosity, and hence the interface is degraded slower.

Figure 53 shows the evolutions of the ratios A_2/A_{inc} and A_1/A_{inc} as a function of the dimensionless parameter ξ.

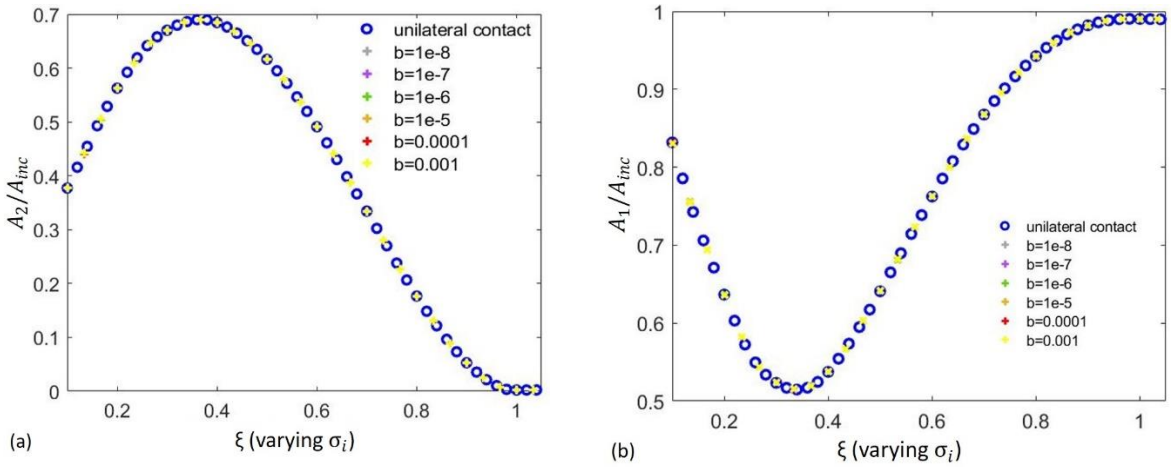

Figure 53 Evolution of the ratioA_2/A_{inc} as a function of the dimensionless parameter $\xi = \frac{p_0}{\sigma_i^{max}}$. (b) Evolution of the ratio A_1/A_{inc} as a function of the dimensionless parameter ξ. *Contact stiffness* $C_N = 10^{10} Pa/m$, decohesion energy $w = 0.1\ J/m^2$ and viscosity $b\epsilon[10^{-8}, 10^{-3}]\ N.s/m$.

The ratios A_2/A_{inc} and A_1/A_{inc} overlap with the unilateral contact ratios, for all evaluated viscosities. Thus, the nonlinear signature at the interface is not sensitive the viscosity in this case. In fact, the second harmonic efficiency is little sensitive to the stiffness in traction for $C_N = 10^{10} Pa/m$ and the interface damage shifts the stiffness value from the latter value to 0.

<u>Second case: contact stiffness $C_N = 2.10^{13}\ Pa/m$, belonging to the second range</u>

Figure 54 shows the evolution of the intensity of adhesion and contact stiffness as a function of ξ, for different viscosities at the interface.

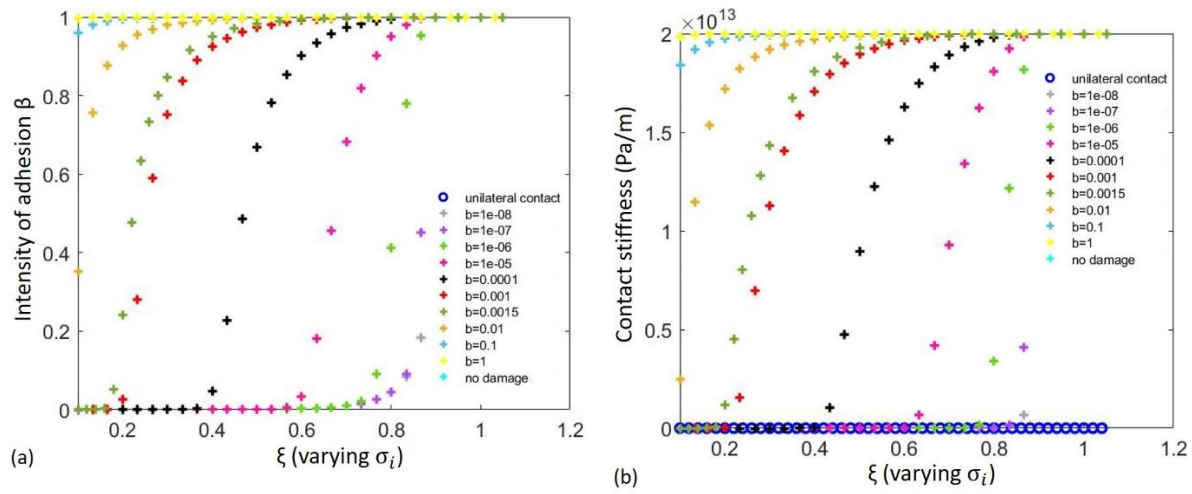

Figure 54 The maximum incident pressure is $max(\sigma_i^{max}) = 25\ MPa$. (a) Intensity of adhesion as a function of the dimensionless parameter ξ and (b) Contact stiffness as a function of the dimensionless parameter ξ. *Contact stiffness $C_N = 2.10^{13} Pa/m$,* decohesion energy $w = 0.1\ J/m^2$ and viscosity $b\epsilon[10^{-8}, 1]\ N.s/m$.

For ξ>0.9, the limit of elasticity is not reached and the interface behaves like a spring with stiffness $C_N = 2.10^{13}$. After that, the interface is damaged gradually. The dynamic at the interface is affected by the viscosity. Indeed, Figure 55 shows the contact pressure as a function of the relative displacement at the contact for different viscosity values. On one hand, when increasing the viscosity the maximum pressure increases. On the other hand, when decreasing the viscosity, the damage velocity increases.

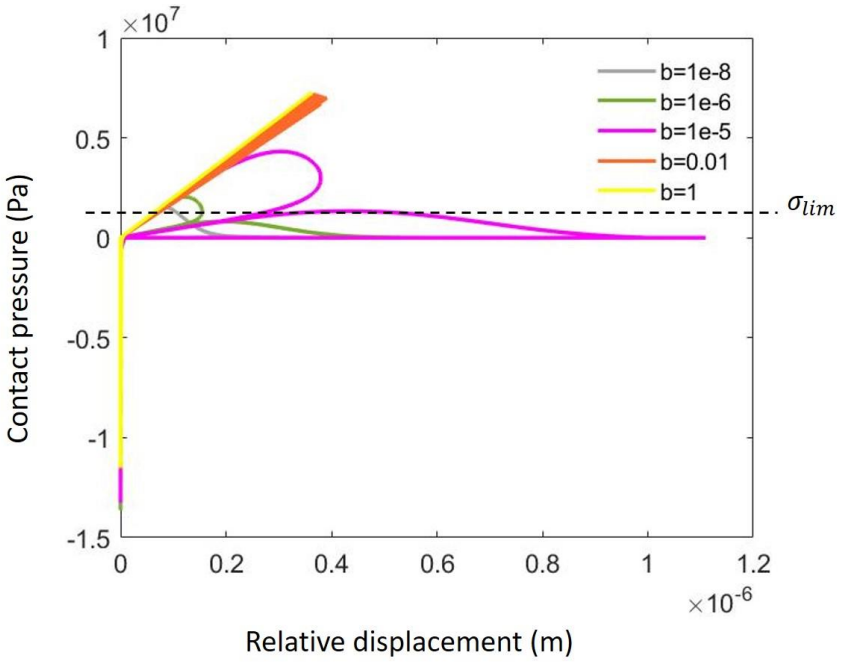

Figure 55 Contact pressure as a function of the relative displacement. Contact stiffness $C_N = 2.10^{13} Pa/m$, decohesion energy $w = 0.1\ J/m^2$, viscosity $b \in [10^{-8}, 1] N.s/m$, $\xi = 0.1$ and $\sigma_{lim} = 1.4\ 10^6 MPa$.

Figure 56 shows the evolutions of the ratios A_2/A_{inc} and A_1/A_{inc} as a function of the dimensionless parameter ξ. When ξ>0.9, the nonlinear signature is identical to the undamaged signature. For lower ξ values, the interface starts the damage process, and the nonlinear signature tends towards the unilateral contact. This shift from the undamaged behaviour to the unilateral contact behaviour is faster as the viscosity decreases.

It is noted that for viscosity values $b > 10^{-4}\ Pa.s$, the maximum of the second harmonic occurs for lower ξ values and particularly lower than $\xi_{opt} = 0.35$. Consequently, the position of the maximum of the nonlinearity is strongly affected by the viscosity in these cases (from

b=0.001 Pa.s to b=0.0015 Pa.s). Note also that the maximum disappears for b greater than 0.01Pa.s.

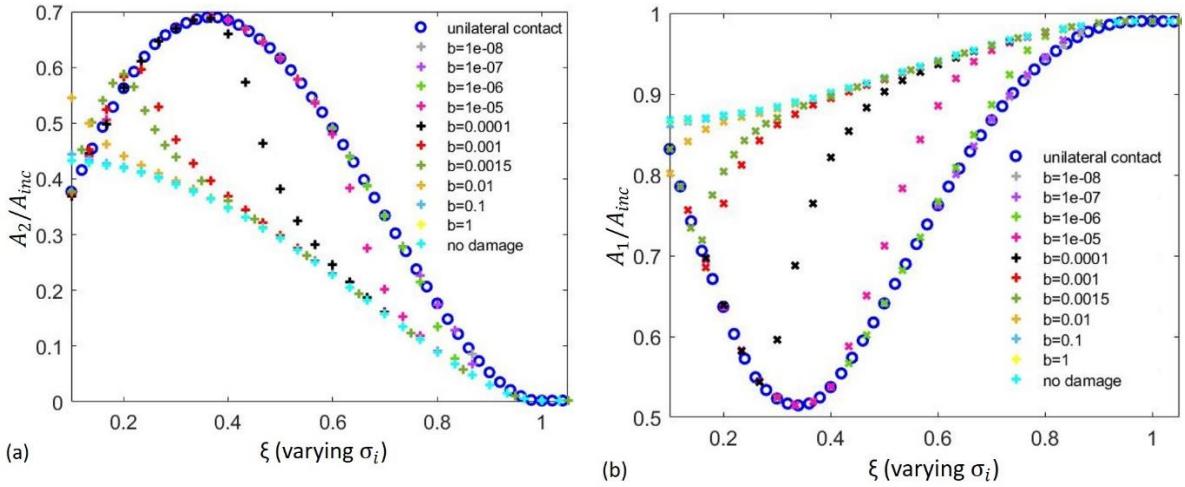

Figure 56 Evolution of the ratio A_2/A_{inc} as a function of the dimensionless parameter $\xi = \frac{p_0}{\sigma_i^{max}}$ and (b) Evolution of the ratio A_1/A_{inc} as a function of the dimensionless parameter ξ. *Contact stiffness* $C_N = 2.10^{13} Pa/m$, decohesion energy $w = 0.1\ J/m^2$ and viscosity $b\epsilon[10^{-8}, 1]\ N.s/m$.

We may note also that for the value of viscosity $b = 10^{-2}\ Pa.s$, the ratios A_2/A_{inc} and A_1/A_{inc} do not tend towards any of the limit cases (undamaged case and totally damaged case), for higher incident wave amplitudes i.e. lower ξ values. In fact, at the end of simulations, the adhesion does not completely vanish ($\beta_{end} = 0.35$) and the stiffness is non-zero ($C_{N_{end}} = 0.25.10^{13} Pa/m$). Hence, the interface behaviour is close to a traction spring with the equivalent stiffness obtained at the end of the simulation $C_{N_{end}}$, which generates, in this case, more nonlinearity compared to the unilateral case (see Figure 33 and Figure 56).

For instance, this latter behaviour is obtained with a viscosity $b = 1.5\ 10^{-3}\ Pa.s$, where the interface is damaged and the stiffness decreases gradually. The nonlinearity generated exceeds the unilateral contact nonlinearity until reaching a peak. After that, the adhesion keeps dropping, the contact stiffness too. The nonlinearity generated decreases until overlapping with the unilateral contact, where the interface is completely damaged.

Furthermore, it should be mentioned that the viscosity, unlike the decohesion energy, is sensitive to frequency variation. Figure 57 (a) shows the evolution of the contact pressure as a function of the relative displacement for two different frequencies. It can be noted that an incident wave with a higher frequency value leads to a higher-pressure amplitude and therefore a slower damage. This can be observed in Figure 57 (b) indicating that, for the same viscosity

value, an incident wave with a lower frequency damages faster and therefore generates more nonlinearity.

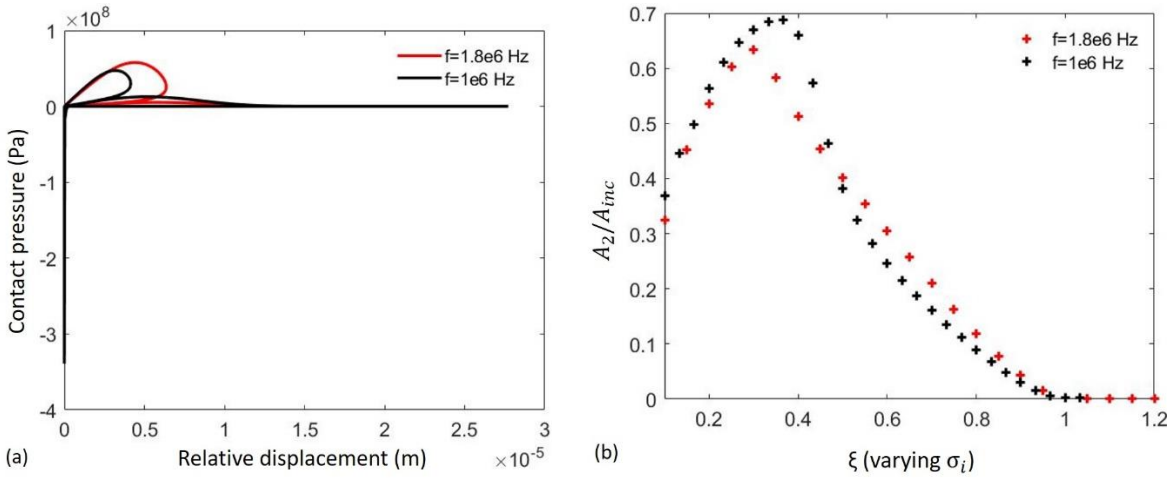

Figure 57 (a) Evolution contact pressure as a function of the relative displacement. (b) Evolution of the ratio A_2/A_{inc} as a function of the dimensionless parameter $\xi = \frac{p_0}{\sigma_i^{max}}$. Contact stiffness $C_N = 2.10^{13} Pa/m$, decohesion energy $w = 0.1\ J/m^2$ and viscosity $b = 10^{-4}\ N.s/m$.

<u>Third case: contact stiffness $C_N = 10^{15}\ Pa/m$, belonging to the third range</u>

Here, the value of the stiffness ($C_N = 10^{15} Pa/m$) belongs to a domain, where the contact between the solid and the rigid wall tends towards a perfect contact in the absence of damage. Figure 58 shows the evolution of the intensity of adhesion and contact stiffness as a function of ξ, for different viscosities at the interface.

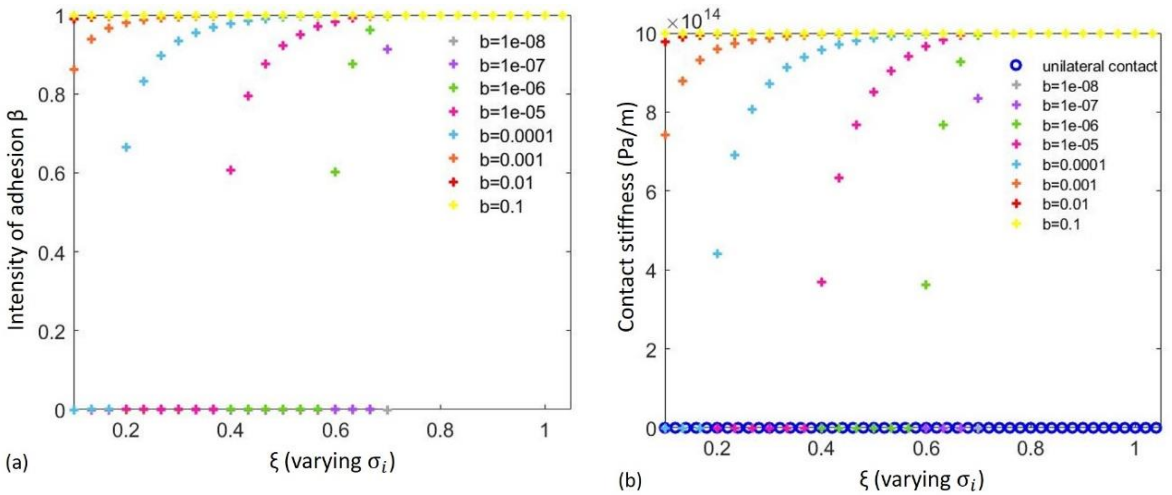

Figure 58 The maximum incident pressure is $max(\sigma_i^{max}) = 25\ MPa$. (a) Intensity of adhesion as a function of the dimensionless parameter ξ (b) Contact stiffness as a function of the dimensionless parameter ξ. *Contact stiffness $C_N = 10^{15} Pa/m$,* decohesion energy $w = 0.1\ J/m^2$ and viscosity $b \epsilon [10^{-8}, 0.1]\ N.s/m$.

Increasing the viscosity leads to a decrease of the damage velocity with respect to ξ and hence a softer interface peel off.

Figure 59 shows the evolutions of the ratios A_2/A_{inc} and A_1/A_{inc}, as a function of the dimensionless parameter ξ.

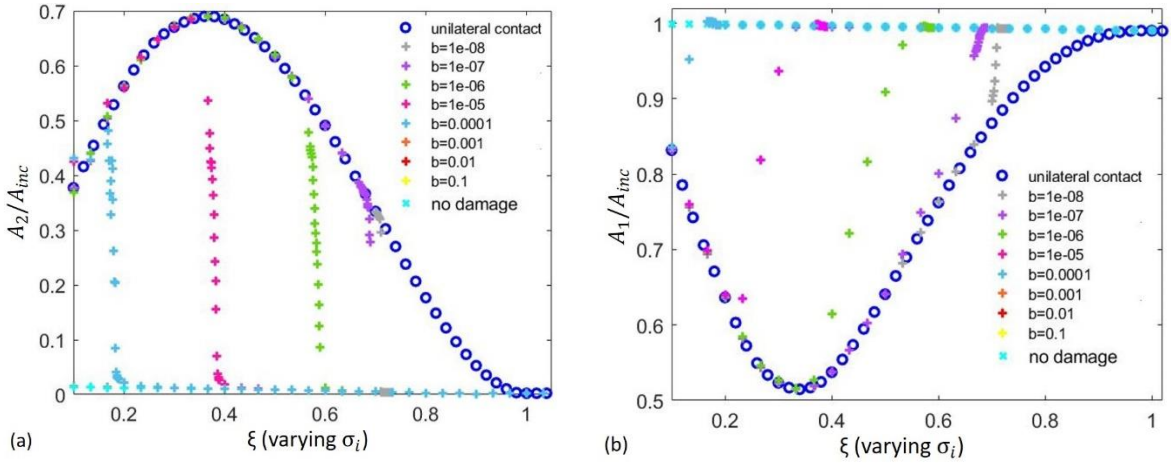

Figure 59 Evolution of the ratio A_2/A_{inc} as a function of the dimensionless parameter $\xi = \frac{p_0}{\sigma_i^{max}}$ and (b) Evolution of the ratio A_1/A_{inc} as a function of the dimensionless parameter ξ. *Contact stiffness* $C_N = 10^{15} Pa/m$, decohesion energy $w = 0.1\ J/m^2$ and viscosity $b\epsilon[10^{-8}, 0.1]\ N.s/m$.

Both Figure 59 (a) and (b) illustrate the transition from the undamaged interface, where there is a low second harmonic generation, and most of the energy is at the fundamental, to the unilateral case, where the interface is completely damaged. Hence, the nonlinearity increases and the fundamental decreases, when increasing the incident wave amplitude, in order to reach the level of nonlinearity of the unilateral contact. Consequently, the variation of the viscosity affects both fundamental and second harmonic evolution. However, the viscosity does not affect the harmonics in a similar way. In fact, the influence of the viscosity on the fundamental is observable for lower ξ values compared to the second harmonic, which does not appear when varying the stiffness and the decohesion energy. This is clearly illustrated in Figure 60 by the detached branches. This observation could be explained by the fact that the viscosity could be interpreted as a viscous damping; whose effect is proportional to the frequency and hence affects differently the two harmonics. It should be noted that the viscosity influences differently A_1 and A_2 in the previous case ($C_N = 2.10^{13} Pa/m$), but the effects are less prominent.

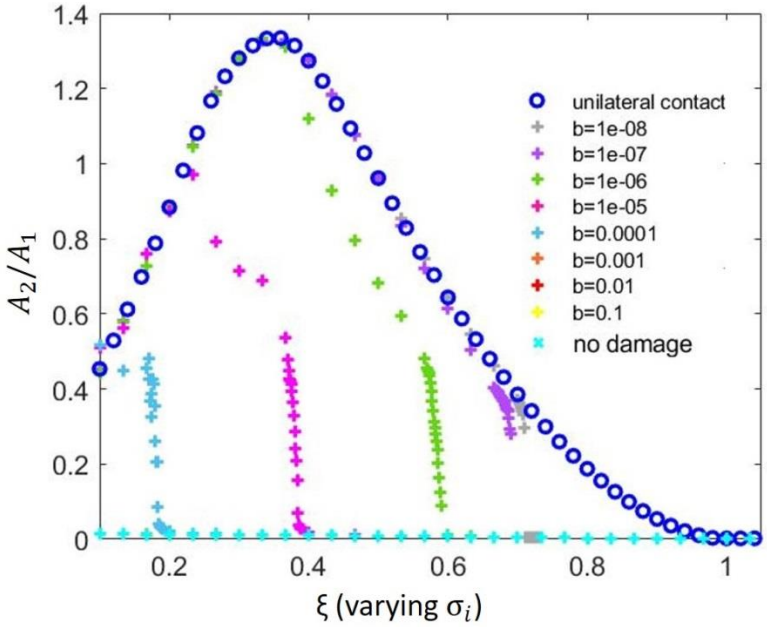

Figure 60 Evolution of the ratio A_2/A_1 as a function of the dimensionless parameter $\xi = \frac{p_0}{\sigma_i^{max}}$. *Contact stiffness* $C_N = 10^{15} Pa/m$, decohesion energy $w = 0.1\ J/m^2$ and viscosity $b\epsilon[10^{-8}, 0.1]\ N.s/m$.

3.1. Identification of contact law parameters

As seen previously, the nonlinear signature through the second harmonic efficiency is affected by interface parameters. This sensitivity that depends on the configuration (incident wave characteristics, materials) can be used to characterize the interface (i.e. determine its different parameters). The previous analysis is primordial to develop inverse method and optimise sensitivity. This section is a discussion on the ability of nonlinear signature to lead to a quantitative determination of interface parameters, considering that the interface behave following RCCM law.

As previously mentioned, the frequency range is essential. Three different ranges have been identified:

i. The first range corresponds to an insensitive dynamic response of the system to any of the RCCM contact law parameters. In the perspective of identifying interface parameters, none of them could be determined in this case, neither the stiffness using the second harmonic evolution nor the viscosity and decohesion energy, since the interface behaviour is equivalent to the unilateral contact law. This range cannot be used for determining parameters.

ii. By contrast, the second zone presents a sensitivity to the different RCCM parameters. This range is particularly interesting for the stiffness identification. Indeed, when the interface is undamaged, the interface behaviour is governed only by the stiffness in

traction. Hence, the stiffness, in this case and for a given frequency, describes fully the system and can, therefore, be identified using the inverse method. Experimental measurements can be performed on fundamental and second harmonic amplitudes A_1 and A_2 of the reflected wave that can be measured. Note that A_1 is preferred to A_{inc} as it is easier to obtain experimentally. Figure 61 shows the evolution of A_2/A_1 as a function of ξ, or experimentally as a function of the incident wave or static pressure.

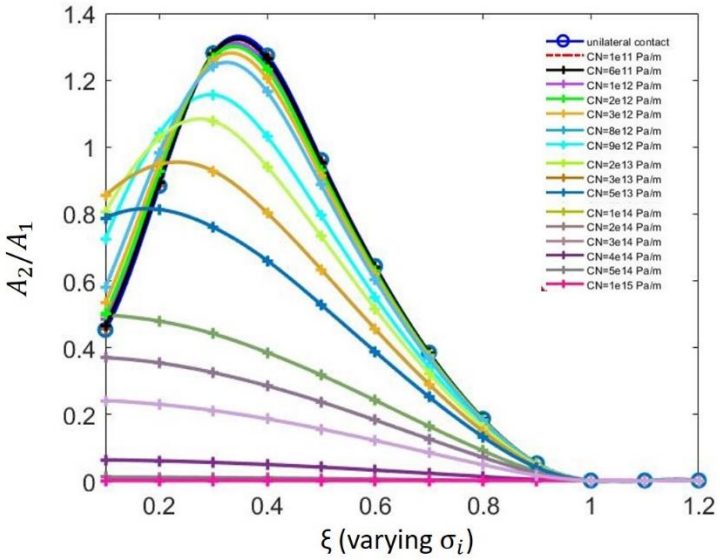

Figure 61 Evolution of the ratio A_2/A_1 as a function of the dimensionless parameter $\xi = \frac{p_0}{\sigma_i^{max}}$. Contact stiffness $C_N \in [0, 10^{15}] Pa/m$, for an undamaged interface.

Once the stiffness is identified, an estimation of the viscosity and decohesion energy can be expected. Indeed, the nonlinear signature is sensitive to the variation of these two parameters and therefore it contains information concerning both of them. To access these data, an incident wave, which amplitude is large enough to damage the interface, must first be applied. The next challenge would be to separate the contributions of these latter parameters on the nonlinear signature. One possible approach for identification would be to study the behaviour of the interface at two different frequencies. Indeed, as seen in section 3.3.3, viscosity is sensitive to the frequency yet this is not the case of the decohesion energy. This is a starting point worth developing in further works for interface characterization.

Note that, in order to estimate or characterize the level of damage or a parameter related to the damage (e.g. the decohesion energy), the interface must be damaged in general. The non-destructive nature of the methodology can therefore be discussed.

In case of characterizing the adhesion of two contacting surfaces, once the adhesion is broken it will reform again. In this context, the methodology remains non-destructive and allows access to damage parameter.

However, in the case of bonding interfaces, this method could be used in two different ways. The first one consists in the identification of a conform bonding. In fact, by increasing the incident wave amplitude to the limit of hold of the interface, the appearance of a damage can be detected via the NL signature of the interface. In this case, the test is destructive for non-conform interfaces.

The second option is to remain in the elastic range and characterise the interface stiffness. Indeed, Siryabe and al. [89] have shown that the interface stiffness drops for non-conforming interfaces. Nevertheless, a correlation between destructive and non-destructive testing is required to link the interface stiffness and the stress at failure.

iii. The third zone is not sensitive to the stiffness variation. In contrast, it is sensitive to the variations in decohesion energy and viscosity. As described in the previous case, both parameters could be estimated.

The limit of the different ranges are determined here for the PMMA material and can differ from an application to another. Indeed, the stiffness of the media has also an impact on the border limits of these ranges, through the acoustic impedance. However, the frequency study can help to overcome this constraint. In fact, the nonlinear signature of the RCCM contact law is sensitive to the frequency, whose impact is strongly related to the value of the stiffness. Hence, the frequency of the incident wave can be adjusted, so that the interface behaviour fits one of the three domains of sensitivity defined above. The value of the frequency will depend from the tested system. Finally note that the numerical curves of § 3.3.3 and 3.3.4 are obtained from initial state (undamaged) for each simulation. However, experimentally, this is only possible if the adhesion is adhesion self-healing. A specific experimental procedure must be developed using the present analysis in order to determine interface parameters considering this aspect.

3.4 Concluding remarks

In this chapter, the nonlinear interaction between a longitudinal wave and a rigid wall has been studied in a one-dimensional model. This type of interactions is manifested by the generation of higher harmonics. The amplitude of the second one is the most important and hence this component is the focus of the analysis.

A longitudinal wave can activate the clapping phenomenon at the interface. The contact dynamic has been modelled here by the RCCM contact law. The convergence of the correspondent numerical scheme has been first verified in both time and space. Despite its simplicity, the 1D model provided information about the impact of the RCCM contact law on the dynamic behaviour of the interface via higher harmonic evolutions. It has been shown that the nonlinear signature at the interface contains information on the different parameters. Consequently, a further parametric analysis is proposed. The first part has been dedicated to study the influence of the contact stiffness C_N and frequency f of the incident wave, while the interface remains undamaged. The second part analysed the influence of the decohesion energy w and the viscosity b on the nonlinear signature of the contact law, when the interface is damaged.

The influence of the frequency has been investigated by introducing a normalized frequency $f_{normalized}$. This latter parameter showed that the maximum of the second harmonic amplitude is obtained for a characteristic frequency, for low values of ξ. The position of the normalized frequency with respect to the characteristic frequency helped explaining the different evolutions of the second harmonic efficiency when varying the frequency.

As for the decohesion energy, the correspondent study has shown that it affects the way of damaging the interface.

Moreover, the nonlinear signature at the contact contains also information about the viscosity. In fact, this parameter affects the interface damaging velocity.

Yet interesting and sufficient for several studies, the results, presented in this section, are obtained in the case of infinite stiffness in compression. In the majority of real cases, asperities at the contact interface introduce a compression stiffness as well. This aspect ought to be considered in order to evaluate its influence on the interface behaviour. A particular law that accounts for this phenomenon will be presented in chapter 4.

Chapter 4: Normal contact stiffness in compression

So far, adhesion phenomenon has been studied by means of the RCCM contact law. This latter allows also for intermittent clapping of the interface and is appropriate for cases where the incident stress is sufficient to overcome the static compression stress σ_0. However, the interface remains closed for lower incident stress, for which the incident wave propagates linearly. Generally, this is not case of real surfaces presenting asperities during compression. In this context, the aim of this chapter is then to present a numerical and experimental analysis to provide a basic insight into the nonlinear vibrational response of a contact interface in compression. The goal is the characterization of the contact law within the compression stage, by evaluating the nonlinear contact response through the definition of a stress-dependent stiffness.

4.1 Approach for the nonlinear stiffness analysis

The approach in this section is based on developing a numerical model with contact interfaces, considering different nonlinear contact models, with different stress-dependent stiffness. A specific contact law is proposed, including a specific evolution of the stiffness for low pressures, and compared to a classical power law [90], fitting experimental values.

An experimental campaign is conducted as well on a specific test bench (See Figure 10) in order to investigate the nonlinear response of the system, tested under a contact pressure of up to 1MPa. By comparing experimental and numerical nonlinear responses, the sensitivity of the system response to the contact interface stiffness is investigated.

In a first phase, the two different stiffness-pressure laws have been defined starting from the literature and specific experimental tests, dedicated to the determination of the contact stiffness at different values of the contact pressure.

Then, experimental and numerical simulations of an impulsive excitation of the system have been carried on. The confrontation of numerical results with experimental measurements allow validating the numerical model on one hand. On the other hand, exploiting the developed model allowed evaluating the impact of the compression stiffness, especially for low-pressure range, on the NL signature of the contact law. This result can be valuable when it comes to interface characterisation. (See Figure 62)

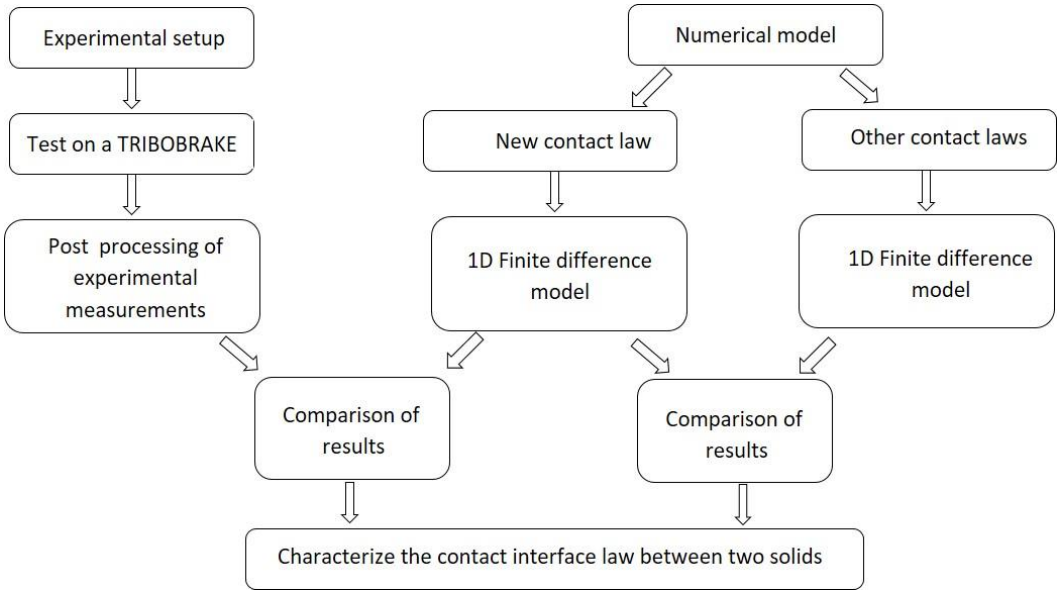

Figure 62 Approach of chapter 4

4.2 New contact law: Modified Power-Law

As a first step, the nonlinear stiffness-pressure laws to be tested have been defined. It should kept in mind that the model used in this study is a one-dimensional model containing two contacting interfaces (see section 2.4 of chapter 2). For both interfaces, the nonlinear contact law is introduced. This law includes a nonlinear stiffness as a function of the contact pressure. The experimental results presented in Table 2 are useful for defining the numerical contact stiffness within the tested range of contact pressures. The procedure describing the measuring of the contact stiffness is presented in section 2.2.1 of chapter 2. The material sample is in aluminium. Nevertheless, for implementing the contact law in the numerical simulations, it is necessary to define the stiffness for the whole pressure range [0; 1 MPa], in which the contact pressure will vary.

A first approximation within this pressure range is obtained by approximating the experimental measurements by a power law function [90] expressed by

$$C_N = \mathrm{C}\sigma^m \qquad 4.4$$

The least squares method allows having a good agreement with the experimental data (Table 2), which are available starting from a pressure of 0.14 MPa. This agreement is obtained for

C=1.81 x10^{10} Pa/m and m=0.35. The power law ("PL" in Figure 63 (a)) is thus defined to approximate the experimental points (Table 2).

While this power law has been built giving consideration to the measurements and the literature dealing with higher pressures, the approximation of the trend at lower pressures is completely arbitrary. In order to model the contact stiffness trend for lower contact pressures, other experimental observations in the literature [6] have been exploited. These experimental results showed the existence of an inflexion point for low contact pressures (Figure 63 (b)). From experimental results (Table 2) and the literature [6], it is then possible to propose a different overall contact stiffness trend, as a function of the contact pressure, including the inflection point between 0.14 and 0 MPa ("Modified PL" in Figure 63).

The goal is to investigate the stiffness-pressure dependence by exploiting the nonlinear contribution of such trend into the system dynamic response. While the trend at high pressure has been fixed by the experimental results, two different trends at low pressure are investigated in parallel, in order to verify the sensitivity of the system response to this branch of the stiffness-pressure curve.

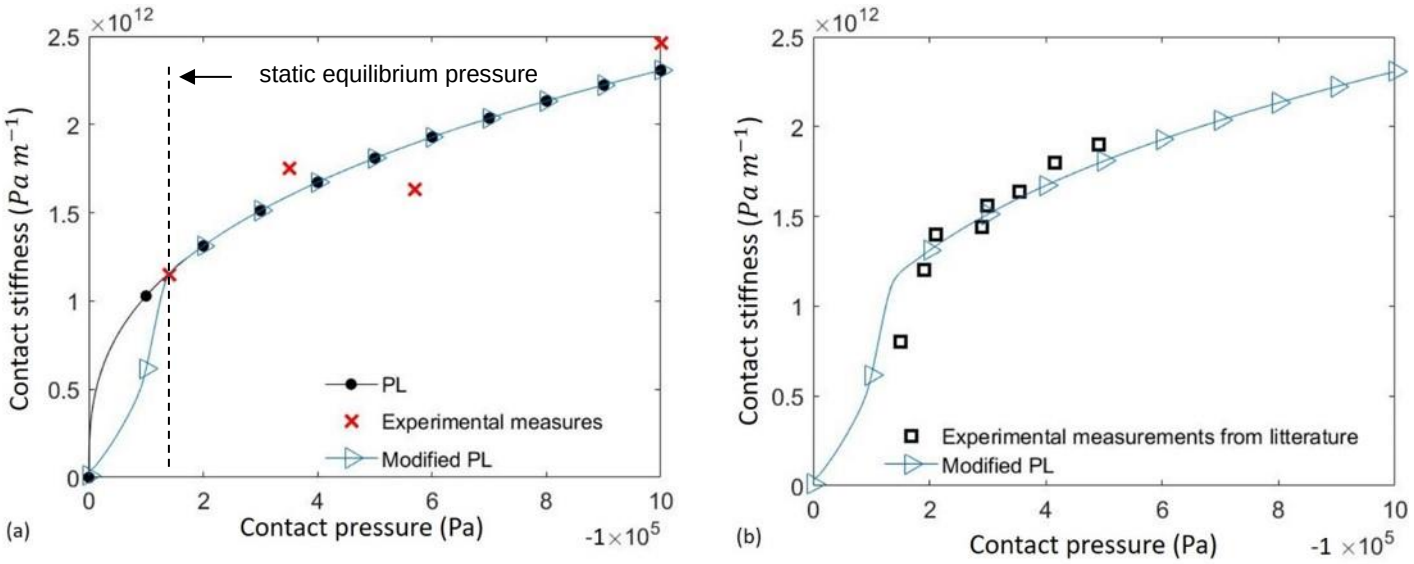

Figure 63. Normal contact stiffness as a function of contact pressure in compression conditions. (a) Experimental results (red cross), Modified PL (blue triangle) and PL (black circle); (b) Modified PL (blue triangle) and experimental data from literature** [6] **(black square)

Finally, the stiffness laws, which will be investigated in the following, are:

- The "PL" law, corresponding to the best approximation of experimental data (Table

2) by a power law.

- The “Modified PL”, defined piecewise. It is equal to “PL” for pressures greater than 0.2 MPa, and for lower pressures, it accounts for the inflexion point reported in [6].

The relationship between the contact pressure and the interfacial gap can then be extracted from the implemented nonlinear relation between stiffness and pressure. For example, the results derived from the “Modified PL” are shown in Figure 64, highlighting the nonlinear response of the interface.

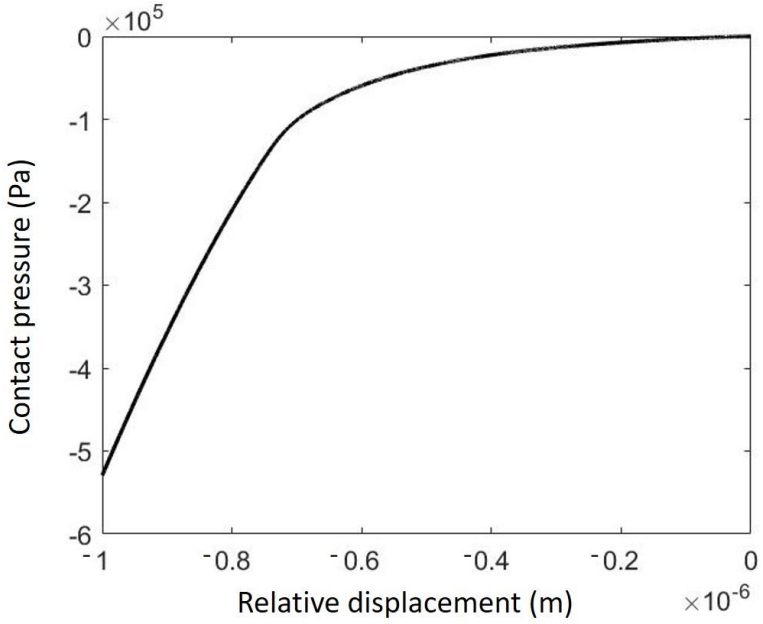

Figure 64. The corresponding contact pressure-relative displacement trend for the ‘Modified PL’.

In the following, the experimental nonlinear response of the system to an impulsive excitation force will be compared with the nonlinear response obtained by the simulations with the different analysed laws. The comparison will allow for a discussion of the different considered laws to simulate the effective interface stiffness nonlinearity.

4.3 Experimental and numerical comparison

4.3.1 Dynamic response of the contact system

The aim of this section is to compare the numerical and experimental nonlinear dynamic responses of the system (Figure 12) to an impulsive excitation, in both time and frequency domains. For the sake of conciseness, the comparison of the time signals with the experiments is first reported only for the "Modified PL"; then, in the following sections, the general results obtained by both the laws will be compared with the experiments.

Experimentally, the test bench, presented in Figure 65, has been used, with an aluminium sample introduced between the disc and the guide. For more details, readers can refer to section 2.2.1 of chapter 2.

Figure 65 **Diagram (a) and numerical model (b) of the set-up.**

An impulsive force was applied to the upper side of the guide by an instrumented hammer (PCB Piezotronics-086C03). The case presented hereafter corresponds to an impulsive force of 32 N. The applied force and the acceleration are measured and shown in Figure 66 (a) and (b), respectively. For the numerical model, the measured experimental force has been interpolated (see Figure 66 (a)) and introduced as a boundary condition in the numerical simulation. The "Modified PL", has been used to simulate the system response to the impulsive force.

Figure 66 (b) shows the respective experimental and numerical accelerations, due to the dynamic system response.

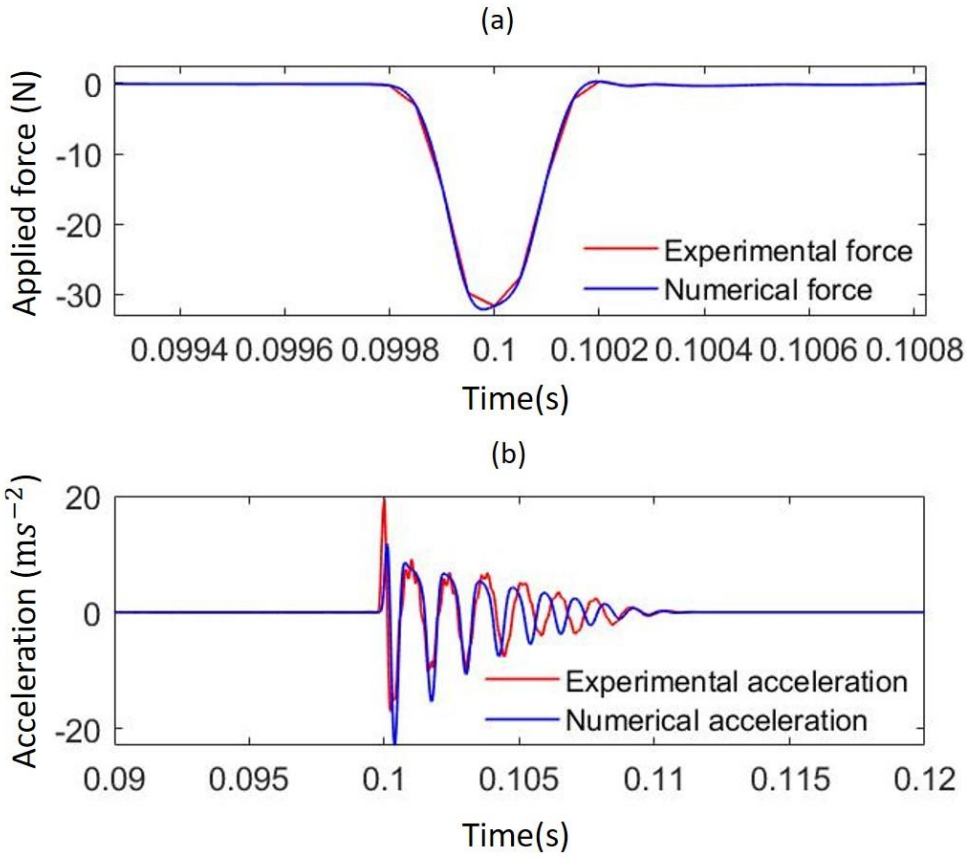

Figure 66. (a) Force signals over time, for a single force and (b) acceleration signals over time obtained with 'Modified PL'. Test performed with maximum contact force of 32 N.

Experimental and numerical responses show good agreement in amplitude and time evolution. Figure 67 shows the Frequency Response Functions (FRF) [91], which provide the response of a system to an external excitation in the frequency domain. They are calculated from both numerical and experimental signals, to characterize the dynamics of the system. The numerical curves shown in Figure 67 correspond to the one obtained with a constant interface stiffness of 8.5 x10^{11} Pa/m (dashed line) and the one obtained with the "Modified PL" presented in Figure 63. The equivalent constant stiffness of 8.5 x10^{11} Pa/m was calculated to obtain the same frequency for the first harmonics of the "Modified PL", to highlight the nonlinear contribution of such pressure-stiffness dependent law on the system response.

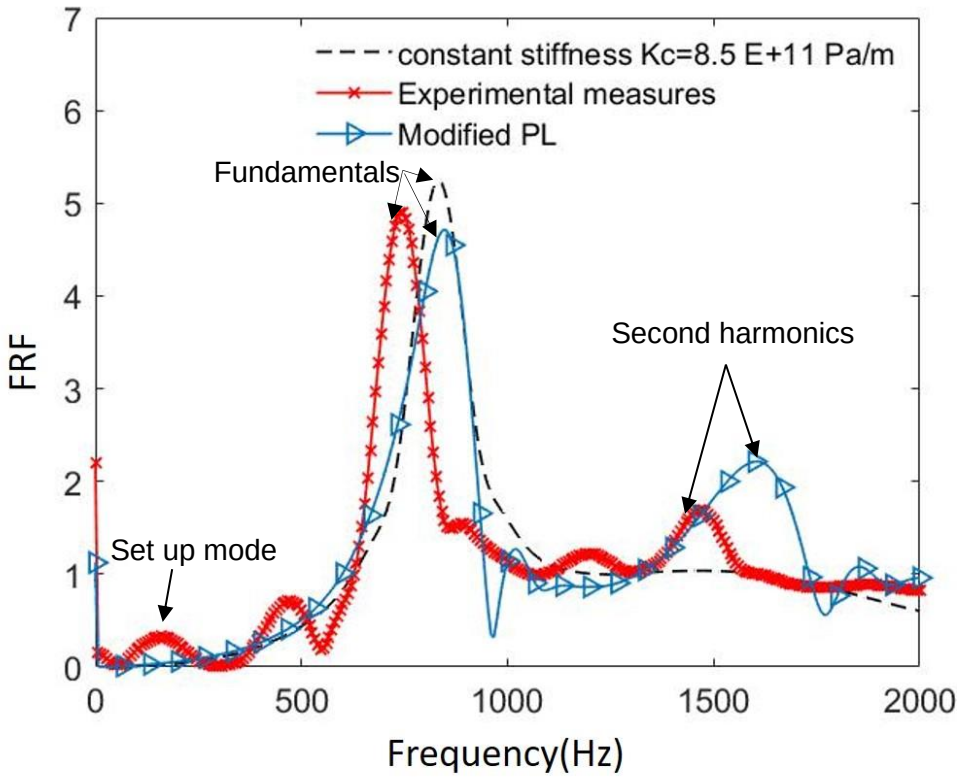

Figure 67. FRFs of the system (receptance, displacement/force). Numerical with nonlinear stiffness (blue triangle), numerical with constant stiffness with C_N=8.5 x1011 Pa/m (dashed line) and experimental (red cross). Test performed with average contact force 32 N.

Only the fundamental (f~800 Hz) and second harmonics (f~1600 Hz) of the mass-spring mode are investigated here. Their results are well decoupled from the rest of the system dynamics, with the next mode of the system with normal component of the displacement being the longitudinal mode of the guide, at about 11 kHz.

The numerical spectra, obtained with either constant or nonlinear stiffness, show a peak around frequency f_1=800 Hz, corresponding to the fundamental frequency of the system mode. This is the natural frequency of the mass-spring mode, where the mass is the guide, while the spring is the series of the two interfaces and the sample stiffness (Figure 65). The comparison shows a good agreement between the numerical and experimental results in terms of frequency and width of the peaks, i.e. damping. The amplitude of the fundamental is well simulated as well, with percentage error less than 10%.

Unlike the spectra obtained with the linear stiffness, the one based on nonlinear stiffness ('Modified PL') show a peak around frequency f_2=2f_1=1600 Hz, which is also recovered experimentally. This peak represents the second harmonic and correlates with the experimental second harmonic.

The presence of the second harmonic in the spectra is due to the nonlinear nature of the contact stiffness. This is confirmed by the absence in the numerical results obtained with the linear

contact stiffness (Figure 67 in dashed line). The occurrence of the second harmonic in experiments can be then correlated with the nonlinearity of the interface stiffness. This correlation is exploited in the following for investigating the representativeness of the studied contact laws on the nonlinear dynamic response of the system.

4.3.2 Nonlinear response of the interface

In order to discuss the proposed trends of numerical contact stiffness, the nonlinear response of the system, directly affected by this factor of nonlinearity, is investigated. A spectrum analysis of the acceleration signals is reported in this section, as a function of the amplitude of the impulsive force, to evaluate the nonlinear contribution of the contact law into the signals and compare with the same signals directly retrieved by the experiments.

It is assumed that an increase in the force, and then in the system response, increases the nonlinear contribution of the interface to the system response. A comparison of experimental and numerical FRFs, derived from the 'Modified PL', is first carried out for different impulsive force amplitudes, ranging from 9N to 32N (Figure 68).

When increasing the force amplitude, the overall average stiffness at the interface decreases, leading to a decrease in mode frequency (Figure 68), both experimentally and numerically. The nonlinearity of the interface stiffness is observable by the appearance of the second harmonic (frequency between 1400Hz and 1800Hz, depending on the amplitude of the impulsive force) in the system response.

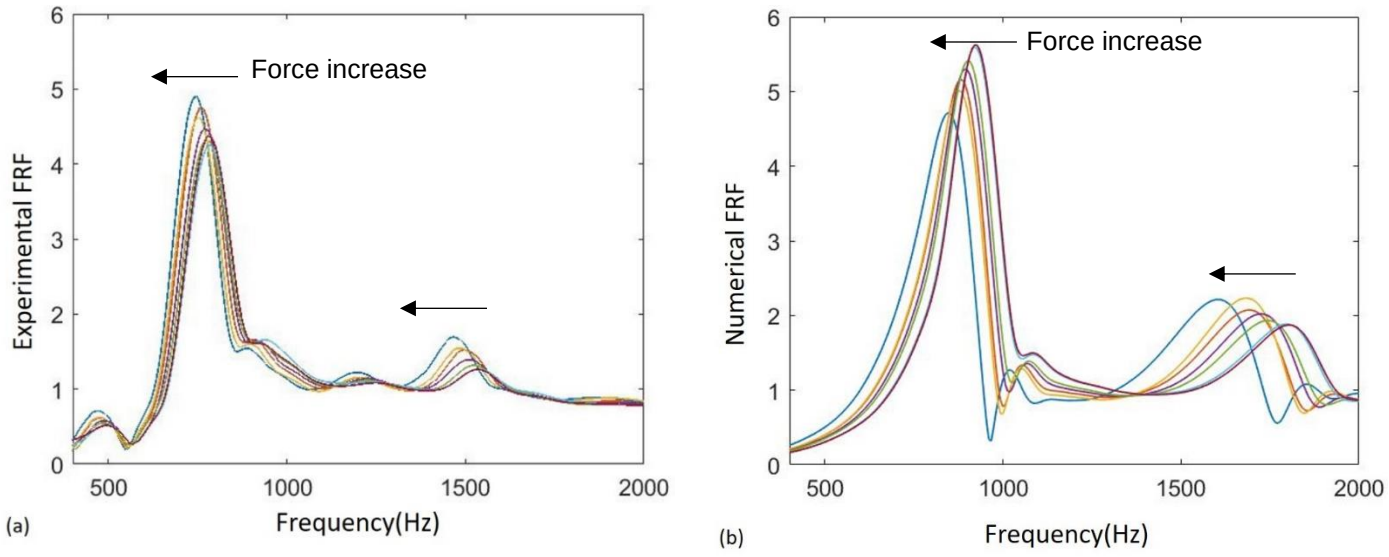

Figure 68. FRFs of the system (receptance, displacement/force). (a) Experimental frequency response and (b) Numerical frequency response plotted with 'Modified PL'. Tests performed with average contact force ranging from 9N to 32 N.

In the following, the numerical results obtained with the different contact laws, presented in Figure 63, are compared with the experimental results in terms of the magnitude of the fundamental and second harmonics, as well as in terms of the frequency of the fundamental one, as a function of the applied force.

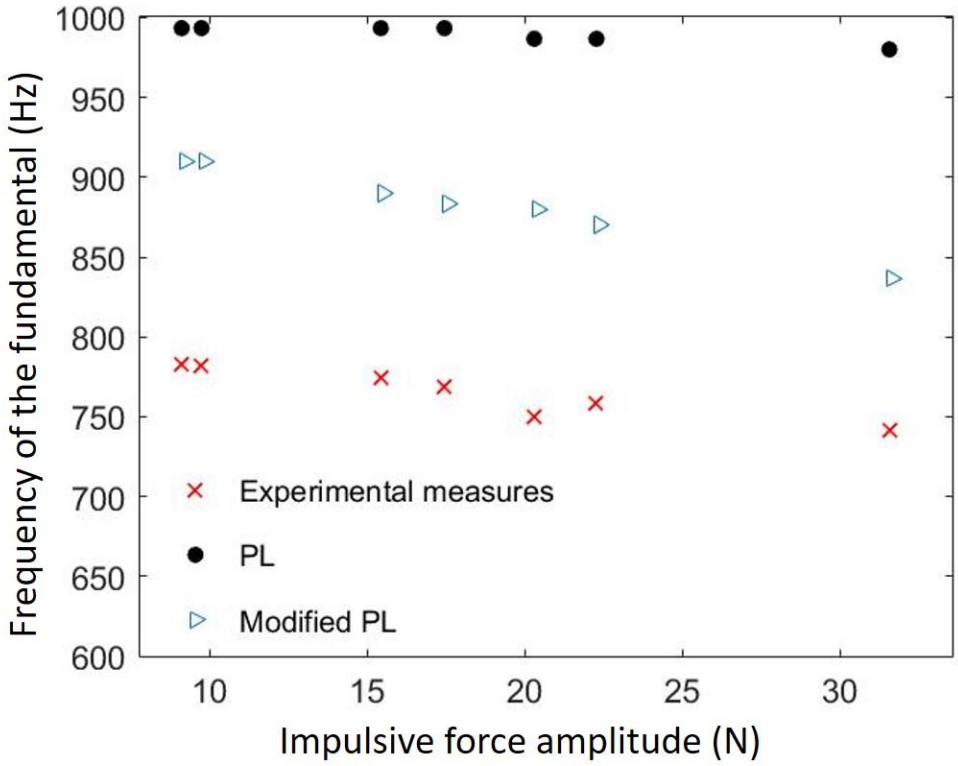

Figure 69. Frequency of the fundamental, as a function of the force amplitude [N]. Experimental measurements (red cross), PL (black circle) and Modified PL (blue triangle).

Figure 69 shows the frequency evolution of the fundamental harmonic as a function of the amplitude of the applied force. As observed in the experimental results, a decrease in frequency was obtained in the numerical simulations with the implemented 'Modified PL'. This decrease is due to the decrease in the effective average stiffness when the oscillation amplitude at the contact increases. Experimentally, this trend has already been observed in [26]. It is worth mentioning that the decrease in frequency when the force amplitude increases (Figure 69) is also recovered by the "PL", but with a lower slope. A slight decrease in frequency (2%) can be observed, in Figure 69 for the "PL", which is lower than for the experimental one (5%). Conversely, because the "Modified PL" introduces a greater decrease

in terms of stiffness, particularly for low contact pressures (as shown in Figure 70 (b)), the decrease in frequency, with the increase of the impulse amplitude, results to be closer to the experimental one.

It should also be noted that, while the trend of the frequency is correctly simulated by the proposed laws, an error in the absolute value of the frequency, around 13%, is observed. This is due to the non-infinite stiffness of the counterpart in the experimental system (tribometer disc), unlike the infinite stiffness in the simulation, which implies a lower experimental frequency. Thanks to the numerical results, the decrease in the frequency of the fundamental can be shown to be related to a decrease in the mean value of contact stiffness, with the increase in the applied force. The mean values of the contact stiffness during the system oscillation has been calculated as the sum of the absolute values of the stiffness C_N at each time step divided by the time of simulation T:

$$C_{N_{avr}} = \frac{1}{\mathrm{T}} \sum_{t=0}^{\mathrm{T}} |C_N(t)| \qquad 4.2$$

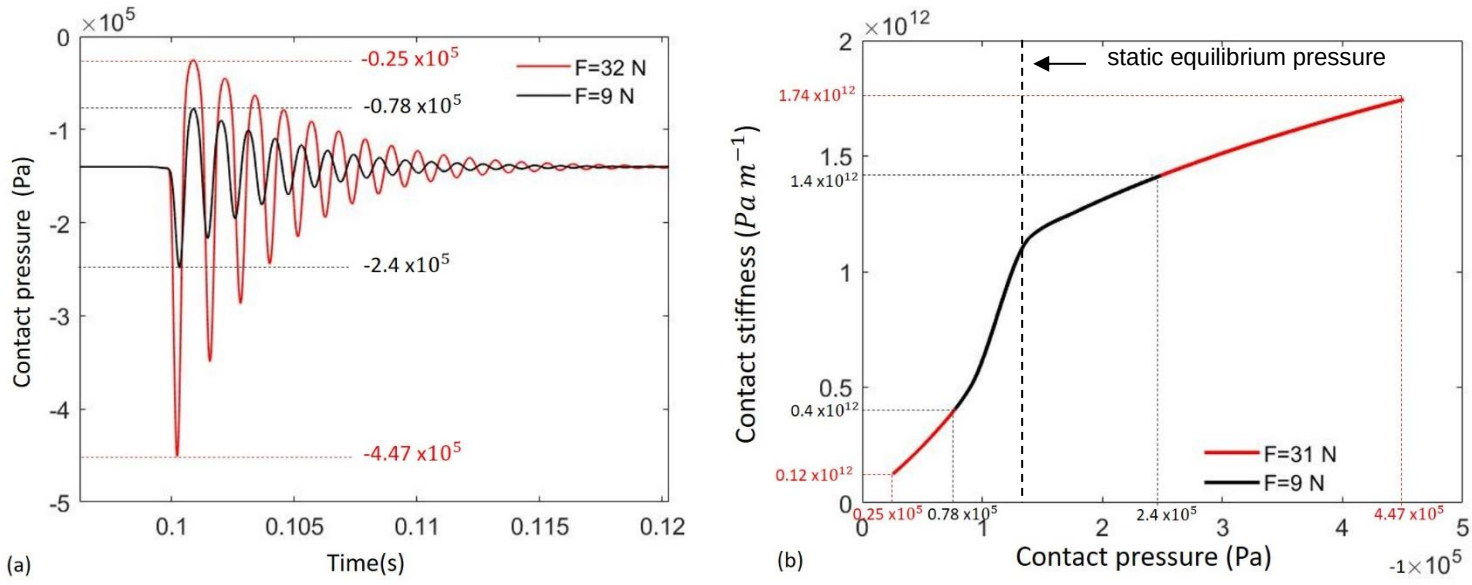

Figure 70. Numerical results for maximum force F=32 N (red) and minimum force F=9 N (black). (a) Numerical contact pressure as a function of time; (b) Numerical stiffness as a function of contact pressure. Test performed on aluminium with Modified PL.

In order to highlight the difference in average stiffness according to the force amplitude, Figure 70 (a) shows the system response to two different force amplitudes, using the "Modified PL". An applied force of 9 N generates a maximum contact pressure of -0.078

MPa, resulting in an average contact stiffness of 0.4 x10^{12} Pa/m, while a force of 32 N generates a maximum contact pressure of -0.025 MPa and an average contact stiffness of 0.12 x10^{12} Pa/m.

Figure 71 shows the evolution of average contact stiffness $C_{N_{avr}}$ for the 'Modified PL' and the 'PL'. The retrieved mean stiffness, for the two respective contact laws, confirm the decrease in average stiffness when the applied force is increased, which explains the decrease in frequency (Figure 69), and get closer to the experimental results for the 'Modified PL'.

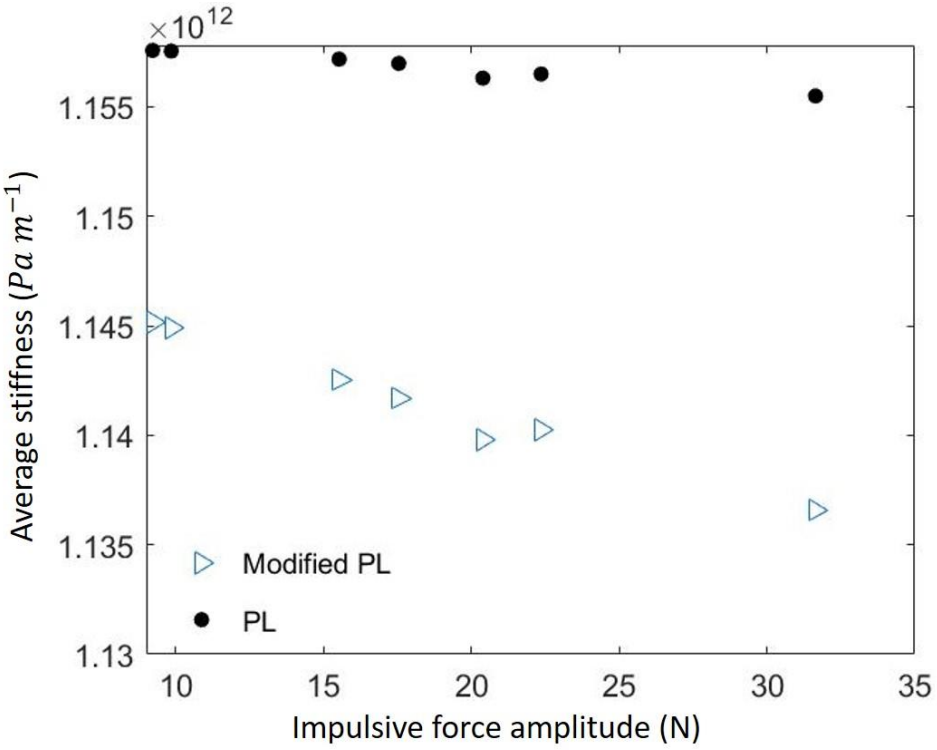

Figure 71. Average contact stiffness as a function of the applied forces. Test performed with average contact force ranging from 9 N to 32 N, with Modified PL (blue triangle) and PL (black circle).

Figure 71 shows the evolution of the amplitude of the fundamental harmonic, as a function of the applied force, for both the experiments and the different contact laws.

Considering the mean value of the fundamental harmonic over the considered range of pressure, the 'Modified PL' produces amplitudes closer to the experimental ones, for this set of experimental measurements.

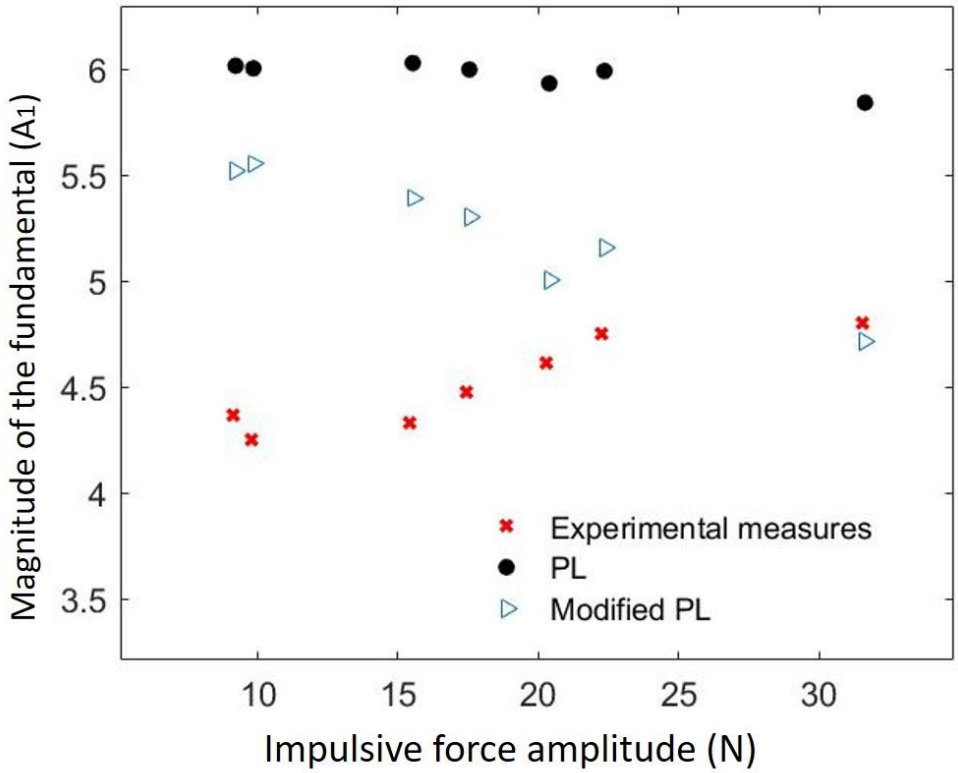

Figure 72. Magnitude of the FRF of the fundamental A1, as a function of the force amplitude. Comparison of the contact laws. Experimental measurements (red cross), Modified PL (blue triangle), and PL (black circle).

Nevertheless, as shown in Figure 72, for both of the implemented laws, the slight experimental increase in the amplitude of the fundamental harmonic (A_1), with respect to the force amplitude, is not retrieved numerically. As mentioned above, this could be explained by the different boundary conditions between the numerical and experimental systems. In fact, the experimental set-up is not completely rigid, due to the deformability of the bench components (disc, shaft, bearings, etc.). Despite using a massive disc to isolate the dynamics of the investigated system (air guide and samples in contact) from the rest of the set-up, as much as possible, a slight error is introduced by the residual flexibility of the system. This flexibility could results as well in a higher response amplitude when increasing the impulsive excitation.

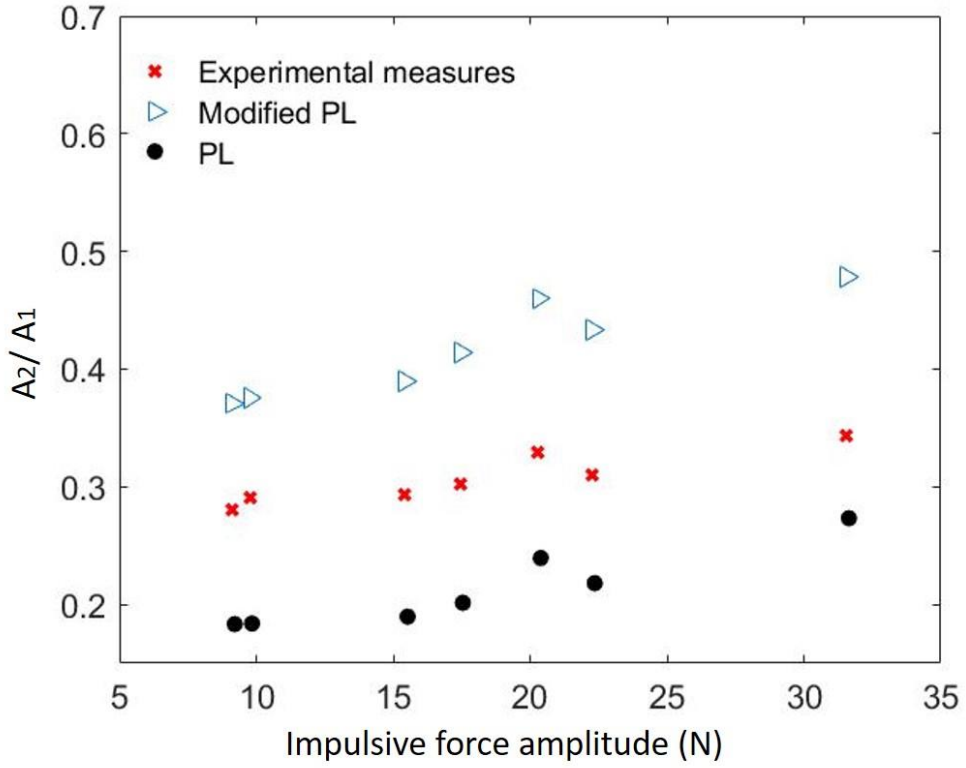

Figure 73. Ratio of magnitudes of the FRF of the second harmonic (A_2) to fundamental (A_1), as a function of the force amplitude. Experimental measurements (red cross), Modified PL (blue triangle) and PL (black circle).

Finally, Figure 73 shows the ratio (A_2/A_1) of the amplitudes of the second harmonic (A_2) to the fundamental one (A_1), obtained both experimentally and numerically, for both contact laws. It can be noted that the amplitude of the second harmonic is normalized by the amplitude of the fundamental, which depends on the energy introduced by the external force at this frequency, in order to highlight the nonlinear contribution originated by the contact interface. The trends of the A_2/A_1 ratio, calculated for all the tested contact laws, are similar to the experimental trend. In general, an increase in the amplitude of the applied force (*x*-axis in Figure 73), and consequently a higher amplitude of the system vibrational response, generates a greater nonlinear contribution, both numerically and experimentally. In fact, a larger oscillation of the contact pressure (especially within the low-contact pressure range, absolute value [0; 0.14 MPa]) generates a more nonlinear response by the system, which leads to a higher distortion of the signals and then a higher second harmonic contribution. Moreover, the higher amplitude observed for the second harmonic of the 'Modified PL' is due to the higher nonlinearity of the stiffness around the equilibrium position, with respect to the 'PL'.

It is also noted that the overall trend of ratio (A_2/A_1) for the different numerical results as well as the experimental measurements is increasing with the applied force. However, different behaviour, corresponding to a decrease in (A_2/A_1), is obtained when passing from an excitation of $F_1 = 20$N to $F_2 = 23$N. This can be explained by analysing the time signals (see Figure 74) of the corresponding impulsive excitation measured experimentally and introduced into the simulation. In fact, as shown in Figure 74 (b), the Fast Fourier Transform spectra of the two forces show that the FFT of F_1 is greater than the one of F_2 for a frequency of 800 Hz. This latter frequency refers to the frequency of the fundamental harmonic. Thus, the force F_1 generates more energy at the interface than F_2 resulting in higher second harmonic value.

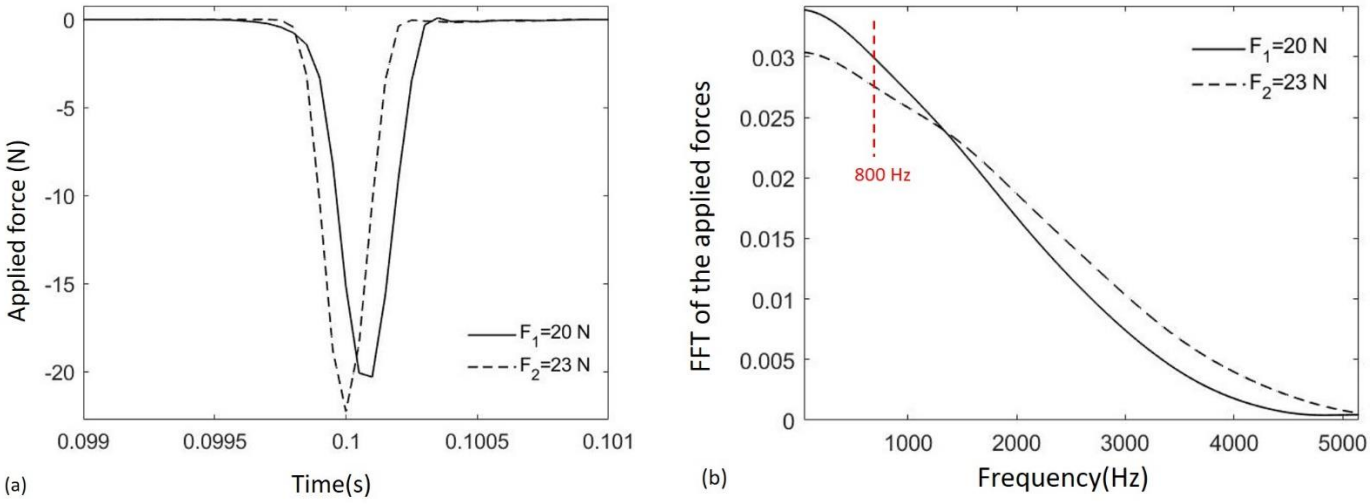

Figure 74. Experimental forces and corresponding ffts.(a) forces over time. (b) Measured ffts. Test performed on aluminium with surface roughness of Ra=1μm. Two forces are applied $F_1 = 20$N N and $F_2 = 23$N.

The overall comparison, based on the analysis reported in this Chapter highlights the fact that the contact interface response depends heavily on the stiffness trend at lower pressures (less than 1MPa). The different stiffness trend at lower pressures, introduced by the 'Modified PL', increases the nonlinearity of the response (second harmonic amplitude) and decreases the average stiffness, i.e. the frequency of the main harmonics.

These results demonstrate that the stiffness trend at lower pressures plays a vital role and should be clearly identified, as it has a huge effect on the nonlinear response of mechanical systems with contact interfaces.

4.4 Concluding remarks

The nonlinear normal stiffness of contact interfaces, due to surface roughness, is a topic of major interest in several areas of application. A consequence of such nonlinearity is the affecting of second harmonic terms, either in acoustic wave propagation through the interface or in the dynamic vibrational response of systems with contact interfaces. For this reason, this Chapter focused on this specific nonlinearity, in the compression phase of the contact, to be added into the nonlinear contact law.

While contact stiffness nonlinearity at higher pressures has been widely discussed in the literature, and generally approximated by a power law, the contact stiffness trend at lower pressures has not been clearly identified. In this chapter, a classical power law, fitted from experimental data at high contact pressures, has been compared with a modified power law implementing an inflection point at lower pressures, where experimental data are not available. The stiffness-pressure trend within the higher contact pressure range was approximated from experimental measurements performed on a dedicated test bench. Within the lower contact pressure range, data from the literature was used to assume the different possible trends.

The nonlinear response of the system, obtained experimentally when exciting a dedicated system with an impulsive force, was analysed and compared with the nonlinear response of the numerical model, where the different contact interface laws have been implemented.

From the numerical simulations, it was possible to identify the effect of the contact nonlinearity on the dynamic response of the system. The decrease in the average contact stiffness with the increase in the impulsive force explains the appearance of the second harmonics and the decrease in the fundamental frequency. In addition, the amplitude of the second harmonic was simulated and explained by the stiffness trend at the contact interface during the system oscillations.

By the comparison with the experimental nonlinear response of the system, the key role of the contact stiffness trend within the lower pressure range has been highlighted, demonstrating the need to identify such parameters with dedicated experimental tests.

Overall, the nonlinear stiffness described in this chapter aims to represent the compliance introduced by rough surface asperities during compression, which has been experimentally observed. However, this law does not describe the adhesion phenomenon corresponding to a loss of contact and is thus limited to cases where the interface remains in contact. By contrast, the RCCM contact studied in chapter 3 describes the interface adhesion during contact loss, but considers an infinitely rigid contact in compression, limiting the validity to perfectly

smooth interfaces. Therefore, these two latter laws are complementary and hence will be combined in the next chapter.

Chapter 5: Contact law in compression and traction

So far, the effects of introducing contact stiffness in compression or traction have been studied separately in different contexts. On one hand, the 'Modified PL' (studied in chapter 4) has proved to be effective in describing a real interface behaviour in compression. In fact, the experimental test-bench used for that study is adapted to the compression tests, but it is difficult to open the interface in the corresponding context. This study supported our choice of a nonlinear model to describe the compression behaviour. On the other hand, the RCCM contact law (studied in chapter 3) introduces adhesion through a damageable stiffness in traction and an infinite rigidity in compression. Yet interesting and sufficient for several studies, in the majority of real cases, asperities and third body at the contact interface introduces a compression stiffness as well. Herein, we present an overall approach for modelling the nonlinear scattering induced by a contact interface by combining the two latter laws: 'Modified PL' in compression and RCCM contact law in traction, with the aim of capturing both the weak nonlinear response of a rough interface and the strong nonlinear response of a "clapping" interface. This association of nonlinear behaviours is absent from the literature and the study of its effect on the wave-interface interaction would make it possible to complete the previous studies in the nonlinear contact framework e.g. the classical work of Richardson for unilateral contact of smooth interface [13], and of Meziane and Blanloeuil [37] and other [23] [92]. Therefore, this chapter aims to set up and validate the numerical model, presented in paragraph 2.3.2 of chapter 2, and to give the first elements of understanding concerning the effects of this association on the generation of second harmonics.

The presentation is organized as follows. The wave scattering configuration is formulated in section 5.1, detailing the particular contact model used to describe the interface behaviour. The governing equations to introduce the analytical solution for the particular case of bilinear law are established in section 5.2. The analytical solution is then used to validate the numerical model and provides important information on the parameters influencing the opening and closing of the interface in this configuration. Results from the numerical simulations and discussion are featured in section 5.3.

5.1 Wave scattering configuration

In order to study the interface behaviour in both traction and compression, the model containing a semi-infinite medium in contact with a rigid wall is considered, as shown in Figure 75. A normal incidence longitudinal plane wave is generated at *x=-L*. It propagates in Ω and interacts with the contact interface at *x=0*, where the RCCM law is imposed in traction and a normal nonlinear stiffness is introduced in compression. Note that the static pressure $p_0 \geq 0$ is imposed in Ω and consequently at the interface too. For more details, the reader can refer to paragraph 2.4 of chapter 2.

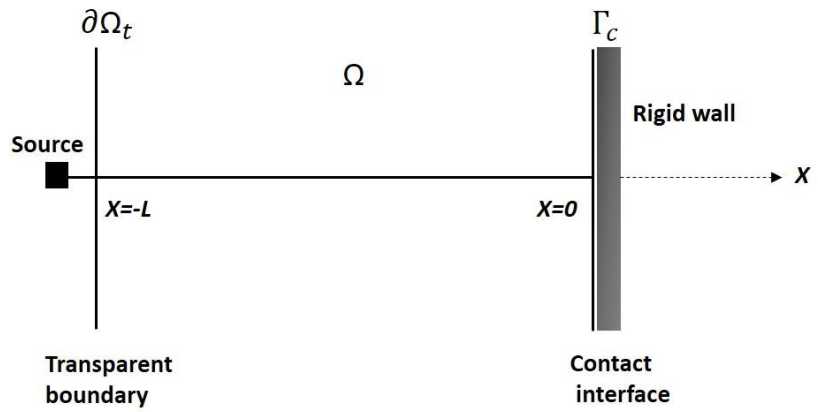

Figure 75 1D Configuration of the propagation of a plane wave through a contact interface located at x=0. L=3m.

$[u]$ denotes the relative displacement between the solid and the rigid wall. In this case

$$[u] = -u(x = 0, t) \qquad 5.1$$

where u is the displacement of the solid. Note that the interface is open when $u(x = 0, t) < 0$ or [u]>0.

The contact pressure is denoted $\sigma(t)$ and the relation between the contact pressure and the relative displacement is described by a contact law that provides the necessary boundary conditions for solving the reflexion problem.

Previous works used a contact law corresponding to unilateral contact in traction and power-law in compression. For more details, readers can refer to [37]. The nonlinear spring introduced in compression aims to represent the nonlinear compliance introduced by rough surface asperities during compression, which has been observed and reported in the literature [36] [19] [92]. However, this latter law introduces a traction-free condition during the loss of contact, which is the case when no adhesion occurs at the contact interface. Nevertheless, in some configuration, or for particular couple of materials in contact, adhesion can occur. This can be described by an interface that is gradually damaged before it is completely peeled off.

As discussed previously in section 1.2.2.4 of chapter 1, the RCCM contact law, using a damageable stiffness of the interface, is well adapted to take into account this evolutive behaviour (Figure 76 (a)).

In compression, the modified power law ('Modified PL') is here introduced. The stiffness-pressure trend, within the higher contact pressure range, was approximated with a power law function [26], whereas, for the lower contact pressure range, data from the literature [6] [34] was used and the presence of an inflexion point in the contact law is assumed Figure 76 (b)). The two laws are complementary and are combined in the present work (Figure 76(c)).

The stress-strain relationship is characterized by a nonlinear stiffness C_{N1} as long as the stress remains negative. At the initial state, the contact pressure is equal to $\sigma_0 = -p_0$ at the interface. When the stress reaches zero, which is attained for a critical relative displacement $[u]_c$, the contact is lost. When the interface is in traction, while the contact pressure is lower than the elastic limit ($\sigma_{lim} = \sqrt{C_{N2}w}$), the interface in traction behaves similarly to a spring with stiffness C_{N2} . When the incident wave is sufficiently large, the contact stiffness starts to decrease until reaching zero. Then, the adhesion is totally broken and the classical Signorini problem is obtained in traction.

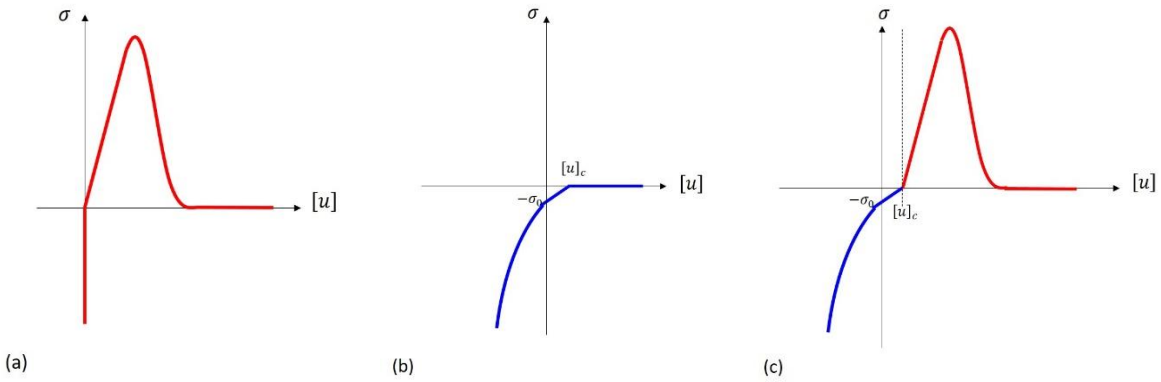

Figure 76 Graphical representation of the interface contact law. Graphical representation for (a) RCCM contact law, (b) Modified power law and (c) combination of modified PL in compression and RCCM contact in traction.

The material used for the modelled solid is PMMA (see Table 1 of chapter 2). The numerical solution to the latter problem is discussed in section 2.4.2 of chapter2. In the following, the purpose is to validate analytically the proposed overall numerical model of the interface, on the particular case of bilinear contact law, i.e. different stiffness values in compression and traction.

5.2 Validation of the numerical model

In this part, the numerical model is validated on the particular case of bilinear law. The semi-analytical solution of the contact problem is calculated first, with and without contact, for a sinusoidal incident wave. Afterwards, the numerical results are compared with the analytical solution allowing validating the latter.

5.2.1 Analytical solution for linear spring with and without contact loss

An incident sinusoidal wave $f(x-ct)$ is here considered:

$$f(x-ct) = Acos(\frac{\omega}{c}(x-ct)) \tag{5.2}$$

where A is a constant homogeneous to a displacement.

First, the expression of the stress $F(t)$ is defined as follows:

$$F(t) = -2Ef'(-ct) = -2\mathrm{A}\omega\rho\mathrm{c}\sin(\omega\mathrm{t}) \tag{5.3}$$

It is assumed that the contact is modelled by a linear spring in compression and a unilateral contact in traction; the corresponding stress at the interface is expressed as follows:

$$\begin{cases} \sigma(t) = -p_0 + C_{N1}[u] & if\ \sigma < 0 \\ \sigma(t) = 0 & if\ \sigma > 0 \end{cases} \tag{5.4}$$

According to the chosen contact law, there is contact as long as the contact pressure is negative $\sigma < 0$. Assuming that the interface is initially closed, there is detachment when the normal stress becomes zero. Knowing its expression, the time T_1, for which the contact stress becomes zero, should be determined. Above this value, the interface is open.

Similarly, the interface is detached as long as the displacement is positive. When it reach again the zero value, there is contact again. Knowing the expression of the displacement, it is thus enough to look for the instant T_2, which corresponds to the new contact phase. In order to determine the solution for the latter problem, the time interval will be reduced to one period $[0, T]$.

5.2.1.1 Without contact loss

If the incident wave amplitude is not large enough, the interface remains in contact and its behaviour is governed by a linear spring. The differential equation reduces to

$$[\dot{u}] + \frac{c}{E} C_{N1} [u] = -\frac{c}{E} F(t) \tag{5.5}$$

which admits the following solution:

$$[u] = \frac{2A}{\sqrt{1 + \left(\frac{\omega_1}{\omega}\right)^2}} \sin(\omega t - \Psi_1) \tag{5.6}$$

where the characteristic frequency of the interface is $\omega_1 = \frac{c}{E} C_{N1}$ and the phase shift is $\Psi_1 = \arctan\left(\frac{\omega_1}{\omega}\right)$. The reflected wave g can be determined from equation (2.3).

This linear solution allows defining the dimensionless load factor ξ. The contact loss occurs for a critical displacement $[u]_c$ for which the stress at the interface reaches zero:

$$[u]_c = \frac{p_0}{C_{N1}} \tag{5.7}$$

The corresponding critical incident wave amplitude A_c, required to cause contact loss, is obtained from the expression of the linear solution $[u]$:

$$A_c = \frac{p_0\sqrt{1+\left(\frac{\omega_1}{\omega}\right)^2}}{2\,C_{N1}} \qquad 5.8$$

Therefore, based on equation 2.7 and 5.8, the corresponding critical incident stress is $\sigma_i^c = p_0\sqrt{1+\left(\frac{\omega}{\omega_1}\right)^2}$ and the dimensionless parameter ξ, which expresses the ratio between the critical incident wave amplitude and the amplitude of the incident wave, is expressed as follows:

$$\xi = \frac{p_0\sqrt{1+\left(\frac{\omega}{\omega_1}\right)^2}}{\sigma_i^{max}} \qquad 5.9$$

For $\xi \geq 1$, the interface remains in contact. According to the Figure 77, the relative displacement [u], induced at the interface, is smaller than the critical displacement $[u]_c$ and the contact pressure is negative and oscillates around the pre-stress value $\sigma_0 = -p_0$. The interface is then completely closed and the wave is reflected linearly.

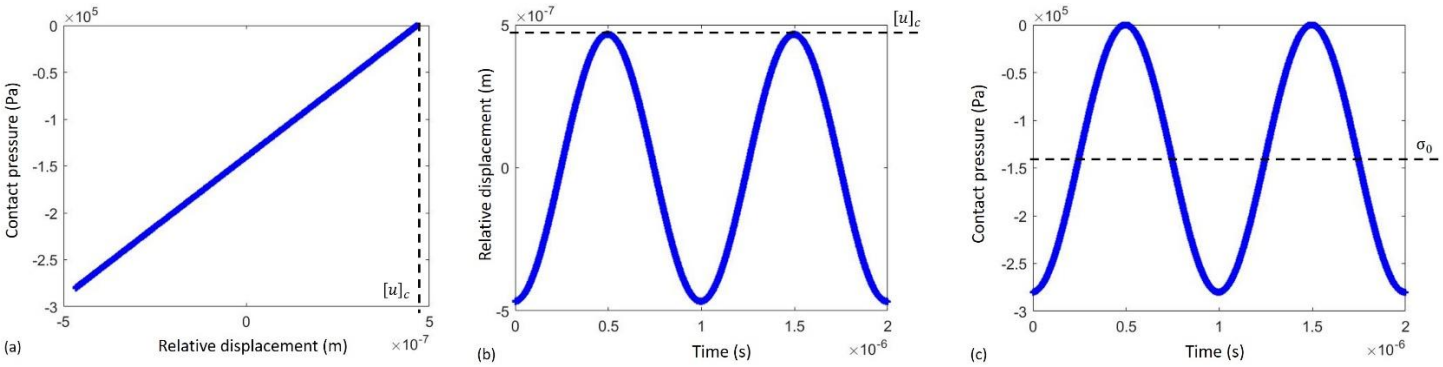

Figure 77 Analytical results for (a) contact pressure as a function of relative displacement, (b) Relative displacement at the interface over time and (c) Contact pressure over time obtained for a linear spring model with loss of contact. The incident wave frequency $f_0 = 1$MHz, static stress $\sigma_0 = -0.14$MPa, the stiffness is $C_{N1} = 3.10^{11}$Pa/m and the dimensionless parameter $\xi = 1$.

However, for $\xi < 1$, the incident wave is large enough to generate contact loss and hence the incident displacement exceeds the critical displacement $[u]_c$. The solution for the problem with clapping is determined in the next section.

Note that the ξ parameter depends on $\omega_1 = \frac{c}{E}C_{N1}$. For unilateral contact $\xi = \frac{p_0}{\sigma_i^{max}}$, which is coherent with the fact that C_{N1} tends toward infinity. The consequence is that the evolution of

second harmonic efficiency with ξ is not obtained for the same incident wave magnitude when changing the contact law in compression (i.e. varying C_{N1}).

5.2.1.2 With contact loss

When the incident wave is large enough, the interface behaviour alternates between compression and traction phases. In order to determine the solution for the latter problem, the time interval will be reduced to one period $[0, T]$. The contact is lost at T_1 and regained at T_2. In $[T_1, T_2]$, the stress cancels and hence the displacement satisfies the following equation:

$$[\dot{u}] + \frac{c}{E} C_{N2} [u] = -\frac{c}{E} F(t) \tag{5.10}$$

Similarly, to the previous case, this equation admits the following solution:

$$[u] = \frac{2A}{\sqrt{1 + \left(\frac{\omega_2}{\omega}\right)^2}} \sin(\omega t - \Psi_2) \tag{5.11}$$

where the characteristic frequency of the interface $\omega_2 = \frac{c}{E} C_{N2}$ and the phase shift $\Psi_2 = \arctan\left(\frac{\omega_2}{\omega}\right)$. This latter solution in equation 5.11 does not satisfy the initial condition:

$$[u(T_1)] = [u]_c \tag{5.12}$$

Accordingly, to ensure the continuity of the relative displacement, it is necessary to add to this solution a transient term corresponding to a solution of the homogeneous form of equation (5.10). This resolution leads to the following result:

$$\begin{cases} [u] = \dfrac{2A}{\sqrt{1 + \left(\frac{\omega_2}{\omega}\right)^2}} \sin(\omega t - \Psi_2) + \left([u]_c - \dfrac{2A}{\sqrt{1 + \left(\frac{\omega_2}{\omega}\right)^2}} \sin(\omega T_1 - \Psi_2) \right) e^{-\omega_0 (t - T_1)} \ for\ T_1 \leq\ t\ \leq T_2 \\ [u(T_1)] = [u]_c \end{cases} \tag{5.13}$$

Similarly, the solution given by equation (5.6) must satisfy the initial condition

$$[u(T_2)] = [u]_c \qquad 5.14$$

Therefore, for $t > T_2$, a transient term, corresponding to a solution of the homogeneous form of equation 5.10, is added. The solution is then given by:

$$\begin{cases} [u] = \dfrac{2A}{\sqrt{1+\left(\frac{\omega_1}{\omega}\right)^2}}\sin(\omega t - \Psi_1) + \left([u]_c - \dfrac{2A}{\sqrt{1+\left(\frac{\omega_1}{\omega}\right)^2}}\sin(\omega T_2 - \Psi_1) \right) e^{-\omega_1 (t-T_2)} \ \ for\ T_2 < t \\ [u(T_2)] = [u]_c \end{cases} \qquad 5.15$$

The analytical solutions obtained for a sinusoidal input are shown in Figure 78. We consider here the case where the pre-stress is $\sigma_0 = -0.14$ MPa.

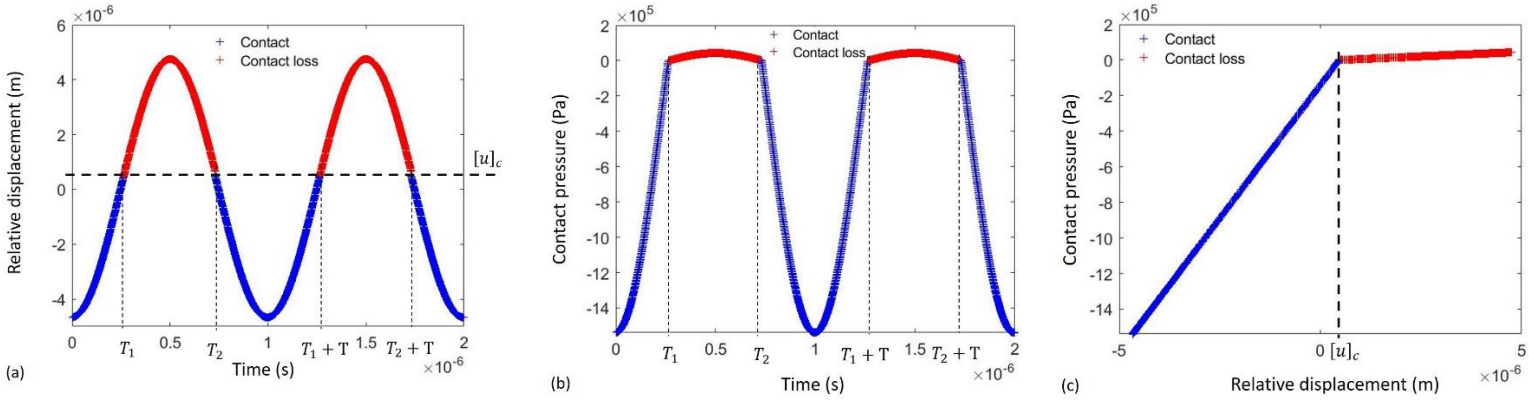

Figure 78 Analytical results for (a) Relative displacement at the interface over time, (b) Contact pressure over time and (c) Contact pressure as a function of relative displacement obtained for a bilinear spring model with loss of contact. The incident wave frequency $f_0 = 1MHz$, static stress $\sigma_0 = -0.14MPa$ and the stiffness is $C_{N1} = 310^{11}$ Pa/m and $C_{N1} = 10^{10}$ Pa/m

Intermittent contact is observed for the considered pre-stress σ_0, which is indicated in Figure 78 by the red curves, corresponding to the loss of contact. Once the critical displacement $[u]_c$ is reached, the interface is detached at $t = T_1$ and the interface behaviour is governed by a linear spring with a stiffness C_{N2} . It remains so until the relative displacement attains the critical displacement again at $t = T_2$. The contact pressure is then negative and the reflection is linear with stiffness C_{N1}. Based on these results, it is noted that the relative displacement and the contact pressure are two parameters that govern the nonlinear acoustic contact.

Figure 79 shows the duration of contact and contact loss phases as a function of the dimensionless parameter ξ.

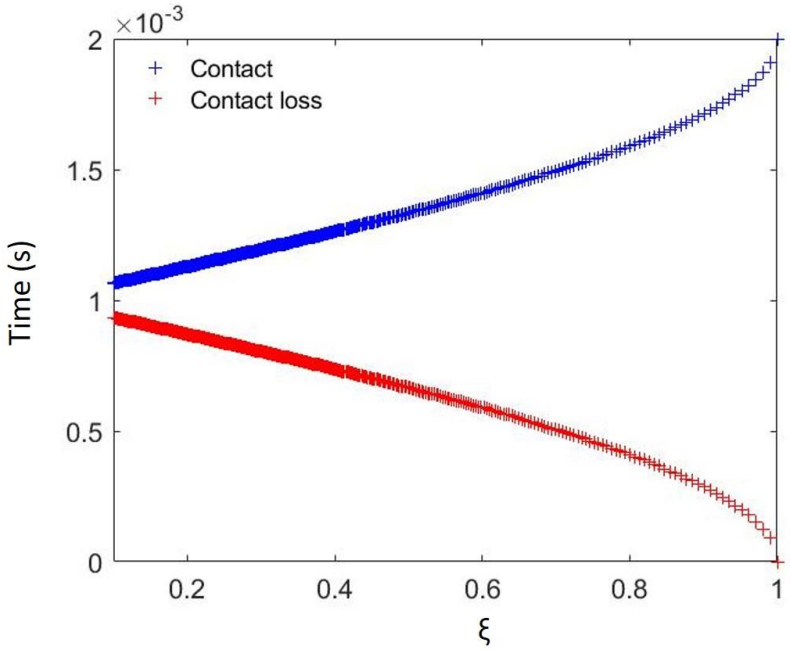

Figure 79 Evolution of the contact and contact loss durations as a function of the dimensionless parameter $\xi = \frac{p_0\sqrt{1+\left(\frac{\omega}{\omega_0}\right)^2}}{\sigma_i^{max}}$

For values of $\xi \geq 1$, the incident stress is not sufficient to generate contact loss and hence the interface remains in contact. By contrast, for $\xi < 1$, the incident stress is large enough to induce contact loss. The duration of each contact or contact loss depends on the incident wave amplitude. In fact, for smaller incident stress, the duration of each contact loss is progressively reduced while the duration of the contact is increased.

5.2.2 Numerical and analytical comparison

The periodic solution obtained by the semi-analytical resolution is used to validate the numerical resolution. Moreover, when verifying the convergence, this solution will be taken as a reference.

The solutions obtained by the two approaches are compared, for a compressive wave, in terms of relative displacement and contact stress. In the example reported in Figure 80, the incident wave frequency is $f_0 = 1$MHz and the system is submitted to a static pressure $p_0 = 0.14$ MPa.

The spatial resolution is such that the wavelength is discretized by 100 space steps. Finally, the computations are performed over a length domain $L = 3$m.

Figure 80 gives the relative displacements, as well as the pressure at the contact $x = 0$, obtained by the semi analytical method in dashed blue curves and by the numerical method in red continues line. Note that in the numerical resolution the incident wave is a 15-cycle pulse with a Hann window.

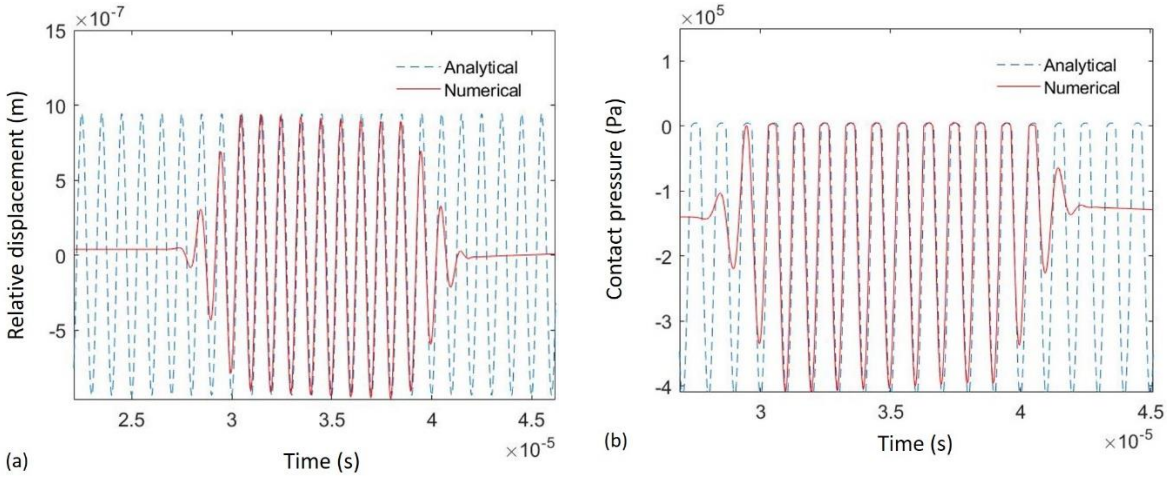

Figure 80 Numerical and analytical results for (a) relative displacement at the interface over time and (b) Contact pressure over time. These results are obtained for a bilinear spring model with loss of contact. The incident wave frequency $f_0 = 10^6$Hz, the static pressure $p_0 = 0.14$MPa and the constant stiffness: in compression $C_{N1} = 3.10^{11}$ Pa/m and $C_{N2} = 10^{10}$ Pa/m in traction.

It can be seen that the numerical response for the tone burst rapidly attains a 'steady state' that is in perfect agreement with the analytical periodic solution, validating the numerical simulation.

In order to verify the convergence of the FD model, the numerical solution is computed for a progressively finer discretization in space and time. As explained previously, the semi-analytical solution is used as a reference to validate the numerical solution. For a given space step, the time step is chosen such that $\delta t = 0.01\delta x/c$. The CFL condition is then respected and the ratio $c\ \delta t/\delta x = 0.01$ is constant. The relative error between the numerical results and the reference one (semi-analytical result) is given in Figure 81. The error is calculated over the maximum displacement.

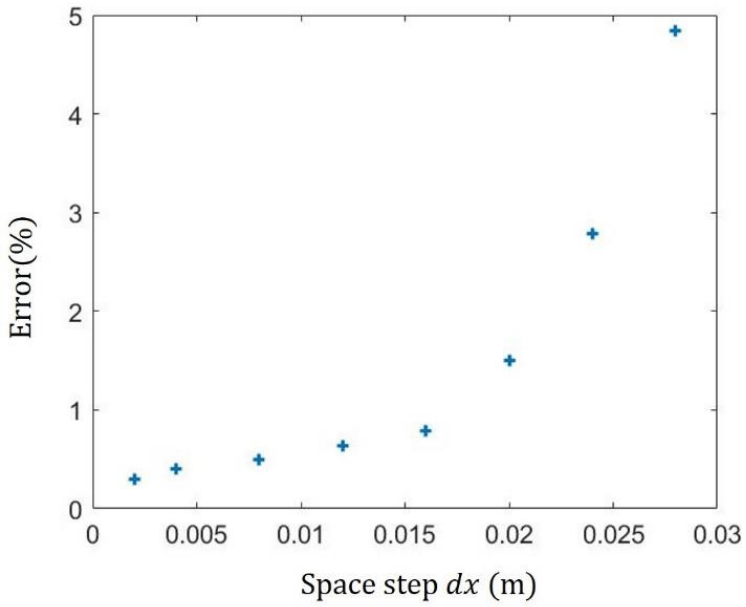

Figure 81 Relative error between the numerical and semi-analytical maximum displacements at the contact as a function of the space step for a longitudinal wave, whose wavelength is $\lambda = 0.4$m.

Figure 81 shows a good agreement between numerical and reference solutions, since the error is less than 5%. As the resolution of the mesh increases, the error decreases. Indeed, the numerical scheme converges.

To conclude, a unidimensional numerical model has been set up to study the reflection of a longitudinal wave on a contact interface, governed by a contact law introducing a nonlinear stiffness in compression and a damageable adhesion in traction. This model was validated with the analytical solution of the bilinear case, with and without contact. Convergence has been demonstrated with respect to the semi-analytical solution, taken as a reference.

In what follows, this 1D numerical model is used to study the interaction between a wave and the modelled of contact interface, in order to obtain information on the nonlinear phenomena related to the contact features.

5.3 Results and discussion

The incident wave is a 15-cycles tone burst, whose frequency is 5.10^3Hz, as shown in Figure 82. The rising and fading of the tone burst are defined by a half Hann window, covering ¼ of the pulse duration, as shown in Figure 82 (a). This tone burst excitation ensures a constant amplitude over several cycles.

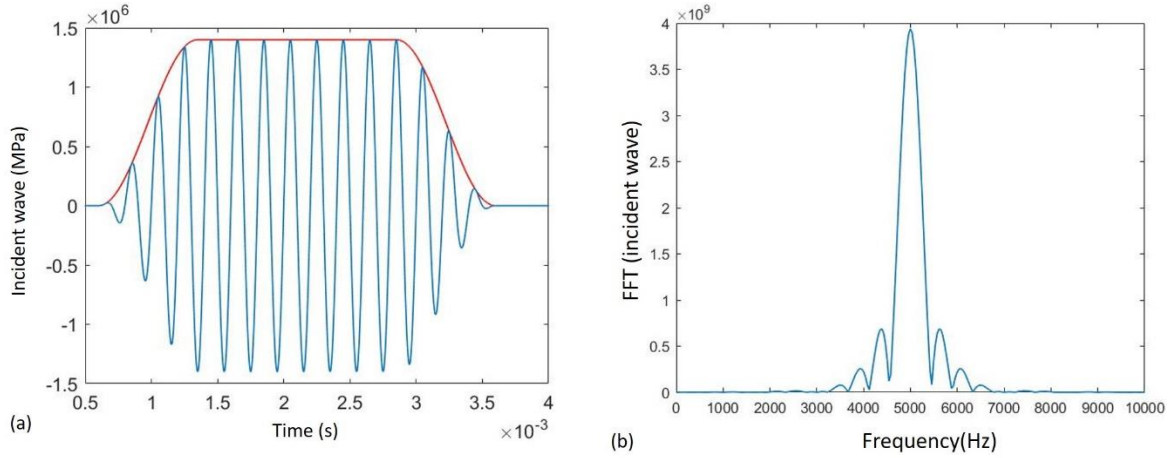

Figure 82 (a) Incident wave (case $\sigma_i^{max} = 1.4\ MPa$): stress generated in Ω over time measured at $x = -L$ and(b) Corresponding FFT of the incident wave. Note that the magnitude of the incident contact stress is double the amplitude of incident wave σ_i. Frequency $f = 5000\ Hz$. 15 cycles have been applied.

This part aims at investigating the dynamic response when introducing a stiffness in compression to a contact interface exhibiting "damaging" adhesion, during the interaction with a compressional wave. Two configurations of stiffness in compression are explored: linear stiffness (1) and nonlinear stiffness (2). These configurations are combined with an RCCM contact law in traction.

The analysis has been carried out in two parts. The first one concerns the impact of a linear stiffness in compression on the nonlinear signature of the interface. The second part is dedicated to investigate the effects of introducing a nonlinear stiffness ('Modified PL') on the nonlinear behaviour of the interface. This latter analysis has been developed first for an elastic/undamaged interface and then for a damaged one. The obtained results have been compared with the RCCM contact law and the unilateral contact, taken here as references.

5.3.1 Linear spring in compression

We consider first the case where the interface is described by a bilinear model with loss of contact. The stiffness in traction is fixed as $C_{N2} = 10^{10}$Pa/m, while the stiffness in compression is varied using three different values. $C_{N1} = 6.10^{11}$ Pa/m and $C_{N1} = 2.10^{11}$ Pa/m refer respectively to the maximum and minimum stiffness value measured experimentally in [26]. In fact, those measurements will be used to define the stiffness-pressure relation in the 'Modified PL'. $C_{N1} = 3.10^{11}$ Pa/m is an intermediate stiffness value. These different configurations of the bilateral law will be compared with the RCCM contact law as well as the

unilateral contact law. Figure 83 shows the evolution of the contact pressure as a function of the relative displacement, for the different contact laws. It can be observed that while increasing (in absolute value) the contact stiffness in compression, the contrast between the stiffness in compression and traction increases. Consequently, the transition from compression phase to traction would induce more nonlinearity.

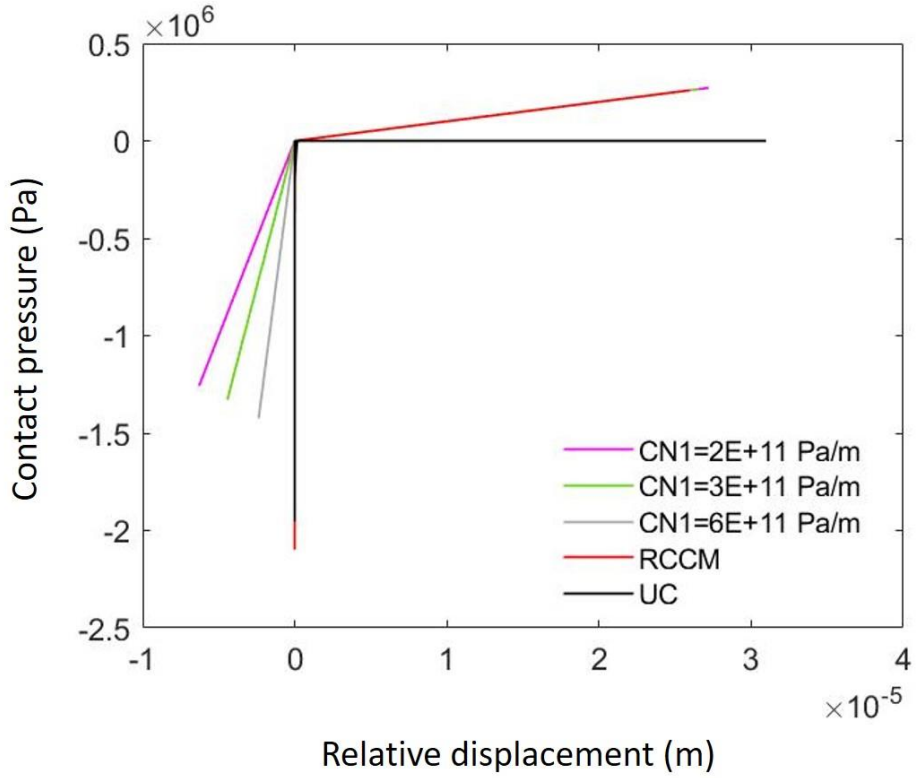

Figure 83 Contact pressure as a function of the relative displacement. $\sigma_i^{max} = 1.4$MPa. ξ =0.1, Contact stiffness C_{N1} ϵ[6.10^{11}, 3.10^{11} , 2.10^{11}]Pa/m, $C_{N2} = 10^{10}$Pa/m , decohesion energy w=1000 J/m^2 , viscosity $b = 10^{-8}$ N.s/m and static pressure p_0= 0.14 MPa

In order to highlight the effect of the introduction of a constant contact stiffness in compression, the second harmonic efficiency is here investigated. In order to assess its value, the reflected wave, selected using a time window, is converted into the frequency domain and filtered to retain either the incident frequency or the second harmonic component. The filtered signals are normalized by the incident wave amplitude.

These simulations are repeated, at each stiffness value, for several incident wave values, leading to different opening conditions of the interface. The incident wave amplitude, and hence the incident stress σ_i, is varied , while the static pressure $p_0 = 0.14\ MPa$ remains fixed. The obtained results are shown as a function of the dimensionless parameter ξ in Figure 84.

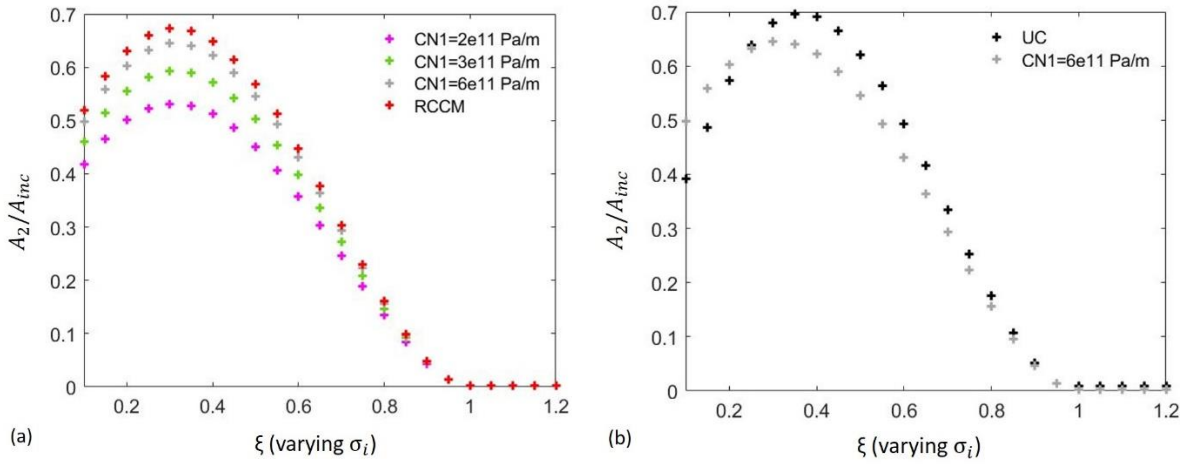

Figure 84 (a) Comparison between bilinear and RCCM contact law for $C_{N2} = 10^{10}$Pa/m in terms of the evolution of the ratio A_2/A_{inc} as a function of the dimensionless parameter ξ. The evaluated stiffness in compression are C_{N1} ϵ[6.10^{11}, 3.10^{11} , 2.10^{11}]Pa/m. decohesion energy $w = 1000\, J/m^2$, viscosity $b = 10^{-8}$ N.s/m. (b) Comparison between a bilinear contact law with C_{N1} =6.10^{11}Pa/m and $C_{N2} = 10^{10}$Pa/m and a unilateral contact law. (See Figure 83 for the different considered contact laws)

Here the incident wave amplitude, and hence the incident stress σ_i, is varied and the static pressure $p_0 = 0.14$ MPa is fixed, which corresponds to a characteristic frequency $f_0 = 5000$ Hz. For values of $\xi > 1$, the incident stress is not sufficient to generate a loss of contact and the response is only dedicated by the linear spring. Hence, no second harmonic is generated, as shown in Figure 84. By contrast, for values of $\xi < 1$, the incident stress is large enough to induce a loss of contact, which leads to the generation of the second harmonic, as shown in Figure 84. This proves the relevance of redefining the dimensionless parameter ξ, given in equation (5.9).

The results shown in Figure 84 (a) confirm that the contact response tends toward that of the RCCM contact law, when increasing the value of the stiffness in compression.

Similarly, when comparing the bilinear model with the unilateral contact in Figure 84 (b), the latter is found to generate more nonlinearity. Indeed, the optimum (maximum value, corresponding to a maximum nonlinearity as a function of ξ) depends on the contrast between stiffness in compression and traction. The more this contrast increases, the higher the optimal value. However, for lower ξ values, the nonlinearity generated by the bilinear model is higher than the one generated by the unilateral contact. This observation, similar to the one in section of chapter 3 concerning the RCCM contact law, means that for certain values of the stiffness in traction the nonlinearity of the unilateral contact is exceeded. The chosen stiffness in traction, $C_{N2} = 10^{10}$Pa/m, is in this range (see Figure 85).

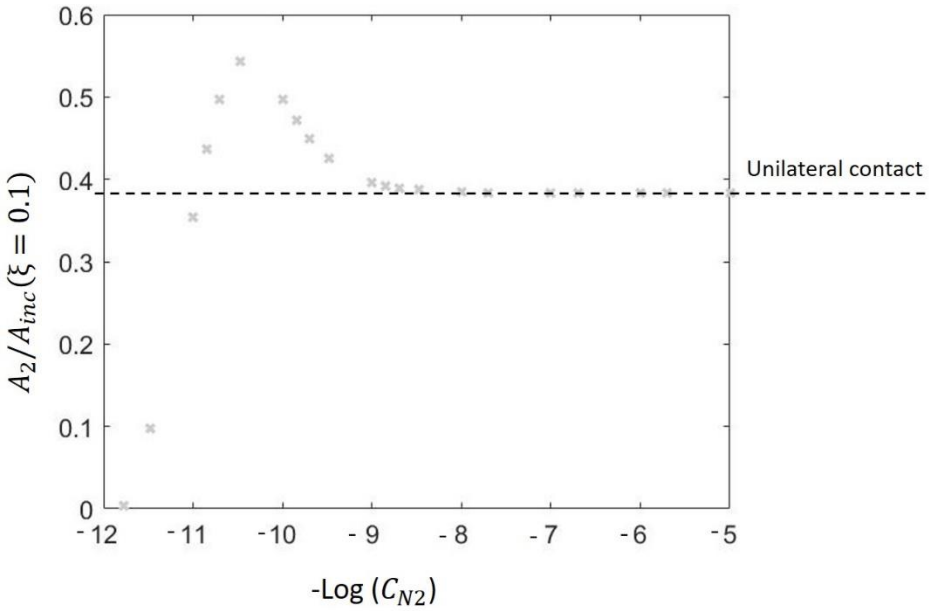

Figure 85 Evolution of the ratio A_2/A_{inc} as a function of the logarithm of the stiffness (the logarithm to the base 10). ξ=0.1. without damaging the interface. $f = 5.10^3 Hz$. This result is obtained for a stiffness value in compression $C_{N1} = 6.10^{11}$Pa/m.

Figure 86 shows the evolution of the second harmonic efficiency A_2/A_{inc}, as a function of the normalized frequency, for the different bilinear models. In order to simplify the calculations, the normalized frequency is evaluated by varying the stiffness value in traction C_{N2}.

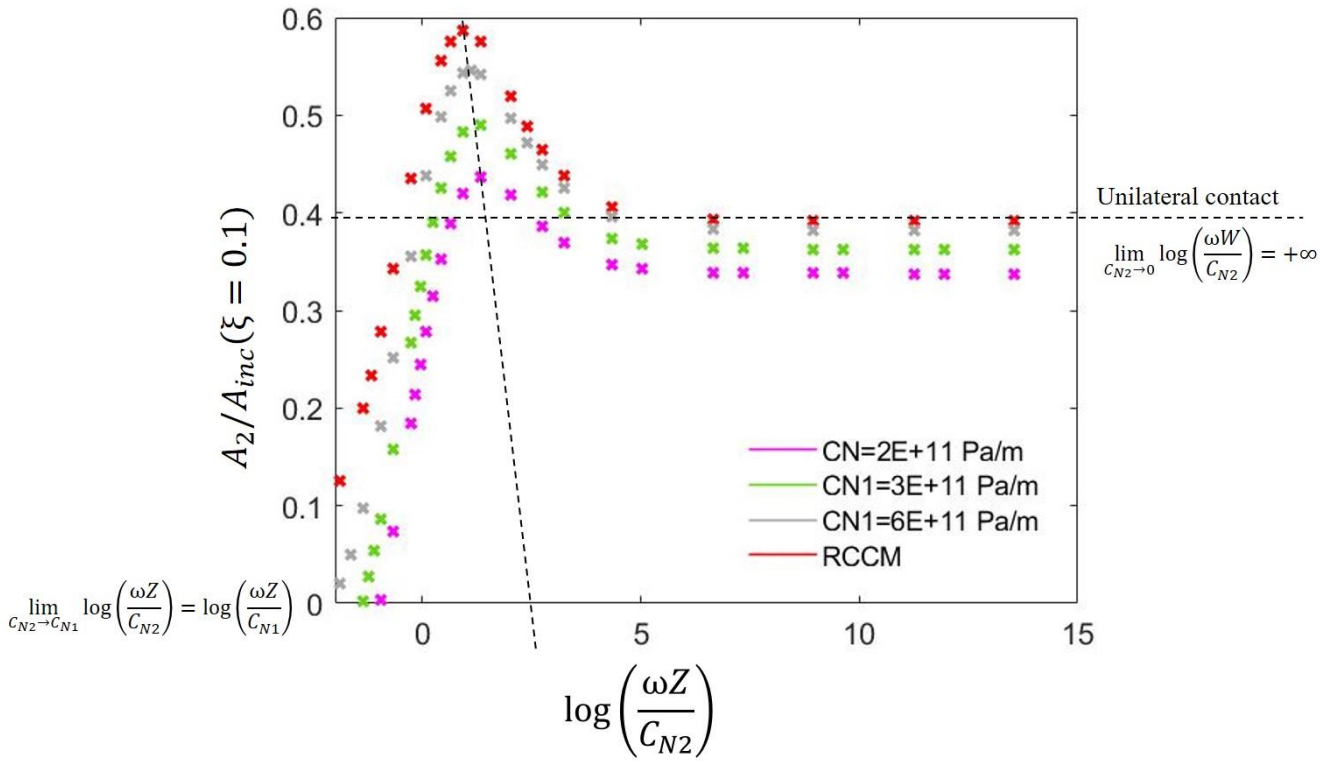

Figure 86 Evolution of the second harmonic efficiency A_2/A_{inc} as a function of the logarithm of the normalized frequency (the logarithm to the base 10) for different stiffness values in compression C_{N1} ϵ [6.10^{11}, 3.10^{11} , 2.10^{11}]Pa/m, without damaging the interface for ξ=0.1. The results are compared with the RCCM contact law.

The results indicate that the lower the value of stiffness in compression, the lower the nonlinearity. Indeed, since the stiffness in compression and traction are linear, the nonlinearity comes only from the shift from compression to traction and vice versa. Again, the nonlinearity is governed by the contrast between stiffness in compression and traction. Hence, the higher this ratio is, the more nonlinearity is generated.

When the stiffness in traction reaches zero, the normalized frequency approaches positive infinity and so does its logarithm. In this case, the right side of the curve tends towards a unilateral contact behaviour in traction and linear spring in compression. However, when the stiffness in traction tends towards the value of stiffness in compression C_{N1}, the second harmonic efficiency A_2/A_{inc} tends towards zero. In fact, this means that the contact law is linear and hence, the left side of the curve approaches a perfect contact behaviour. This behaviour is never reached in the case of the unilateral contact since the compressive stiffness is infinite.

It is also noticed that the peak of the second harmonic efficiency A_2/A_{inc} shifts towards higher normalized frequency values when decreasing the compressive stiffness. As mentioned above, the normalized frequency is evaluated by considering only the stiffness in traction. This approximation leads to an underestimation of the equivalent stiffness value (since the stiffness in traction is lower than in compression). Therefore, the normalized frequency, for which the optimum is reached, is overestimated and hence it shifts to the right.

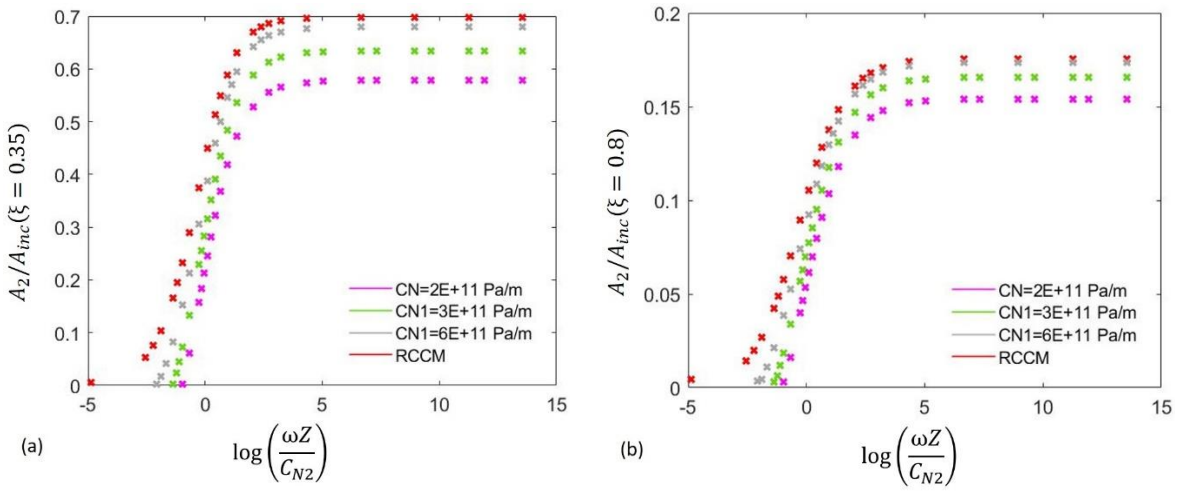

Figure 87 Evolution of the second harmonic efficiency A_2/A_{inc} as a function of the logarithm of the normalized frequency (the logarithm to the base 10) for different stiffness values in compression C_{N1} ϵ [6.10^{11}, 3.10^{11} ,

2. 10^{11}]Pa/m, without damaging the interface. The results are compared with the RCCM contact law. (a) ξ=0.35 and (b) ξ=0.8.

Figure 87 gives the evolution of the second harmonic efficiency as a function of the logarithm of the normalized frequency for $\xi = 0.35$ and $\xi = 0.8$. It can be noticed, similarly to the RCCM contact law that for the bilinear contact laws the maximum, observed for $\xi = 0.1$, disappears. This comforts the observations made in Chapter 3. Moreover, the area of sensitivity to the stiffness in traction varies according to the value of the stiffness introduced in compression.

To conclude, it can be seen that the introduction of a compression stiffness does not fundamentally modify the observations discussed in Chapter 3:

- Existence of intervals of sensibility
- The maximum of second harmonic efficiency observed for lower ξ, when varying the normalized frequency
- The second harmonic efficiency as a function of ξ is similar in terms of evolution to the RCCM case.

However, the nonlinear signature is affected by the stiffness in compression. This is noticeable in terms of the magnitude of the second harmonic efficiency and the offset of the maximum observed for lower ξ, when changing normalized frequency. Indeed, for the bilinear case, the generation of the second harmonic is increased when the contrast between stiffness in compression and traction is increased. In addition, the domain of sensitivity of the nonlinear signature to the stiffness in traction vary according to the stiffness introduced in compression. As expected, similarly to the RCCM and unilateral contact laws, no second harmonic is generated while in compression ($\xi > 1$). One would expect this to change with the introduction of a nonlinear stiffness in compression.

5.3.2 Nonlinear stiffness in compression

In this section, the nonlinear stiffness in compression is introduced. The stiffness-pressure relation is shown in Figure 88. This relationship follows the power law for higher levels of pressure and introduces an inflexion point at lower pressures. For further information, details are given in section 4.1 of chapter 4.

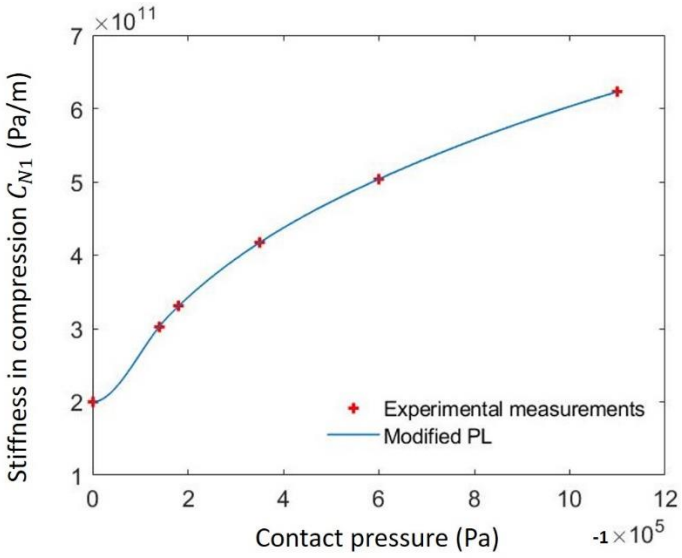

Figure 88 Normal contact stiffness as a function of contact pressure in compression conditions. Experimental results (red cross); Modified PL (blue continuous line). The contact pressure is the absolute value of the contact stress when in compression.

This analysis has been carried out in two parts. The first one without damaging the interface, i.e. the behaviour of the contact law in traction is governed by a linear spring, where $C_{N2} = 10^{10}$Pa/m. In the second part, the interface is damaged. When appropriate, the Modified PL will be compared with the reference cases of the RCCM contact law, the unilateral law and the bilinear law. For this latter law, the value of the constant stiffness in compression corresponds to the static pressure $p_0 = 0.14$ MPa , i.e. $C_{\mathrm{N1}} = 3.10^{11}$Pa/m.

The aim of this part is to better understand the dynamic behaviour of a real interface by studying the influence of a nonlinear stiffness in compression on its overall nonlinear signature.

5.3.2.1 Undamaged interface

In order to identify the influence of the Modified PL in compression, the corresponding numerical solution has been computed and compared with both an infinitely rigid and a linear spring model in compression.

In traction, the interface is assumed to be governed by a linear spring contact law with $C_{\mathrm{N2}} = 10^{10}$Pa/m. This value is set to ensure a sufficiently large contrast between compression and traction stiffness (here the ratio is 30), in order to be able to study the related effects due to this contrast on the second harmonic. In fact, an interface with two comparable stiffness in compression and traction have a similar behaviour to a linear contact and hence will not generate a second harmonic (Chapter3).

Figure 89 shows the evolution of the contact stiffness as a function of the relative displacement, for different tested configurations of stiffness in compression. It indicates that, in addition to the nonlinearity due to the contrast between stiffness in compression and traction, the Modified PL introduces a nonlinearity due to the trend of the stiffness in compression.

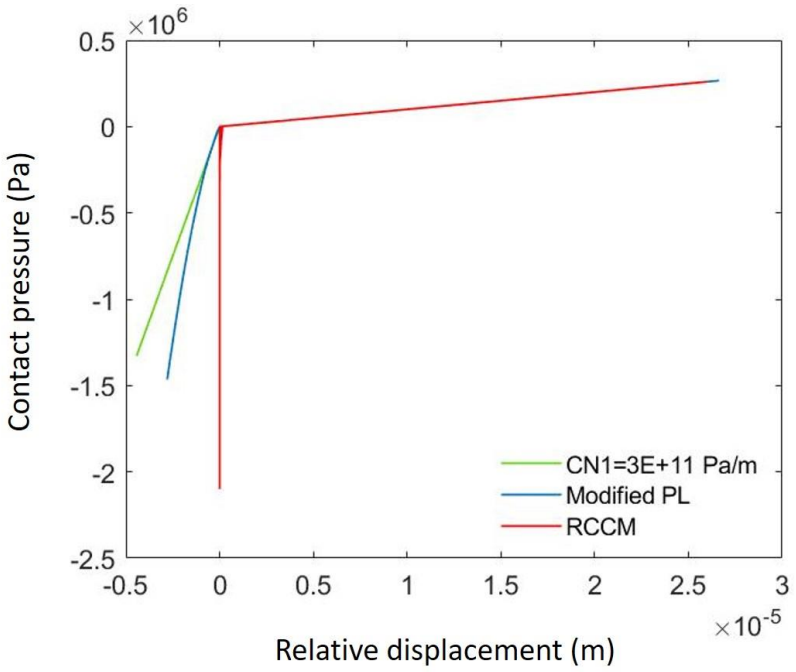

Figure 89 Contact pressure as a function of the relative displacement. $\sigma_i^{max} = 1.4$MPa. ξ =0.1. Contact stiffness in traction $C_{N2} = 10^{10}$Pa/m, decohesion energy w=1000 J/m^2 , viscosity $b = 10^{-8}$ N.s/m. p_0= 0.14 MPa.

Figure 90 (a) and (b) show that the evolutions of the relative displacement and contact pressure, obtained with the Modified PL, compared here with the ones obtained with the RCCM contact model and the linear spring model in compression. These parameters are evaluated for $\xi = 0.8$ in order to observe the impact of either the introduction of the linear or nonlinear stiffness in compression on the time signals.

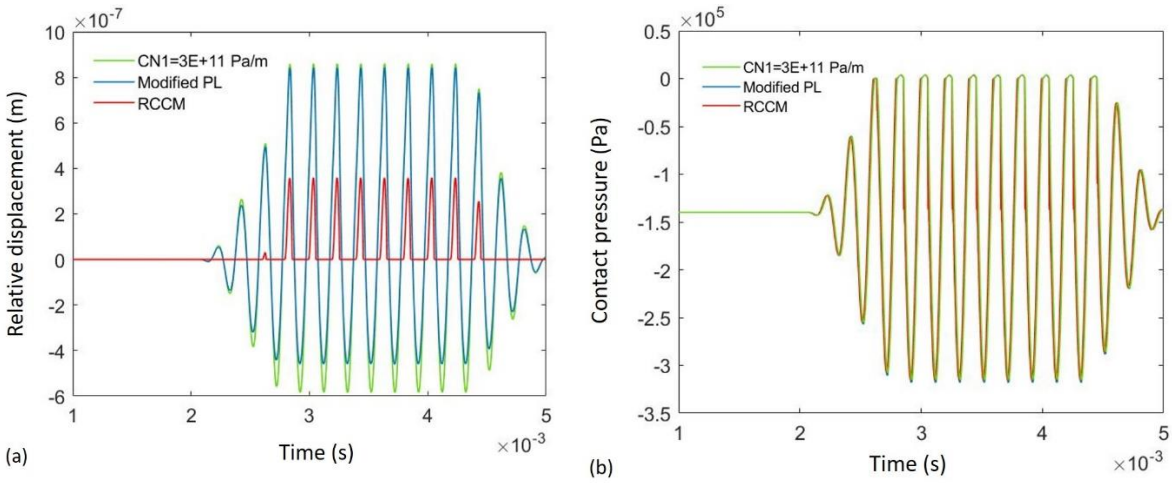

Figure 90 Numerical results for (a) relative displacement at the interface over time. (b) Contact pressure over time. The incident wave frequency $f_0 = 5.10^3$Hz, static pressure $p_0 = 0.14$MPa and a constant stiffness in compression $C_{N2} = 10^{10}$Pa/m .$\xi = 0.8$.

Considering the time signals for the latter laws, it is noticeable that the displacement obtained with the RCCM law is much smaller than those obtained with the Modified PL and linear spring $C_{N1} = 3.10^{11}$Pa/m. As expected, the Modified PL law affects more significantly the amplitude of the displacement during the compression phase. However, the relative contact pressures are comparable for all the studied contact laws.

Despite the comparable displacements in traction in the case of linear and nonlinear stiffness, the nonlinearity exhibited by the Modified PL is expected to be the most significant one for $\xi = 0.8$. In fact, as shown in Figure 91, when decreasing the incident wave amplitude, the duration of each contact loss is progressively reduced while the duration of contact phase is increased. Hence, for $\xi = 0.8$, the interface is subject to larger compression phases and hence the second harmonic generation will be amplified by the nonlinearity in compression.

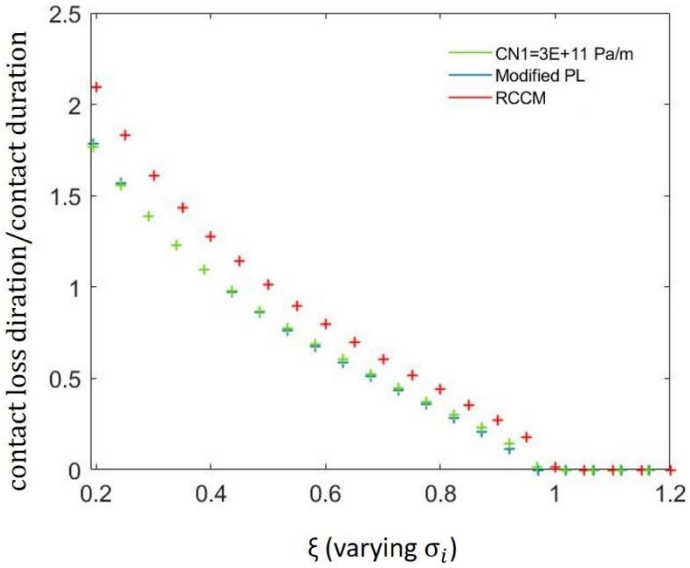

Figure 91 ***Ratio between contact loss and contact durations. The incident wave frequency*** $f_0 = 5.10^3 Hz$***, static pressure*** $p_0 = 0.14 MPa$ ***and a constant stiffness in compression*** $C_{N2} = 10^{10} Pa/m$ **.**

In order to verify this assumption, Figure 92 shows the evolutions of the ratios A_2/A_{inc} and A_1/A_{inc} as a function of the dimensionless parameter ξ. It can be noted that the evolution (form and amplitude) of both the ratios are clearly affected by changes in the compressive stiffness.

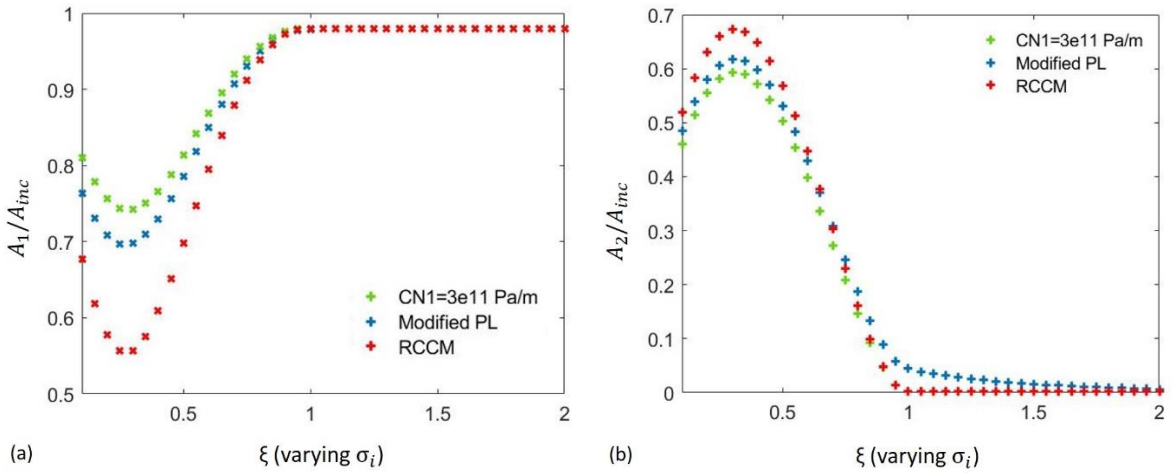

Figure 92 (a) Evolution of the ratio A_1/A_{inc} **as a function of the dimensionless parameter ξ. (b) Evolution of the ratio** A_2/A_{inc} **as a function of the dimensionless parameter** ξ**, decohesion energy** $w = 1000\, J/m^2$ **, viscosity** $b = 10^{-8}$ **N.s/m.**

The results show as well that the second harmonic efficiency is affected by the stiffness-pressure relation in compression. In fact, in contrast to the case with linear and infinite rigidity in compression, the case with nonlinear stiffness introduces additional nonlinearity to the system. Indeed, the nonlinearity is no longer due to only the stiffness contrast between compression and traction, but also to the stiffness trend in compression. Hence, for values of

$\xi < 1$, the nonlinearity obtained with a Modified PL is higher than the one obtained with the linear spring. The nonlinearity derived from the RCCM law remains the most important, for lower values of ξ, given that the contrast between the stiffness in compression and traction is very high (infinite stiffness in compression).

However, it can be seen that increasing ξ the relative contribution of the nonlinearity in compression increases and, for $\xi > 1$, the second harmonic efficiency is no longer zero for the 'Modified PL', due to the nonlinear stiffness-pressure relation in compression. This observation remains valid whatever the value of the stiffness in traction. In fact, Figure 93 shows the evolution of the contact pressure as a function of the relative displacement for different stiffness values in traction C_{N2}.

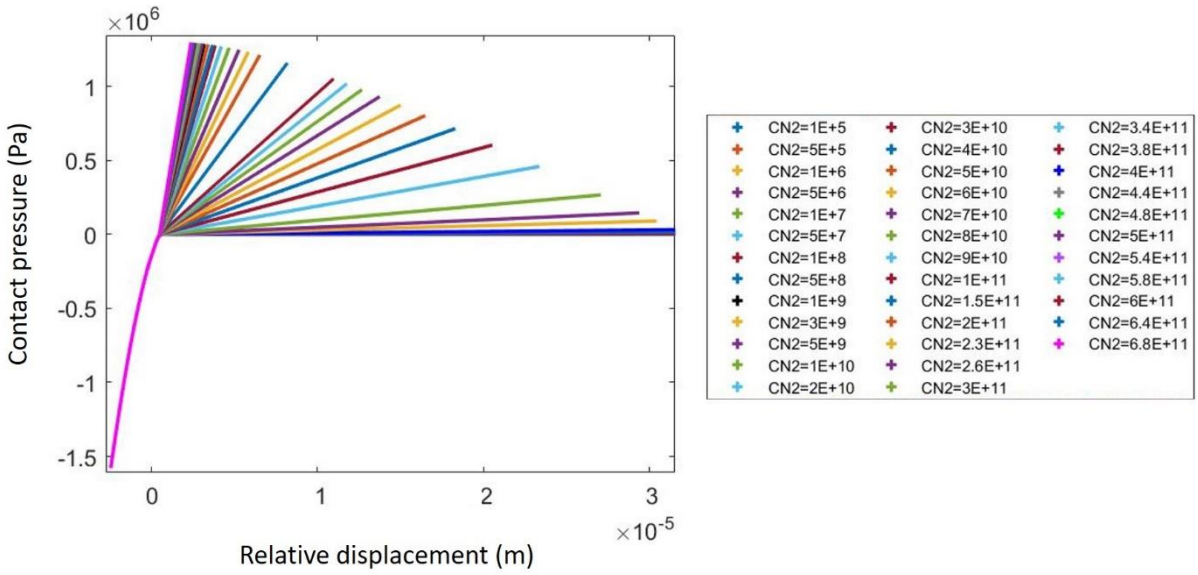

Figure 93 Contact pressure as a function of the relative displacement. $\sigma_i^{max} = 1.4\ MPa$. $\xi = 0.1$. Contact stiffness in compression governed by the modified PL, decohesion energy $w = 1000\ J/m^2$ and viscosity $b = 10^{-8}\ N.s/m$.

The variation of the stiffness in traction affects the contrast compression/traction stiffness, but the nonlinearity in compression is maintained due to the nonlinear law ('Modified PL') introduced in compression. This is shown in Figure 94, where the second harmonic efficiency, as a function of the dimensionless parameter ξ, is reported for different stiffness in traction. In fact, for $\xi > 1$, all the curves overlap, as the only existing nonlinearity is due to the modified PL. However, for $\xi < 1$,the higher the stiffness in traction, the lower the nonlinearity due to the ratio between the stiffness in traction and compression, which tends towards 1 (case of a linear stiffness contact).

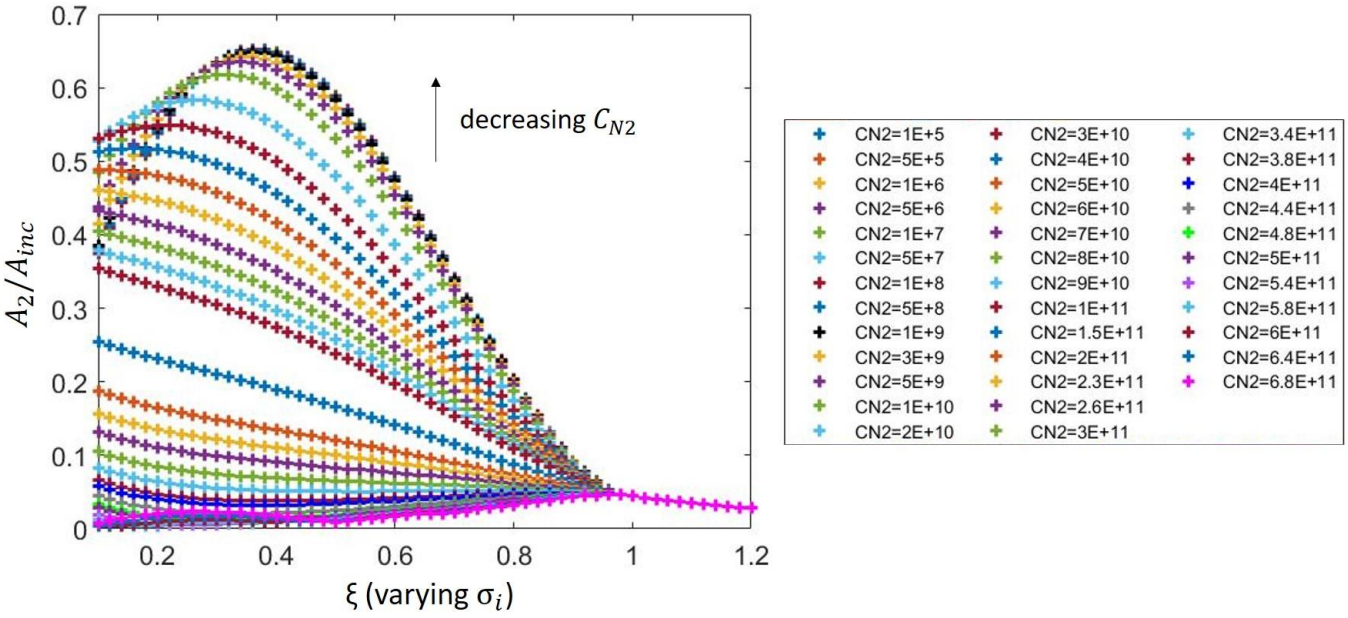

Figure 94 Evolution of the ratio A_2/A_{inc} as a function of the dimensionless parameter ξ for stiffness in compression governed by the Modified PL. decohesion energy $w = 1000\ J/m^2$ and viscosity $b = 10^{-8}\ N.s/m$.

Moreover, we obtain a similar result as in section 3.3.1 of chapter3. As previously, three different stiffness-dependant domains can be identified:

<u>First range: contact stiffness $C_{N2} < 10^9\ Pa/m$</u>

Within this range, the second harmonic efficiency is not (or at least very little) sensitive to a variation in the traction stiffness C_{N2}. The nonlinearity exhibited by the interface is the most important in this case.

<u>Second range: contact stiffness $10^9 < C_{N2} < 4.10^{11}\ Pa/m$</u>

The nonlinear response is largely stiffness-dependent within these bounds. In fact, when increasing the stiffness within the range$]10^9, 4.10^{11}[$, the second harmonic efficiency A_2/A_{inc} drops. The traction/compression stiffness ratio shifts from zero (the previous case) to 1, leading to a lower value of the second harmonic efficiency (lower nonlinearity). It is also noted that the maximum in the second harmonic, obtained at $\xi = 0.35$ for the previous case, is shifted to the left when increasing the contact stiffness, until vanishing (a maximum in the second harmonic amplitude does no longer exist for a value of stiffness of about $1.10^{11}\ Pa/m$).

Third range: contact stiffness $C_N > 4.10^{11}\ Pa/m$

The compression/traction stiffness ratio tends toward 1. In fact, there is barely a second harmonic generation due to the shift between compression and traction. The only nonlinearity is due to the nonlinear contact law in compression and hence the sensitivity to the stiffness is particularly small. Likewise, the ratio A_2/A_{inc} is quasi-independent from the applied stiffness in traction.

These 3 different areas of sensitivity can be identified also in Figure 95. This latter figure shows the evolution of the second harmonic efficiency as a function of the normalized frequency, for three different stress states: $\xi = 0.1$ corresponding to the most important incident wave amplitude, $\xi = 0.35$ corresponding to optimal position and $\xi = 0.8$ corresponding to the phase where the interface is subjected to more compression than traction. It is recalled that the normalized frequency is computed while varying the stiffness in traction C_{N2}.

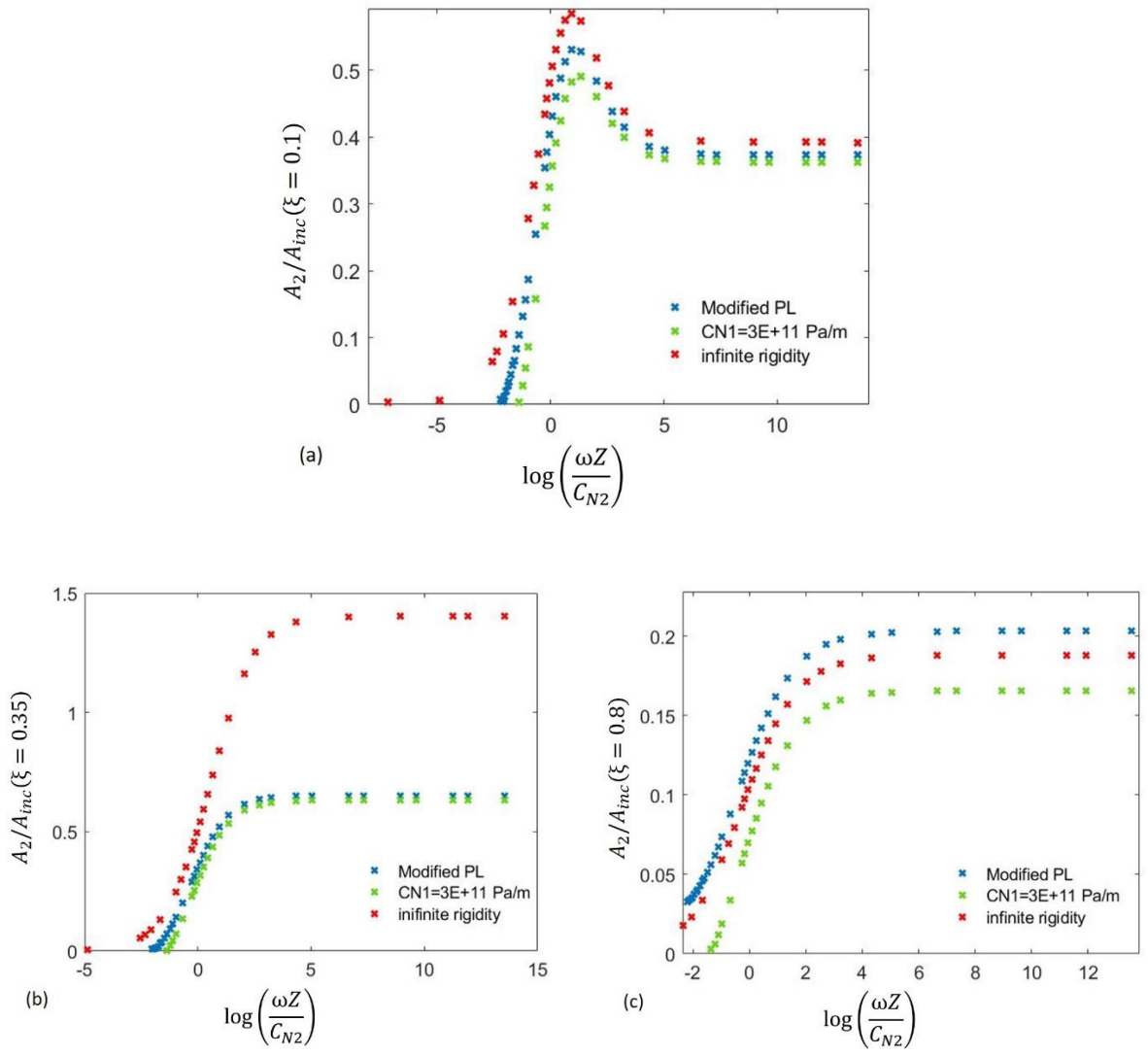

Figure 95 Evolution of the second harmonic efficiency A_2/A_{inc} as a function of the normalized frequency for frequencies $f = 5\ 10^3\ Hz$, without damaging the interface. (a) $\xi = 0.1$, (b) $\xi = 0.35$ and (c) $\xi = 0.8$.

These results provide a comprehensive characterization of a CAN in the presence/or not of nonlinearity during the contact. For higher normalized frequency values, the stiffness in traction approaches zero, while lower frequency values tend towards the equivalent stiffness in compression. Hence, the equivalent stiffness in compression can be estimated numerically. In fact, the second harmonic efficiency reaches zero when the interface response is linear meaning that the stiffness in compression and in traction are equal. By identifying the value of the stiffness in traction for which there is no longer second harmonic generation, the equivalent stiffness in compression can be deduced. In between these two domains lies the area where the nonlinear signature of the contact law varies with the normalized frequency.

One can notice that an infinite rigidity in compression generates particularly more nonlinearity for $\xi = 0.35$, as shown in Figure 95 (b). This latter value refers to the incident wave amplitude required to generate a maximum rate of transition between compression and traction phases. Therefore, the parameters governing the nonlinearity for $\xi = 0.35$, is the contrast between stiffness in compression and traction. However, for $\xi = 0.8$, the interface is more subject to compression and hence the nonlinearity of the modified PL governs. Therefore, the second harmonic efficiency obtained with the modified PL is the most important for $\xi = 0.8$ as shown in Figure 95(c).

5.3.2.2 Damaged interface

In this paragraph, the parameters of the presented simulations may lead to interface damage (β_{end} <1 at the end of the simulations). The value of the stiffness in traction is chosen in the domain where the NL signature of the contact law is most sensitive to the variation of C_{N2}, i.e. $C_{N2} \in]10^9, 4.10^{11}[$. The incident wave amplitude, and hence the dimensionless parameter ξ, is varied, while the static pressure p_0 is fixed. The simulation parameters are listed in Table 8.

Normal stiffness C_N (Pa/m)	**Viscosity b (Pa.s)**	**Decohesion energy w (J/m^2)**	**Frequency f (Hz)**
$\mathbf{10^{10}}$	10^{-8}	0.1	5.10^3

Table 8 simulation parameters for the damaged interface study

Figure 96 shows the evolution of the intensity of adhesion and contact stiffness as a function of ξ, for different contact laws. Each dot in the graphic represents the ending values of the adhesion intensity and contact stiffness, at the end of the corresponding simulation.

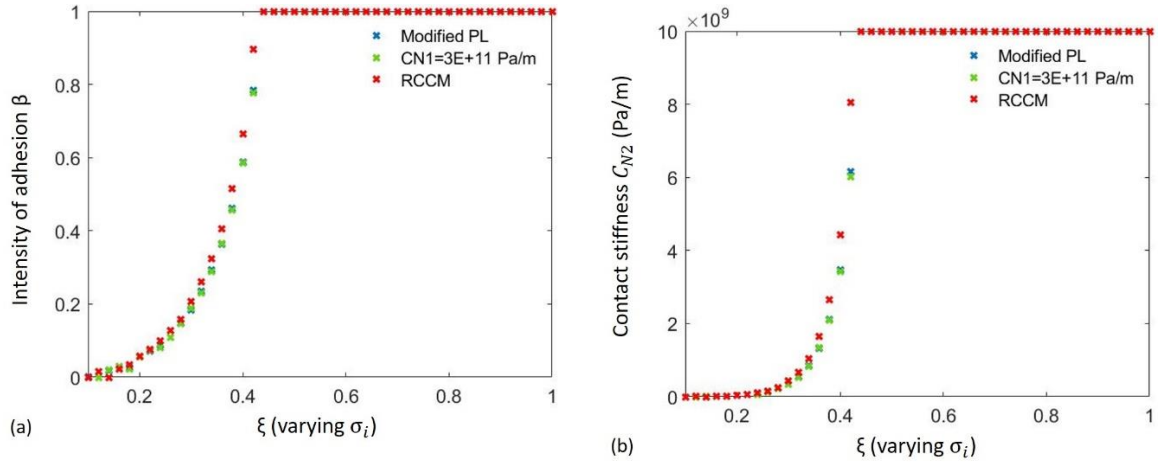

Figure 96 The maximum incident pressure is $max(\sigma_i^{max}) = 1.4\ MPa$. (a) Damage coefficient as a function of the dimensionless parameter ξ and (b) Contact stiffness as a function of the dimensionless parameter ξ, decohesion energy $w = 0.1\ J/m^2$ and viscosity $b = 10^{-8}\ N.s/m$.

As long as the incident wave amplitude is not enough to damage the interface, the adhesion is complete (β_{end}=1), the final contact stiffness in traction is equal to the initial one and the interface traction behaviour is elastic. Increasing the incident wave amplitude, the damage of the interface occurs gradually. Then, the intensity of adhesion β and the apparent stiffness $\beta^2 C_{N2}$ decrease. When adhesion vanishes totally (β=0), the interface becomes traction-free ($C_{N2} = 0$). This behaviour could be identified also in Figure 97, which shows the contact pressure as a function of the relative displacement.

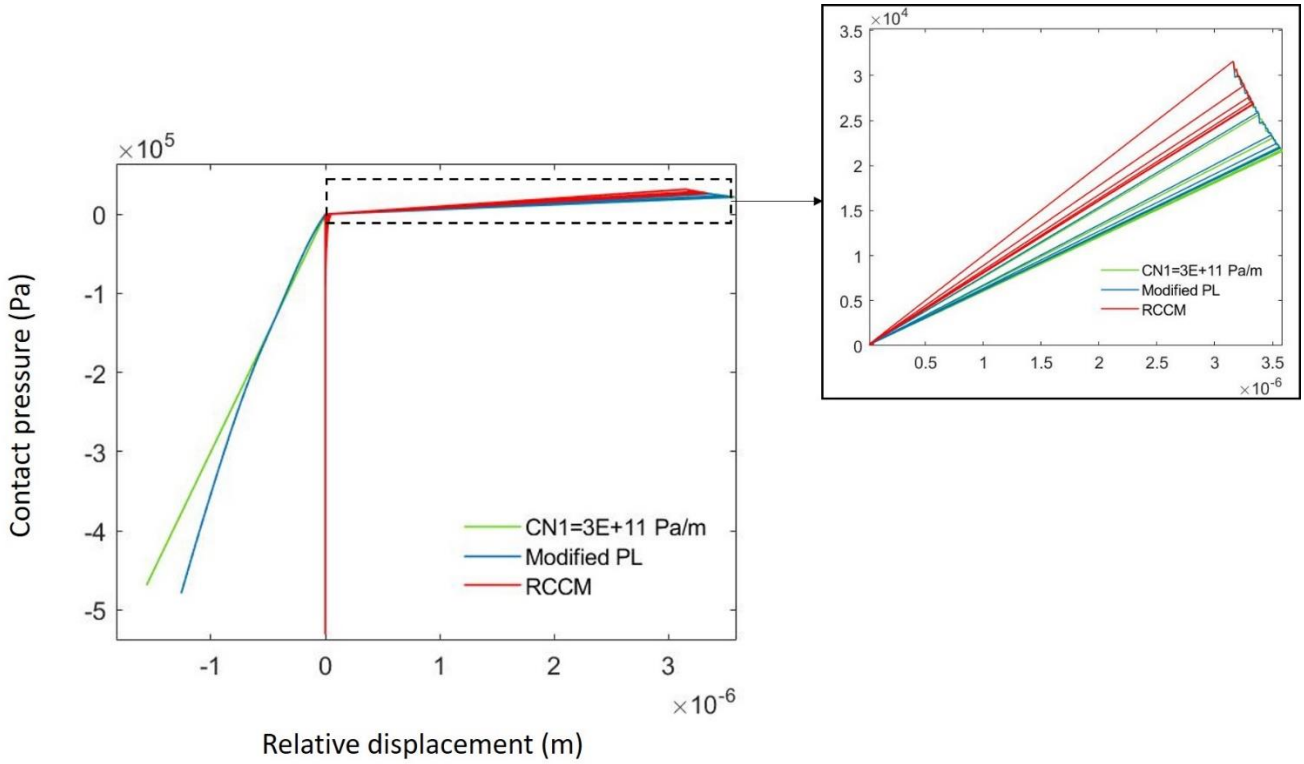

Figure 97 Contact pressure as a function of the relative displacement. σ_i^{max}= 1.4 MPa. ξ =0.1, decohesion energy w=0.1 J/m^2 , viscosity $b = 10^{-8}$ N.s/m and static pressure p_0= 0.14 MPa

Figure 98 (a) and (b) show the evolutions of the relative displacement and contact pressure, obtained with the 'Modified PL', the RCCM contact and linear spring in compression. These parameters are evaluated for $\xi = 0.36$ in order to observe the impact of damaging the interface on the time signals.

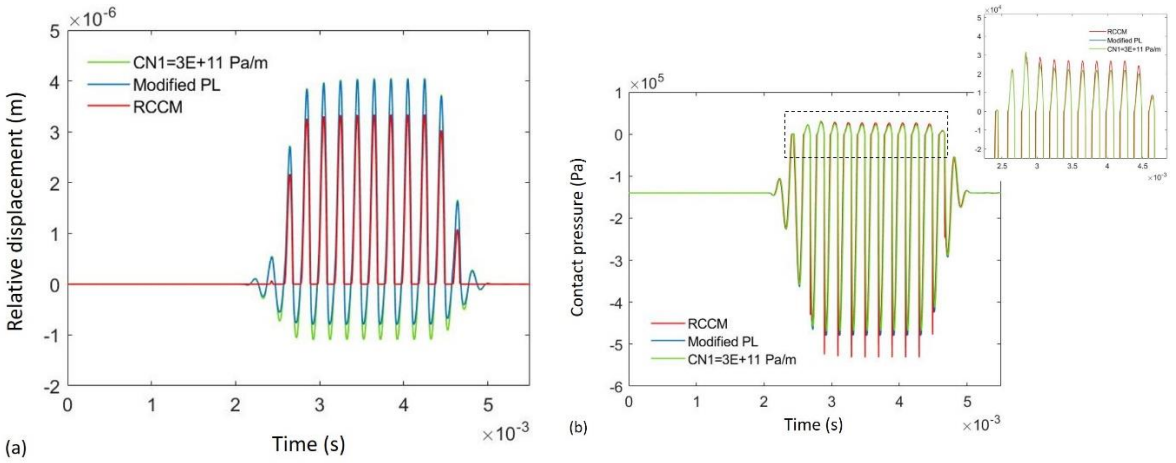

Figure 98 Numerical results for (a) relative displacement at the interface over time. (b) Contact pressure over time. The incident wave frequency $f_0 = 5.10^3 Hz$ and static pressure $p_0 = 0.14 MPa$.

It can be noted that the contact law in compression has an impact on the way the interface is damaged. Indeed, the time signals derived from linear and nonlinear stiffness law in compression appear to be the most affected by the damage. Note that, as the interface damages, the contact pressure decreases (since the stiffness decreases) but the displacement does not seem to be greatly affected.

Figure 99 shows the evolutions of the ratios A_2/A_{inc} and A_1/A_{inc} as a function of the dimensionless parameter ξ.

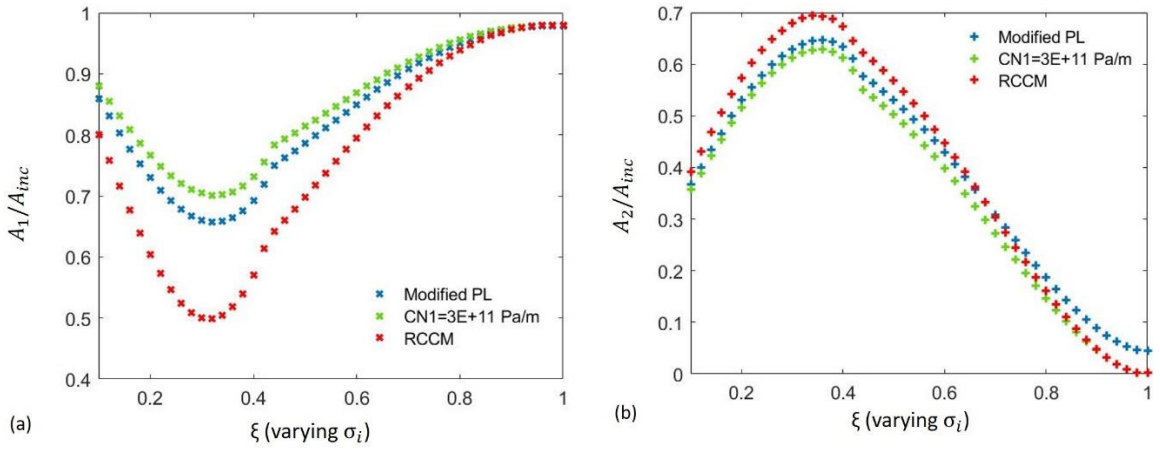

Figure 99 (a) Evolution of the ratio A_1/A_{inc} as a function of the dimensionless parameter ξ and (b) Evolution of the ratio A_2/A_{inc} as a function of the dimensionless parameter ξ, decohesion energy $w = 0.1\ J/m^2$, viscosity $b = 10^{-8}$ N.s/m.

The same findings, as for the undamaged interface, are retained. In fact, while the interface is exposed to lower ξ values, the nonlinearity derived from the RCCM contact law is the most significant one. However, when the interface is more subject to compression (higher ξ values), the nonlinearity generated by the 'Modified PL' is dominant.

Note also that the form of the second harmonic efficiency is highly dependent on the damage parameters, i.e. the decohesion energy w and the viscosity b. Indeed, as seen in Chapter 3, the decohesion energy sets the threshold incident stress required to damage the interface.

Figure 100 shows the evolution of the intensity of adhesion and contact stiffness as a function of ξ, for different decohesion energies.

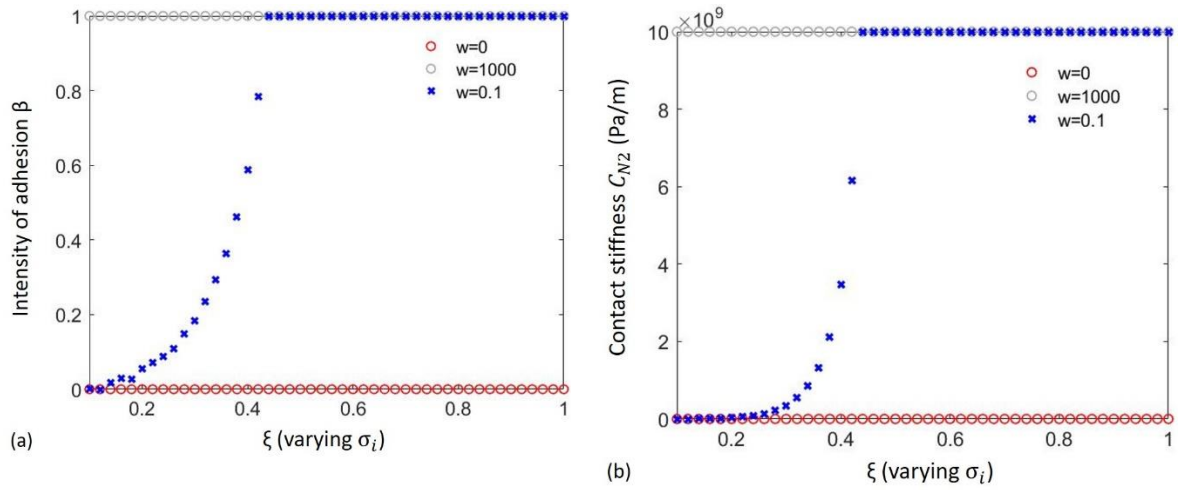

Figure 100 Themaximum amplitude of the incident pressure is $max(\sigma_i^{max}) = 1.4\ MPa$. (a) Damage coefficient as a function of the dimensionless parameter ξ and (b) Contact stiffness as a function of the dimensionless parameter ξ, decohesion energy $w\epsilon[0, 0.1, 1000]\ J/m^2$ and viscosity $b = 10^{-8}\ N.s/m$.

Again, when increasing the decohesion energy, the damage at the interface occurs for lower values of ξ, for higher incident wave magnitude. In fact, the increase of the decohesion energy leads to the increase in the elastic limit. Hence, the incident amplitude threshold, sufficient to damage the interface, increases and the damage of the interface occurs for a lower value of the dimensionless parameter ξ.

Figure 101 shows the evolutions of the ratios A_2/A_{inc} and A_1/A_{inc} as a function of the dimensionless parameter ξ, for three values of the decohesion energy w.

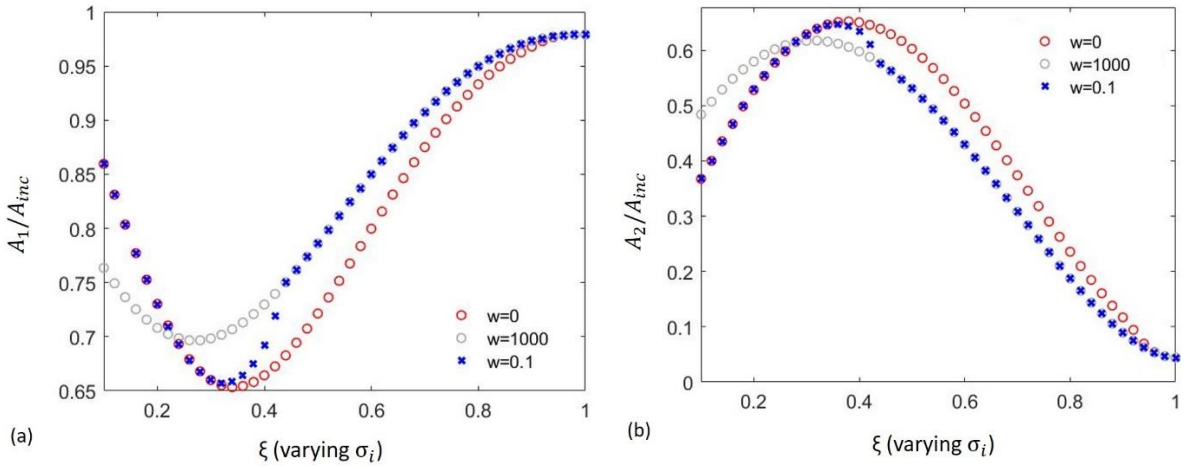

Figure 101 (a) Evolution of the ratio A_1/A_{inc} as a function of the dimensionless parameter ξ and (b) Evolution of the ratio A_2/A_{inc} as a function of the dimensionless parameter ξ, decohesion energy $w\epsilon[0, 0.1, 1000]\ J/m^2$ and viscosity $b = 10^{-8}$ N.s/m.

Considering an increasing amplitude of the incident wave (decreasing ξ), until the limit of elasticity is not reached, the interface behaviour is similar to a model with a Modified PL in compression and linear spring in traction (see Figure 101). The generated nonlinearity is due to the contrast of the stiffness in traction and compression and the nonlinearity due to the NL stiffness in compression. Consequently, the evolutions of A_2/A_{inc} and A_1/A_{inc} are identical to the ones obtained with an undamaged interface ($w = 1000\ J/m^2$). After that, the damage of the interface occurs and, consequently, the nonlinearity coefficient increases due to that damage, because the contrast between traction and compression stiffness increases. When the adhesion vanishes totally, the interface is completely damaged and the nonlinear signature is equivalent to the unilateral contact in traction and Modified PL in compression. Note that the passage between the two different behaviours is clearly visible on the nonlinear signature (A_2/A_{inc} and A_1/A_{inc}).

To conclude, these results show that the nonlinear response of the interface is modified by the presence of the nonlinear stiffness in compression, especially for high value of ξ. Again, it is showed that the nonlinear signature at the interface is affected by the different parameters of the system (medium, interface laws, incident wave). A deep understanding of these effects and evolutions is necessary for their possible exploitation in order to characterize a contact interface.

5.4 Concluding remarks

A new interface model that combines nonlinear stiffness in compression and RCCM contact law in traction has been investigated both analytically and numerically. The analytical solution, derived in the case of bilinear contact law, has been used to validate the numerical model and taken as a reference for verifying the convergence. Moreover, the analytical solution indicates the existence of a critical displacement required to trigger the loss of contact. Therefore, the dimensionless parameter ξ has been adapted to this new configuration and used to investigate the evolution of the second harmonic efficiency, distinguishing between the cases with and without clapping. The numerical model has been then used to consider the nonlinear stiffness-pressure relationship in compression ('Modified PL') and the RCCM contact in traction. The results show that the NL signature at the interface is clearly modified by the presence of the nonlinear stiffness in compression. In fact, for lower ξ values, the second harmonic shows a peak of amplitude and then slowly decreases when increasing ξ. Moreover, its amplitude does

not cancel when in compression. These results show how the proposed model is able to represent the different contact interface responses, affected by both the nonlinearities, due respectively to the shift between compression and traction and to the nonlinear stiffness in compression. The nonlinear signature at the interface is affected by the different parameters of the system (medium, interface laws, incident wave). A deep understanding of these effects and evolutions is necessary for their use in order to characterize a contact interface. The proposed approach allows for this analysis and in particular, it allows choosing the configurations the most sensitive to the parameters of the interface. This observation pave the way to the exploitation of the nonlinear response for an inverse analysis of the interface features, envisaged in the future.

General conclusion

The main objective of the thesis is the analysis of the nonlinear interaction between a longitudinal wave and a contact interface, in view of the development of characterization tools by non-destructive structural dynamic and ultrasound means. In this context, our approach was based on the combination of numerical analyses and experimental tests to improve our understanding of the physical mechanisms involved in the nonlinear contact.

6.1 Original main contributions

The first original contribution of this was the combination of both structural dynamic and acoustic approaches for investigating the nonlinear interface response to external excitations. Numerical and experimental tools have been assembled together to provide an overall approach able to account for the different phases of the interface-wave interaction.

Moreover, the mechanisms emerging during wave-interface interaction are diverse and therefore require different modelling approaches, which can be complex and time-consuming from a numerical point of view. In this work, a flexible numerical tool has been first implemented to take into account different contact laws. Modelling was carried out using the Finite Difference method and implemented in a Matlab code. This innovative tool will be highly useful, particularly when different phenomena related to nonlinear contact are considered.

This tool was initially used to study the adhesion phenomena described by the RCCM contact law. A first analysis of the reflected wave showed that the nonlinear signature of the interface contains information directly linked to the different interface parameters. Consequently, a further parametric analysis was proposed. The parameters in question are the parameter of the RCCM contact law (contact stiffness, viscosity and decohesion energy) and the frequency of the incident wave.

On one hand, this analysis provides insights on how the different parameters influence the nonlinear signature of the considered contact law, via analysing the second harmonic evolution. On the other hand, it allowed identifying the governing parameters of the law, which in a further process, could be retrieved by inverse method. This step, once fully developed, will represent a significant advance in the field of contact interface characterization.

However, in the majority of real cases, asperities and third body at the contact interface introduce a nonlinear compression stiffness as well. The RCCM law, by itself, is therefore not sufficient to describe this aspect. Hence, numerical and experimental analyses have been performed to provide a basic insight into the nonlinear vibrational response of a closed interface, as a basis for evaluating the nonlinear contact through stress-dependent stiffness in compression. A specific contact law has been proposed, including different specific evolutions of the stiffness for low pressures. From the numerical simulations, it was possible to identify the effect of this further contact nonlinearity on the dynamic response of the system. The results from the parametrical analysis and the comparison with the experiments highlighted the key role played by the nonlinear stiffness trend at lower contact pressures, where data from the experimental literature are lacking, demonstrating the need to identify such parameter with dedicated experimental tests.

So far, the effects of introducing contact nonlinearities in compression or traction have been studied separately in different contexts. Therefore, the last step of this work was to present an overall approach for modelling the nonlinear scattering induced by a contact interface, by combining traction and compression nonlinearities in an overall contact law. The derived law combines then the different phenomena involved in the nonlinear contact, namely compliance due to surface roughness, clapping and adhesion, which completes our approach and allows reaching the initial objective of the thesis.

The numerical results showed how the proposed approach is able to represent the different contact interface responses, affected by both the nonlinearities, due respectively to the shift between compression and traction and to the nonlinear stiffness in compression. This aspect has been highlighted by comparing the overall contact law with the RCCM and the NL stiffness laws.

Finally, the proposed approach allows choosing the configurations the most sensitive to the parameters of the interface. This observation paves the way to the exploitation of the nonlinear response of an interface for the inverse analysis of its main features.

6.2 Outlines and future steps

From a numerical point of view, two main aspects are worth of further investigation. First, as shown in Chapter 3, the reflected wave contains the nonlinear signature of the interface, which is directly related to the different contact parameters. The exploitation of this nonlinear

response could allow obtaining information about the interface parameters and, thus, characterising with inverse approaches the contact interface. Hence, the parametric analysis proposed in Chapter 3 should be further carried on using the overall contact law proposed in Chapter 5. This analysis will aim at better understanding the dynamic behaviour of the interface while considering the different nonlinear phenomena, both in traction and compression.

The second interesting issue concerns development of a methodology based on inverse method for the interface characterisation, exploiting the developed numerical tools and the provided analysis of the nonlinear interaction between wave and the interface. The general methodology proposed in this thesis is promising and could be refined in order to develop a numerical approach for contact parameters identification via inverse methods. This technique could allow identifying even more parameters, including information on surface roughness, if the contact law describing both the adhesion and compression stiffness is exploited.

Experimentally, two interesting aspects can be further developed as well. In fact, the results of this work showed that the stiffness-pressure trend at lower pressures has a major effect on the nonlinear response of systems with contact interfaces. Therefore, experimentally, the interface behaviour in compression ought to be further investigated in order to identify the effective stiffness-pressure trend within the lower pressure range.

Finally, the numerical process set to identify the interface parameters could be used experimentally. The confrontation of numerical results with the experimental measurements will enable to validate the proposed technique and bring to reliable tools for interface characterization and/or damage detection.

Bibliography

[1] B. Armstrong-Hélouvry, “Control of Machines with Friction,” *Journal of tribology,* vol. 114, p. 637, 1992.

[2] I. M. KOC, T. ERAY, B. SÜMER and N. Cerci, “An active force controlled laparoscopic grasper by using a smart material actuation,” *Tribology International,* vol. 100, pp. 317-327, 2016.

[3] B. Bhushan, Tribology and Mechanics of Magnetic Storage Devices, New York: Springer Science & Business Media, 2012.

[4] D. Türkmen, I. M. Koc and B. Sümer, “Adhesive Pillar Based Air Levitation System for Contactless Manipulation of Fine Objects,” *Procedia engineering,* vol. 120, pp. 1124-1127, 2015.

[5] D. Tonazzi, F. Massi, L. Baillet, J. Brunetti and Y. Berthier, “Interaction between contact behaviour and vibrational response for dry contact system,” *Mechanical Systems and Signal Processing,* vol. 110, pp. 110-121, 2018.

[6] X. Shi and A. Polycarpou, “Measurement and modeling of normal contact stiffness and contact damping at the meso scale,” *Journal of viration and acoustics,* vol. 127, pp. 52-60, 2005.

[7] S. C.H. and H. S.H., “Hysteresis in the closure of a nominally flat crack,” *Journal of Geophysical Research,* vol. B8, p. 88, 1983.

[8] K. Worden and G. Tomlinson, “Nonlinearity in Structural Dynamics: Detection, Identification and Modelling,"," in *IOP Publishing Ltd*, Bristol, 2001.

[9] M. Friswell and J.E.T.Penny, “Crack modeling for structural health monitoring,” *StructuralHealthMonitoring ,* vol. 1, p. 139–1482, 2002.

[10] P.Gudmundson, “The dynamic behaviour of slender structures with cross-sectional cracks,” *Journal of the Mechanics and Physics of Solids,* vol. 31(4), pp. 329-345, 1983.

[11] D. Dutta, H. Sohn, K. A. Harries and P. Rizzo, “A nonlinear acoustic technique for crack detection in metallic structures,” *Structural Health,* vol. 8(3), p. 251–262, 2009.

[12] L. A. Ostrovsky, “ Wave processes in media with strong acoustic nonlinearity,” *The Journal of the Acoustical Society of America,* vol. 90(6), p. 3332–3337 , 1991.

[13] J. M. Richardson, “Harmonic Generation at an Unbonded Interface: I.Planar Interface Between Semi-Infinite Elastic Media,” *Int. J. Eng. Sci.,* vol. 17, p. 73–85, 1979.

[14] R. J.M., “Acoustic Harmonic Generation at Diffusion Bonds,” *Eng.Sci,* vol. 17, p. 73, 1979.

[15] K. L. Johnson, Contact Mechanics, United Kingdom: Cambridge university press, 1985.

[16] J. A. Greenwood and J. P. B. Williamson, “Contact of nominally flat surfaces,” *Proceedings of the royal society of London,* vol. 295, p. 300–319, 1966.

[17] J. M. Richardson, “Harmonic Generation at an Unbonded Interface: I.Planar Interface Between Semi-Infinite Elastic Media,” *Int. J. Eng. Sci.,* vol. 17, p. 73–85, 1979.

[18] O. V. Rudenko, “Nonlinear Acoustic Properties of a Rough Surface Contact and Acoustodiagnostics of a Roughness Height Distribution,” *Acoust. Phys.,* vol. 40, p. 593–596, 1994.

[19] B. W. Drinkwater, R. S. Dwyer-Joyce and P. Cawley, “A Study of the Interaction Between Ultrasound and a Partially Contacting Solid-Solid Interface,” *Proceedings of the Royal Society of London,* vol. 452, p. 2613–2628, 1996.

[20] A. A. Polycarpou and A. Soom, “Boundary and Mixed Friction in the Presence of Dynamic Normal Loads. I. System Model,” *Journal of tribology,* vol. 117, p. 261–266, 1995.

[21] Y. Song, C. Hartwigsen, D. McFarland, A. Vakakis and L. Bergman, “Simulation of dynamics of beam structures with Bolted Joints using adjusted Iwan beam elements,” *Journal of sound and vibration,* vol. 273, p. 249–276, 2004.

[22] J. Jin, P. Johnson and P. Shokouhi, “An integrated analytical and experimental study of contact acoustic nonlinearity at rough interfaces of fatigue cracks,” *JOURNAL OF THE MECHANICS AND PHYSICS OF SOLIDS,* vol. 135, 2020.

[23] S. BIWA, S. NAKAJIMA and N. OHNO, “On the acoustic nonlinearity of solid-solid contact with pressure-dependent interface stiffness,” *Journal of applied mechanics,* vol. 71, pp. 508-515, 2004.

[24] V. V. Aleshin and A. Papangelo, “Friction-induced energy losses in mechanical contacts subject to random vibrations,” *International Journal of Solids and Structures,* vol. 190, pp. 148-155., 2020.

[25] L. Pastewka, N. Prodanov, B. Lorenz, M. H. Müser, M. O. Robbins and B. N. Persson, “Finite-size scaling in the interfacial stiffness of rough elastic contacts,” *Physical Review E,* vol. 87(6), p. 062809, 2013.

[26] D.Tonazzi, F.Massi, M.Salipante and Y.Berthier, “Estimation of the normal contact stiffness for frictional interface in sticking and sliding condition,” *Lubricants,* vol. 7, p. 56, 2019.

[27] K. Kendall and D. Tabor, “An ultrasonic study of the area of contact between stationary and sliding surfaces,” *Proceedings of the Royal Society of London,* vol. 323, pp. 321-340, 1971.

[28] V. Aleshin, O. Bou Matar and K. Van Den Abeele, “Method of memory diagrams for mechanical frictional contacts subject to arbitrary 2D loading,” *International Journal of Solids and Structures,* vol. 60, pp. 84-95, 2015.

[29] V. Aleshin, S. Delrue, A. Trifonov, O. Bou Matar and K. Van Den Abeele, “Two dimensional modeling of elastic wave propagation in solidscontaining cracks with rough surfaces and friction – Part I: Theoretical Background,” *Ultrasonics,* vol. 82, pp. 11-18, 2018.

[30] V. Aleshin, S. Delrue, A. Trifonov, O. Bou Matar and K. Van Den Abeele, “Two dimensional modeling of elastic wave propagation in solidscontaining cracks with rough surfaces and friction – Part II: Numerical implementation,” *Ultrasonics,* vol. 82, pp. 19-30, 2018.

[31] S. Biwa, “Second-Harmonic Generation at Contacting Interfaces,” *Nonlinear Ultrasonic and Vibro-Acoustical Techniques for Nondestructive Evaluation. Springer, Cham,* pp. 263-299, 2019.

[32] A. SAIDOUN, A. MEZIANE, M. RÉNIER, C. BACON, F. ZHANG and H. WALASZEK, “Influence of contact interface morphology on the nonlinear interaction between a longitudinal wave and a contact interface with friction : A numerical study, submitted to wave motion.,” *Article submitted for publication.*

[33] K. A. Van Den Abeele, J. Carmeliet, J. A. Ten Cate and P. A. Johnson, “Nonlinear elastic wave spectroscopy (NEWS) techniques to discern material damage, Part II: Single-mode nonlinear resonance acoustic spectroscopy,” *Journal of Research in Nondestructive Evaluation,* vol. 12(1), pp. 31-42, 2000.

[34] M. Gonzalez-Valadez, A. Baltazar and R. Dwyer-Joyce, “Study of interfacial stiffness ratio of a rough surface in contact using a spring model,” *Wear,* vol. 268, pp. 373-379, 2010.

[35] H. Teufelsbauer, Y. Wang, M. Chiou and W. Wu, “Flow–obstacle interaction in rapid granular avalanches: DEM simulation and comparison with experiment,” *Granular Matter,* vol. 11, pp. 209-220, 2009.

[36] S. Biwa, S. Hiraiwa and E. Mastumoto, “Stiffness evaluation of contacting surfaces by bulk and interface waves,” *Ultrasonics,* vol. 47, p. 123–129, 2007.

[37] P. BLANLOEUIL, A. MEZIANE, L. R. F. ROSE and al., “Analytical and numerical 1D modelling of the nonlinear scattering at a rough-surface contact interface with clapping,” *Journal of Sound and Vibration,* vol. 485, p. 115519, 2020.

[38] L. J., “ Formulation de l'endommagement des interfaces,” *C.R. Acad. Sci. ,* vol. SErie II, pp. 1047-1050, 1992.

[39] A. Needlman, “ A continuum model for void nucleation by inclusion debonding,” *J. Appl. Mech. ,* vol. 54, pp. 525-531, 525-531..

[40] V. Tvergaard, “ Effect of fiber debonding in a whisker-reinforced metal,” *Mater. Sci. Engrg. ,* vol. AI25 , pp. 203-213., 1990.

[41] J. Chaboche, R. Girard and P. Levasseur, “ Numerical analysis of composite systems by using interphase/interface models,” *Comput.Mech,* vol. 20, pp. 3-11, 1997.

[42] M. C. L. C. M. Raous, “ A consistent model coupling adhesion, friction, and unilateral contact.,” *Computer methods in applied mechanics and engineering,* Vols. 177(3-4), pp. 383-399, 1999.

[43] M. Frémond, “Adhérence des solides,” *Journal de Mécanique Théorique et Appliquée,* vol. 6, p. 383–407, 1987.

[44] M. Frémond, “Contact with adhesion,” *Nonsmooth Mechanics and Applications,* pp. 177-221, 1988.

[45] M. BENTAHAR and R. E. GUERJOUMA, “Monitoring progressive damage in polymer-based composite using nonlinear dynamics and acoustic emission.,” *The Journal of the Acoustical Society of America,* vol. 125, pp. EL39-EL44, 2009.

[46] K. V. D. Abeele and F. Windels, “Characterization and imaging of microdamage using nonlinear resonance ultrasound spectroscopy (NRUS) : An analytical model,” in *Universality of Nonclassical Nonlinearity,*, New York, Springer , 2006, p. 369–388.

[47] L. A. Ostrovsky and P. A. Jonhson, “Dynamic nonlinear elasticity in geomaterial,” *Rivista del nuovo cimento,* vol. 24(7), 2001.

[48] K. E.-A. V. D. Abeele, J. Carmeliet, J. A. T. Cate and P. A. Johnson, “Nonlinear elastic wave spectroscopy (NEWS) techniques to discern material damage, part II : Single-

mode nonlinear resonance acoustic spectroscopy," *Research in Nondestructive Evaluation,* vol. 12(1) , pp. 31-42, 2000.

[49] C. Payan, V. Garnier, J. Moysan and P. A. Johnson., "Applying nonlinear resonant ultrasound spectroscopy to improving thermal damage assessment in concrete," *Journal of the Acoustical Society of America,* vol. 121(4), p. 125–130, 2007.

[50] M. Muller, A. Sutin, R. Guyer, M. Talmant, P. Laugier and P. A.Johnson, "Nonlinear resonant ultrasound spectroscopy (nrus) applied to damage assessment in bone," *Journal of the Acoustical Society of America,* vol. 118(6), p. 3946–3952, 2005.

[51] M. Meo, U. Polimeno and G. Zumpano, "Detecting damage in composite material using nonlinear elastic wave spectroscopy methods," *Applied Composite Materials,* vol. 15, p. 115–126, 2008.

[52] M. A. Breazeale and D. O. Thompson, "Finite-amplitude ultrasonic waves in aluminum," *Applied Physics Letters,* vol. 3(5), p. 77–78, 1963.

[53] A. Gedroits and V. A. Krasilnikov, "Sov. Phys.," *JETP ,* vol. 16, pp. 1122-1126, 1963.

[54] A. Hikata, B. B. Chick and C. Elbaum, "Effect of dislocations on finite amplitude ultrasonic waves in aluminum," *Applied Physics Letters,* vol. 3(11), pp. 195-197, 1963.

[55] V. V. S. Jaya Rao, E. Kannan, R. V. Prakash and K. Balasubramaniam, "Fatigue damage characterization using surface acoustic wave nonlinearity in aluminum alloy AA7175-T7351," *Journal of Applied Physics,* vol. 104(12), p. 123508, 2008.

[56] O. Buck, W. L. Morris and J. M. Richardson, " Acoustic harmonic generation at unbonded interfaces and fatigue cracks," *Applied Physics Letters,* vol. 33(5), p. 371 – 373, 1978.

[57] T. Nam, T. Lee, C. Kim, K. Y. Jhang and N. Kim, "Harmonic generation of an obliquely incident ultrasonic wave in solid–solid contact interfaces," *Ultrasonics,* vol. 52(6), pp. 778-783, 2012.

[58] S. Biwa, S. Yamaji and E. Mastumoto, "Quantitative evaluation of harmonic generation at contacting interface," *American Institute of Physics,* p. 978, 2008.

[59] T. H. Lee and K. Y. Jhang, "Experimental investigation of nonlinear acoustic effect at crack," *NDT & E International,* vol. 42(8), pp. 757-764, 2009.

[60] D. Yan, "The detectability of kissing bonds in adhesive loints using ion-linear ultrasonic techniques," (Doctoral dissertation, University of Bristol), 2010.

[61] J. H. Cantrell and W. T. Yost, "Nonlinear ultrasonic characterization of fatigue microstructures," *International Journal of fatigue,* vol. 23, pp. 487-490, 2001.

[62] J. Y. Kim, L. J. Jacobs, J. Qu and J. W. Littles, "Experimental characterization of fatigue damage in a nickel-base superalloy using nonlinear ultrasonic waves," *The Journal of the Acoustical Society of America,* vol. 120(3), pp. 1266-1273, 2006.

[63] S. V. Walker, J. Y. Kim, J. Qu and L. J. Jacobs, "Fatigue damage evaluation in A36 steel using nonlinear Rayleigh surface waves," *Ndt & E International,* vol. 48, pp. 10-15, 2012.

[64] D. J. Barnard, L. J. H. Brasche, D. Raulerson and A. D. Degtyar, "Monitoring fatigue damage accumulation with Rayleigh wave harmonic generation measurements," *AIP Conference Proceedings ,* vol. 657, pp. 1393-1400, 2003.

[65] J. Frouin, S. Sathish, T. E. Matikas and J. K. Na, “Ultrasonic linear and nonlinear behavior of fatigued Ti–6Al–4,” *Journal of materials research,* vol. 14(4), pp. 1295-1298, 1999.

[66] P. Blanloeuil, “Analyse de la non-linéarité acoustique de contact pour l’évaluation et le contrôle non destructif,” (Doctoral dissertation), 2013.

[67] A. Mukhopadhyay, R. Sarkar, S. Punnose, J. Valluri, T. K. Nandy and K. Balasubramaniam, “Scatter in nonlinear ultrasonic measurements due to crystallographic orientation change induced anisotropy in harmonics generation,” *Journal of Applied Phys,* vol. 111(5), p. 054905, 2012.

[68] C. S. Kim, I. K. Park and K. Y. Jhang, “Nonlinear ultrasonic characterization of thermal degradation in ferritic 2.25 Cr–1Mo steel,” *Ndt & E International,* vol. 42(3), pp. 204-209, 2009.

[69] A. Ruiz, N. Ortiz, A. Medina, J. Y. Kim and L. J. Jacobs, “Application of ultrasonic methods for early detection of thermal damage in 2205 duplex stainless steel,” *Ndt & E International,* vol. 54, pp. 19-26, 2013.

[70] J. H. Cantrell and W. T. Yost, “Determination of precipitate nucleation and growth rates from ultrasonic harmonic generation,” *Applied Physics Letters,* vol. 77(13), pp. 1952-1954, 2000.

[71] D. Yan, B. W. Drinkwater and S. A. Neild, “Measurement of the ultrasonic nonlinearity of kissing bonds in adhesive joints,” *Ndt & E International,* vol. 42(5), pp. 459-466, 2009.

[72] Ohara.Y, Mihara.T and Yamanaka.K, “Effect of adhesion between crack planes on subharmonic and dc responses in nonlinear ultrasound,” *Ultrasonics,* vol. 44, p. 194–199, 2005.

[73] X. A. Verbeek, L. A. Ledoux, J. M. Willigers, P. J. Brands and A. P. Hoeks, “Experimental investigation of the pulse inversion technique for imaging ultrasound contrast agents,” *The Journal of the Acoustical Society of America,* vol. 107(4), pp. 2281-2290, 2000.

[74] K. Y. Jhang, “Applications of nonlinear ultrasonics to the NDE of material degradation,” *Ultrasonics, Ferroelectrics and Frequency Control, IEEE Transactions,* vol. 47(3), pp. 540-548, 2000.

[75] M. Fukuda, T. Harada and K. Imano, “Application of high-polymer adhesive tape to closed-crack detection using second-harmonic ultrasonic pulse waves,” *Acoustical Science and Technology,* vol. 36(2), pp. 175-177, 2015.

[76] G. L. Jones and D. R. Kobett, “Interaction of elastic waves in an isotropic solid,” *The Journal of the Acoustical society of America,* vol. 35(1), pp. 5-10, 1963.

[77] K. Y. Jhang, “Nonlinear ultrasonic techniques for nondestructive assessment of micro damage in material: a review. I,” *International journal of precision engineering and manufacturing,* vol. 10(1), pp. 123-135, 2009.

[78] P. Duffour, M. Morbidini and P. Cawley, “ A study of the vibro-acoustic modulation technique for the detection of cracks in metals,” *The Journal of the Acoustical Society of America,* vol. 119(3), pp. 1463-1475, 2006.

[79] J.-Y. Kim, V. A. Yakovlev and S. I. Rokhlin, “Surface acoustic wave modulation on a partially closed fatigue crack,” *The Journal of the Acoustical Society of America,* vol. 115(5), p. 1961–1972, 2004.

[80] V. Zaitsev, V. Nazarov, V. Gusev and B. Castagnede, “Novel nonlinear-modulation acoustic technique for crack detection,” *NDT & E International,* vol. 39(3), pp. 184-194, 2006.

[81] K. Zacharias, B. E., I. Hatzokos, R. I. T. and A. Trochidis, “Microdamage evaluation in human trabecular bone based on nonlinear ultrasound vibro-modulation (NUVM),” *Journal of biomechanics,* vol. 42(5), pp. 581-586, 2009.

[82] V. V. Kazakov, A. Sutin and P. A. Johnson, “Sensitive imaging of an elastic nonlinear wave-scattering source in a solid,” *Applied Physics Letters,* vol. 821(4), pp. 646-648, 2002.

[83] M. Vila, F. Vander Meulen, S. Dos Santos, L. Haumesser and O. B. Matar, “Contact phase modulation method for acoustic nonlinear parameter measurement in solid,” *Ultrasonics,* Vols. 12(1-9), pp. 1061-1065, 2004.

[84] A. J. Croxford, P. D. Wilcox, B. W. Drinkwater and P. B. Nagy, “The use of non-collinear mixing for nonlinear ultrasonic detection of plasticity and fatigue,” *The Journal of the Acoustical Society of America,* vol. 126(5), pp. EL117-EL122, 2009.

[85] Z. ZHANG, P. B. NAGY and W. HASSAN, “On the feasibility of nonlinear assessment of fatigue damage in hardened IN718 specimens based on non-collinear shear wave mixing,” *AIP Conference Proceedings,* p. 060003, 2016.

[86] I. Solodov, N. Krohn and G. Busse, “CAN: an example of nonclassical acoustic nonlinearity in solids,” *Ultrasonics,* vol. 40 , p. 621–625, 2002.

[87] K. Yamanaka, T. Mihara and T. Tsuji, “Nondestructive Evaluation-Evaluation of Closed Cracks by Model Analysis of Subharmonic Ultrasound,” *Japanese Journal of Applied Physics-Part 1 Regular Papers and Short Notes,* vol. 43(5), pp. 3082-3087, 2004.

[88] D. Owens and R. Wendt, “Estimation of the surface free energy of polymers,” *J Appl Polym Sci ,* vol. 13, pp. 1741-1747 , 1969.

[89] E. Siryabe, M. Rénier, A. Meziane, J. Galy and M. Castaings, “ANISOTROPIE APPARENTE D'UN ADHÉSIF INDUITE PAR DES INTERPHASES IMPARFAITES ET ÉVALUATION DES RAIDEURS D'INTERFACES D'UN ASSEMBLAGE COLLÉ.,” in *JOURNEES COFREND 2017*, 2017.

[90] S. Biwa, S. Hiraiwa and E. Mastumoto, “Pressure-dependent stiffnesses and nonlinear ultrasonic response of contacting surfaces,” *Journal of Solid Mechanics and Materials Engineering,* vol. 3(1), p. 10–21, 2009.

[91] F. Asma and A. Bouazzouni, “Finite element model updating using FRF measurements,” *Shock and Vibration,* vol. 12, pp. 377-388, 2005.

[92] C. Pecorari, “Nonlinear interaction of plane ultrasonic waves with an interface between rough surfaces in contact,” *Journal of the Acoustical Society of America,* vol. 113(6), p. 3065–3072, 2003.

[93] G. Adams, “Contact modeling - force,” *Tribology International,* vol. 33, p. 431–442, 2000 .

[94] A. Baltazar, S. I. Rokhlin and C. Pecorari, “On the Relationship Between Ultrasonic and Micromechanical Properties of Contacting Rough Surfaces,” *Journal of the Mechanics and Physics of Solids,* vol. 50, p. 1397–1416, 2002.

[95] F. Massi, Y. Berthier and B. L., “Contact surface topography and system dynamics of brake squeal,” *Wear,* vol. 265, pp. 1784-1792, 2008.

[96] L. Landau and E. Lifshitz, Theory of Elasticity, Oxford: 3rd ed. Elsevier Ltd, 1986, p. Oxford.

[97] K. McCall and R. Guyer, “A new theoretical paradigm to describe hysteresis,discrete memory and nonlinear elastic wave propagation in rock,” *Nonlinear Processes in Geopgysics 3,* pp. 89-101, 1996.

[98] V. Gusev, V.Tournat and B.Castagnede, Nonlinear acoustic phenomena in micro-inhomogeneous media, London: Materials and Acoustic Handbooks, ISTE Ldt, 2009.

[99] C. P. a. al, “Determination of third order elastic constants in a complex solid applying coda wave interferometry,” *Applied physics letters,* vol. 94, p. 011904, 2009.

[100] R. El.Guerjouma, M. Deschamps and A. Gérard, “Acoustoélasticité sous incidence variable : une détermination des constantes élastiques du troisième ordre,” *Acustica,* vol. 77, 1992.

[101] G. Dace, R. Thompson and O. Buck, “Measurement of the acoustic harmonic generation for caracterization using contact transducer,” *Review of progress in Quantitative Nondestructive Evaluation(RPQNDE),,* vol. 11, pp. 2069-2076, 1992.

[102] A. LeBrun, Méthodes ultrasonores de caractérisation des matériaux endommagés, 1997: Thèse de doctorat, Université Paris VI-Pierre et Marie Curie.

[103] O. B. Matar, S. D. Santos, M. Vila and F. Meulen, “Acoustic Nonlinear Parameter Measurement in Solid with a Contact Phase Modulation Method,” *IEEE ULTRASONICS SYMPOSIUM,* vol. 881, 2002.

[104] K. Abeele, P.A.Johnson and A.Sutin, “NEWS techniques to discern material damage, Part I: NWMS(NonlinearWaveModulationSpectroscopy),” *Nondestructive Evaluation,* vol. 12, p. 17–30, 2000.

[105] L. Zarembo and V. Krasil’nikov, “Nonlinear phenomena in the propagation of elastic waves in solids,” *Soviet Physics Uspekhi,* vol. 13(6), p. 778, 1971.

[106] J.-M. Baik and R. Thompson, “Ultrasonic scattering from imperfect interfaces : A quasi-static model,” *Journal of Nondestructive Evaluation,* vol. 4, p. 177–196, 1984.

[107] N. Haines, “The theory of sound transmission and reflection at contacting surfaces,” CEGB Berkeley Nuclear Laboratories, Berkeley, UK, 1980.

[108] Korshak.B.A, S. Y and B. M., “ Dc effects, sub-harmonics, stochasticity and "memory" for contact acoustic nonlinearity,” *Ultrasonics,* vol. 40, p. 707–716, 2002.

[109] M. Scalerandi, V. Agostini, P. P. Delsanto, K. E.-A. V. D. Abeele and P. A. Johnson, “Local interaction simulation approach to modeling nonclassical, nonlinear behavoir in solids,” *Journal of the Acoustical Society of America,* vol. 113, 2003.

[110] S. Biwa, A.Suzuki and N. Ohno, “Evaluation of interface wave velocity, reflection coefficients and interfacial stiffnesses of contacting surfaces,” *Ultrasonics,* vol. 43, p. 495–502, 2005.

[111] Yamanaka.K, Mihara.T and Tsuji.T, “Evaluation of closed cracks by model analysis of subharmonic ultrasound,” *Japanese Journal of Applied Physics,* vol. 43(5B), p. 3082–3087, 2004.

[112] V. Aleshin and K. V. D. Abeele, “Microcontact-based theory for acoustics in microdamaged materials,” *Journal of the Mechanics and Physics of Solids,* vol. 55(2), pp. 366-390, 2007.

[113] F. Tranquart and al., “Clinical use of ultrasound tissue harmonic imaging,” *Ultrasound in Medicine and Biology ,* vol. 25(6), pp. 889-894, 1999.

[114] W. Morris, O. Buck and R. Inman., “Acoustic harmonic generation due to fatigue damage in high-strength aluminum,” *Journal of Applied Physics ,* vol. 50(11), pp. 6737-6741, 1979.

[115] J. H. Cantrell and W. T. Yost, “Nonlinear ultrasonic characterization of fatigue microstructures,” *International Journal of fatigue 23 (2001), p. 487-490.,* vol. 23 , pp. 487-490, 2001.

[116] J.-Y. Kim and al., “Experimental characterization of fatigue damage in a nickel-base superalloy using nonlinear ultrasonic waves,” *The Journal of the Acoustical Society of America,* vol. 120(3), pp. 1266-1273, 2006.

[117] G. Shui and al., “Nonlinear ultrasonic evaluation of the fatigue damage of adhesive joints,” *NDT & E International ,* vol. 70, pp. 9-15, 2015.

[118] K. V. D. Abeele, “Nonlinear Elastic Wave Spectroscopy combined with Time Reversal for the localization of defects,” in *4th Workshop on "Nonlinear acoustics*, GDRE-US, 2014.

[119] M. C. L. C. M. Raous, “Un modèle couplant adhérence et frottement pour le contact entre deux solides déformables.,” *Comptes Rendus de l'Académie des Sciences-Series IIB-Mechanics-Physics-Chemistry-Astronomy,* vol. 9, pp. 503-509, 1997.

[120] Y. Monerie, “Fissuration des matériaux composites rôle de l’interface fibre-matrice,” *Thesis, Université de la Méditerranée, Marseille, France,* 2000.

[121] M. Friswell and J. Penny, “A simple, nonlinear model of a cracked beam,” in *10th International Modal Analysis Conference*, San Diego, California, 1992.

[122] Yamanaka.K, Mihara.T and Tsuji.T, “Evaluation of closed cracks by model analysis of subharmonic ultrasound,” *Japanese Journal of Applied Physics,* vol. 43(5B), p. 3082–3087, 2004.

[123] J.M. and Richardson, “Harmonic Generation at an Unbonded Interface: I. Planar Interface Between Semi-Infinite Elastic Media,” *Int. J. Eng. Sci,* vol. 17, p. 73–85, 1979.

[124] M. Bossy, Gobet, E. and D. Talay, “A symmetrized Euler scheme for an efficient approximation of reflected diffusions,” *Journal of applied probability,* vol. 41, pp. 877-889, 2004.

[125] J. Krolikowski and J. Szczepek, “Prediction of Contact Parameters using Ultrasonic Method,” *Wear,* vol. 148, p. 181–195, 1991.

[126] A. M. Sutin and V. E. Nazarov, “Nonlinear acoustic methods of crack diagnostics,” *Radiophysics and quantum electronics,* Vols. 38(3-4), pp. 109-120, 1995.

[127] V. E. Nazarov and A. M. Sutin, “Nonlinear elastic constants of solids with cracks,” *The Journal of the Acoustical Society of America,* vol. 102(6), pp. 3349-3354, 1997.

[128] T. Nam, T. Lee, C. Kim, K. Y. Jhang and N. Kim, “Harmonic generation of an obliquely incident ultrasonic wave in solid–solid contact interfaces,” *Ultrasonics,* vol. 52(6), pp. 778-783, 2012.

[129] C. Pecorari, “Adhesion and nonlinear scattering by rough surfaces in contact: Beyond the phenomenology of the Preisach–Mayergoyz framework,” *The Journal of the Acoustical Society of America,* vol. 116(4), pp. 1938-1947, 2004.

[130] S. Biwa, S. Hiraiwa and E. Matsumoto, “Experimental and theoretical study of harmonic generation at contacting interface,” *Ultrasonics,* vol. 44, pp. 1319-1322, 2006.

[131] C. R. Farrar and K. Worden, “An introduction to structural health monitoring. Philosophical Transactions of the Royal Society A: Mathematical,” *Physical and Engineering Sciences,* vol. 365(1851), pp. 303-315, 2007.

[132] M. J. Crocker, Handbook of noise and vibration control., Hoboken: John Wiley & Sons, 2007.

[133] A. L. Thuras, R. T. Jenkins and H. T. O'Neil, “Extraneous frequencies generated in air carrying intense sound waves,” *The Journal of the Acoustical Society of America,* vol. 6(1), pp. 57-57., 1934.

[134] L. A. Ostrovsky, S. N. Gurbatov and J. N. Didenkulov, “Nonlinear acoustics in Nizhni Novgorod (A review),” *Acoustical Physics,* vol. 51(2), pp. 114-127, 2005 .

[135] T. Bateman, W. P. Mason and H. J. McSkimin, “Third-order elastic moduli of germanium,” *Journal of Applied Physics,* vol. 32(5), pp. 928-936, 1961.

[136] B. McKavanagh and F. D. Stacey, “Mechanical hysteresis in rocks at low strain amplitudes and seismic frequencies,” *Physics of the Earth and Planetary Interiors,* vol. 8(3), pp. 246-250, 1974.

[137] G. S. Shui and Y. S. Wang, “ Nondestructive evaluation of material damage using nonlinear Rayleigh waves approach,” *Advanced Materials Research,* vol. 463, pp. 1522-1526, 2012.

[138] A. Klepka, W. J. Staszewski, T. d. M. D. Uhl, F. Scarpa and K. F. Tee, “Impact damage detection in composite chiral sandwich panels,” *Key Engineering Materials,* vol. 518, pp. 160-167, 2012.

[139] T. Kujawska, J. Wójcik and A. Nowicki, “Determination of B/A of biological media by measuring and modeling nonlinear distortion of pulsed acoustic wave in two-layer system of media.,” *Acoustical Imaging,* vol. 30 (5), pp. 295-303, 2011.

Abstract

The past decades have been marked by a significant increase in research interest in nonlinearities in cracked solids. As a result a number of different nonlinear methods have been developed for damage detection. However, there still limited understanding of physical mechanisms related to the various nonlinearities due to contacts. This thesis is addressed to study the nonlinear interaction between a wave and an interface while taking into account adhesion, in order to, eventually, propose an efficient NDT method for characterization of contact interfaces. The study of the second-harmonic evolution to characterize the damage will be the focus of this work. The nonlinear interaction between a longitudinal wave and a contact interface is considered in one-dimensional medium by using the Finite Elements method.

Numerically, the contact interface is modelled by combining two approaches. One is based on acoustic methods and used in traction, while the other one is based on vibration methods and used in compression. The first one, consists in modelling the contact with an RCCM law. The study propose a detailed analysis on the interface behaviour in traction while taking into account the adhesion. It allows identifying the key parameters that govern the nonlinear signature of the RCCM contact law and so better understanding the interaction between a compression wave and a contact interface that exhibits adhesion in traction. The second one, used in compression, is based on a nonlinear interface stiffness model where the stiffness property of the contact interface is described as a function of the nominal contact pressure. The study consists in a complementary numerical and experimental analysis of nonlinear vibrational response due to the contact interface. It shows that the stiffness-pressure trend at lower pressures has a major effect on the nonlinear response of systems with contact interfaces. Finally, in order to exploit the proposed contact law defined in compression and traction, a strategy to identify the interface parameters during the interaction between a wave and an interface is proposed. The numerical results are promising in view of the characterization of contact interfaces.

Keywords: nonlinear dynamic response; nonlinear acoustics; second harmonics; experiments; numerical modelling; Finite Elements; interface stiffness

Résumé

Les dernières décennies ont été marquées par un intérêt accru pour les non-linéarités dues aux défauts localisés dans les solides (les fissures fermées par exemple) et aux interfaces de contact en général. En conséquence, un certain nombre de méthodes non-linéaires ont été développés pour la détection de ces défauts et caractérisation des interfaces de contact. Cependant, la compréhension des mécanismes physiques liés aux non-linéarités due contact reste limitée. Dans ce cadre, ce travail de thèse vise à étudier l'interaction non-linéaire entre une onde et une interface tout en intégrant plusieurs mécanismes liés au contact, afin de proposer, à terme, une méthode CND efficace pour la caractérisation des interfaces. L'étude de l'évolution du second harmonique pour caractériser ce type de défauts localisés et plus généralement les interfaces de contact sera au cœur de ce travail.

L'interaction non-linéaire entre une onde longitudinale et une interface de contact est modélisée en combinant deux approches. L'une est basée sur des méthodes acoustiques et utilisée en traction, tandis que l'autre est basée sur l'analyse vibratoire structurelle et utilisée en compression. La première consiste à modéliser le contact avec une loi RCCM. L'étude propose une analyse détaillée du comportement de l'interface en traction tout en intégrant l'adhérence. Elle permet d'identifier les paramètres clés qui régissent la signature non-linéaire de la loi RCCM et ainsi permet de mieux comprendre la physique derrière cette interaction non-linéaire. La deuxième méthode, utilisée en compression, est basée sur un modèle de rigidité d'interface non-linéaire où la rigidité d'interface est décrite en fonction de la pression de contact nominale. L'étude consiste en une analyse numérique et expérimentale complémentaires de la composante non-linéaire de la réponse dynamique du système due à la présence d'interface de contact. Elle montre que la tendance de la rigidité à faibles pressions a un effet majeur sur la réponse non-linéaire des systèmes avec des interfaces de contact. Enfin, les lois de contact proposées en compression et traction sont combinées en une seule loi pour permettre une meilleure corrélation entre les différents mécanismes de contact en compression et en traction et donc une meilleure caractérisation de la réponse non-linéaire du système. Les résultats numériques sont prometteurs en vue de la caractérisation d'interfaces de contact à partir de la réponse non-linéaire du système excité par une source extérieure et applicables à la détection non-destructive de l'endommagement.

Mots clés: réponse dynamique non-linéaire ; acoustique non-linéaire ; second harmonique ; Expérimental ; modélisation numérique ; éléments finis ; rigidité d'interface.

Sommario

Gli ultimi decenni sono stati caratterizzati da un crescente interesse per le non linearità inerenti al danneggiamento (difetti) dei solidi ed alle interfacce di contatto. Di conseguenza, diversi metodi di analisi non-lineare sono stati sviluppati per l'individuazione del danno e per la caratterizzazione delle interfacce di contatto. Tuttavia, la comprensione dei meccanismi fisici relativi alle non linearità di contatto rimane limitata.

In questo contesto, il lavoro di tesi è indirizzato all' analisi dell'interazione non lineare tra un'onda ed un'interfaccia, integrando diversi meccanismi legati al contatto, al fine di proporre gli strumenti idonei ad una metodologia di analisi non-distruttiva efficiente, per la caratterizzazione delle interfacce. Lo studio dell'evoluzione della seconda armonica per caratterizzare le proprietà di difetti localizzati e più in generale delle interfacce di contatto è dunque al centro di questo lavoro.

L'interazione non lineare tra un'onda longitudinale e un'interfaccia di contatto è stata qui analizzata combinando due approcci: uno basato sull'analisi di propagazione acustica, ed utilizzato per caratterizzare l'interfaccia in trazione; l'altro basato sull'analisi della vibrazione strutturale, ed utilizzato per la caratterizzazione dell'interfaccia in compressione. Il primo consiste nel modellare il contatto con una legge RCCM. Lo studio propone un'analisi dettagliata del comportamento dell'interfaccia in trazione, integrando l'adesione tra le due superfici in contatto. I parametri principali, che regolano la firma non lineare della legge RCCM, sono stati identificati, permettendo quindi una migliore comprensione della fisica alla base di questa interazione non lineare. Il secondo metodo, usato in compressione, si basa su un modello di rigidezza non lineare dell'interfaccia, in cui la rigidezza dell'interfaccia è descritta in funzione della pressione di contatto. Lo studio consiste in un'analisi complementare, numerica e sperimentale, della componente non-lineare della risposta dinamica del sistema, dovuta alla presenza di un'interfaccia di contatto. Si è così evidenziato come la non-linearità della rigidezza di contatto alle basse pressioni ha un effetto importante sulla risposta non-lineare del sistema. Infine, le leggi di contatto proposte in compressione e trazione sono state combinate in una unica legge di contatto, per permettere una correlazione più fine tra le non-linearità associate alle differenti fasi del contatto, sia compressione che trazione, e le caratteristiche della risposta non-lineare del sistema . I risultati numerici sono promettenti, in vista dello sviluppo di metodologie inverse per la caratterizzazione delle proprietà delle

interfacce di contatto a partire dalla risposta non-lineare ad una eccitazione esterna, applicabile nell’identificazione non-distruttiva del danno e dei contatti.

Parole chiave: risposta dinamica non lineare; acustica non lineare; seconda armonica; sperimentale; modellazione numerica; elementi finiti; rigidità dell'interfaccia.